

Unravelling the mechanisms of motor neuron degeneration in relation to TDP-43 pathology in amyotrophic lateral sclerosis

Evelien Van Schoor

Jury:

Supervisor:	Prof. Dietmar R. Thal
Co-supervisors:	Prof. Ludo Van Den Bosch Prof. Philip Van Damme
Chair examining committee:	Prof. Ghislain Opdenakker
Chair public defense:	Prof. Tania Roskams
Jury members:	Prof. Frederik De Smet Prof. Kristl Claeys Prof. Rosa Rademakers Prof. Joachim Weis

Dissertation presented in
partial fulfilment of the
requirements for the degree of
Doctor in Biomedical Sciences

December 2022

"The brain is a world consisting of a number of unexplored continents and great stretches of unknown territory"

– Santiago Ramon y Cajal

A word of appreciation

Firstly, I would like to thank my promotor, **Prof. Dietmar R. Thal**, for this amazing opportunity and for the support throughout the last five years. Thank you for the guidance and supervision, for your enthusiasm and passion for neuropathology (and football of course!), for always making time to discuss results during meetings, and for the very quick replies and meticulous revisions. You are a very involved PI and your door was always open whenever I needed to talk to you. I have learned so much during my PhD, thank you for everything!

Secondly, I would like to thank my co-promotor, **Prof. Ludo Van Den Bosch**. Thank you for the opportunity to perform part of my experiments in your lab, this allowed me to learn many new techniques. I am also very grateful for the desk space you provided me with, this way I did not have to run back and forth between two buildings all day 😊. Thank you for making time for progress meetings, for your enthusiasm when discussing results and for your constructive feedback. You made sure I was really a part of the Neurobiology lab, not only scientifically but also at non-scientific lab events. It has been amazing and I have you to thank for that!

Thirdly, I would like to thank my co-promotor, **Prof. Philip Van Damme**. Thank you for attending my progress meetings and providing me with valuable feedback on my project and manuscripts throughout the years. I very much appreciate the time you spent on this. You often made me look at my results from a different perspective, which allowed me to improve my work substantially.

I would also like to thank my internal jury members, **Prof. Kristl Claeys** and **Prof. Frederik De Smet**, for their guidance and feedback throughout the course of my PhD. Thank you for making time for all the milestones and presentations. Also a major thank you to my external jury members, **Prof. Rosa Rademakers** and **Prof. Joachim Weis**, for making time to review this thesis manuscript.

My PhD was a great experience thanks to all of my colleagues. Thank you to all the past and present members of the lab of Neuropathology. You have made these five years a lot of fun in and outside of the lab. I really enjoyed our dinners, game nights, escape rooms and laser shooting activities. **Simona**, you were always there whenever I needed help with something. You're a very kind, patient and generous person, and I think you don't realize how valuable you are to your colleagues. I really enjoyed all of our scientific and non-scientific chats in and outside of the lab. I wish you all the best in Hasselt, and I hope we stay in touch! **Sandra**, you were there with me from the start, discovering everything together. It was nice that we could help each other during the first year of our PhD. You are a good listener and always have some advice ready. You're doing great work in the lab, I love how you are so

passionate about neuropathology. I wish you all the best with your postdoc. **Jolien**, I'm happy I got to know you better these last years. You're a very kind and passionate person and I'm always impressed with your meticulous way of working. I enjoyed our many talks about plants, mental health and even cats 😊. Good luck with your senior postdoc and your cute family. **Bas**, it was so nice to work together with you on the cell death projects. You're kind, calm and easy to work with. Good luck with the rest of your PhD, I'm convinced you'll do a great job. **Marta**, never a dull moment with you around. I admire how determined you are. I really enjoyed our chats, and I wish you all the best in your new job, I'm sure you're doing equally great. **Xiaohang**, it was nice having you as a colleague. I wish you all the best for the future with your new job and your family. **Lieselot**, I missed my neuropathology ALS buddy in the lab these last two year. Thank you for being such a passionate and driven colleague. **Luís**, thank you for literally setting up the lab when you started your PhD. Thanks to you, everything was up and running by the time Sandra and I started. Good luck with your further career. **Tessa**, you're not part of the Neuropathology lab anymore, but I still remember you as my first lab rotation student, singing along with songs on the radio while you were doing experiments with us. You're such a cheerful and inspirational person, I miss having you around! Good luck finishing your PhD. **Greg, Klara and Grigoria**, it was nice to get to know all of you in the last year of my PhD. Greg, you're a special one, but I definitely enjoyed having you around. I love your weird kind of humor. Thanks for your advice on the moon fazes, I'm sure it helped my western blots ;-). Klara, thank you so much for all your help with statistics, I learned a lot from you. Grigoria, your smile is contagious; you're a great researcher and person. I wish all three of you best of luck with your projects. **Eline**, I'm happy you will be continuing my project, good luck! And last but not least, **Alicja**. Thank you for making me feel welcome when I started my PhD, for always being there to help me with whatever I needed. You're very valuable to the lab and will for sure be missed. I would also like to thank all the members of the **TCWO** lab, in particular Kathleen, Marleen and Annelies, and of course Yanti for organizing the after-work drinks 😊.

As I was also part of the lab of my co-promotors during my PhD, I would like to thank everyone from the lab of Neurobiology. Thank you for welcoming me in your lab, for helping me, especially in the beginning whenever I was lost and could not find what I was looking for (which happened many times), and for providing valuable feedback during lab meetings. Thank you for including me in the many non-scientific events you organized, I really enjoyed it! **Wenting**, you taught me everything there is to know about differentiating iPSC-derived motor neurons. I still remember following you around in the SCIL lab, impressed with the work you were doing. You are such a hardworking and kind person, I really enjoyed working with you. I wish you all the best in your new job. **Elke**, I'm really happy I got to know you. You're a great friend and were always there when I needed to vent about something or just needed to complain hehe 😊. It was great to share an office and go through the last steps of our PhD

together. You did fantastic work and I'm fully convinced you'll do equally great in your next job. It's a pity we couldn't go to Chicago together, but I definitely enjoyed our Encals trips ☺ I wish you and Johan all the best and I'm sure we will keep in touch (even though you exchanged the beautiful city of Leuven for Ghent)! **Valérie**, I know you do not like these extensive thank-you-messages, but I do want to use this opportunity to thank you for introducing me into the zebrafish world and for helping me so much with my project. Good luck finalizing your postdoc project, and I really hope you get some more sleep in the future ☺ **Jimmy**, I enjoyed working with you on your (way too many) projects, you're a great scientist and colleague. It was nice to get to know you and Sam (your wife, not girlfriend!) better at your wedding and in Edinburgh. You're a great couple and will be amazing parents. **Yvonne, Christine G., Silke, Lisha and Melissa**, I had a great time at our post-Encals Edinburgh city trip. Melissa, I enjoyed sharing an office with you. Thank you for being so kind, for making sure our plants did not die, and for all the delicious cookies you brought to our office. You really are one of a kind. I think I never met anyone who is as selfless as you are. Best of luck with your PhD and please be careful and don't get any more injuries! Silke, it was nice to organize Wetenschap op Stap together with you and Jimmy. Always stay your cheerful happy self, it is contagious ☺. Good luck with your PhD, you're doing a great job. Lisha, it was nice getting to know you better during our city trip, you're a very sweet person. Good luck with finalizing your PhD. Yvonne, you're a very hardworking and kind person, I enjoyed our chats in Edinburgh. I wish you all the best with the next steps in your life and career. **Dufie**, little did I know that apart from being the best student one could ask for, you are also a very talented bachata dancer. You really got me curious to try one of those classes ;-). Congrats again on your well-deserved FWO funding, and I wish you all the best with your fishy PhD project. **Katarina**, from the first moment I met you, you made an impression. You're a fantastic researcher and I really admire the confidence you radiate. I'm convinced you will do amazing work as a postdoc in your home country, best of luck with your academic career. **Arun**, you are one of the kindest persons I know. I enjoyed working with you, and I wish you all the best with your family and in your new job. **Donya**, always full of energy and new ideas. It was nice to have you around and talk to someone about TDP. I wish you all the best. **Nuray**, thank you for your energy and openness, and for involving me in all activities even before I had a desk space in the lab. I had a great time at the lab of Neurobiology the past few years, and that is for a big part thanks to you. **Kristel**, although none of my cell experiments made it in this thesis, you made sure that all the iPSC-related work was always very well organized and coordinated. Thanks for that! **Rob and Alessio**, you made the hours I spent in the iPSC flow much more fun. Rob, I always enjoyed chatting with you. Best of luck with your postdoc in Germany. Alessio, I'm already jealous of future Italian lunches, you guys make the best lasagna. Apart from your cooking and bachata skills, you're also just a really nice colleague. Best of luck with your PhD! **Nicole**, thank you for being so kind and for putting so much effort in the eco-team and so many other activities that are organized in the lab, I really

enjoyed all of it! **Wendy V.**, thank you for all the plant-related advice, I now almost consider myself a plant propagating expert ☺. **Mathias**, thanks for all your help with the confocal over the years, you are very valuable to the lab. Good luck finalizing your PhD. **Joke De Vocht**, I enjoyed working with you and Maria. It was always nice to catch up on research and personal stuff. I wish you the best for your scientific career and your beautiful family. **Maria**, you're so easy to work with. I'm happy you could stay here in Leuven and now have a nice (and challenging) PhD project, good luck! **Stijn**, I'm still impressed with your morning run on the lab weekend before everyone else was awake. Thank you for teaching me spikeball. I wish you all the best in your new job, they are lucky to have you! **Annet**, I enjoyed working with you, you are a very kind and witty colleague. I hope you have the time of your life while exploring our beautiful planet. **Fouke**, I love your energy and passion for yoga and vegan food. It was nice to get to know you better at Encals and I'm impressed with your career path. Good luck with your postdoc! **Kara**, you're doing a great job taking over the management of the zebrafish facility. Thank you for organizing everything so well and for being such a nice colleague. **Christine M.** and **Wendy S.**, I really enjoyed sharing an office with you. You're both such calm, friendly and helpful colleagues and it was nice to have our regular chats. **Claudia**, I'm happy you got a desk in our office. Thank you for joining me on a concert so last minute, it was nice to get to know you and your boyfriend better. Good luck with your scientific career. **Bennie** and **Matilde**, the newest Italian additions. Bennie, thank you for being such an energetic colleague. I wish you all the best with your challenging project, you'll do great. Matilde, I enjoyed getting to know you over the past few months. I love your energy and no-nonsense mentality. We make a great foosball team ;-). **Raheem**, it is nice to have you back in the lab. All the best with your studies and your family. **Tom**, you are such a fantastic and hardworking scientist. I wish you all the best in your academic career, and am fully convinced you will continue to do great work. **Thibaut**, you come across as a calm and rather quiet person, but since the lab weekend I know that still waters run deep ;-). It was nice to get to know you better, good luck with your postdoc. **Adria**, the Grinch of the lab. Thank you for being your grumpy and honest self, but also for your energy and enthusiasm. **Nikita**, it is a pity that I only recently got to know you better. Thank you for being such a kind and calm colleague. **Pegah**, it was nice to catch up every so often. Good luck with your further career. **Paraskevi**, thank you for being such a kind colleague. Good luck with finalizing your PhD. **Begga**, although I did not get to know you that well, you were always very kind to me. To the new people in the lab: **Daniëlle**, **Lenja**, **Lieselotte**, **Frederik**, **Louise**, **Margot**, I wish you all the best with your projects. Enjoy your time in this amazing lab! Finally, I also want to thank some ex colleagues. **Tijs**, **Elisabeth** and **Jolien S.**, thank you for making time to answer my many questions about jobs in industry. You all gave me very useful tips and feedback, I really appreciate it. I wish you all the best in your personal lives as well as in your impressive careers.

Ik wil ook graag de allerliefste Biomedische vriendinnen bedanken. **Marie**, het was fijn om geregeld bij te praten (met een ijsje uiteraard) en samen te ontspannen. We hebben de afgelopen jaren beiden een hobbelig traject afgelegd, maar we hebben het gehaald! Ik ben super trots op ons, en ik wens je het allerbeste in de toekomst, zowel op persoonlijk als professioneel vlak. **Eva**, dankjewel voor alle steun. Ik ben blij dat we na Gent contact zijn blijven houden, en ik geniet er elke keer enorm van als we elkaar zien en onze verhalen vertellen! Je bent intussen een fantastische wetenschapper, en ik wens je een mooie toekomst samen met Jens. Ook een dikke dankjewel aan **Margo, Sarah** en **Liese**. Het was altijd fijn om samen te kunnen lachen en ontspannen. Sarah, het deed deugd om af en toe bij elkaar ons hart te luchten. Ik wens je super veel succes met het afronden van je doctoraat! Ten slotte wil ik ook mijn familie bedanken. **Mama en papa**, dankjewel om mij altijd door dik en dun te steunen. Ik denk dat er weinig ouders zoveel begrijpen van het PhD onderwerp van hun dochter ;-). Dankjewel om altijd geïnteresseerd te luisteren als ik enthousiast was over iets, maar ook als het eens tegen stak en ik mijn frustraties moest uiten. **Ineke**, lieve zus, dankjewel voor alle steun! Ook bedankt aan mijn grootouders, om er altijd voor mij te zijn. Als laatste wil ik nog mijn allerliefste **Wouter** bedanken. Ik heb zoveel aan jou gehad de afgelopen twee jaar. Je steunt mij onvoorwaardelijk in alles wat ik doe. Op naar nieuwe uitdagingen samen.

Evelien

Table of Contents

A word of appreciation.....	i
List of abbreviations	ix
Abstract	1
Nederlandstalige samenvatting	3
GENERAL INTRODUCTION	5
1. Amyotrophic lateral sclerosis	5
1.1. Clinical features	5
1.2. Genetics.....	6
1.3. Neuropathological characteristics.....	7
2. Frontotemporal dementia.....	8
2.1. Clinical features and classification	9
2.2. Genetics.....	10
2.3. Neuropathological characteristics and classification	10
3. TDP-43 toxicity and spreading.....	11
3.1. TDP-43 toxicity.....	11
3.2. TDP-43 prion-like spreading	13
4. ALS neurodegenerative pathomechanisms.....	16
4.1. Neuronal degeneration: cell death mechanisms	16
4.1.1. Apoptosis.....	16
4.1.2. Necroptosis.....	18
4.1.3. Pyroptosis.....	19
4.1.4. Autophagy-related cell death.....	22
4.2. Axonal degeneration	24
4.2.1. Axonal dysregulation in ALS	24
4.2.2. TUBA4A in ALS: why microtubules are more than just a loading control	26
5. Modelling ALS neurodegeneration.....	28
OBJECTIVES.....	31
CHAPTER I: Necrosome-positive granulovacuolar degeneration is associated with TDP-43 pathological lesions in the hippocampus of ALS/FTLD cases.....	33
1. Abstract	34
2. Introduction.....	35
3. Materials and methods	36
4. Results	41

5. Discussion	49
6. Supplementary information	53
CHAPTER II: Increased pyroptosis activation in white matter microglia is associated with neuronal loss in ALS motor cortex	59
1. Abstract	60
2. Introduction.....	60
3. Materials and methods	62
4. Results	67
5. Discussion.....	77
6. Supplementary information	83
CHAPTER III: Frontotemporal lobar degeneration case with an N-terminal <i>TUBA4A</i> mutation exhibits reduced <i>TUBA4A</i> levels in the brain and TDP-43 pathology	95
1. Abstract	96
2. Introduction.....	96
3. Materials and methods	97
4. Results	100
5. Discussion.....	105
6. Conclusions.....	107
7. Supplementary information	108
CHAPTER IV: <i>TUBA4A</i> downregulation as observed in ALS <i>post-mortem</i> motor cortex causes ALS-related abnormalities in zebrafish.....	111
1. Abstract	112
2. Introduction.....	112
3. Materials and methods	114
4. Results	117
5. Discussion	122
6. Supplementary information	125
GENERAL DISCUSSION	133
1. Neuronal demise in ALS: a delicate interplay between cell death pathways?	134
2. Cytoskeletal defects in ALS.....	136
3. The dying-back versus dying-forward hypothesis.....	137
4. The role of pathological TDP-43 in ALS	139
5. Concluding remarks and future perspectives	142
Scientific acknowledgements and personal contributions	145
Conflicts of interest statement.....	146
References.....	147
Curriculum Vitae.....	159

List of abbreviations

AAA	ATPases associated with diverse cellular activities	eIF4G	Eukaryotic translation initiation factor 4 G
AD	Alzheimer's disease	EMA	European Medicines Agency
ALRs	Absent in melanoma-like receptors	EPS	Extrapyramidal symptoms
ALS	Amyotrophic lateral sclerosis	ER	Endoplasmic reticulum
ALS+FTLD-TDP	Cases with ALS and FTLD-TDP	EXT2	Exostosin glycosyltransferase 2
ALS/FTLD	Cases with TDP-43 proteinopathy with ALS and/or FTLD	F-actin	Filamentous actin
AMO	Antisense oligonucleotide morpholinos	FADD	Fas-associated protein with death domain
APAF1	Cytochrome c-apoptotic protease activating factor 1	fALS	Familial ALS
APP	Amyloid precursor protein	FDA	Food and Drug Administration
ASC	Apoptosis-associated speck-like protein containing a CARD	FDG	Fluorodeoxyglucose
ATG	Autophagy-related gene	FL	Full-length
ATP	Adenosine triphosphate	FTLD	Frontotemporal lobar degeneration
ATXN2	Ataxin 2	FTD	Frontotemporal dementia
Aβ	Amyloid beta	FTLD-FUS	FTLD with FUS pathology
bvFTD	Behavioral variant FTD	FTLD-tau	FTLD with tau pathology
C9orf72	Chromosome 9 open reading frame 72	FTLD-TDP	FTLD with TDP-43 pathology
CA	Cornu ammonis	FUS	Fused in sarcoma
CARD	Caspase recruitment domain	G3BP	Ras GTPase-activating protein-binding protein 1
CBS	Corticobasal syndrome	GAPDH	Glyceraldehyde-3-phosphate dehydrogenase
CCP	Cytosolic carboxypeptidase	GCI	Glial cytoplasmic inclusions
CERAD	Consortium to Establish a Registry for Alzheimer's disease	GFNI	Granulofilamentous neuronal inclusions
CFEOM	Congenital fibrosis of the extra-ocular muscles	GOF	Gain-of-function
cFLIP	Cellular FLICE-like inhibitory protein	GRN	Progranulin
CHCHD10	Coiled-coil-helix-coiled-coil-helix domain containing 10	GSDMD	Gasdermin D
CHMP2B	Charged multivesicular body protein 2b	GSDMD-NT	Gasdermin D N-terminal region
ciAP1/2	cellular inhibitor apoptosis protein 1/2	GVD	Granulovacuolar degeneration
CK1δ	Casein kinase 1 delta	GVDn+	GVD positive for the activated necrosome
CNS	Central nervous system	HA	Hemagglutinin
CSF	Cerebrospinal fluid	HD	Huntington's disease
CTFs	C-terminal fragments	HDAC6	Histone deacetylase 6
CYLD	Cylindromatosis lysine 63 deubiquitinase	Hpf	Hours post fertilization
DAB	3,3'-diaminobenzidine	HRP	Horseradish peroxidase
DAMPs	Damage-associated molecular patterns	HSPs	Heat shock proteins
DCTN1	Dynactin 1	IBMPFD	Inclusion body myopathy with Paget's disease of bone and FTD
DN	Dystrophic neurites	IF	Intermediate filament
DPR	Dipeptide repeat protein	IFN	Interferon
DR	Death receptor	IHC	Immunohistochemistry
DSB	Double stranded break	IL	Interleukin
		iPSC	induced pluripotent stem cell
		KIF5A	Kinesin family member 5A
		LAMP1	Lysosomal-associated membrane protein 1
		LATE	Limbic-predominant age-related TDP-43 encephalopathy
		LATE-NC	LATE neuropathological change

LBD	Lewy body dementia	PSP	Progressive supranuclear palsy
LOF	Loss-of-function	PSPS	PSP syndrome
LLPS	Liquid-liquid phase separation	pTDP-43	Phosphorylated TDP-43
LMN	Lower motor neuron	PTMs	Post-translational modifications
LNA	Locked nucleic acid	PYD	Pyrin domain
LPS	Lipopolysaccharide	p62/SQSTM1	Sequestosome-1
LSPS	Liquid-to-solid phase separation	RAN	Repeat associated non-ATG
LUBAC	Linear ubiquitin chain assembly complex	RIN	RNA integrity number
lvPPA	Logopenic variant PPA	RIPK1/3	Receptor-interacting protein kinase 1/3
MAPs	Microtubule-associated proteins	ROS	Reactive oxygen species
MAPT	Microtubule-associated protein tau	RRM	RNA recognition motif
MLKL	Mixed lineage kinase domain-like protein	RT-qPCR	Reverse transcription quantitative polymerase chain reaction
MND	Motor neuron disease	sALS	Sporadic ALS
MRI	Magnetic resonance imaging	SD	Semantic dementia
MSA	Multi system atrophy	SDS-PAGE	Sodium dodecyl sulfate-polyacrylamide gel electrophoresis
MT	Microtubule	SIRT2	Sirtuin 2
MTL	Medial temporal lobe	SOD1	Superoxide dismutase 1
NCI	Neuronal cytoplasmic inclusions	SPAST	Spastin
NES	Nuclear export signal	SQSTM1	Sequestosome-1
NF-H	Neurofilament heavy	SV2	Synaptic vesicle 2
NFT	Neurofibrillary tangle	svPPA	Semantic variant PPA
nfvPPA	Non-fluent variant PPA	TARDBP	Transactive response DNA-binding protein
NFκB	Nuclear factor-κB	TBCB	Tubulin folding cofactor B
NII	Neuronal intranuclear inclusions	TBS	Tris-buffered saline
NLRs	Nucleotide-binding domain leucine-rich repeat-containing receptors	TBK1	TANK-binding kinase 1
NLRP3	NOD-, LRR- and pyrin domain-containing protein 3	TDP-43	Transactive response DNA-binding protein 43kDa
NLS	Nuclear localization signal	TEER	Touch-evoked escape response
NMJs	Neuromuscular junctions	TIA1	TIA1 cytotoxic granule associated RNA binding protein
OPTN	Optineurin	TLL	Tubulin tyrosine ligase
PAMPs	Pathogen-associated molecular patterns	TLRs	Toll-like receptors
PBS	Phosphate-buffered saline	TNF	Tumour necrosis factor
PD	Parkinson's disease	TRADD	TNF receptor-associated death domain protein
PET	Positron emission tomography	TRAF2	TNF receptor-associated factor 2
PFA	Phosphate-buffered formaldehyde	TRAIL	TNF-related apoptosis-inducing ligand
PFN1	Profilin 1	TREM2	Triggering receptor expressed on myeloid cells 2
PI3K	Phosphatidylinositol 3-kinase	TSZ	TNFα+Smac-mimetic+zVAD-fmk
PLS	Primary lateral sclerosis	TTLL	Tubulin tyrosine ligase-like
PMA	Progressive muscular atrophy	TUBA4A	Alpha tubulin 4A
pMLKL	Phosphorylated mixed lineage kinase domain-like protein	UBQLN2	Ubiquilin 2
PPA	Primary progressive aphasia	UMN	Upper motor neuron
pRIPK1/3	Phosphorylated receptor-interacting protein kinase 1/3	UTR	Untranslated region
PRP	Prion protein	VCP	Vasolin containing protein
PRPH	Peripherin	WM	White matter
PRRs	Pattern recognition receptors	WT	Wild-type
PSEN	Presenilin		

Abstract

Amyotrophic lateral sclerosis (ALS) is a neurodegenerative disorder characterized by the loss of motor neurons, leading to progressive muscular paralysis. This devastating disease affects about 1-2 persons per 100.000 per year with a disease onset around mid-adulthood. Patients usually die 2-5 years after the first symptoms due to respiratory failure. The major pathological hallmark of 97% of ALS patients is the cytoplasmic mislocalization and aggregation of transactive response DNA-binding protein 43kDa (TDP-43) in the brain and spinal cord. The role of TDP-43 pathology in motor neuron degeneration is still uncertain, as there is evidence that inclusion bodies might represent an inert aggregation state of pathological TDP-43, or even have a protective function. Apart from TDP-43 pathology, another hallmark of ALS is the specific degeneration of the upper and lower motor neurons. Most research investigating cell death mechanisms in ALS has focused on apoptosis. More recently, evidence pointed towards a role for necrotic cell death, such as necroptosis or pyroptosis, in ALS. Until now, it is not yet clear what the importance of different types of cell death is in ALS, and if pathological TDP-43 plays a role herein. Finally, apart from dysfunction of the neuronal cell body, affected nerve cells also display axonal degeneration. It is becoming increasingly apparent that microtubules play a critical role in axonal pathology. As such, mutations in tubulin alpha 4A (*TUBA4A*) were recently associated with ALS, highlighting the importance of cytoskeletal stability in ALS.

The aim of this PhD project was to clarify the mechanisms of neuronal and axonal degeneration in ALS. For this, we used *post-mortem* central nervous system tissue from ALS and frontotemporal lobar degeneration (FTLD) patients, as well as two *in vivo* models: TDP-43^{A315T} transgenic mice and zebrafish. Specifically, we investigated the activation of necroptosis and pyroptosis pathways in relation to TDP-43 pathology. Additionally, we looked into cytoskeletal disturbances, focusing on the role of *TUBA4A* dysfunction in genetic as well as sporadic ALS and FTLD.

First, we investigated the involvement of different types of necrotic cell death in ALS in relation to TDP-43 pathology. We did not detect a significant activation of the necroptosis pathway in ALS-affected brain and spinal cord regions using *post-mortem* tissue. However, in patients with FTLD with TDP-43 pathology (FTLD-TDP), necroptosis activation, reflected by the presence of phosphorylated mixed lineage kinase domain-like protein (pMLKL), was observed in hippocampal regions and was associated with the burden of TDP-43 pathology. On the other hand, microglial pyroptosis activation was increased in the ALS precentral white matter and correlated with neuronal loss in the motor cortex, but not with TDP-43 pathological aggregation. Similar results were obtained in symptomatic TDP-

43^{A315T} transgenic mice, where microglial pyroptosis activation was significantly increased in the motor cortex upon symptom onset, and correlated with neuronal demise.

Secondly, we assessed the role of tubulin alterations in axonal and neuronal degeneration in ALS, focusing on *TUBA4A* specifically. We pathologically described a patient with the semantic variant of primary progressive aphasia with a frameshift mutation c.187del (p.Arg64Glyfs*90) in *TUBA4A*. The patient displayed underlying FTLD-TDP type C pathology. No truncated TUBA4A protein was detected, although total full-length TUBA4A levels were decreased in the brain, suggestive of a haploinsufficiency mechanism. We observed a similar TUBA4A protein downregulation in the brain of sporadic ALS patients, which we were able to mimic in zebrafish by the injection of antisense oligonucleotide morpholinos. This led to a motor axonopathy and a disturbed motor behavior, both of which were morpholino dose-dependent and could be rescued by the addition of human wild-type *TUBA4A* mRNA.

In conclusion, our findings provide new insights into the mechanisms of motor neuron and axonal degeneration in ALS. It is clear that several disease mechanisms are at play in ALS, amongst which microglial pyroptosis activation, cytoskeletal disturbances and protein aggregation, as demonstrated in this thesis. This indicates that ALS is a multifactorial disease, which can be initiated through different pathways. Ultimately, it will be key to elucidate the pathogenicity of distinct affected pathways in ALS in order to come to a multi-targeted approach that can be of benefit for the majority of ALS patients, which do not have a clear genetic cause of this devastating disease.

Nederlandstalige samenvatting

Amyotrofe laterale sclerose (ALS) is een neurodegeneratieve aandoening gekenmerkt door het verlies van motorische neuronen, hetgeen leidt tot een progressieve verlamming van de spieren. Deze aandoening komt voor bij ongeveer 1-2 personen per 100.000 per jaar en begint gewoonlijk rond middelbare leeftijd. Patiënten overlijden meestal 2-5 jaar na de eerste symptomen door respiratoir falen. Het voornaamste pathologische kenmerk van 97% van de patiënten met ALS is de abnormale cytoplasmatische lokalisatie en aggregatie van 'transactive response DNA-binding protein 43kDa' (TDP-43) in de hersenen en het ruggenmerg. De rol van TDP-43 in het afsterven van motorische neuronen is nog onduidelijk. Er zijn aanwijzingen dat TDP-43 inclusies een inert aggregatiestadium van pathologisch TDP-43 vertegenwoordigen, of dat ze zelfs een beschermende functie zouden hebben. Naast TDP-43 pathologie wordt ALS ook gekenmerkt door de specifieke degeneratie van de bovenste en onderste motorische neuronen. Het merendeel van het wetenschappelijk onderzoek naar celdood mechanismen in ALS was voornamelijk gefocust op apoptose. Meer recent onderzoek toont aan dat necrotische celdood, zoals necroptose en pyroptose, een rol zou spelen in ALS. Tot heden is het onduidelijk wat de bijdrage is van de verschillende types celdood in ALS, en in welke mate TDP-43 hier een rol in speelt. Naast een disfunctie van het neuronale cellichaam, vertonen zenuwcellen ook degeneratie van de axonen. Het wordt meer en meer duidelijk dat microtubuli een belangrijke rol spelen in deze axonale pathologie. De recente ontdekking van genetische mutaties in tubuline alfa 4A (*TUBA4A*) in ALS benadrukt het belang van de stabiliteit van het cytoskelet in ALS.

Het doel van dit PhD project was om de mechanismen van neuronale en axonale degeneratie in ALS te ontrafelen. Hiervoor maakten we gebruik van centraal zenuwstelsel weefsel van patiënten met ALS en frontotemporale lobaire degeneratie (FTLD), alsook van twee *in vivo* modellen: TDP-43^{A315T} transgene muizen en zebrafissen. We onderzochten de activatie van necroptose en pyroptose en de rol van TDP-43. Daarnaast bestudeerden we mogelijke abnormaliteiten van het cytoskelet, waarbij we specifiek focusten op de rol van *TUBA4A* disfunctie in genetische en sporadische ALS en FTLD.

Allereerst onderzochten we de rol van verschillende types necrotische celdood in ALS. We detecteerden geen significante necroptose activatie in *post-mortem* hersenen en ruggenmerg van ALS patiënten. Echter, in patiënten met FTLD met TDP-43 pathologie (FTLD-TDP) observeerden we necroptose activatie in hippocampale regio's, gereflecteerd door de aanwezigheid van gefosforyleerd mixed lineage kinase domain-like protein (pMLKL). Dit was geassocieerd met de hoeveelheid TDP-43 pathologie. Anderzijds was er meer microgiale pyroptose activatie aanwezig in de precentrale witte stof van ALS patiënten, wat correleerde met het verlies van neuronen in de motorische cortex, maar

niet met TDP-43 pathologie. We verkregen gelijkaardige resultaten in symptomatische TDP-43^{A315T} transgene muizen, waar microgliale pyroptose activatie significant hoger was in de motorische cortex bij het optreden van symptomen, wat eveneens correleerde met een verlies van neuronen.

Ten tweede evalueerden we de rol van tubuline veranderingen in axonale en neuronale degeneratie in ALS, waarbij we specifiek of *TUBA4A* focusten. We rapporteerden een pathologische analyse van een patiënt met de semantische variant van primaire progressieve afasie met een frameshift mutatie c.187del (p.Arg64Glyfs*90) in *TUBA4A*. De patiënt vertoonde onderliggende FTLD-TDP type C pathologie. We detecteerden geen verkort TUBA4A eiwit, hoewel het totale TUBA4A eiwitniveau lager was in de hersenen van deze patiënt, suggestief voor een haploinsufficiëntie mechanisme. We observeerden een gelijkaardige daling van TUBA4A eiwitniveaus in de hersenen van patiënten met sporadische ALS, hetgeen we konden nabootsen in zebrafissen door de injectie van antisense oligonucleotide morfolinos. Dit leidde tot een motorische axonopathie en een verstoorde motoriek. Beide fenotypes waren afhankelijk van de morfolino dosis, en werden sterk verminderd waargenomen wanneer humaan wild-type *TUBA4A* mRNA mee werd geïnjecteerd.

Onze bevindingen brengen nieuwe inzichten in de mechanismen van motor neuron en axonale degeneratie in ALS. Het is duidelijk dat verschillende ziektemechanismen een rol spelen in ALS, waaronder microgliale pyroptose activatie, verstoringen van het cytoskelet en eiwitaggregatie, zoals aangetoond in deze thesis. Dit wijst erop dat ALS een multifactoriële ziekte is, welke geïnitieerd kan worden via verschillende pathways. Uiteindelijk zal het cruciaal zijn om de pathogeniciteit van de verschillende ziektemechanismen in ALS te bepalen om tot een combinatoriële behandeling te komen met het doel om patiënten met deze vreselijke ziekte te helpen.

GENERAL INTRODUCTION

1. Amyotrophic lateral sclerosis

Amyotrophic lateral sclerosis (ALS) was first described in 1874 by Jean-Martin Charcot and is also known as motor neuron disease (MND) or Lou Gehrig's disease, after the famous baseball player Lou Gehrig, who died from the disease (1,2). ALS is a neurodegenerative disorder characterized by progressive muscular paralysis resulting from the loss of motor neurons in the motor cortex, brainstem and spinal cord. 'Amyotrophy' refers to the atrophy of muscles, while 'lateral sclerosis' reflects the hardening of the anterior and lateral corticospinal tracts by axonal degeneration and gliosis (3). ALS is an orphan disease with an incidence of 1-2 persons per 100.000 per year and a lifetime risk estimated to be 1 in 400. The mean age of onset varies between 55-65 years. Patients usually die 2-5 years after disease onset due to respiratory failure (2-4).

1.1. Clinical features

The majority of ALS patients presents with classical spinal-onset symptoms, while 25% display bulbar-onset (due to an initial loss of motor neurons in the brainstem) and only 3-5% show respiratory-onset (5). Classical spinal-onset ALS usually starts with asymmetric, painless weakness in a limb, which later on progresses to paralysis of nearly all skeletal muscles. It can include or evolve to symptoms of lower motor neuron (LMN; located in the brainstem and spinal cord) dysfunction including fasciculations, cramps and muscle wasting, or upper motor neuron (UMN; located in the motor cortex) dysfunction presenting as spasticity and muscle weakness (6). Patients with bulbar-onset ALS on the other hand present with dysarthria, dysphagia, facial weakness and tongue fasciculations. These patients have a worse prognosis, with a mean survival of approximately two years (5). Patients with respiratory-onset ALS show orthopnea or dyspnea, possibly in combination with mild spinal cord or bulbar signs, with a mean survival of only 1.4 years (5). Some subsets of motor neurons, such as those innervating the extraocular muscles or sphincters, are spared until late in the disease (3). The diagnosis of ALS requires progressive UMN and LMN symptoms in one out of four body segments (cranial/bulbar, cervical, thoracic or lumbosacral), or clinical or electromyographic LMN symptoms in two body segments, as defined in the El-Escorial criteria (7-9). More restricted phenotypes are primary lateral sclerosis (PLS) with only UMN involvement, and progressive muscular atrophy (PMA) with exclusive LMN involvement (6).

Apart from motor neuron symptoms, up to 50% of ALS patients also develop some cognitive and/or behavioral impairment, with 13% presenting with comorbid behavioral variant frontotemporal dementia (bvFTD; cf. infra) (10). Apart from this clinical overlap, ALS and bvFTD also share pathological

(e.g. presence of transactive response DNA-binding protein 43kD (TDP-43) protein pathology) and genetic (e.g. *C9orf72* repeat expansion) features, suggesting that ALS and bvFTD constitute extremes of a disease spectrum, with patients presenting with overlapping ALS and bvFTD in the center (3).

Until today, only two disease-modifying treatments are available, i.e. riluzole and edaravone (11). Riluzole is a glutamatergic neurotransmission inhibitor and was the first approved drug for ALS in 1995. However, it does not have an effect on symptoms and only poses modest benefits on survival (12). More recently, edaravone, an antioxidant drug, was approved for use by the US regulatory authorities Food and Drug Administration (FDA), but not by the European Medicines Agency (EMA) (13,14). Its use as a treatment for ALS is still under debate. Other than these two drugs, patients are often treated symptomatically to improve their quality of life. Examples are physiotherapy, muscle relaxants, nutritional support and noninvasive ventilation (15).

1.2. Genetics

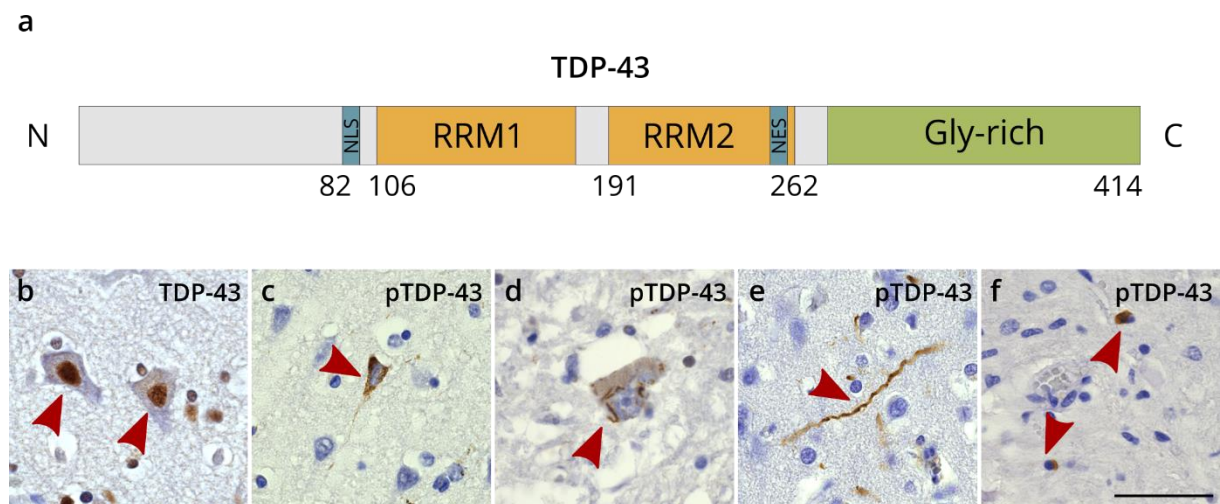
The majority of ALS cases (~90%) are considered sporadic (sALS), meaning that there is no family history of the disease, although gene mutations can rarely occur. The other 10% of cases are classified as familial ALS (fALS), where the genetic mutation is usually inherited in an autosomal dominant manner (2,3,16). The first ALS gene to be identified was superoxide dismutase 1 (*SOD1*) in 1993 (17). Mutations in *SOD1* account for up to 20% of fALS and 1-2% of sALS cases (18,19). After that, it took 15 years until the discovery of the next ALS-related gene, i.e. transactive response DNA-binding protein (*TARDBP*) in 2008 (20), in which mutations are found in only 4% of fALS and 1% of sALS patients (18,19). Later on, mutations in the gene fused in sarcoma (*FUS*) (4% fALS; 1% sALS) and repeat expansions in chromosome 9 open reading frame 72 (*C9orf72*) (25-55% fALS; 5% sALS) were identified (18,19). This *C9orf72* hexanucleotide repeat expansion ranges from hundreds to thousands of repeat units in patients. In contrast, non-affected individuals usually have a repeat length of only 2-30 repeats (21). Recently, a case with a repeat length of 38 displaying the typical clinical picture of ALS was described (22), shedding light on the pathogenic threshold of the *C9orf72* repeat expansion to trigger TDP-43 pathology and the development of ALS (cf. 1.3).

Mutations in these four genes (i.e. *SOD1*, *TARDBP*, *FUS* and *C9orf72*) explain more than 75% of the familial ALS cases. Variants in other genes occur only in a minority of fALS and sALS cases, and include amongst others *TBK1*, *OPTN*, *SQSTM1*, *VCP*, *PFN1*, *KIF5A*, *TUBA4A*, and *UBQLN2* (18,23,24). Functionally, these ALS-related genes can be divided into three distinct groups: genes implicated in protein homeostasis, genes involved in RNA stability, function and metabolism, and genes with a function in cytoskeletal dynamics (3). This pinpoints crucial pathways that may be relevant for ALS

pathobiology. Therefore, further elucidation of the genetic basis of ALS will aid in understanding the pathological molecular mechanisms underlying the disease.

1.3. Neuropathological characteristics

At autopsy, ALS patients typically display degeneration of motor neurons in the primary motor cortex, the brainstem and in the anterior horn of the spinal cord. Additionally, scarring of the lateral tracts of the spinal cord can be observed. As about 97% of ALS patients exhibit cytoplasmic accumulation of TDP-43 in neurons of the brain and spinal cord, ALS is considered a TDP-43 proteinopathy (10,25,26). In patients with *FUS* and *SOD1* mutations on the contrary, the main aggregate components are FUS and SOD1 proteins respectively, with TDP-43 aggregates rarely observed (27,28). TDP-43 was discovered in 2006 as the main aggregating protein in ALS cases displaying ubiquitin-positive tau-negative and α -synuclein-negative inclusions (25,26). It is a 414 amino acid DNA/RNA-binding protein that is predominantly located in the nucleus, but is able to shuttle between the nucleus and the cytoplasm. It contains two RNA recognition motifs (RRMs), a glycine-rich prion-like C-terminal domain, a nuclear localization signal (NLS) and a nuclear export signal (NES) (Fig. 1a,b) (29). In ALS, TDP-43 mislocalizes to the cytoplasm, where it accumulates in aggregates. In these pathological conditions, TDP-43 is often phosphorylated, ubiquitylated and cleaved into C-terminal fragments (30,31). Apart from neuronal inclusions, which can present as neuronal cytoplasmic inclusions or dystrophic neurites, TDP-43 can also accumulate in glial cells (Fig. 1c-f) (32,33).

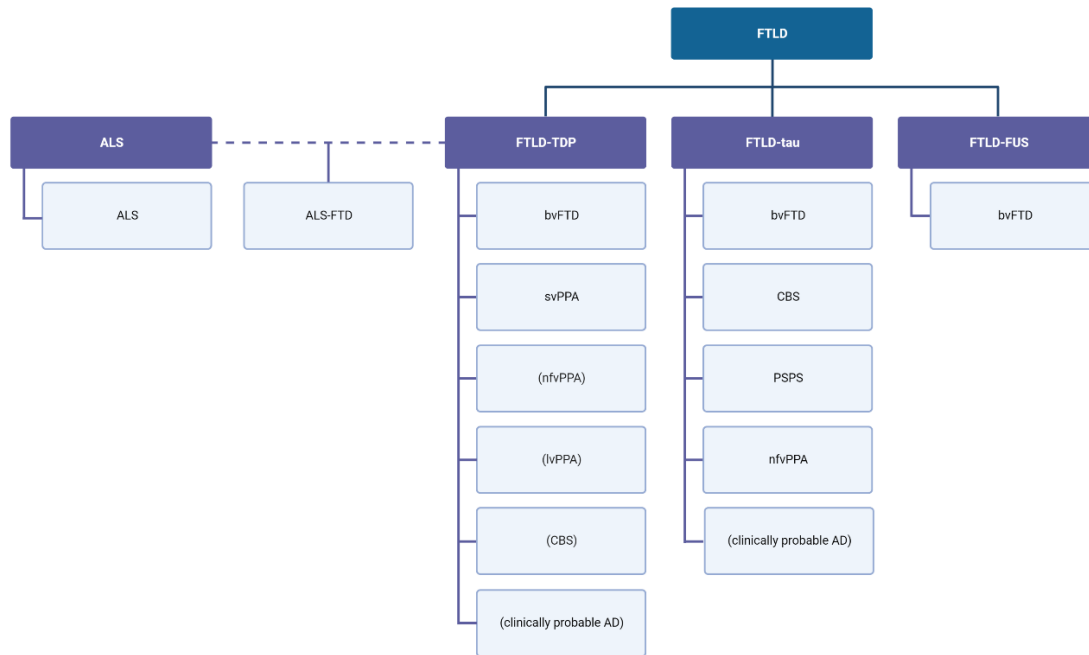


General introduction - Figure 1. TDP-43 protein structure and pathological lesions. a. TDP-43 consists of two RNA-recognition motifs (RRM), a nuclear localization signal (NLS), a nuclear export signal (NES) and a C-terminal glycine-rich prion-like domain. N: amino-terminus, C: carboxyl-terminus. b. Normal nuclear TDP-43-positive staining of pyramidal neurons in the motor cortex. c-f. pTDP-43 staining in ALS patient tissue showing neuronal cytoplasmic inclusions in the motor cortex (c) and the spinal cord (d), as well as dystrophic neurites (e) and glial inclusions (f). Scale bar represents 50 μ m.

Carriers of a *C9orf72* repeat expansion also reveal intranuclear RNA foci and cytoplasmic inclusions composed of dipeptide repeat proteins (DPRs). These DPR inclusions result from unconventional repeat associated non-ATG (RAN) translation of the GGGGCC repeat expansion (34). Translation of the sense transcript from three different reading frames gives rise to three distinct DPRs, poly(glycine-alanine (GA)), poly(glycine-proline (GP)) and poly (glycine-arginine (GR)). On the other hand, the antisense transcript generates poly(GP), poly(proline-arginine (PR)) and poly(proline-alanine (PA)). DPR pathology is abundantly present in the cerebellum, all neocortical areas and the hippocampus of *C9orf72* ALS/FTD patients, with moderate levels of pathology in subcortical areas and limited DPR lesions in lower motor neurons (35). In addition, DPR pathology was found in circadian sleep/wake-associated cells and along the hypothalamic-pituitary axis, possibly reflecting sleep/wake disturbances and neuroendocrine alterations observed in ALS/FTD (36,37). However, no association between DPR pathology and the degree of neurodegeneration was observed, contrary to TDP-43 pathology (35,38).

2. Frontotemporal dementia

FTD was first described by Arnold Pick back in 1892, but the first clinical and neuropathological consensus criteria were only defined in 1994 (39,40). As the name implies, FTD is characterized by degeneration of the frontal and temporal lobes (41). It is a heterogeneous clinical syndrome that can include symptoms such as progressive changes in behavior, language and personality, usually with relative sparing of memory function (42,43). FTD is the second most common dementia in persons under the age of 65 following Alzheimer's disease, with an incidence approximated at 2-4 persons per 100.000 per year and a lifetime risk estimated to be 1 in 742 (43,44). The age of onset varies between 45-80 years, depending on the clinical subtype (cf. infra 2.1) (43). The neuropathological correlate for FTD is referred to as frontotemporal lobar degeneration (FTLD). As mentioned earlier, some patients clinically present with ALS-FTD, with ALS-FTLD as corresponding neuropathology, stressing the overlap between both diseases (Fig. 2).



General introduction - Figure 2. The ALS-FTLD-TDP spectrum with the different FTLD subtypes and their clinical correlates. Illustration of the ALS-FTLD-TDP spectrum with FTLD subtypes FTLD-TDP, FTLD-tau and FTLD-FUS along their accompanying clinical presentations. AD = Alzheimer’s disease, bvFTD = behavioral variant FTD, svPPA = semantic variant PPA, nfvPPA = non-fluent variant PPA, lvPPA = logopenic variant PPA, CBS = corticobasal syndrome, PSPS = progressive supranuclear palsy syndrome. Less frequent phenotypes are in parentheses.

2.1. Clinical features and classification

FTD can be categorized into three distinct clinical syndromes, based on clinical presentation: behavioral variant FTD (bvFTD), non-fluent/agrammatic variant primary progressive aphasia (nfvPPA) and semantic variant PPA (svPPA or semantic dementia) (41,42). BvFTD encompasses 60% of all FTD cases and is characterized by changes in behavior, such as disinhibition, impulsive or inappropriate behavior, self-neglect, apathy, lack of insight and loss of empathy (39,43,45). PPA comprises 40% of FTD and is characterized by language deficits such as anomia (i.e. impaired word retrieval) (43). Patients with nfvPPA display non-fluent speech, with as two main features agrammatism and speech apraxia, the latter being effortful, halting speech (46,47). In svPPA on the other hand, spontaneous speech is fluent, but patients display deficits in single-word comprehension and/or object recognition (46). FTD can also clinically overlap with ALS as discussed earlier, with up to 20% of FTD patients developing motor neuron symptoms (47). Additionally, FTD can overlap with atypical Parkinsonian disorders, such as corticobasal syndrome and progressive supranuclear palsy (42,47). The expected survival for FTD patients ranges from three to eleven years from disease onset, depending on the clinical subtype (44). Currently, no disease-modifying treatment is available. Symptomatic treatments focusing on neurotransmission are widely used, based on efficacy in treating other neurodegenerative or psychiatric disorders with similar clinical involvement. Examples include selective serotonin reuptake inhibitors, acetylcholinesterase inhibitors, antipsychotics and antiepileptic drugs (47).

2.2. Genetics

FTD also has a strong genetic component with approximately 30-50% of patients showing a family history of dementia, psychiatric disease or motor symptoms, of which at least 10% have a clear autosomal dominant inheritance pattern (47,48). In 1988, the microtubule-associated protein tau (*MAPT*) gene was the first gene found to be linked to FTD, accounting for 5-20% of familial cases and rarely being observed in sporadic cases (49,50). Only in 2006, a second major FTD-associated gene was discovered: progranulin (*GRN*) (51,52). Mutations in *GRN* account for 5-20% of familial FTD and 1-5% of sporadic FTD (50). Five years later, repeat expansions in *C9orf72* were identified as a third major genetic component in patients with FTD, explaining 21% of familial and 6% of sporadic FTD cases (21,50). Apart from these three genes, autosomal dominant mutations in *VCP*, *CHMP2B*, *TARDBP*, *FUS*, *SQSTM1*, *CHCHD10*, *TBK1*, *TIA1*, *EXT2* and *OPTN1* account for less than 6% of all FTD cases (48,53). Importantly, there is a significant overlap in the genetic background of ALS and FTD. Genes that can be involved in the development of ALS as well as of FTD include *C9orf72*, *TARDBP*, *FUS*, *TBK1*, *VCP* and *SQSTM1*. Furthermore, patients with mutations in *C9orf72*, *TBK1* and *SQSTM1* can clinically present with both ALS and FTD (54).

2.3. Neuropathological characteristics and classification

FTLD is an underlying neuropathological correlate of FTD. FTLD can be classified into three main pathological subtypes, depending on the protein that is aggregated: FTLD-tau, FTLD-TDP and FTLD-FUS (Fig. 2) (39). FTLD-TDP can be the underlying neuropathology of bvFTD and svPPA, and in rare instances of nvPPA, logopenic variant PPA (lvPPA) or corticobasal syndrome (CBS) (41). Patients with FTLD-tau pathology usually present with bvFTD, nvPPA, CBS or progressive supranuclear palsy syndrome (PSPS) syndrome, while FTLD-FUS patients clinically show early onset bvFTD (55). In this thesis, we will focus on FTLD-TDP, which is, like ALS, a TDP-43 proteinopathy. In these patients, TDP-43 inclusions are mainly located in the frontotemporal cortex and hippocampus (25,26). The types of TDP-43-positive lesions detected include neuronal cytoplasmic inclusions (NCI), neuronal intranuclear inclusions (NII), dystrophic neurites (DN), glial cytoplasmic inclusions (GCI) and granulofilamentous neuronal inclusions (GFNI). Based on the type and distribution of these lesions in the neocortex, FTLD-TDP was further subdivided into different subtypes (56,57). FTLD-TDP type A cases show numerous NCI and short DN in layer II, with rare NII (Fig. 3). Clinically, it is associated with bvFTD and nvPPA, while genetically it is linked to *GRN* mutations. In FTLD-TDP type B, mainly NCI are present in all cortical layers, with few DN in the white matter (Fig. 3). This subtype clinically mainly presents as bvFTD, possibly in combination with ALS. Genetically, it is most often associated with *C9orf72* repeat expansions. Long DN in layer II are characteristic for FTLD-TDP type C, with only few NCI and no white matter pathology (Fig. 3). Clinically, these patients usually present with svPPA or bvFTD, with no known genetic associations. The

less common FTLD-TDP type D is characterized by the presence of lentiform NII in superficial as well as deep layers, with few NCI and absence of white matter pathology (Fig. 3). This is associated with a familial syndrome caused by *VCP* mutations, namely inclusion body myopathy with Paget's disease of bone and frontotemporal dementia (IBMPFD). More recently a fifth subtype, i.e. FTLD-TDP type E, was identified and clinically associated with rapidly progressive bvFTD (57). Cases with this subtype present with abundant GFNI and fine dot-like gray matter grains affecting all cortical layers, with the presence of oligodendroglial inclusions in the white matter (Fig. 3). Similar to type D, type E is a rare subtype, with 81-96% of FTLD-TDP cases classifying as subtypes A, B or C (39). On a final note regarding neuropathology in FTLD-TDP, cases carrying a *C9orf72* repeat expansion also display DPR pathology similar to ALS cases (35), as discussed above.

	Type A	Type B	Type C	Type D	Type E
I					
II					
III					
IV					
V					
VI					
WM					

General introduction - Figure 3. FTLD-TDP pathological subtypes. Overview of FTLD-TDP pathological subtypes, including type A, B, C, D and E with representative TDP-43 pathological lesions in different layers (I-VI) of the gray matter (neuronal and glial pathology) and in the white matter (glial pathology). WM: white matter.

3. TDP-43 toxicity and spreading

3.1. TDP-43 toxicity

As mentioned before, TDP-43 is predominantly localized in the nucleus, but can shuttle to the cytoplasm. Its localization to the nucleus occurs through active transport, while export to the cytoplasm can also take place by passive diffusion (58). Importantly, TDP-43 regulates its own expression levels via a negative feedback loop, in which it binds a region in the 3' untranslated region (UTR) of its own *TARDBP* transcript (58,59). This tight regulation is critical to maintain proper levels of functional TDP-43 (60). Apart from its role in DNA/RNA-binding, TDP-43 was also shown to be involved in both the assembly and maintenance of stress granules. Moreover, TDP-43 regulates the expression of several stress granule proteins, such as *G3BP*, *TIA-1* and *eIF4G* (61,62). Interestingly, the TDP-43 C-

terminal region can undergo liquid-liquid phase separation (LLPS) to form dynamic protein droplets. Detrimental mutations, stress and aging are thought to drive these droplets to undergo liquid-to-solid phase separation (LSPS), eventually leading to the formation of pathological protein aggregates (61). This pathological aggregation can cause TDP-43 to become dysfunctional by reducing its nuclear localization (58).

The identification of ALS-related mutations in *TARDBP* is indicative of a causal role for TDP-43 in ALS pathogenesis. The observed consequences of *TARDBP* mutations include increased aggregation propensity, enhanced cytoplasmic localization, altered protein stability, resistance to proteases, and modified binding interactions (61). However, it remains debated if the resulting TDP-43 protein aggregates are a primary cause of ALS, an inert byproduct of the disease, or the result of a protective cellular response to neurotoxicity (63). There is evidence supporting both a loss-of-function (LOF) and a toxic gain-of-function (GOF) following the cytoplasmic mislocalization and aggregation of TDP-43. Nuclear TDP-43 depletion seems to precede the formation of cytoplasmic pathological aggregates, and it is argued that TDP-43-associated alterations in mRNA metabolism resulting from a LOF are more crucial in disease pathogenesis compared to the aggregation of TDP-43 (61). Indeed, a study suggested that the increase in cytoplasmic TDP-43, and therefore reduction in nuclear levels, but not the aggregation of TDP-43, is neurotoxic (64). In addition, both mice heterozygous for *TARDBP* and mice overexpressing wild-type TDP-43 displayed impaired motor function (60), indicating the importance of maintaining physiological levels of TDP-43. It was also shown that transgenic models expressing mutant *TARDBP* do not necessarily exhibit TDP-43 pathological aggregates in their brain and spinal cord, suggesting nuclear depletion of TDP-43 as a crucial event for neurodegeneration, as these mice presented with typical ALS motor symptoms (65). This questions the toxicity of TDP-43 protein aggregates as observed in *post-mortem* tissues of 97% of ALS patients, and suggests that inclusion bodies might represent an inert aggregation state of pathological TDP-43. In fact, similar to other neurodegenerative disorders, protein aggregates may not be as toxic as their preceding soluble oligomers (66–68).

Apart from hyperphosphorylation and ubiquitination of TDP-43, the protein is also cleaved into C-terminal fragments (CTFs). These 25kDa and 35kDa CTFs were detected in ALS and FTLD-TDP brain tissue in the detergent-insoluble fraction (25). It is thought that the remaining N-terminal fragment of TDP-43 is rapidly degraded following cleavage of the full-length (FL) protein (69). Contrary to brain tissue, these CTFs are not detected in ALS spinal cord aggregates (70), questioning its toxicity and relevance for motor neuron degeneration. Furthermore, multiple studies showed that transgenic mice expressing TDP-43 CTFs do not exhibit a clear ALS-like phenotype of motor dysfunction (69). Overall, the question remains what the truly toxic TDP-43 species is in ALS disease pathogenesis.

3.2. TDP-43 prion-like spreading

In recent years, misfolded proteins have been shown to act as seeds of aggregation that can sequester their native isoforms and convert these into pathological molecules. This resembles the replication of infectious prions and is therefore called 'prion-like spreading' (63). In contrast to the evidence for tau and α -synuclein transmission, evidence for prion-like spreading of TDP-43 is only beginning to emerge. Similar to prion diseases, motor neuron loss and TDP-43 pathology start focally and, during the progression of the clinical disease, spread across central nervous system (CNS) regions in a spatiotemporal manner (63). This implies that TDP-43 pathology not solely affects the pyramidal motor system, but rather progresses towards a multisystem neurodegenerative disorder (32). A sequential spreading of TDP-43 pathology in ALS has been proposed, whereby TDP-43 seems to initially spread from the motor neocortex towards other brain regions (71). This spreading was defined by four stages. In the first stage, where ALS cases have the lowest burden of phosphorylated TDP-43 (pTDP-43) pathology, lesions are observed in the motor cortex, brainstem nuclei and motor neurons of the spinal cord. Next, the pathology involves the prefrontal neocortex, the brainstem reticular formation, the precerebellar nuclei and the red nucleus in stage two. In stage three, pathology further spreads into the postcentral neocortex and striatum, whereas stage four involves anteromedial portions of the temporal lobe, such as the hippocampus. Based on this sequential spreading of pTDP-43 pathology, the authors suggest that pTDP-43 seeds propagate along axonal pathways (72). Similar conclusions were obtained for pTDP-43 pathology in bvFTD, where also four patterns of pTDP-43 propagation were determined. Here, pathology initiates in the orbital gyrus, the gyrus rectus and the amygdala in stage one. Next, pathology spreads towards the middle frontal and anterior cingulate gyrus, as well as the anteromedial temporal lobe, the superior and medial temporal gyri, the striatum, red nucleus, thalamus and precerebellar nuclei in stage two. With further progression to stage three, pTDP-43 is detected in the motor cortex, bulbar somatomotor neurons and the spinal cord. Finally, cases with stage four display pTDP-43 lesions in the visual cortex (73). Although the distance between the brain regions involved in ALS and FTD is often substantial, affected neurons are connected by axonal projections, suggesting that physical contact between nerve cells might be important for the spreading of pathology (74). Indeed, there is evidence that TDP-43 can be transported through the axon anterogradely as well as retrogradely (75). Interestingly, TDP-43 cytoplasmic inclusions were also found in other neurodegenerative disease, such as Alzheimer's disease (AD) (up to 57% of cases), Parkinson's disease (PD) and Huntington disease (HD) (58,76). In AD, TDP-43 pathology was reported to first appear in the amygdala and to spread towards entorhinal and hippocampal areas, as well as to the occipitotemporal and inferior temporal cortical areas and, finally, the frontal cortex and basal ganglia (77,78). TDP-43 pathology was recently also described in medial temporal lobe structures in

older adults, named limbic-predominant age-related TDP-43 encephalopathy neuropathological change (LATE-NC), and was associated with an amnesic dementia syndrome (79). This indicates that TDP-43 pathology can affect different neuronal subtypes and CNS regions, depending on the neurodegenerative disease.

Apart from the sequential spreading pattern of pTDP-43 in several neurodegenerative diseases, additional evidence for prion-like properties comes from the structure of the TDP-43 protein. The C-terminal region of TDP-43 comprises a glycine-rich domain and a part enriched in glutamine and asparagine (Q/N) amino acids. This shows sequence similarities to yeast prion proteins and is therefore referred to as the prion-like domain (58,61). It was shown that proteins containing such a prion-like domain are more vulnerable to changes that affect their physical properties, eventually altering their physical state and converting them into pathological aggregates (58,80). Interestingly, this C-terminal region contains most of the ALS-associated *TARDBP* mutations, as well as pathological phosphorylation sites (61). It was shown that the expression of TDP-43 CTFs in cell lines as well as primary motor neurons led to the formation of abnormally phosphorylated and ubiquitinated cytoplasmic aggregates as well as splicing abnormalities, indicating that TDP-43 CTF expression can recapitulate key pathological features of ALS (70,75). Another group confirmed this, showing that TDP-43 CTFs could drive the co-aggregation of full-length (FL) TDP-43, therefore affecting the function of FL TDP-43 in a dominant negative way, by reducing its nuclear localization (81). On the other hand, Zhang and colleagues showed that the expression of a 25kDa TDP-43 CTF induced cell death through a toxic gain-of-function, without affecting the functionality of FL TDP-43 (82).

In 2011, Furukawa and colleagues for the first time showed *in vitro* evidence of a TDP-43 seeding reaction. They triggered the intracellular aggregation of overexpressed HA-tagged endogenous TDP-43 by transfection with fibrillary aggregates derived from *in vitro* TDP-43. The resulting aggregates were sarkosyl-insoluble and ubiquitinated, similar to aggregates found in ALS patient tissue. However, these inclusions were not hyperphosphorylated. Their data indicate that TDP-43 fibrils can function as seeds to trigger the aggregation of endogenous TDP-43 (83). Two years later, Nonaka *et al.* reported the induced aggregation of overexpressed HA-tagged TDP-43 in SH-SY5Y cells following transduction of the insoluble protein fraction derived from ALS or FTLD-TDP *post-mortem* brain tissue. The resulting aggregates were ubiquitinated and hyperphosphorylated, and could be used to seed further aggregation in cultures of naïve cells, supporting a pathological prion-like propagation of TDP-43 in ALS and FTLD-TDP (84). Other groups later confirmed this in neuronal cultures (85–87). Similar results were obtained with the addition of ALS/FTD-derived cerebrospinal fluid (CSF) to cultured cells, where pathological TDP-43 present in the CSF could seed endogenous TDP-43 mislocalization and aggregation (88). Importantly, Shimonaka *et al.* identified the specific C-terminal regions responsible for the

templated aggregation of TDP-43. When they transduced synthetic TDP-43 peptides 274-313 and 314-353 in cells, this led to seed-dependent aggregation of phosphorylated TDP-43 (89).

In 2018, Porta and colleagues for the first time showed the seeding and propagation of TDP-43 pathology *in vivo*. They injected brain-derived FTL-DTP extracts in transgenic mice expressing a cytoplasmic NLS mutant of human TDP-43 in forebrain neurons. This led to the formation of pTDP-43-positive neuronal cytoplasmic inclusions in the neocortex and hippocampus. They observed spreading of pTDP-43 pathology via the connectome, along with a maturation of pTDP-43-positive aggregates (90). Interestingly, they demonstrated that distinct TDP-43 species or strains from FTL-DTP brains might confer different seeding capabilities (90), which was confirmed by other groups (91,92). More recently, a study by Smethurst *et al.* demonstrated seeded aggregation and propagation of TDP-43 following exposure of human induced pluripotent stem cell (iPSC)-derived motor neurons to ALS *post-mortem* spinal cord homogenates (93). These motor neurons were more vulnerable to TDP-43 aggregation and toxicity compared to human iPSC-derived astrocytes. Furthermore, astrocytes were neuroprotective to the seeded aggregation in motor neurons. Finally, they concluded that the toxicity was conferred by TDP-43 oligomers present in the ALS spinal cord extracts (93). This important research using human iPSC-derived motor neurons and glial cells not only allows the examination of seeding and propagation in disease-relevant cell types, but also provides researchers with the opportunity to study the effects of ALS-related mutations in patient-derived cells.

Finally, with regard to the route of TDP-43 propagation, it has been shown that TDP-43 can be transported between neurons by means of axonal transport (75). On the other hand, several groups showed interneuronal transmission of pathogenic TDP-43 through the medium of cultured cells via microvesicles or exosomes (85,88). Other researchers, who did not observe the transfer of TDP-43 through conditioned medium, could not recapitulate this (86,94). Ultimately, results from *in vitro*, mouse and human *post-mortem* studies suggests that TDP-43 is mainly propagated via axonal pathways. There is growing evidence for a prion-like seeding and spreading mechanism of TDP-43 pathology in neurodegenerative diseases, indicating that in ALS and FTL-DTP, TDP-43 aggregation most likely does not independently originate in distinct CNS regions following cellular insults, but starts focally and propagates as the disease develops. More research focusing on TDP-43 toxicity and spreading in motor neurons *in vitro* and *in vivo* is needed to elucidate the exact pathogenic mechanisms of motor neuron protein pathology, as well as the role of the surrounding glial cells. Furthermore, the question remains to what extent TDP-43 oligomers and aggregates are instrumental in the eventual degeneration of motor neurons.

4. ALS neurodegenerative pathomechanisms

4.1. Neuronal degeneration: cell death mechanisms

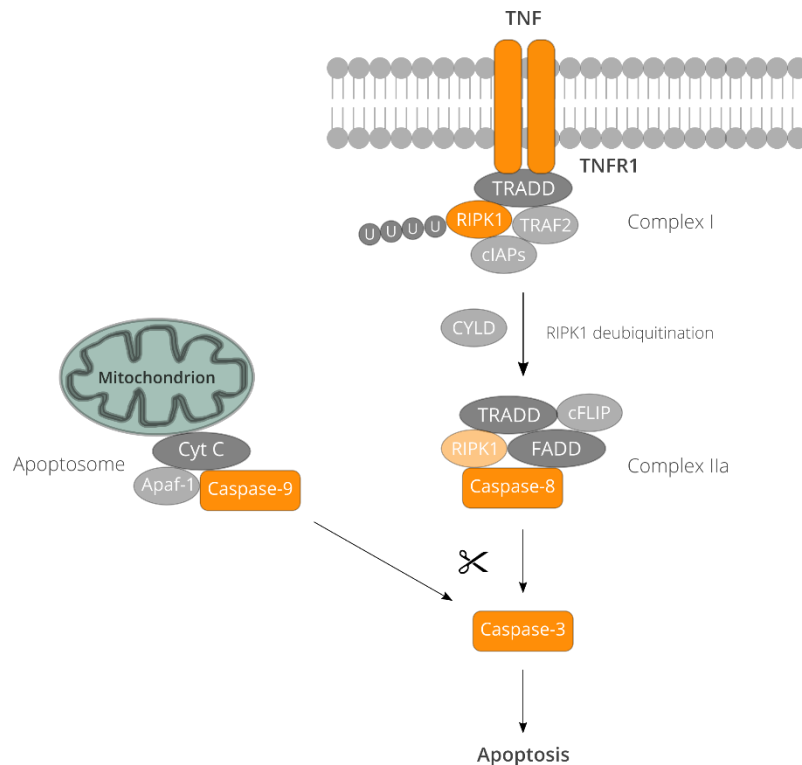
Apart from protein aggregation, another main pathological hallmark of ALS is the specific degeneration of the upper and lower motor neurons. This motor neuron dysfunction and death is thought to drive ALS. Most research investigating cell death mechanisms in ALS has been done in models of familial ALS. Some of these models suggest that apoptosis plays a role in motor neuron death (95). However, there is lack of evidence on this pathway in human tissue. Some recent studies proposed that other cell death mechanisms (such as necroptosis, pyroptosis and autophagy) might play a role in ALS-related neurodegeneration (64,96–99). It remains unclear which cell death types are responsible for motor neuron loss in ALS. Here, we will give an overview of different types of regulated cell death and their possible role in ALS.

4.1.1. Apoptosis

Programmed cell death is important for a variety of physiological processes, such as organ development, epithelial cell renewal and selection of lymphocytes. However, cell death can also take place following stress, injury or infection, and is in that case linked to tissue damage and disease (100). Cells undergoing apoptotic cell death are morphologically characterized by shrinkage of both the nucleus and the cytoplasm, chromatin condensation, nuclear fragmentation and the formation of apoptotic bodies (101). There is usually no inflammatory reaction as the apoptotic cells are quickly phagocytosed by surrounding cells, and these engulfing cells do not produce anti-inflammatory cytokines (102). The apoptosis pathway can be initiated through an intrinsic or an extrinsic signaling pathway, both of which depend on the activity of caspases (95,103).

In the intrinsic apoptosis pathway, also called the mitochondrial pathway, certain stimuli can cause alterations in the inner mitochondrial membrane, resulting in the opening of the mitochondrial permeability transition pore. As a consequence, cytochrome c is released from mitochondria and binds to the cytochrome c-apoptotic protease-activating factor 1 (APAF1) complex as well as to pro-caspase-9, forming the apoptosome (Fig. 4). This complex activates the caspase cascade starting with caspase-9, which induces the activation of effector caspases, such as caspase-3. These effector caspases then cleave several substrates, ultimately leading to apoptotic cell death (95,102,103) (Fig. 4). Contrary, the extrinsic pathway, also referred to as the death receptor pathway, is activated by ligand binding to death receptors (DR) from the TNF family (e.g. TNFR1, Fas). When TNF binds to its corresponding death receptor, cytoplasmic adaptor proteins are recruited, leading to the formation of complex I (102). This complex consists of TNF receptor-associated death domain protein (TRADD), receptor-interacting protein kinase 1 (RIPK1), TNF receptor-associated factor 2 (TRAF2), cellular inhibitor apoptosis protein

1/2 (cIAP1/2) and the linear ubiquitin chain assembly complex (LUBAC) (Fig. 4). This complex, in which RIPK1 is ubiquitinated by cIAP1, favors pro-inflammatory signaling and cell survival (100,104). However, deubiquitination of RIPK1 by cylindromatosis lysine 63 deubiquitinase (CYLD) promotes apoptosis or necrosis through the formation of the cytoplasmic death-inducing signaling complex, referred to as complex II. In addition to RIPK1, this complex also recruits pro-caspase-8, Fas-associated protein with death domain (FADD) and cellular FLICE-like inhibitory protein (cFLIP) (complex IIa) (105,106). FADD and caspase-8 eventually promote apoptosis through the activation of downstream effector caspases (e.g. caspase-3), and inhibit necroptosis through cleavage of RIPK1, RIPK3 and CYLD (95,100,103,107) (Fig. 4). Importantly, expression levels of FLIP_L are crucial in the control of necroptosis and apoptosis. High FLIP_L levels lead to heteromeric caspase-8-FLIP_L in complex II, preventing complex IIa-dependent apoptosis and thus favoring necroptosis (cf. 4.1.2) (100).



General introduction - Figure 4. Schematic overview of the extrinsic and intrinsic apoptosis pathway. TNF: tumor necrosis factor, TNFR1: TNF receptor 1, TRADD: TNFR1-associated death domain protein, RIPK: receptor-interacting protein kinase, TRAF2: TNF receptor-associated factor 2, cIAP: cellular inhibitor apoptosis protein, CYLD: cylindromatosis lysine 63 deubiquitinase, FADD: Fas-associated death domain protein, cFLIP: cellular FLICE-like inhibitory protein, Cyt C: cytochrome c, Apaf-1: cytochrome c-apoptotic protease-activating factor 1.

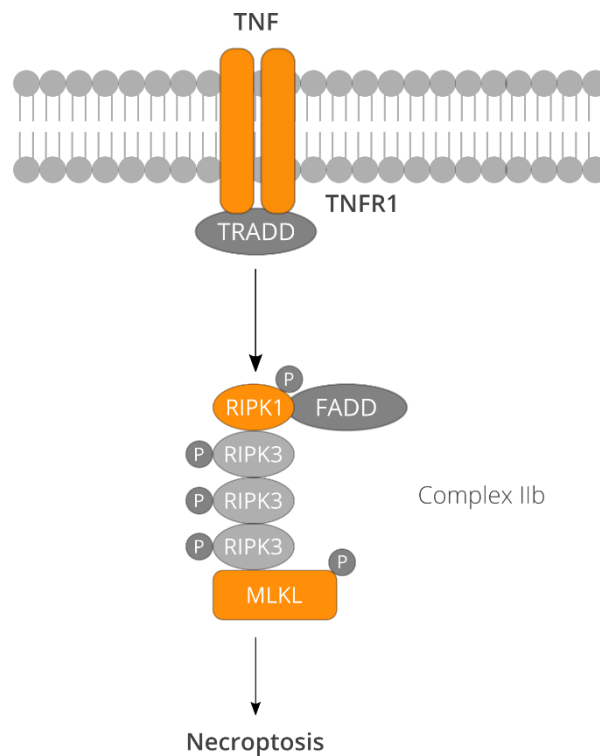
Importantly, it was shown that *TBK1*, which is a major ALS/FTD disease gene, inhibits RIPK1 through its phosphorylation at Thr189. This suggests that in patients with *TBK1* haploinsufficiency mutations, reduced *TBK1* levels allow RIPK1 to initiate apoptotic cell death (108). Moreover, there is evidence from a mutant *SOD1* mouse model suggesting that apoptosis is an underlying mechanism of mutant *SOD1*-related cell death (109). However, data from human cases give conflicting results (95). Overall,

evidence for a clear role of apoptosis in ALS disease pathogenesis is missing, which led researchers to focus on other types of regulated cell death, such as necroptosis and pyroptosis, which will be discussed in the following paragraphs.

4.1.2. Necroptosis

Unlike apoptosis, other forms of regulated cell death (i.e. cell death through a dedicated molecular mechanism) such as necroptosis and pyroptosis (cf. 4.1.3) are characterized by rupture of the plasma membrane, resulting in extracellular leakage of the intracellular contents, eliciting a local inflammatory reaction (110,111). Necroptosis and pyroptosis are the two best studied types of regulated necrosis, with other less-known types including parthanatos, ferroptosis and NETosis (cell death associated with the release of neutrophil extracellular traps) (101). Necroptosis specifically is a caspase-independent form of programmed necrosis, and is characterized by loss of plasma membrane integrity, cell and organelle swelling and increased cytoplasmic granularity (95,101).

Necroptosis can be initiated through the activation of death receptors (DRs), with TNF receptor 1 (TNFR1) as the best characterized example (95). Possible triggers of the necroptosis pathway include TNF, Fas, TNF-related apoptosis-inducing ligand (TRAIL), interferon (IFN), lipopolysaccharide (LPS), DNA damage, ER stress, increased reactive oxygen species (ROS), viral infection and anti-cancer drugs (101,107). The initiation of the pathway starts in a similar way as apoptosis, with ligation of TNF to TNFR1 leading to the recruitment of RIPK1 and TRADD through their death domains, as well as cIAP1/2, TRAF2 and LUBAC, forming the membrane-bound complex I (Fig. 4,5) (105). Next, RIPK1 is deubiquitinated and phosphorylated, which prevents its dissociation from the complex. As explained above (cf. 4.1.1), complex IIa, also containing FADD, can induce apoptosis. However, necroptosis can be initiated through complex IIb when caspase-8 is inactive or absent (103,107,112). Next, RIPK1 recruits RIPK3 through their RIP homotypic interaction motifs (RHIM) and activates RIPK3 by phosphorylation at Ser227, which is crucial for the recruitment and phosphorylation of mixed lineage kinase domain-like protein (MLKL), the effector protein of the necroptotic pathway (113,114). These three phosphorylated proteins, together with TRADD and FADD, form the necrosome complex (103) (Fig. 5). In this complex, RIPK3 phosphorylates MLKL at Thr357 and Ser358, leading to oligomerization of MLKL through its N-terminal domain, followed by translocation to lipid rafts on the cellular plasma membrane (115). There, it induces an ion influx either directly by formation of membrane pores of approx. 4 nm, or indirectly through the association with ion channels (101,116). This gives rise to increased osmotic pressure, water influx and eventually cell swelling and plasma membrane rupture (117). As discussed above, the presence of caspase-8 can inhibit a cell from executing the necroptosis pathway, and favors apoptosis through cleavage of RIPK1 and RIPK3. Therefore, caspase-8 seems to represent a molecular switch that controls apoptosis, necroptosis and pyroptosis (95,112).



General introduction - Figure 5. Schematic overview of the necroptosis pathway. TNF: tumor necrosis factor, TNFR1: TNF receptor 1, TRADD: TNFR1-associated death domain protein, FADD: Fas-associated death domain protein, RIPK: receptor-interacting protein kinase, MLKL: mixed lineage kinase domain-like protein.

Based on ALS transgenic mouse models, some studies suggested a role for necroptosis in ALS disease pathogenesis (99,108), while others later on opposed this and showed that necroptosis is dispensable for motor neuron degeneration in ALS (118,119). In human ALS *post-mortem* tissue, Ito and colleagues detected elevated levels of RIPK1, RIPK3 and MLKL (99), although they did not elaborate on the phosphorylated and therefore activated forms of these proteins. Furthermore, it was shown that human ALS astrocytes trigger selective death of motor neurons *in vitro* through a caspase 3-independent form of programmed cell death with necrotic morphology, which they postulated to be necroptosis (98).

4.1.3. Pyroptosis

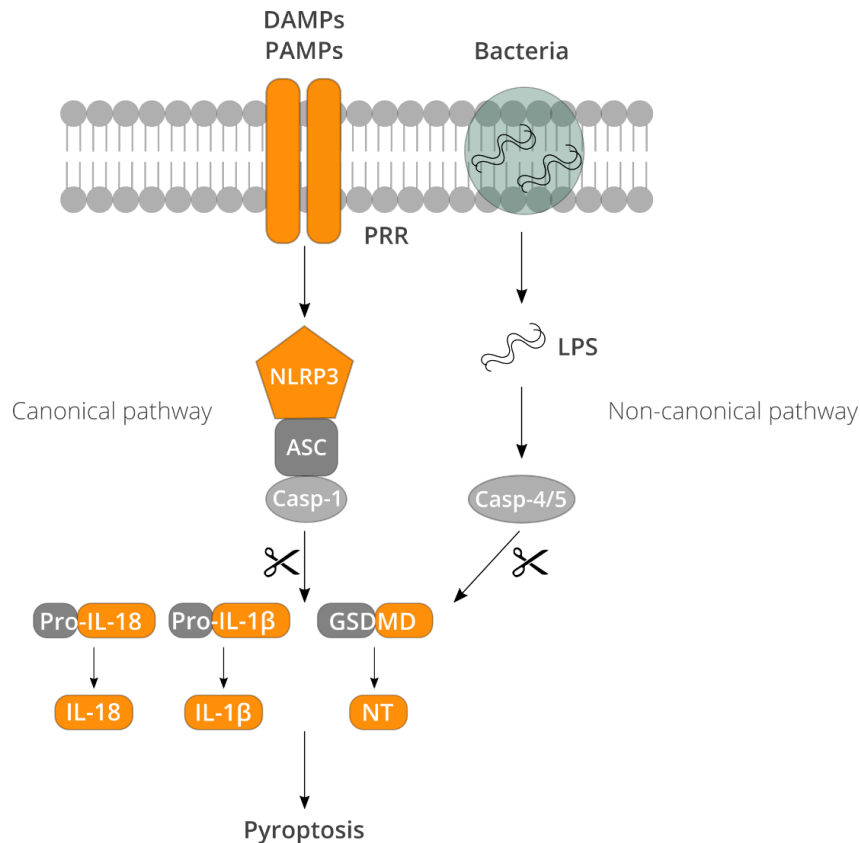
Pyroptosis is a pro-inflammatory type of cell death, which can be initiated through activation of the inflammasome complex. This is a multi-protein complex mainly located in immune cells, neurons, microglia and astrocytes in the CNS (120). It is composed of a sensor protein, apoptosis-associated speck-like protein containing CARD (ASC) and caspase-1 (Fig. 6) (121). The sensor proteins are classified into three different types of cytosolic receptors, including nucleotide-binding domain and leucine-rich repeat-containing receptors (NLRs), absent in melanoma-like receptors (ALRs) and pyrin receptors. The ASC adaptor protein acts as a bridge by linking the pyrin (PYD) domain of the sensor protein to the caspase recruitment domain (CARD) of pro-caspase-1. However, some inflammasomes can directly

recruit pro-caspase-1, without the intervention of the adaptor protein ASC (e.g. NLRP1b, NLRC4) (122). NLRP3 is the best characterized NLR, and AIM2 is a well-known example of an ALR (120,123). NLRP3 is thought to be the main sensor for sterile inflammatory stimuli, while for example NLRC4 mainly acts as a sensor for bacterial infection (124). The activation of the inflammasome requires both a priming and an activation step. First, during the priming step cells activate the NF κ B pathway through the stimulation of toll-like receptors (TLRs), leading to an upregulation of the expression of the inflammasome sensor protein and cytokine targets at the transcriptional level. Next, the inflammasome is assembled by plasma membrane pattern recognition receptors (PRRs) during the activation step, and acts as a cytosolic scaffold responsible for the detection and elimination of pathogen-associated molecular patterns (PAMPs) and damage-associated molecular patterns (DAMPs) (110,120,123,125). In the CNS, PRRs are mainly expressed on microglia, macrophages and astrocytes (121). The inflammasome can be activated by a wide range of stimuli, including K⁺ efflux, extracellular ATP, ROS, lysosomal rupture and aggregated or misfolded proteins (120,126).

Activation of the inflammasome can occur through the typical canonical signaling pathway, or an alternative non-canonical pathway (120). In the canonical pathway, inflammasome activation causes cleavage of pro-caspase-1 into active caspase-1 fragments of 20kDa (p20). Thereafter, caspase-1 cleaves biologically inactive pro-IL-1 β and pro-IL-18 into their respective mature inflammatory cytokines IL-1 β and IL-18. Additionally, caspase-1 cleaves and therewith activates Gasdermin D (GSDMD), which causes the release of an N-terminal fragment (GSDMD-NT) (Fig. 6). This region becomes active after cleavage, as the C-terminus of GSDMD functions as an intramolecular inhibitor when connected to the N-terminus (127). GSDMD-NT then oligomerizes and binds to acidic phospholipids, such as phosphoinositides, on the inner part of the plasma membrane to form death-inducing pores with a diameter of 10-20 nm (120–122,128–130). This causes potassium efflux, intracellular and extracellular ion imbalance, cell swelling and rupture of the plasma membrane, resulting in the massive leakage of cytosolic contents in the extracellular environment, including the pro-inflammatory cytokines IL-1 β and IL-18, inducing focal inflammation and pyroptotic cell death (121). It is thought that cleaved GSDMD, which functions as the effector of pyroptotic cell death, can target and perforate multiple organelles, in addition to the cellular plasma membrane (128). Extracellular IL-18 and IL-1 β in turn can recruit and activate other immune cells, therefore expanding the local inflammatory response through secondary expression of multiple inflammation-associated genes (121,126).

In the non-canonical signaling pathway, which does not contain the typical inflammasome, caspase-4/5 (caspase-11 in mice) is the main player. This pathway can be activated by the presence of LPS released from gram-negative bacteria. The CARD domain of pro-caspase-4/5 directly binds to the lipid

A tail of intracellular LPS, acting both as a sensor and effector with mature caspase-4/5 inducing cleavage of GSDMD. This leads to pyroptotic cell death and the secretion of pro-inflammatory cytokines in a similar manner as in the canonical pathway (Fig. 6) (120,131). The main role of the non-canonical inflammasome is clearance of invaded pathogens and alerting neighboring cells, and eventually removal of infected cells by pyroptosis (132).



General introduction - Figure 6. Schematic overview of the canonical and non-canonical pyroptosis pathway. DAMPs: damage-associated molecular patterns, PAMPs: pathogen-associated molecular patterns, PRR: pattern recognition receptor, LPS: lipopolysaccharide, NLRP3: NOD-, LRR- and pyrin domain-containing protein 3, ASC: apoptosis-associated speck-like protein containing a CARD, Casp-1: caspase-1, Casp-4/5: caspase-4/5, pro-IL-18: pro-interleukin 18, pro-IL-1β: pro-interleukin 1β, GSDMD: Gasdermin D, NT: N-terminal fragment.

Initially, pyroptosis was regarded as a host response to remove the niche of bacteria. However, there is now evidence supporting a role for pyroptosis in non-infectious cell death processes, such as in neurodegenerative disorders (124,131). In the CNS, it is thought that microglia, astrocytes and neurons can all initiate pyroptosis and express its related downstream molecules and receptors, taking part in the local inflammatory reaction (121). The NLRP3 inflammasome is likely implicated in multiple neurodegenerative disorders. It was shown that the inflammasome could be activated through abnormal protein aggregation, including for example amyloid-β in Alzheimer's disease (133) and α-synuclein in Parkinson's disease (134).

In ALS, most research related to the inflammasome complex has been conducted in mutant SOD1 animal models. Multiple studies showed an upregulation of the expression of several NLRP3 inflammasome proteins, as well as the pro-inflammatory cytokines IL-18 and IL-1 β in the CNS of SOD1 mice (135–137) and rats (138) compared to controls. Furthermore, it was shown that mutant SOD1 could activate microglia, leading to caspase-1 activation and consequent cleavage of IL-1 β . This was not the case when microglia were deficient for NLRP3, suggesting that NLRP3 is the key inflammasome in mediating SOD1-induced microglial pyroptosis activation (97,139). Importantly, deficiency for caspase-1 or IL-1 β , or treatment with a recombinant IL-1 β receptor antagonist extended the lifespan of SOD1 mice and reduced inflammation (139). Regarding TDP-43, there is evidence that mutant and aggregated forms of TDP-43 can trigger NLRP3 inflammasome-dependent IL-1 β and IL-18 secretion in microglia *in vitro*, which was shown to be toxic to motor neurons (140,141). In the absence of microglia, TDP-43 was not toxic to motor neurons (141). Additionally, there is some evidence for inflammasome and pyroptosis activation in ALS patients. Elevated levels of IL-18 in ALS patient serum (142) and elevated *NLRP3* mRNA in blood (143) were detected. In human *post-mortem* ALS tissue, some studies observed increased expression of NLRP3, ASC, caspase-1 and IL-18 (137,144).

4.1.4. Autophagy-related cell death

Autophagy is crucial in the degradation of cellular proteins, organelles and RNA to maintain cellular homeostasis (95). Autophagy comprises three main steps: 1) initiation, 2) vesicle expansion and closure, and 3) autophagosome maturation and its fusion with the late endosome, followed by degradation. Autophagy is initiated when the ULK kinase complex is activated, which is controlled by mTORC1. When mTORC1 is active, it inhibits autophagy through phosphorylation of ULK. In contrast, when mTORC1 is inhibited, the activity of the ULK complex is promoted, leading to translocation of the ULK complex to a specific location on the endoplasmic reticulum (ER) marked by autophagy-related protein 9 (ATG9) (145,146). Next, Beclin1 and class II phosphatidylinositol 3-kinase (PI3K) are recruited to the ER, building the so-called omegasome (145,147). This complex then recruits WIPI2B, which allows the E3-like complex ATG12-ATG5-ATG16L to join the forming phagophore. Pro-LC3 is first cleaved by ATG4 to form cytosolic LC3-I, which then is conjugated to a phosphoethanolamine by the LC3 ubiquitin-like lipidation complex to form the membrane-associated LC3-II (147,148). Then, autophagy receptors, such as p62/SQSTM1, bind cargo and transport it into the forming phagophore through binding of LC3-II. The double membrane of the phagophore then expands around the cargo, forming the characteristic double-membrane autophagosome, which further matures. The autophagosome fuses with an endosome containing vacuolar ATPases (v-ATPase) through SNARE-mediated fusion, leading to acidification of the autophagosome. Thereafter, the autophagosome can fuse with a lysosome, which provides the degradative enzymes to break down the cargo in the resulting

autolysosome. Finally, LC3-II is converted back to LC3-I on the exterior part of the autolysosome, and both nutrients and membranes are recycled (145,148,149).

Although autophagy usually promotes cell survival, it has also been recognized as a key regulator and, in some cases, executor of cell death (150,151). The term 'autophagic cell death' is still somewhat controversial. Therefore, it is important to clarify what is considered as autophagic cell death, compared to cell death that is accompanied by autophagy (152). According to Denton and colleagues, the different roles of autophagy in cell death can be defined in three distinct mechanisms. The first type is autophagy-associated cell death, where the induction of autophagy occurs simultaneously with the induction of another cell death pathway, such as apoptosis. Here, autophagy does not play an active role in the cell death pathway. The second type is autophagy-mediated cell death, in which the induction of autophagy triggers the activation of a cell death pathway. Finally, the third mechanism is autophagy-dependent cell death. This is a relatively unknown distinct cell death mechanism that occurs independently of for example apoptosis or necroptosis (153). It is morphologically characterized by extensive intracellular phagosome formation, which reflects the autophagic digestion of cytosolic contents and organelles (101). One example of a cell death type that can be initiated by chronic autophagy inhibition is karyoptosis, which is characterized by nucleophagy and the excretion of nuclear components (151,154).

In contrast to autophagy-dependent cell death, more is known about autophagy-mediated cell death, where the autophagy machinery is involved in a substantial crosstalk with several other forms of cell death. Autophagy was shown to be closely linked to necroptosis. For example, researchers showed that increased autophagy initiation through reduced mTORC1 activity inhibited necroptosis, possibly by degradation of RIPK1 (151,155). On the other hand, the presence of p62/SQSTM1 was required for the assembly and activation of the necrosome, indicating that the autophagy machinery functions as a scaffold for necroptosis activation (156). In turn, activation of necroptosis was demonstrated to suppress autophagy (150,151,157). A similar relationship was described for autophagy and apoptosis, where apoptosis activation had an inhibitory effect on autophagy, while on the other hand autophagy efficiently inhibited apoptosis (151). There is also evidence for a link between autophagy and pyroptosis, as it was shown that autophagic pathways degraded NLRP3 inflammasome components and suppressed the secretion of IL-1 β (123). Overall, there seems to be a complex interplay between different types of regulated cell death, with autophagy as an important mediator.

Autophagy has been implicated in ALS disease pathogenesis. Apart from the presence of autophagy-related proteins (e.g. p62/SQSTM1) in TDP-43-positive lesions (158), upregulation of autophagy was shown to enhance clearance of TDP-43 aggregates and improve neurodegenerative symptoms

(149,159,160). In addition, several ALS-related genes play a role in autophagy, such as *OPTN*, *TBK1*, *CHMP2B* and *p62/SQSTM1* (149). It was also shown that a reduction in C9orf72 protein levels due to repeat expansions in *C9orf72* could inhibit autophagy initiation (161). Thus, apart from playing an important role in clearance of pathological aggregates in neurodegenerative diseases, autophagy is involved in the initiation and inhibition of several cell death pathways. More research is needed to elucidate the precise regulatory mechanisms to be able to modulate this pathway, favoring abnormal protein clearance and halting detrimental neurodegenerative pathways.

4.2. Axonal degeneration

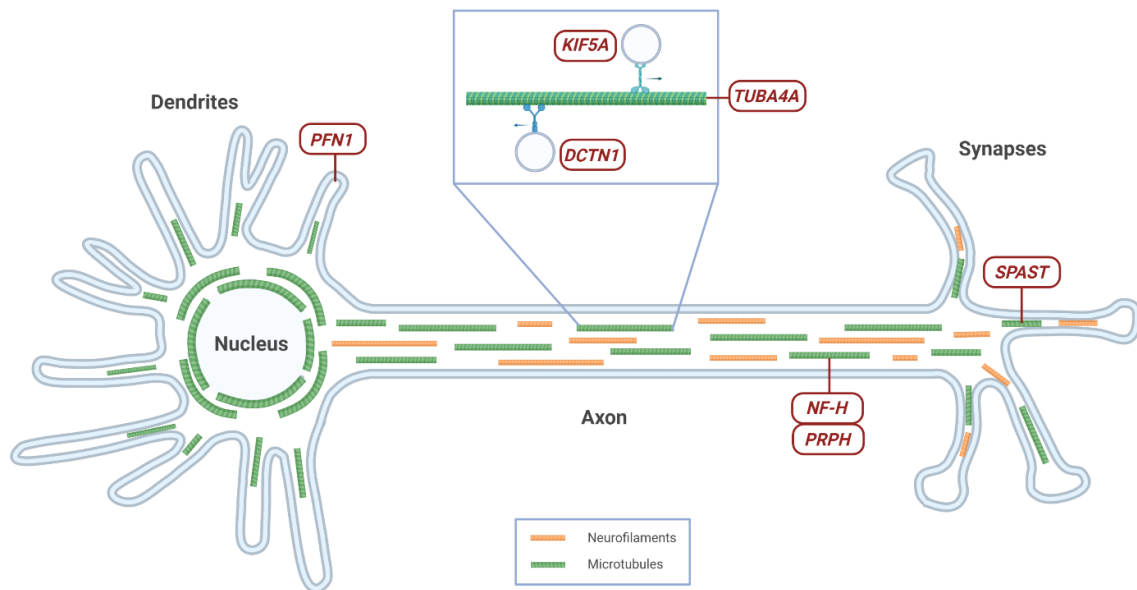
4.2.1. Axonal dysregulation in ALS

Apart from detrimental changes in neuronal cell bodies, pathological alterations in the axon (i.e. axonopathy) have also been described in ALS. This axonal degeneration has been postulated to precede motor neuron cell body degeneration, referred to as the “dying-back hypothesis” (162,163). This proposes that the pathology begins at the synaptic distal ends of axons and proceeds towards the cell body in a “dying-back” pattern. Indeed, there is evidence for morphological and functional abnormalities in the neuromuscular junctions (NMJs) in ALS models (164,165). As neurons are the most asymmetric cells, with axons reaching up to one meter in length, these cells have a crucial requirement for axonal transport to maintain their morphology and function (3). This ensures the constant transport of proteins and cellular organelles, as well as mRNA for local axonal translation (19,164). Two types of axonal transport have been described, which can be distinguished based on their speed. Fast axonal transport occurs at a rate of 50-400 mm per day and generally carries vesicles and organelles such as mitochondria, while slow axonal transport progresses at less than 8 mm per day and carries cytoskeletal and soluble proteins (163,164). Axonal transport occurs both anterograde (i.e. from the cell body to the periphery) and retrograde (i.e. from the periphery to the cell body) and is microtubule (MT)-dependent (23). Axonal transport defects have been described in several neurodegenerative diseases (19). In ALS, the earliest evidence came from *post-mortem* studies showing the abnormal accumulation of neurofilaments and microtubules in the central nervous system (166,167). Later on, axonal transport was shown to be impaired in ALS mouse models as well as in iPSC-derived motor neurons with ALS-related mutations in *TARDBP*, *FUS* and *SOD1* (168–173).

As discussed earlier, ALS-related genes can be categorized into distinct groups, depending on the cellular pathways in which they are involved. The recent discovery of ALS-related genes involved in cytoskeletal dynamics countered the perspective that the observed dysfunction of cytoskeletal proteins in ALS is a result rather than a possible cause of the disease (23). One of the first described ALS-related genes with a function in the cytoskeleton is neurofilament heavy (*NF-H*) (174). This is a type of intermediate filament (IF), which is important for maintenance of the cytoskeletal architecture

(23) (Fig. 7). A mouse model overexpressing *NF-H* supported its causality, as these mice presented with characteristic ALS pathology (175). Furthermore, neurofilament levels in CSF, plasma and blood of patients have been established as a diagnostic tool and predictor of disease progression (176,177). Apart from *NF-H*, peripherin (*PRPH*) is another gene with a function in intermediate filaments in which mutations have been associated with ALS (Fig. 7) (16,23). As *in vitro* and *in vivo* studies on *PRPH* are lacking, the detrimental effects of these mutations remain unclear. Apart from intermediate filaments, a link between actin and ALS was demonstrated in 2012 with the identification of mutations in profilin 1 (*PFN1*) (178). Profilin 1 is important in the polymerization of filamentous (F)-actin, and mutations in this gene were linked to dysregulation of actin dynamics with disruption of axonal growth (23) (Fig. 7).

Several genes related to MTs and MT-dependent axonal transport were reported in patients with ALS. Mutations in dynactin subunit 1 (*DCTN1*) were identified in fALS and sALS patients. This protein is part of the dynactin complex, which takes part in axonal transport through binding of both MTs and dynein, with the latter being the motor protein responsible for retrograde axonal transport (Fig. 7). Mutations in *DCTN1* were shown to decrease the ability of this protein to bind MTs, and dynactin 1 depletion leads to NMJ instability, functional abnormalities and motor defects in zebrafish (23,179). In line with this, kinesin family member 5A (*KIF5A*), which is involved in anterograde axonal transport, was also confirmed as an ALS-related gene (180) (Fig. 7). Apart from motor proteins, mutations in spastin (*SPAST*) were associated with an ALS phenotype (181,182). Spastin belongs to the ATPases associated with diverse cellular activities (AAA) family, which induces MT severing and thus increases MT disassembly, thereby affecting axonal transport (23) (Fig. 7). Finally, mutations in α -tubulin 4A (*TUBA4A*) were identified in fALS and sALS patients (183,184). *TUBA4A* is one of nine α -tubulin subunit genes, therefore building the MT network (Fig. 7). As we focus on *TUBA4A* in this thesis, this gene will be discussed in more detail in the next section.



General introduction - Figure 7. Overview of the neuronal cytoskeleton indicating the role of ALS-related genes. Neurofilaments are indicated in orange, microtubules in green. *PFN1* = profilin 1; *KIF5A* = kinesin family member 5A; *DCTN1* = dynactin subunit 1; *TUBA4A* = tubulin alpha 4A; *NF-H* = neurofilament heavy; *PRPH* = peripherin; *SPAST* = spastin.

4.2.2. *TUBA4A* in ALS: why microtubules are more than just a loading control

Microtubules (MTs) are composed of heterodimers of α - and β -tubulin and are an essential part of the cytoskeleton. These heterodimers are assembled in a head-to-tail fashion at the growing (+) ends of MTs, forming sheets of longitudinal protofilaments. Lateral interactions between these protofilaments ensure closure of the hollow MTs, which typically have an outer diameter of approx. 25 nm (185,186). MTs are dynamic and can alternate between phases of polymerization and depolymerization, which is referred to as “dynamic instability” (187). MTs regulate several cellular functions, such as cell division, organelle positioning and motility (188). In neurons, MTs are especially important for the long extending axons, in which they serve as “tracks” for axonal transport of organelles, proteins and RNA granules (186). In axons, MTs are uniformly oriented with their plus ends towards the synapses, while in dendrites MTs are of mixed polarity (189).

In humans, nine α -tubulin and nine β -tubulin isoforms are expressed from distinct genes. Tubulins are evolutionary highly conserved, and mainly show sequence variation within isoforms in their unstructured, negatively charged C-terminal tails (187,190). These C-terminal tails are located on the outside of MTs and are involved in the binding of motor proteins, such as dynein and kinesin, and other microtubule associated proteins (MAPs) to the MT backbone (189). MTs can undergo several post-translational modifications (PTMs), such as acetylation, detyrosination, glutamylation, glycylation, polyamination and glutathionylation (186). Acetylation occurs on a lysine at position 40 (K40) on the luminal surface of α -tubulin, and was shown to be associated with increased stability of MTs by

preventing MT breakage (187). Furthermore, acetylation is important for the recruitment of MAPs (188). This PTM is reversible, with tubulin acetyltransferase α TAT1 responsible for acetylation, and histone deacetylase 6 (HDAC6) and Sirtuin 2 (SIRT2) exerting deacetylation (188). Evidence of deacetylation of α -tubulin has been demonstrated in several neurodegenerative diseases, such as AD, PD, HD and ALS (191). Contrary, other PTMs occur on the C-terminal tail of tubulin. During detyrosination, the final C-terminal tyrosine residue of α -tubulin is removed by tubulin tyrosine carboxypeptidase, which can be reversed by tubuline tyrosine ligase (TLL) (185). Detyrosination is associated with long-lived stable MTs and was shown to inhibit MT depolymerization (191). Interestingly, *TUBA4A* and *TUB8A* are the only tubulin isoforms that do not contain this final tyrosine residue, which suggests that their expression involves the generation of more stable MTs. Finally, both α - and β -tubulin can undergo the ligase-mediated addition of glutamate residues to their C-terminal tail by enzymes from the tubulin tyrosine ligase-like (TTLL) family, which can be reversed by cytosolic carboxypeptidase (CCP) enzymes (188). Polyglutamylation is thought to influence the binding of motor proteins and other MAPs and regulate axonal transport (191). Overall, neurons are characterized by a MT cytoskeleton with numerous PTMs, as they are usually acetylated at K40, detyrosinated and polyglutamylated (187). These stable MTs are essential for maintaining neuronal functions such as axonal transport. Disturbances in MT stability were shown to be involved in neurodegenerative diseases (192).

Evidence for a functional specification of different tubulin isoforms comes from *in vitro* studies as well as from tubulinopathies, which is a broad spectrum of diseases caused by mutations in tubulin genes (185,188,189). Most tubulin mutations lead to disorders related to neurodevelopmental defects (193). For example, mutations in *TUBA1A* lead to lissencephaly, cerebellar malformations and basal ganglia defects, while *TUBB2B* and *TUBB3* variants cause axon guidance disorders such as congenital fibrosis of the extra-ocular muscles (CFEOM). *TUBB5* mutations are also related to neurodevelopment deficits, as they can cause microcephaly with severe mental retardation (185). In contrast, mutations in *TUBB1* cause macrothrombocytopenia, which is a blood disorder affecting platelet formation, while *TUBB8* mutations lead to arrest of meiotic oocytes, resulting in female sterility (185). This phenotypic variety illustrates the functional specification of different tubulin isoforms and implies a different spatial and temporal expression. Indeed, the expression of *TUBB1* is restricted to the hematopoietic system, while *TUBB8* is enriched in oocytes. The neurodevelopmental defect-associated tubulin genes show an expression restricted to the CNS, which can change over time. For example, *TUBA1A* and *TUBB3* are typically expressed in post-mitotic neurons, while *TUBB2* is initially expressed in neurons, but is postnatally found in astrocytes and oligodendrocytes (185).

In 2014, mutations in *TUBA4A* were identified in patients with ALS with or without cognitive deficits, suggesting that MTs may be a primary driver of ALS pathophysiology (183,184). The expression of *TUBA4A* was shown to increase over time (23), possibly explaining why variants in this gene cause a later age disease phenotype such as ALS, contrary to developmental disorders as discussed above. These *TUBA4A* mutations are located in the C-terminal part of the protein. Smith and colleagues demonstrated that some of these *TUBA4A* variants inefficiently formed α/β -tubulin dimers *in vitro* and disrupted MT network stability in a dominant-negative manner (183). More recently, *TUBA4A* mutations were identified in patients with FTD often with a family history of Parkinsonism (194,195), as well as in a PD patient (196). In these FTD and PD patients, *TUBA4A* variants were detected in the N-terminal part of the protein, and a haploinsufficiency mechanism was suggested, contrary to the proposed dominant-negative mechanism attributed to C-terminal *TUBA4A* mutations (195,196). Interestingly, a downregulation of α -tubulin subunit genes was suggested in patients with sporadic ALS (197,198), extending the relevance of *TUBA4A* to the majority of ALS cases. Altogether, *TUBA4A* adds to the list of ALS-associated genes with a role in the cytoskeleton, stressing the importance and possible causality of cytoskeletal defects in ALS.

5. Modelling ALS neurodegeneration

To study a neurodegenerative disease such as ALS, animal models can be very valuable to model the disease. The first mouse model for ALS was created in 1994 (199). This model expressed $SOD1^{G93A}$ under the human *SOD1* promoter. Afterwards, numerous additional *SOD1* mouse models were created, displaying variable phenotypes, age of disease onset and survival (200). Most models reproduce human *SOD1* pathology to some extent, with ubiquitinated *SOD1* inclusions, motor neuron deficits and eventually fatal paralysis (200). However, a major disadvantage is the limited representation, as only a fraction of ALS patients has mutations in *SOD1*, and *SOD1* mice do not present with TDP-43 pathology. For TDP-43, the first mouse models created overexpressed human TDP-43^{WT} under the mouse prion promoter. However, this did not reproduce the pathological degenerative features typical for ALS (200). Later, several known *TARDBP* mutations were introduced, such as A315T, Q331K and G348C (200,201). Of these, mPrp-hTDP-43^{A315T} mice developed motor dysfunction and paralysis, with underlying ubiquitin-positive inclusions and motor neuron loss. Although TDP-43-positive lesions were not present, loss of nuclear TDP-43 staining could be observed in these mice (65).

Alternative animal models are frequently used in ALS research, such as fruit fly (*Drosophila melanogaster*), zebrafish (*Danio rerio*) and a nematode (*Caenorhabditis elegans*) (202). *Drosophila melanogaster* is often used for the study of ALS-related genes, as the complete fly genome has been

sequenced showing that approx. 75% of human disease genes have a fly orthologue, while this is approx. 80% for *Danio rerio*. Apart from generating transgenic zebrafish lines, zebrafish are also often used for the microinjection of antisense morpholinos or DNA/RNA, allowing the study of the effects of downregulation or overexpression of certain genes of interest (202,203). Finally, *C. elegans* also has a well-developed nervous system with about 42% of human disease genes having a *C. elegans* orthologue, enabling the study of neurodegenerative diseases. As with *Drosophila*, *C. elegans* is mostly used for modeling genetics (202).

Apart from *in vivo* research, iPSCs are increasingly used in the ALS field. These pluripotent stem cells are generated from human patient or control fibroblasts through reprogramming using a combination of transcription factors (204,205). From iPSCs, several distinct cell types relevant for ALS can be produced such as motor neurons, but also microglia, astrocytes and muscle cells (171,206–209). As such, the molecular effects of ALS-related mutations can be studied in disease-relevant cell types *in vitro*. However, this does not reflect the complexity of ALS, where several cell types interact during disease pathogenesis. Therefore, research is now also focusing on the development of co-culture systems to study the interaction between different cell types in the context of ALS (210,211).

Although ALS research has disentangled many molecular pathways involved in this devastating disease over the last years, in which the identification of new genetic variants related to ALS played a crucial role, it remains unclear which cell death pathway(s) is/are involved in motor neuron degeneration. A recent shift in the focus from apoptosis to other programmed types of cell death, such as necroptosis and pyroptosis, in neurodegenerative diseases might be a promising avenue in the ALS field. Additionally, although much research has focused on axonal transport defects in the context of axonal disturbances and pathology in ALS in recent years (170,171,212,213), investigating the role of ALS-related cytoskeletal genes could provide more insights in the underlying molecular pathways. Therefore, this PhD project focused on further unravelling motor neuron as well as axonal degeneration in ALS, by investigating the impact of two types of regulated cell death (i.e. necroptosis and pyroptosis) in ALS in relation to TDP-43 pathology, as well as assessing the role of a recent ALS-related cytoskeletal gene (i.e. *TUBA4A*) in ALS axonal degeneration and pathology. The results obtained in this thesis, as discussed in the following chapters, might not only provide new insights in motor and axonal degeneration mechanisms in ALS, but could also aid in identifying new therapeutic treatment strategies to counter neurodegeneration in ALS.

OBJECTIVES

The general aim of this PhD thesis was to clarify the mechanisms of neuronal and axonal degeneration in ALS. For this, we used *post-mortem* central nervous tissue from ALS and/or FTLD patients, as well as two *in vivo* models: TDP-43^{A315T} transgenic mice and zebrafish. We hypothesized that neurodegeneration in ALS includes on one hand the activation of regulated cell death pathways (such as necroptosis and pyroptosis) with an important role for TDP-43 pathology, and on the other hand disturbances in axonal integrity, with the latter as a possible initiator of ALS disease pathogenesis. To unravel this hypothesis, we set out the following objectives:

(1) To determine the role of necroptosis activation in relation to TDP-43 pathology and neuronal loss in ALS/FTLD *post-mortem* tissue using immunohistochemical and biochemical techniques.

To address this objective, we analyzed *post-mortem* brain and spinal cord tissue from ALS/FTLD patients and controls using antibodies against the main necroptosis proteins. Additionally, we explored the relation with the burden of pTDP-43 pathology (**Chapter I**).

(2) To determine the role of pyroptosis activation in relation to TDP-43 pathology and neuronal loss in ALS *post-mortem* tissue as well as TDP-43^{A315T} transgenic mice.

For this, we analyzed the expression of proteins involved in the inflammasome as well as pyroptosis effector proteins in ALS and control *post-mortem* brain and spinal cord, and studied the correlation with the burden of pTDP-43 pathology in the respective CNS regions. Furthermore, we used asymptomatic and symptomatic TDP-43^{A315T} transgenic mice in addition to wild-type mice to confirm the results obtained in human autopsy cases (**Chapter II**).

(3) To assess tubulin-related changes in ALS/FTLD *post-mortem* tissue and to evaluate the possible detrimental effects of such ALS-related alterations in an *in vivo* model.

For this, we investigated the expression of the ALS-related gene *TUBA4A* in sporadic ALS/FTLD *post-mortem* brain and spinal cord, as well as in an FTLD autopsy case with an R64Gfs*90 *TUBA4A* mutation and TDP-43 pathology (**Chapter III, IV**). Additionally, we assessed the functional consequences of *TUBA4A* downregulation using antisense morpholinos in zebrafish (**Chapter IV**).

CHAPTER I: Necrosome-positive granulovacuolar degeneration is associated with TDP-43 pathological lesions in the hippocampus of ALS/FTLD cases

This chapter is based on the following publication as first author:

Necrosome-positive granulovacuolar degeneration is associated with TDP-43 pathological lesions in the hippocampus of ALS/FTLD cases

Evelien Van Schoor (1,2,3), Marta J. Koper (1,3,4), Simona Ospitalieri (1), Lieselot Dedeene (1,2,3,5,6), Sandra O. Tomé (1), Rik Vandenberghe (7,8), David Brenner (9), Markus Otto (9), Jochen Weishaupt (9), Albert C. Ludolph (9), Philip Van Damme (2,3,8), Ludo Van Den Bosch (2,3), Dietmar Rudolf Thal (1,10)

1. Laboratory of Neuropathology, Department of Imaging and Pathology, KU Leuven (University of Leuven), Leuven Brain Institute (LBI), Leuven, Belgium.
2. Laboratory of Neurobiology, Department of Neurosciences, KU Leuven (University of Leuven), Leuven Brain Institute (LBI), Leuven, Belgium.
3. Center for Brain & Disease Research, VIB, Leuven, Belgium.
4. Laboratory for the Research of Neurodegenerative Diseases, Department of Neurosciences, KU Leuven (University of Leuven), Leuven Brain Institute (LBI), Leuven, Belgium.
5. Laboratory for Molecular Neurobiomarker Research, Department of Neurosciences, KU Leuven (University of Leuven), Leuven Brain Institute (LBI), Leuven, Belgium.
6. Laboratory Medicine, University Hospitals Leuven, Leuven, Belgium.
7. Laboratory of Cognitive Neurology, Department of Neurosciences, KU Leuven (University of Leuven), Leuven, Belgium.
8. Department of Neurology, University Hospitals Leuven, Leuven, Belgium.
9. Department of Neurology, Ulm University, Ulm, Germany.
10. Department of Pathology, University Hospitals Leuven, Leuven, Belgium.

Corresponding author: Dietmar R. Thal

Neuropathology and Applied Neurobiology (2020) DOI: 10.1111/nan.12668

1. Abstract

Aim

Granulovacuolar degeneration (GVD) in Alzheimer's disease (AD) involves the necrosome, which is a protein complex consisting of phosphorylated receptor-interacting protein kinase 1 (pRIPK1), pRIPK3 and phosphorylated mixed lineage kinase domain-like protein (pMLKL). Necrosome-positive GVD was associated with neuron loss in AD. GVD was recently linked to the *C9ORF72* mutation in amyotrophic lateral sclerosis (ALS) and frontotemporal lobar degeneration with transactive response DNA-binding protein (TDP-43) pathology (FTLD-TDP). Therefore, we investigated whether GVD in cases of the ALS-FTLD-TDP spectrum (ALS/FTLD) shows a similar involvement of the necrosome as in AD, and whether it correlates with diagnosis, presence of protein aggregates and cell death in ALS/FTLD.

Methods

We analysed the presence and distribution of the necrosome in post-mortem brain and spinal cord of ALS and FTLD-TDP patients (n = 30) with and without the *C9ORF72* mutation, and controls (n = 22). We investigated the association of the necrosome with diagnosis, the presence of pathological protein aggregates and neuronal loss.

Results

Necrosome-positive GVD was primarily observed in hippocampal regions of ALS/FTLD cases and was associated with hippocampal TDP-43 inclusions as the main predictor of the pMLKL-GVD stage, as well as with the Braak stage of neurofibrillary tangle pathology. The central cortex and spinal cord, showing motor neuron loss in ALS, were devoid of any accumulation of pRIPK1, pRIPK3 or pMLKL.

Conclusions

Our findings suggest a role for hippocampal TDP-43 pathology as a contributor to necrosome-positive GVD in ALS/FTLD. The absence of necroptosis-related proteins in motor neurons in ALS argues against a role for necroptosis in ALS-related motor neuron death.

2. Introduction

Amyotrophic lateral sclerosis (ALS) is an orphan disease that affects 1-3 individuals per 100 000 per year (3,214). It is a neurodegenerative disease characterized by the progressive degeneration of both upper and lower motor neurons, leading to muscle weakness and consequent paralysis (10). Patients usually die due to respiratory failure within 2-5 years after disease onset (2). The majority of ALS cases are sporadic, but up to 10% are familial, most commonly caused by mutations in chromosome 9 open reading frame 72 (*C9ORF72*), superoxide dismutase 1 (*SOD1*), transactive response DNA-binding protein (*TARDBP*) and fused in sarcoma (*FUS*) genes (18,215). The major pathological hallmark of 97% of ALS patients is the cytoplasmic mislocalisation and aggregation of transactive response DNA-binding protein 43kDa (TDP-43) in the brain and spinal cord (25). TDP-43 inclusions are also found in 50% of patients with frontotemporal lobar degeneration (FTLD), referred to as FTLD-TDP (216). These diseases are TDP-43 proteinopathies. TDP-43 also accumulates in Alzheimer's disease (AD), limbic-predominant age-associated TDP-43 encephalopathy (LATE), Lewy body disease, and, to a lesser extent, in normal control subjects over the age of 65 years (79,217). ALS and FTLD-TDP have been suggested to be part of a clinicopathological spectrum (ALS/FTLD), sharing similar pathological mechanisms that affect different populations of central nervous system neurons (218). Another common characteristic of ALS and FTLD-TDP is the hexanucleotide repeat expansion in the *C9ORF72* gene as the most frequent disease-linked mutation. In families with a *C9ORF72* mutation, some family members develop FTLD-TDP, whereas others develop ALS (219,220). Additionally, up to 25% of ALS patients show characteristics of FTLD-TDP, pointing to a continuum between these diseases (5).

Necroptosis is a caspase-independent form of programmed necrosis (95). It is characterized by loss of cell membrane integrity, cell and organelle swelling, increased cytoplasmic granularity, and finally membrane rupture and leakage of cellular contents into the extracellular space, which can elicit a significant immune response (95,101). Necroptotic cell death can be triggered by ligands of the death receptor family (e.g. tumour necrosis factor, TNF), as well as viruses and anti-cancer drugs (101). The phosphorylation and oligomerization of mixed lineage kinase domain-like protein (MLKL) and its translocation to the cell membrane are essential for the execution of necroptosis (115,117). MLKL is phosphorylated by receptor-interacting protein kinase 3 (RIPK3), which is phosphorylated and, thereby, activated by phosphorylated RIPK1 (pRIPK1). Activated through phosphorylation, pRIPK1, pRIPK3 and pMLKL form the necrosome, with pMLKL being the final executor of necroptotic cell death (14,18,19). There is some evidence pointing towards a role for necroptosis in motor neuron death in ALS. Re *et al.* (98) showed that human ALS astrocytes induced necroptosis specifically in cultured motor neurons. Another study reported increased levels of RIPK1, RIPK3 and MLKL in *post-mortem* ALS spinal cord (99). However, this study did not elaborate on the phosphorylated and, therefore, activated forms

of these proteins. In ALS mouse models there is conflicting evidence on the role of necroptosis. While some studies suggest a relevant contribution (99,108), others argue against a major significance of necroptosis in motor neuron degeneration (118,119).

We have recently shown that all components of the necrosome, i.e. pRIPK1, pRIPK3 and pMLKL, are detectable in granulovacuolar degeneration (GVD) in the brains of AD patients (221). GVD lesions are composed of multiple granulovacuolar bodies, which are membrane-bound vacuoles with dense core granules, considered to resemble late-stage autophagic organelles (222). Along with many other proteins such as abnormally phosphorylated tau protein (p-tau), phosphorylated amyloid β -peptide (A β) and casein kinase 1, phosphorylated TDP-43 (pTDP-43) can be detected in GVD granules (223–226). GVD prevalence is high in patients with AD and is predominantly found in degenerating pyramidal neurons in the medial temporal lobe (MTL), from where it spreads to other brain regions following a pattern, defined as the GVD stages (227). Given that necrosome-positive GVD lesions in AD correlated with neuronal loss, it was proposed that these lesions could be of major relevance for AD-associated neuron loss.

Another study showed that GVD was associated with the *C9ORF72* mutation in ALS/FTLD-TDP patients (comprising of ALS, FTLD-TDP and mixed patients). GVD-containing neurons frequently had dipeptide repeat (DPR) inclusions, which are presumably toxic protein products of the *C9ORF72* repeat expansion (228). However, it is still unclear whether GVD detected in the brains of patients with ALS/FTLD also exhibits the activated necrosome, and if so, whether this correlates with the *C9ORF72* mutation or neuron loss in ALS/FTLD, or whether necrosome accumulation in GVD is solely related to AD-specific pathologies in these patients.

3. Materials and methods

Human autopsy cases

Brain and spinal cord tissues were collected in accordance with the applicable laws in Belgium (UZ Leuven) and Germany (Ulm, Bonn and Offenbach). The recruitment protocols for collecting the brains were approved by the ethical committees of the University of Ulm (Germany) and of UZ-Leuven (Belgium). This study was approved by the UZ Leuven ethical committee (Belgium). Tissues were collected with an average *post-mortem* interval of 38 h. After autopsy, the right hemisphere was dissected in coronal planes and frozen at -80°C . The left hemisphere was fixed in 4% phosphate-buffered formaldehyde. 18 ALS cases (8 *C9orf72* and 10 sporadic), 9 FTLD-TDP (2 *C9orf72* and 7 sporadic), 3 ALS+FTLD-TDP (1 *C9orf72* and 2 sporadic) and 22 non-neurodegenerative controls were included in this study (Table 1). The diagnosis of ALS or FTD was based on clinical assessment according

to the consensus criteria for ALS (7,8,229) and FTD (45,46). The *post-mortem* diagnosis of ALS and FTLT-DTP was pathologically confirmed by assessment of the pTDP-43 pathology. Braak NFT stage (230), A β MTL phase (231), and the Consortium to Establish a Registry for Alzheimer's disease (CERAD) score (232) were determined based on immunohistochemical staining with antibodies against A β and p-tau (Suppl. Table 1).

Ch. I - Table 1. List of cases. The table provides information regarding age (= age at death), sex, diagnosis, the presence of the *C9ORF72* mutation, the presence of poly(GA) pathology in the frontal cortex, pMLKL GVD stage, A β MTL phase, Braak NFT stage, CERAD score, hippocampal pTDP-43 score, disease duration (months) and PMI (hours). Abbreviations: f = female; m = male; ALS = amyotrophic lateral sclerosis; FTLT = frontotemporal lobar degeneration; control = non neurodegenerative disease control; A = aneurysm; AGD = argyrophilic grain disease; ARTAG = aging-related tau astroglipathy; CLL = chronic lymphoid leukemia; CM = carcinoma metastasis; GB = Guillian-Barre syndrome; I = infarction; IHC = immunohistochemistry; MI = microinfarction; n.a. = not applicable; n.d. = not determined; PART = primary age-related tauopathy; RP-PCR = repeat-primed polymerase chain reaction; SVD = small vessel disease; SVE = subcortical vascular encephalopathy; T = trauma; PMI = *post-mortem* interval.

Case n°	Age	Gender	Diagnosis	C9ORF72		pMLKL GVD stage	A β MTL phase	Braak NFT stage	CERAD	pTDP-43 score	Disease duration	PMI (hours)
				by RP-PCR	by poly(GA) IHC							
1	58	f	ALS, PART	normal	no	1	0	2	0	0	18 months	24
2	62	f	ALS	n.d.	no	0	0	1	0	0	12 months	24
3	51	m	ALS	normal	no	0	0	1	0	1	8 months	24
4	49	m	ALS, PART	normal	no	0	0	1	0	0	45 months	24
5	46	m	ALS	normal	no	0	0	1	0	0	40 months	24
6	62	m	ALS, MI, I, ARTAG, PART, AGD	normal	no	1	0	1	0	1	154 months	12
7	53	m	ALS	normal	no	0	0	1	0	0	92 months	24
8	74	m	ALS	normal	no	2	1	1	0	0	47 months	24
9	68	f	ALS	normal	no	1	0	1	0	2	n.d.	192
10	56	f	ALS	normal	no	0	1	1	0	0	48 months	72
11	57	f	ALS, FTLD-TDP Type B	normal	no	1	1	1	0	4	22 months	24
12	61	m	ALS, FTLD-TDP Type B	normal	no	0	0	1	0	5	32 months	2
13	62	f	FTLD-TDP Type C	normal	no	1	0	0	0	4	144 months	12
14	79	m	FTLD-TDP Type C	normal	no	4	0	1	0	5	135 months	24
15	69	f	FTLD-TDP Type C, CLL, ARTAG	normal	no	4	0	1	0	4	78 months	24
16	79	f	FTLD-TDP Type A, ARTAG	normal	no	2	1	1	0	4	127 months	24
17	81	f	FTLD-TDP Type C, AGD, ARTAG	normal	no	4	2	2	0	4	138 months	24
18	38	m	FTLD-TDP Type A	normal	no	0	0	1	0	3	27 months	48
19	63	m	FTLD-TDP Type A, p-preAD	normal	no	2	3	2	0	5	24 months	12
20	57	m	ALS, p-preAD	mutant	yes	1	1	1	0	1	17 months	n.d.
21	49	m	ALS, PART	mutant	yes	2	0	1	0	0	46 months	24
22	48	m	ALS	mutant	yes	2	0	1	0	0	18 months	24
23	57	m	ALS	mutant	yes	4	0	1	0	2	19 months	20
24	75	m	ALS	mutant	yes	0	0	2	0	2	n.d.	24
25	50	m	ALS, Wernicke Encephalopathy	mutant	yes	1	0	1	0	0	n.d.	24
26	46	f	ALS	mutant	yes	1	0	1	0	1	20 months	120
27	68	m	ALS, SVD	n.d.	yes	1	2	2	0	1	36 months	144
28	55	m	ALS, FTLD-TDP Type B	mutant	yes	4	0	3	0	5	30 months	12
29	58	f	FTLD-TDP Type B, AGD	mutant	yes	2	1	1	0	4	48 months	24
30	58	m	FTLD-TDP Type B	mutant	yes	1	0	1	0	5	36 months	9
31	46	m	Control	n.d.	no	0	0	1	0	0	n.a.	29
32	36	m	Control	n.d.	no	0	0	0	0	0	n.a.	48
33	66	f	Control, AGD	n.d.	no	0	0	0	0	0	n.a.	48
34	69	f	Control	n.d.	no	0	0	0	0	0	n.a.	24
35	61	m	Control, CM	n.d.	no	0	0	0	0	0	n.a.	24
36	61	m	Control	n.d.	no	0	0	0	0	0	n.a.	24
37	32	m	Control	n.d.	no	0	0	0	0	0	n.a.	n.d.
38	64	m	Control	n.d.	no	0	0	0	0	0	n.a.	24
39	67	m	Control	n.d.	no	0	0	0	0	0	n.a.	n.d.
40	60	m	Control, I	n.d.	no	1	0	0	0	0	n.a.	24
41	74	m	Control, CM, I, MI	n.d.	no	0	0	0	0	0	n.a.	72
42	62	m	Control	n.d.	no	1	0	0	0	0	n.a.	48
43	56	m	Control	n.d.	no	0	0	0	0	0	n.a.	48
44	45	m	Control	n.d.	no	0	0	0	0	0	n.a.	24
45	64	m	Control	n.d.	no	0	0	0	0	0	n.a.	n.d.
46	18	m	Control, T	n.d.	no	0	0	0	0	0	n.a.	24
47	61	m	Control, SVD	n.d.	no	1	0	0	0	0	n.a.	48
48	73	m	Control, SVD, CM	n.d.	no	1	0	2	0	0	n.a.	48
49	55	m	Control, A, I	n.d.	no	0	0	0	0	0	n.a.	96
50	74	f	Control, AGD, SVE	n.d.	no	0	0	1	0	0	n.a.	24
51	35	m	Control, Limbic encephalopathy	n.d.	no	0	0	0	0	0	n.a.	72
52	54	m	Control, GB	n.d.	no	0	0	1	0	0	n.a.	24

***C9ORF72* repeat expansion determination**

DNA was extracted from peripheral blood and/or cerebellum according to standard protocols. Analysis of the hexanucleotide repeat length in intron 1 of *C9ORF72* was performed by fragment length analysis by PCR and repeat-primed PCR (RP-PCR) as previously described (233). In three cases, we confirmed the RP-PCR result by Southern blotting (21). In addition, the presence of poly(GA) pathology was immunohistochemically assessed in the frontal cortex of all cases. The genetic determination of the *C9ORF72* repeat expansion as well as the presence of poly(GA) pathology are shown in Table 1.

Immunohistochemistry

Histological examination was performed on 5 µm-thick sections cut from formalin-fixed, paraffin-embedded tissue of frontal, pre- and postcentral, temporal and entorhinal cortex, hippocampus, hypothalamus, amygdala and spinal cord. Sections were stained with antibodies against pTDP-43, poly(GA), pMLKL, pRIPK1, RIPK1, pRIPK3, RIPK3, p-tau^(S202/T205) and Aβ₁₇₋₂₄ (Suppl. Table 1). Staining was performed with the BOND-MAX automated IHC/ISH Stainer (Leica Biosystems, Wetzlar, Germany) using the Bond Polymer Refine Detection kit (DS9800, Leica Biosystems). Briefly, slides were deparaffinized and epitopes were retrieved with low or high pH buffer. After incubation with Envision Flex Peroxidase-Blocking Reagent (Dako, Glostrup, Denmark), slides were incubated with primary antibodies for 30 min, followed by secondary antibody incubation. DAB was used for visualization. Counterstaining with haematoxylin and dehydration were carried out in an autostainer, followed by mounting in an automated cover-slipper (Leica Biosystems). A dephosphorylation assay was carried out to validate the presence of RIPK1 and RIPK3 in GVD (Suppl. Fig. 1).

For immunofluorescence double labelling using primary antibodies from different species (Suppl. Table 1), an antibody cocktail of the respective antibodies was applied, followed by a cocktail of species-specific Cy2/3-conjugated secondary antibodies (Jackson ImmunoResearch, Ltd, West Grove, PA, USA). For double labelling with primary antibodies raised in the same species (Suppl. Table 1), a sequential staining was performed using a rabbit-on-rabbit staining protocol adapted from previously described methods (234). Briefly, a coupling method was used to avoid cross-reactivity of secondary antibodies. The first rabbit primary antibody was used as described above, followed by a Cy2/3-labelled goat anti-rabbit secondary antibody. The second rabbit primary antibody was coupled to a donkey anti-rabbit Fab fragment conjugated to a Cy2/3 dye for 20 min (2 µg Fab fragment per 1 µg primary antibody) prior to its incubation with the sample. Next, normal rabbit serum (Jackson ImmunoResearch) was added for another 10 min to capture the unbound Fab fragments (10 µl serum per 1 µg Fab fragment). Then, the mix was applied to the slides to visualize the second primary antibody. Controls to rule out cross-reactivity were performed (Suppl. Fig. 2). Fluorescent-labelled slides were mounted using

ProLong Gold Antifade Mountant containing DAPI (Thermo Fisher Scientific, Rockford, IL, USA) for counterstaining of the nuclei.

Images were acquired using the Leica DM2000 LED microscope coupled to a Leica DFC 7000 T camera. Images were processed using ImageJ and combined into figures using Inkscape.

GVD staging

GVD staging was evaluated based on pMLKL immunohistochemistry using the GVD staging system proposed by Thal *et al.* (227) in a modified form applicable for ALS and FTLD-TDP cases. Each stage was defined as follows: stage 0, no GVD; stage 1, GVD limited to the subiculum and/or CA1/CA2 and/or the dentate gyrus; stage 2, GVD reaching CA4/CA3 and/or the entorhinal cortex; stage 3, GVD reaching the temporal neocortex; stage 4, GVD reaching the amygdala and/or the hypothalamus; and stage 5, GVD reaching the frontal cortex.

pTDP-43 scoring in the hippocampus

pTDP-43 pathology was assessed in the hippocampus of all cases. A semi-quantitative grading system was used by assessing the total amount of pathology, including neuronal cytoplasmic and intranuclear inclusions, glial inclusions and dystrophic neurites positive for pTDP-43. pTDP-43-positive GVD lesions were not considered in this analysis. pTDP-43 severity assessment was adapted from Mackenzie *et al.* (35). In detail, pTDP-43 pathology was graded as being absent (0), rare (1), occasional (2), mild (3), moderate (4) or numerous (5). These scores were referred to as pTDP-43 scores. Inclusions were considered “rare” if only a few lesions could be found in the entire hippocampus section, “occasional” if lesions were relatively easy to find but not present in every 20x microscopic field, “mild” when lesions were present in every 20x microscopic field, “moderate” when multiple lesions were present in every 20x microscopic field, and “numerous” when abundant lesions were present in every 20x microscopic field, as shown in Suppl. Fig. 3.

Quantification of neuronal density in the hippocampal CA1 region

For quantification of neuronal density in the hippocampal CA1 region, three consecutive images (0.632 x 0.474 mm) of anti-pMLKL stained sections were taken using the Leica DM2000 LED microscope using a 20x objective (221). Criteria regarding morphological conditions of cells to be included were determined before quantification. Neurons were identified based on the nuclear pattern of the counterstaining. Image analysis was performed using ImageJ.

Protein extraction

For biochemistry, the right hemispheres were cut in approx. 1 cm thick slabs and frozen at -80°C. Fifty mg of brain tissue was weighed and mechanically homogenized in 0.5 ml 2% SDS in TBS (Tris-buffered saline) with Nuclease (Pierce™ Universal Nuclease, Thermo Fisher Scientific) and a cocktail of protease/phosphatase inhibitors (Halt, Thermo Fisher Scientific) using a micropestle. Samples were sonicated, followed by a centrifugation at 14 000 *g* for 30 min. The resulting supernatant was used. Protein concentrations were determined using the Pierce BCA Protein Assay Kit (Thermo Fisher Scientific).

Cell culture and treatment

Human neuroblastoma SH-SY5Y cells were cultured in DMEM/F12 (Thermo Fisher Scientific) supplemented with Penicillin-Streptomycin (Thermo Fisher Scientific) and maintained at 37°C in a CO₂ incubator with a controlled humidified atmosphere composed of 95% air and 5% CO₂. For induction of necroptosis, SH-SY5Y cells were stimulated for 4 h at 37°C with TSZ, which is a combination of TNFα (30 ng/ml, Sigma-Aldrich), Smac-mimetic (10 μM, Selleckchem, Munich, Germany) and zVAD-fmk (20 μM, Millipore, Billerica, USA). For collecting cells, they were washed with PBS and lysed in RIPA buffer (Sigma-Aldrich) containing PhosSTOP (Sigma-Aldrich) and a protease inhibitor cocktail (Sigma-Aldrich). Protein concentrations were measured using the Pierce BCA Protein Assay Kit (Thermo Fisher Scientific). Cell lysates were used for validation of antibodies and as a positive control for western blot. The use of the human cell line for this experiment was approved by the UZ Leuven ethics committee.

Western blotting

For western blotting, 10 μg of protein was loaded on a Bis-Tris 4-12% gradient SDS-PAGE (Invitrogen, Thermo Fisher Scientific) in MOPS-SDS running buffer (Alfa Aesar, Haverhill, MA, USA), electrophoresed at 150V for 60 min, and transferred to a nitrocellulose membrane (Semidry transfer, Biorad, Hercules, CA, USA). Membranes were blocked with 5% non-fat dried milk (AppliChem, Darmstadt, Germany) or 5% BSA (Sigma-Aldrich) in PBS 0.1% Tween-20 (PBST). Primary antibodies and the corresponding dilutions are listed in Suppl. Table 1. Secondary antibodies were goat anti-rabbit IgG-HRP or goat anti-mouse IgG-HRP (1:10 000, polyclonal, Dako). Blots were developed with SuperSignal West Pico or Dura plus ECL reagent (Thermo Fisher Scientific). Digital images were acquired using the Amersham Imager 600 (GE Healthcare, Chicago, IL, USA). All blots were stripped (Restore Western Blot Stripping Buffer, Thermo Fisher Scientific) of bound antibodies and re probed with GAPDH to control for equal protein loading. Band intensities were measured using ImageJ and were normalized to GAPDH.

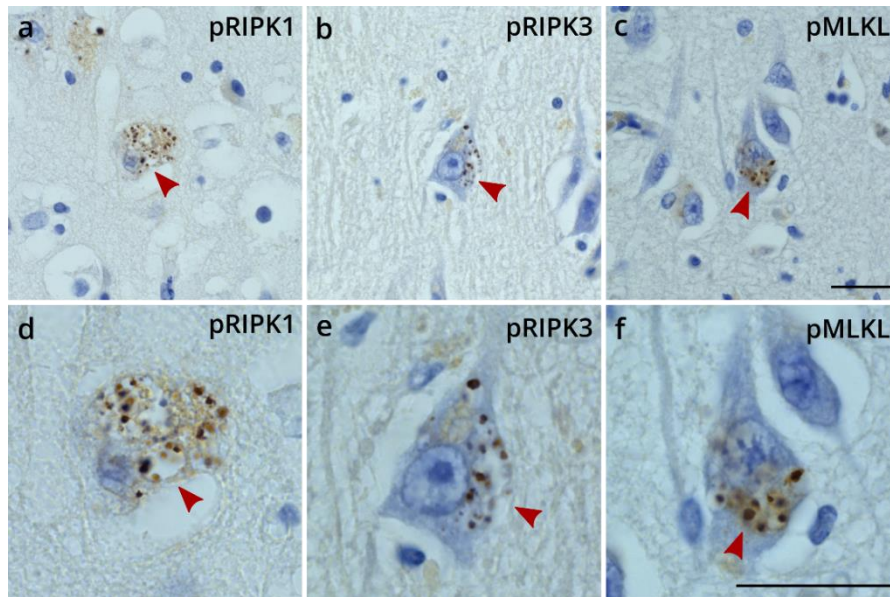
Statistical analysis

Statistical analyses were performed using IBM SPSS (version 26) and Graphpad Prism (version 8.2.0.) software. Multinomial logistic regressions controlled for age and sex, or a one-way ANOVA or Kruskal-Wallis test followed by Tukey's or Dunn's multiple comparisons were used to determine the significant difference between three groups. When analysing nominal data, a Fisher's exact test was used. To examine the correlation between pMLKL GVD stage and several parameters, partial Pearson's correlation analysis (controlled for age and sex) was performed. To estimate the effect of explanatory variables on pMLKL GVD stage and neuronal density, we conducted linear regression analyses. Data are presented as mean \pm SEM.

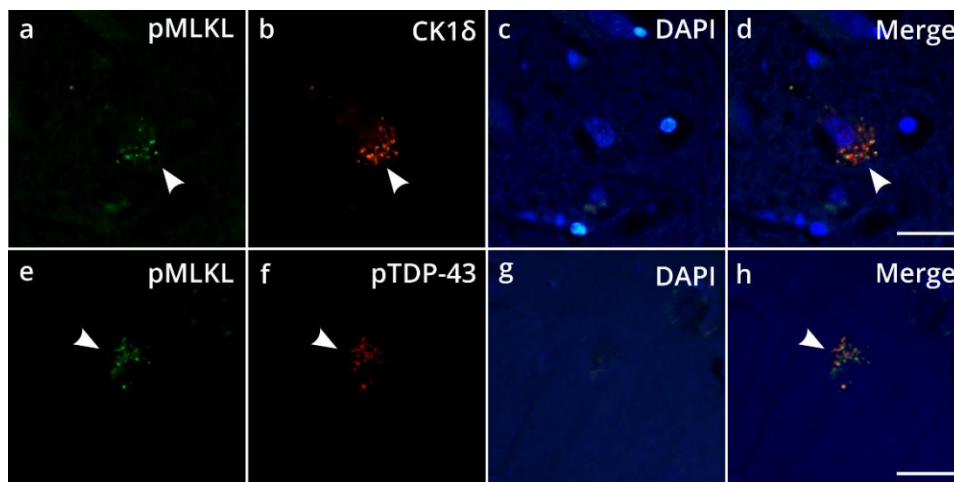
4. Results

Activated necrosome components are present in GVD lesions in the ALS/FTLD brain

To investigate the presence of activated necrosome proteins in GVD in the ALS/FTLD brain, we performed a pathological analysis on human *post-mortem* brain tissue from ALS (n = 18), FTLD-TDP (n = 9), ALS+FTLD-TDP (n = 3) and control cases (n = 22). The hippocampus, entorhinal cortex, temporal cortex, amygdala, hypothalamus and frontal cortex were used. Immunohistochemical staining showed positive immunoreactivity for pRIPK1 (Fig 1 a, d), pRIPK3 (Fig 1 b, e) and pMLKL (Fig 1 c, f) in 11 out of 18 ALS, 8 out of 9 FTLD-TDP, 2 out of 3 ALS+FTLD-TDP and 4 out of 22 control cases. More specifically, these activated necrosome proteins were present in GVD lesions in neurons (Fig 1). We refer to these lesions as GVDn+ (GVDn+, i.e. GVD positive for the activated necrosome). Immunoreactivity was predominantly found in hippocampal neurons of the dentate gyrus, regions of the Ammon's horn (CA1-CA4), the subiculum and the entorhinal cortex. Additionally, GVDn+ was sporadically present in neurons in the temporal cortex (Brodmann area 36), the hypothalamus and the amygdala. The distribution pattern of GVDn+ of all cases as represented by the GVD stages is shown in Table 1. The frontal cortex was devoid of GVDn+ in all cases, explaining the absence of GVD stage 5 in our cohort. Antibody specificity was evaluated by dephosphorylation of the tissue as previously shown in AD cases (221) and detection of non-phosphorylated RIPK1 and RIPK3 in GVD (Suppl. Fig. 1). Double immunofluorescence showed the co-localization of GVDn+ with established GVD markers, i.e. pTDP-43 and CK1 δ (Fig 2; Suppl. Fig. 2). To confirm the presence of pMLKL in GVD, another primary antibody against pMLKL was used, showing the same immunoreactivity for GVD in the ALS/FTLD brain (Suppl. Fig. 4). For all further analyses, pMLKL was used as a marker for GVDn+ as previously described (221).



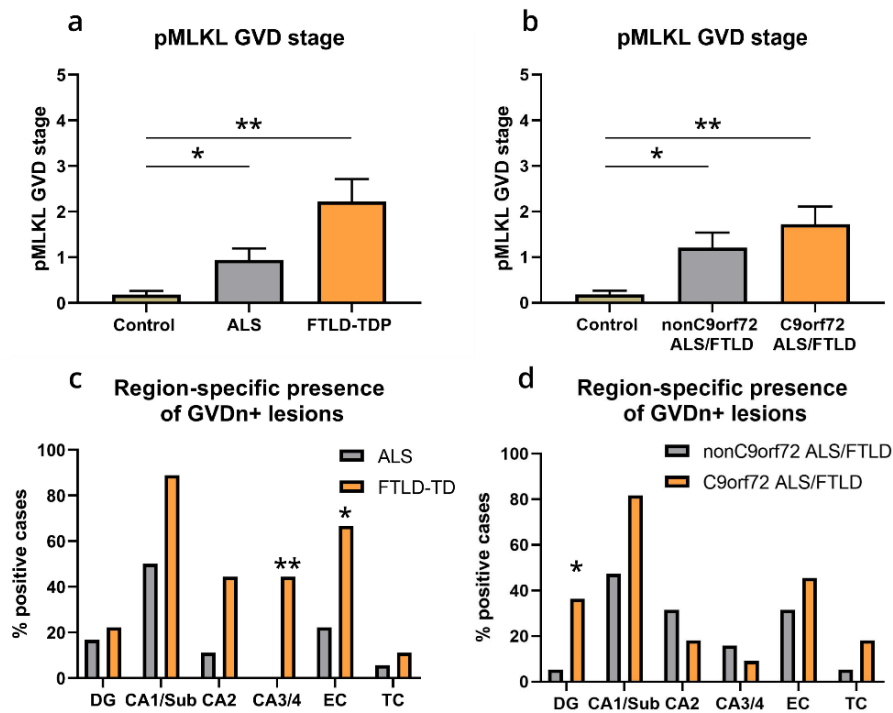
Ch. I - Figure 1. GVD lesions in cases of the ALS/FTLD spectrum are positive for all activated necrosome components. Immunohistochemical detection of activated necrosome components (pRIPK1, pRIPK3, pMLKL) in representative ALS and FTLD-TDP brains (cases 6 and 30) shows a specific immunoreactivity for pRIPK1 (**a, d**), pRIPK3 (**b, e**) and pMLKL (**c, f**) in GVD granules in CA1 hippocampal pyramidal neurons (arrowheads). **d, e** and **f** are magnifications of **a, b** and **c** respectively. GVD-free neurons were negative for these three markers. Scale bars represent 30 μm .



Ch. I - Figure 2. pMLKL-positive GVD lesions colocalize with established GVD markers. GVD granules in representative hippocampal CA1 pyramidal neurons in the ALS/FTLD brain positive for pMLKL (**a, e**) are also immunoreactive for the established GVD markers CK1 δ (**b, d**; arrowhead) and pTDP-43 (**f, h**; arrowhead). Staining of a representative FTLD-TDP case (case 17). Control conditions are depicted in Suppl. Fig. 2. Scale bars represent 25 μm .

Distribution of pMLKL-positive GVD and the association with diagnosis

To assess the severity of pMLKL-positive GVD in ALS, FTLD-TDP and control cases, we determined the pMLKL GVD stage (227). ALS ($p = 0.021$) and FTLD-TDP cases ($p = 0.003$) showed higher pMLKL GVD stages compared to control cases (Fig 3a; nominal regression corrected for age and sex). When analysing the effect of the *C9ORF72* mutation, we observed a difference in pMLKL GVD stage for both C9orf72 and non-C9orf72 ALS/FTLD groups compared to controls, which was more pronounced for C9orf72 ALS/FTLD ($p = 0.003$) than for non-C9orf72 ALS/FTLD cases ($p = 0.021$) (Fig 3b; nominal regression corrected for age and sex). However, non-C9orf72 ALS/FTLD cases were not different from C9orf72 ALS/FTLD cases with respect to the pMLKL GVD stage ($p = 0.371$; Fig 3b). The number of cases positive for pMLKL GVD was higher in C9orf72 ALS/FTLD (10/11) compared to non-C9orf72 ALS/FTLD cases (11/19), but this did not reach significance ($p = 0.1$; Fisher's exact test). Next, we assessed the percentage of GVDn+ positive cases per affected brain region. In all regions, the percentage of affected cases was numerically higher in the FTLD-TDP compared to the ALS group (Fig 3c). This reached significance in the CA3/4 hippocampal region ($p = 0.0072$; Fisher's exact test) and the entorhinal cortex ($p = 0.0393$; Fisher's exact test). ALS/FTLD cases carrying a *C9ORF72* mutation tended to have + GVDn more often in the CA1/subiculum region and in later affected regions (entorhinal and temporal cortex) compared to non-C9orf72 ALS/FTLD cases, although not significant (Fig 3d). We also observed that C9orf72 ALS/FTLD cases showed an increased occurrence of pMLKL-positive GVD in the dentate gyrus of the hippocampus compared to non-C9orf72 ALS/FTLD cases ($p = 0.0472$; Fisher's exact test; Fig 3d). To further investigate the link between pMLKL-positive GVD and the *C9ORF72* mutation, we evaluated the spatial relationship between DPR pathology and GVDn+ by immunofluorescence labelling of the hippocampus of C9orf72 ALS/FTLD cases. We did not observe co-localization between pMLKL-positive GVD lesions and poly(GA), poly(GP) or poly(GR) inclusions. However, we detected neurons bearing both poly(GA) aggregates and GVDn+ granules in the cytoplasm, although these lesions did not co-localize with one another (Suppl. Fig. 5 a-d and e-h). In addition, we found neurons with GVDn+ lesions in the absence of DPRs (Suppl. Fig. 5 i-l) and neurons exhibiting poly(GA) aggregates but no GVD (Suppl. Fig. 5 m-p). For poly(GP) and poly(GR), we found similar co-existence with pMLKL-positive GVD in neurons, but to a lesser extent.

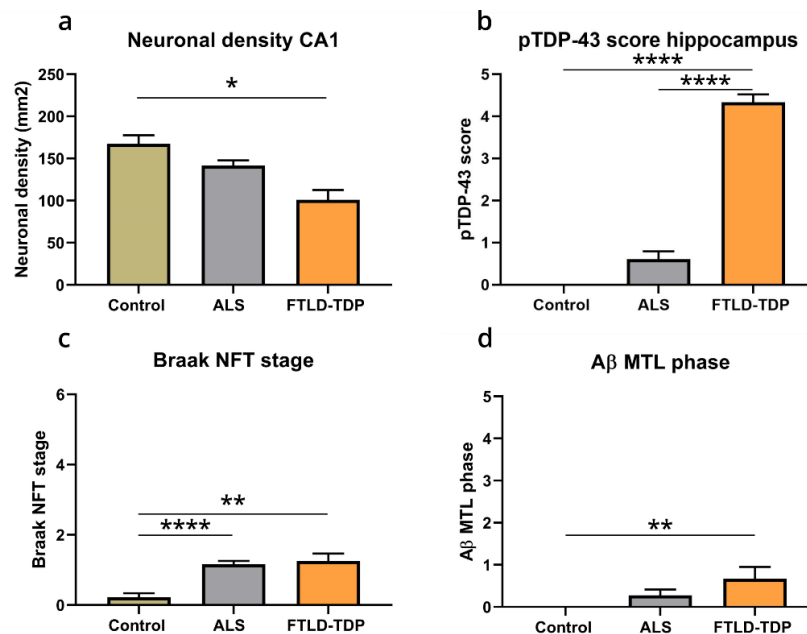


Ch. I - Figure 3. Distribution of pMLKL-positive GVD and the link with diagnosis. (a-b) Graphs show pMLKL GVD stage based on pMLKL-immunoreactivity in GVD lesions (221,227) among control, ALS and FTLN-TDP cases (a) and ALS/FTLD cases with and without *C9ORF72* mutation (b). FTLN-TDP and ALS cases with or without *C9ORF72* mutation showed higher pMLKL GVD stages than control cases. Multinomial regression corrected for age and sex was used for statistical analysis. Data are presented as mean ± SEM. * $p < 0.05$; ** $p < 0.01$. (c) Percentage of cases positive for GVDn+ lesions in a given region of ALS and FTLN-TD cases. A Fisher's exact test shows a significant difference in the CA3/4 region ($p = 0.0072$) and the entorhinal cortex ($p = 0.0393$). * $p < 0.05$; ** $p < 0.01$. (d) Percentage of cases positive for GVDn+ lesions in a given region of non-*C9orf72* ALS/FTLD and *C9orf72* ALS/FTLD. A Fisher's exact test shows a significant difference in the dentate gyrus ($p = 0.0416$). * $p < 0.05$.

To evaluate the effect of the *C9ORF72* mutation on the level of proteins involved in necroptotic cell death, i.e. RIPK1, pRIPK1, RIPK3, pRIPK3, MLKL and pMLKL, we performed western blot on extracts from frozen hippocampal tissue (Suppl. Fig. 6). TSZ-treated SH-SY5Y cells were used as positive control. MLKL expression was not different between the three groups ($p = 0.1646$). We detected a small numerical increase in RIPK1 and RIPK3 expression in *C9orf72* ALS/FTLD cases compared to control cases, although not significant. pRIPK1 levels, however, were increased in *C9orf72* ALS/FTLD cases compared to control cases ($p = 0.0019$) and non-*C9orf72* cases ($p = 0.0295$), with non-*C9orf72* ALS/FTLD cases showing no significant difference in relation to control levels ($p = 0.3087$). Significant amounts of pRIPK3 and pMLKL could not be detected by their corresponding antibodies in human brain homogenates, as shown previously (221).

Neuronal density in hippocampal CA1 region is decreased in FTLD-TDP cases

Since it has previously been shown that GVD in AD correlates with neuronal loss, we quantified neuronal densities in the CA1 region of the hippocampus in ALS/FTLD and control cases. Multinomial regression corrected for age and sex showed a decrease in CA1 neuronal density in FTLD-TDP compared to control cases ($p = 0.015$; Fig 4a), which almost reached significance when compared to ALS cases ($p = 0.082$). ALS cases showed a trend towards a lower neuronal density, however this was not significant ($p = 0.101$; Fig 4a). When investigating differences in the presence of pathological protein aggregates among ALS, FTLD-TDP and control cases, we noticed that the hippocampal pTDP-43 pathology score was higher in FTLD-TDP cases compared to ALS and control cases ($p < 0.0001$; Kruskal-Wallis test with Dunn's multiple comparisons; Fig 4b). Such differences were not observed among these disease groups for Braak NFT stage and A β MTL phase (Fig 4c, d). Compared to controls, neuronal density was reduced in the non-C9orf72 ALS/FTLD ($p = 0.024$) and in the C9orf72 ALS/FTLD group ($p = 0.044$) (Suppl. Fig. 7a; multinomial regression corrected for age and sex). The non-C9orf72 ALS/FTLD and C9orf72 ALS/FTLD groups were not different ($p = 0.996$) (Suppl. Fig. 7a). There was also no difference between C9orf72 versus non-C9orf72 ALS/FTLD cases regarding hippocampal pTDP-43 score, Braak NFT stage and A β MTL phase (Suppl. Fig. 7b-d; Kruskal-Wallis with Dunn's multiple comparisons).



Ch. 1 - Figure 4. Neuronal density in the hippocampal CA1 region is decreased in FTLD-TDP cases. (a) Quantitative data representing neuronal densities (neurons/mm²) in the CA1 region of the hippocampus of controls (n = 22), ALS (n = 18) and FTLD-TDP (n = 9) cases. Multinomial regression corrected for age and sex was used for statistical analysis of the data. (b-d) Mean hippocampal pTDP-43 score (b), Braak NFT stage (c) and A β MTL phase (d) are shown for the different groups. Kruskal-Wallis test followed by Dunn's multiple comparisons was used for statistical analyses. Data are presented as mean \pm SEM. * $p < 0.05$; ** $p < 0.01$; *** $p < 0.0001$.

TDP-43 and tau pathological protein lesions are associated with a higher pMLKL GVD stage and a lower neuronal density in the hippocampal CA1 region

A Pearson’s partial correlation analysis corrected for age and sex (n = 52) revealed that pMLKL GVD stage correlated with Braak NFT stage ($r = 0.491$; $p = 0.001$) and hippocampal pTDP-43 score ($r = 0.538$; $p < 0.001$), but not with A β MTL phase ($r = 0.216$; $p = 0.159$). Furthermore, neuronal density in the hippocampal CA1 region correlated with Braak NFT stage ($r = -0.397$; $p = 0.008$) and hippocampal pTDP-43 score ($r = -0.541$; $p < 0.001$). The pMLKL GVD stage was not associated with neuronal density ($r = -0.193$; $p = 0.209$). *Post-mortem* interval did not correlate with any of these parameters (n = 48; $p = 0.126 - 0.946$) (Suppl. Table 2) and was therefore not considered as control variable in the following regression analysis.

In separate linear regression models with pMLKL GVD stage as dependent variable, Braak NFT stage ($\beta = 0.501$; $p < 0.001$) and pTDP-43 score ($\beta = 0.603$; $p < 0.001$) were reliable predictors of pMLKL GVD stage, whereas A β MTL phase was less strongly associated with pMLKL GVD stage, however still significant ($\beta = 0.320$; $p = 0.021$) (Table 2, part 1). When we repeated these analyses including age and sex as additional independent variables, only Braak NFT stage ($\beta = 0.440$; $p = 0.001$) and pTDP-43 score ($\beta = 0.554$; $p < 0.001$) remained significant predictors of pMLKL GVD stage, whereas A β MTL phase did not ($\beta = 0.239$; $p = 0.088$; Table 2, part 2). Next, we used a model that combined pTDP-43 score and Braak NFT stage, showing pTDP-43 score as the best predictor of pMLKL GVD stage in our cohort ($\beta = 0.472$; $p < 0.001$), with Braak NFT stage remaining significant ($\beta = 0.281$; $p = 0.026$; Table 2, part 3). When adding age and sex to the model term, pTDP-43 score was again the best predictor ($\beta = 0.444$; $p = 0.001$) of pMLKL GVD stage compared to Braak NFT stage ($\beta = 0.257$; $p = 0.043$). Age and sex did not have an effect on pMLKL GVD stage in this model (Table 2, part 4).

Ch. I - Table 2. Linear regression model for pMLKL GVD stage. Influence of predictor variables, i.e. the Braak NFT stage, the A β MTL phase and hippocampal pTDP-43 score on pMLKL GVD stage in different linear regression model terms as defined in parts 1-4. Age and sex were included in the model as potential confounders but were not statistically significant. * $p < 0.05$; ** $p < 0.01$; *** $p < 0.001$.

Part 1

Predictor variable	Coefficient β	p value
Braak NFT stage	0.501	$p < 0.001$ ***

Dependent variable: pMLKL GVD stage

Predictor variable	Coefficient β	p value
A β MTL phase	0.320	$p = 0.021$ *

Dependent variable: pMLKL GVD stage

Predictor variable	Coefficient β	p value
pTDP-43 score	0.603	$p < 0.001$ ***

Dependent variable: pMLKL GVD stage

Part 2

Predictor variable	Coefficient β	<i>p</i> value
Braak NFT stage	0.440	<i>p</i> = 0.001**
Age	0.219	<i>p</i> = 0.100
Sex	-0.043	<i>p</i> = 0.738

Dependent variable: pMLKL GVD stage

Predictor variable	Coefficient β	<i>p</i> value
A β MTL phase	0.239	<i>p</i> = 0.088
Age	0.266	<i>p</i> = 0.068
Sex	-0.038	<i>p</i> = 0.784

Dependent variable: pMLKL GVD stage

Predictor variable	Coefficient β	<i>p</i> value
pTDP-43 score	0.554	<i>p</i> < 0.001***
Age	0.195	<i>p</i> = 0.115
Sex	0.030	<i>p</i> = 0.800

Dependent variable: pMLKL GVD stage

Part 3

Predictor variable	Coefficient β	<i>p</i> value
pTDP-43 score	0.472	<i>p</i> < 0.001***
Braak NFT stage	0.281	<i>p</i> = 0.026*

Dependent variable: pMLKL GVD stage

Part 4

Predictor variable	Coefficient β	<i>p</i> value
pTDP-43 score	0.444	<i>p</i> = 0.001**
Braak NFT stage	0.257	<i>p</i> = 0.043*
Age	0.159	<i>p</i> = 0.187
Sex	0.023	<i>p</i> = 0.843

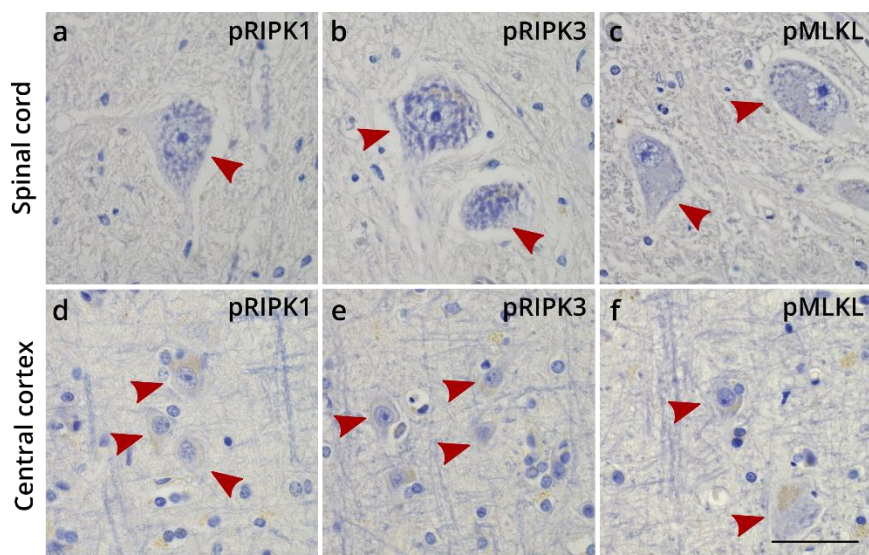
Dependent variable: pMLKL GVD stage

Next, we performed linear regression with hippocampal neuronal density as dependent variable and Braak NFT stage, A β MTL phase, pTDP-43 score and pMLKL GVD stage as separate predictor variables (Suppl. Table 3). Both Braak NFT stage ($\beta = -0.412$; $p = 0.004$) and pTDP-43 score ($\beta = -0.551$; $p < 0.001$) were significant predictors of hippocampal neuronal loss. A β MTL phase ($\beta = -0.212$; $p = 0.156$) and pMLKL GVD stage ($\beta = -0.225$; $p = 0.132$) were not significantly associated with a decrease in neuronal density in ALS/FTLD (Suppl. Table 3, part 1). When including age and sex in our models, both Braak NFT stage ($\beta = -0.402$; $p = 0.008$) and pTDP-43 score ($\beta = -0.573$; $p < 0.001$) remained very good predictors of loss of hippocampal neurons (Suppl. Table 3, part 2). However, when we combined Braak NFT stage and pTDP-43 stage in a model, pTDP-43 score was the best predictor of hippocampal neuronal loss (β

= -0.460; $p = 0.003$; Suppl. Table 3, part 3). This was also true when age and sex were included in the model ($\beta = -0.481$; $p = 0.003$; Suppl. Table 3, part 4).

ALS-affected regions do not show elevation of necroptosis-related proteins

To investigate the involvement of necroptosis in brain and spinal cord regions that exhibit severe motor neuron loss in ALS, we performed staining for pRIPK1, pRIPK3 and pMLKL in the spinal cord and precentral cortex of ALS cases. Motor neurons in the ALS spinal cord and precentral cortex were devoid of phosphorylated necroptotic proteins (Fig 5). As described above, most FTLD-TDP cases showed immunoreactivity for pRIPK1, pRIPK3 and pMLKL in GVD lesions in the hippocampus and rarely in the temporal cortex. However, the frontal cortex was negative for the necrosome. To investigate this further, we performed western blots on extracts from central cortex (precentral gyrus) from ALS cases and frontal cortex from FTLD-TDP cases, as these are the respective brain regions showing disease-related neurodegeneration. TSZ-treated SH-SY5Y cells were used as positive control. In ALS cases, RIPK1, RIPK3, pRIPK1 and MLKL were not elevated in the central cortex compared to control cases (Suppl. Fig. 8). In contrast to ALS, the frontal cortex of FTLD-TDP cases showed a significant increase of RIPK1 compared to control ($p < 0.0001$) and ALS cases ($p = 0.0013$), as well as of pRIPK1 compared to control ($p = 0.0454$) and ALS cases ($p = 0.0007$) (Suppl. Fig. 8). There was a trend towards higher MLKL levels in FTLD-TDP compared to control cases, although not statistically significant ($p = 0.0675$). RIPK3 levels were not different between control cases and FTLD-TDP cases ($p = 0.6770$). Significant amounts of pRIPK3 and pMLKL could not be detected by their corresponding antibodies in brain homogenates from control, ALS and FTLD-TDP cases.



Ch. I - Figure 5. ALS-affected regions do not show activated necrosome proteins by immunohistochemistry. (a-f) Immunohistochemical staining for pRIPK1 (a, d), pRIPK3 (b, e) and pMLKL (c, f) in the spinal cord and central cortex of ALS patients. Arrowheads indicate lower (a-c) and upper (d-f) motor neurons negative for the respective proteins. Staining of representative ALS cases (a-c case 2; d-f case 8). Scale bar represents 50 μm .

5. Discussion

Here, we showed that 1) GVD lesions in the ALS/FTLD-TDP brain exhibit the activated components of the necrosome, i.e. pRIPK1, pRIPK3 and pMLKL, 2) hippocampal FTLD-related TDP-43 lesions contribute to the development of necrosome-positive GVD, in addition to tau pathology, and 3) the activated necrosome was not detectable in motor neurons in the spinal cord and motor cortex typically degenerating in ALS. To our knowledge, this is the first time that necrosome accumulation in GVD could be linked with cytoplasmic TDP-43 inclusions and threads as potential trigger/accelerator of GVD development in FTLD-TDP. Importantly, GVD in association with TDP-43 lesions selectively affected hippocampal neurons but not motor neurons. Moreover, in FTLD-TDP cases we observed a decrease in neuronal density in the hippocampal CA1 region. This could not be attributed to comorbid AD pathology, but to FTLD-like TDP-43 pathology.

Necrosome-positive GVD lesions were predominantly present in hippocampal regions, and sporadically in the temporal cortex, the amygdala and the hypothalamus. We did not observe upregulation of necroptosis-related proteins in ALS-affected spinal cord or central cortex motor neurons. Thus, necrosome accumulation in association with GVD selectively affects hippocampal neurons. Whether co-existing tau pathology is a prerequisite for the development of GVD, as supported by animal and *in vitro* studies (235,236), requires further study. However, the absence of activated necrosome compounds in spinal cord and motor cortex argues against the involvement of necroptosis in ALS motor neuron death. In line with our results, but contrary to previous evidence (99,108), two studies recently demonstrated that necroptosis might be dispensable for motor neuron degeneration in a SOD1 mouse model for ALS (118,119). This, together with our findings, indicates that the potential of therapeutic targeting of the necroptosis pathway in ALS may be limited. Further work is needed to unravel which cell death mechanisms are responsible for upper and lower motor neuron degeneration in this disease.

Recently, Koper *et al.* showed that GVDn+ in AD was associated with tau but not A β pathology. The presence of GVDn+ correlated with neuronal loss in the hippocampal CA1 region and the frontal cortex, suggesting a role for GVDn+ and tau pathology as potential drivers of neuronal loss in AD (221). In our cohort, GVDn+ correlated highly with Braak NFT stage and the pTDP-43 pathology score, but not with A β MTL phase. Although the initial formation of GVD has been thought to be triggered by pathological tau (235), our data shows that pTDP-43 lesions are also associated with GVD. This indicates that other toxic proteins apart from tau could play a role in the development of GVD and its associated necrosome accumulation, e.g. TDP-43 and possibly dipeptide repeat proteins. This could explain the increased prevalence of GVD in FTLD-TDP, as in this group the hippocampus is severely affected by TDP-43 pathology, in contrast to ALS cases. Likewise, the presence of DPR proteins in *C9ORF72* expansion

carriers might play a role in the increased prevalence of GVD in these cases, as reported by Riku *et al.* (228). The effect of TDP-43 pathological lesions other than GVD on the development of GVD might have been undetected in AD due to a lack of investigation of TDP-43 inclusions. It remains unclear whether the occurrence of TDP-43 inclusions in 50-70% of AD cases (48, 49) also plays a role in GVD development in AD. While we showed that the severity of non-GVD pTDP-43 pathology in the hippocampus can predict the pMLKL GVD stage, pTDP-43 is also a well-established GVD marker (223). How pathological proteins like tau and pTDP-43 are involved in necrosome-positive GVD remains unclear. Cellular and animal models displaying aggregates of these pathological proteins might help to unravel their contribution to GVD and the involvement of the necrosome.

In contrast to what Riku *et al.* observed based on H&E-identified GVD (228), we could neither find a significant relationship between the *C9ORF72* repeat expansion and GVDn+, nor did we observe a convincing relationship between GVDn+ lesions and *C9orf72*-related DPR pathology. This could be due to the limited number of *C9orf72*-positive cases in our cohort. However, our *C9orf72* cases with long repeat sequences exhibited high densities of poly(GA)-positive DPRs in CA1/subiculum region (22). Therefore, it is not likely that in our cases co-localization between poly(GA) and pMLKL-positive GVD would have been overlooked. However, we observed that more *C9orf72* ALS/FTLD cases displayed GVDn+ in the dentate gyrus compared to non-*C9orf72* cases, which is in line with findings from Riku *et al.* (228). We also observed an increase in pRIPK1 levels in the hippocampus of *C9orf72* ALS/FTLD compared to non-*C9orf72* ALS/FTLD cases. Therefore, we were able to partially show a relation between necrosome-positive GVD and the *C9ORF72* mutation. A possible explanation for the association between GVDn+ and the *C9ORF72* mutation observed by Riku *et al.* is the role of the *C9orf72* protein in autophagy. It has been demonstrated that loss of *C9orf72* impairs autophagy and induces cell dysfunction and death (96,239–241). *C9ORF72* expansion cases have been shown to exhibit decreased levels of the *C9orf72* protein, which could have an effect on autophagic pathways (242). In addition, GVD lesions are known to be positive for autophagic markers (e.g. LAMP1, CHMP2B) and are thought to represent late-stage autophagic organelles (222). Therefore, it is possible that reduced levels of the *C9orf72* protein in *C9ORF72* expansion cases stimulate GVDn+ formation in neurons through the alteration of autophagic pathways.

A recent study by Hanna-Addams *et al.* strengthens the relationship between necroptosis and GVD (243). They showed that casein kinase 1 (CK1) proteins (α , δ and ϵ) are responsible for RIPK3 phosphorylation at Serine 227 and suggested that CK1 proteins are components of the necrosome. Interestingly, all three CK1 isoforms are present in GVD (223). On the other hand, Goodall *et al.* demonstrated that p62/SQSTM1 recruits RIPK1 and mediates necrosome assembly in association with the autophagy machinery, which functions as a scaffold. This complex is retained as the

autophagosome matures, allowing increased necrosome activation (156). This strengthens the link between autophagy and necroptosis and suggests that necrosome-positive GVD detected in the brain reflects the accumulation of the necrosome in autophagic vesicles. Whether this eventually results in necroptotic cell death or whether the necrosome is 'trapped' in late-stage autophagic vacuoles is still unclear. In addition, it was shown that TBK1 can inhibit the activity of RIPK1 by preventing its trans-phosphorylation. Therefore, TBK1 loss-of-function mutations as observed in more than 10% of familial ALS/FTLD cases could lead to increased RIPK1 activity (108). The activation of RIPK1 may lead to apoptosis or necroptosis, depending on the activity of caspase-8. Extensive neuroinflammation in the frontotemporal cortex accompanies TDP-43 pathology in FTLD patients (244), and the expression of pro-inflammatory mediators was shown to be increased in ALS/FTLD (245,246), which likely is driven by a response to tissue damage in the brain (247). Such inflammatory response can be the result of necroptotic cell death. In contrast, apoptotic cell death is thought to cause less damage to the surrounding cells without significant microgliosis (100). Interestingly, some studies reported the presence of activated caspase-3, the executioner of apoptosis, in GVD lesions in AD (248–250). However, activated caspase-8, which enables the activation of caspase-3, was not detected in GVD (249). This, in combination with the absence of apoptotic morphological features in cells bearing GVD (223), and the presence of an inflammatory response in the ALS/FTLD brain argues against a role for apoptosis in GVD-related neuronal death. Given the presence of the activated necrosome and the microglia response to GVD (221), we speculate that necroptosis-related processes are more likely involved in the degeneration of GVD-bearing neurons than apoptosis.

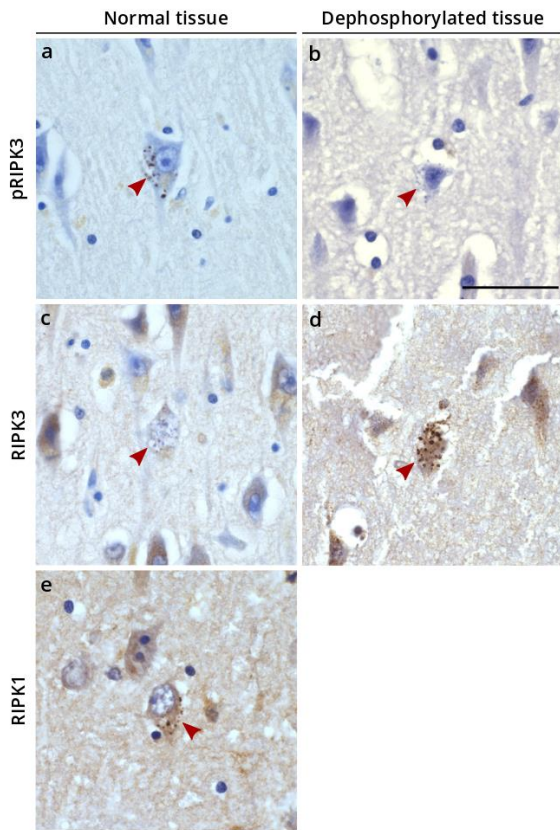
The observed increase in RIPK1 and pRIPK1 protein levels in FTLD-TDP frontal cortex might reflect the higher GVDn+ severity in these cases. However, based on immunohistochemistry, we did not detect GVDn+ lesions in the frontal cortex. Therefore, it is possible that this elevation in RIPK1 and its phosphorylated form might relate to other functions of the RIPK1 protein, as it also plays a role in apoptotic and inflammatory pathways (105). Additionally, we did not find a significant relationship between the presence of GVDn+ and hippocampal neuronal death in ALS/FTLD. This could be due to the low GVD stage in comparison with e.g. AD cases, where GVDn+ is highly associated with neuronal death. Therefore, it is not yet clear to what extent GVDn+ has an impact on disease progression and neuronal loss in ALS/FTLD-TDP cases.

One of the limitations of this study is the small number of C9orf72 cases (n = 11), especially the subgroup of C9orf72 FTLD-TDP cases (n = 3). Another limitation is that we were not able to assess significant amounts of pMLKL and pRIPK3 protein levels in human brain tissues by western blotting. This could be due to too low concentrations of these proteins in the brain lysates, and possible cleavage or aggregation of the proteins due to autolytic *post-mortem* processes or due to its physiological

function. Furthermore, functional assays are needed to further investigate the role of pathological protein aggregates in the development of necrosome-positive GVD.

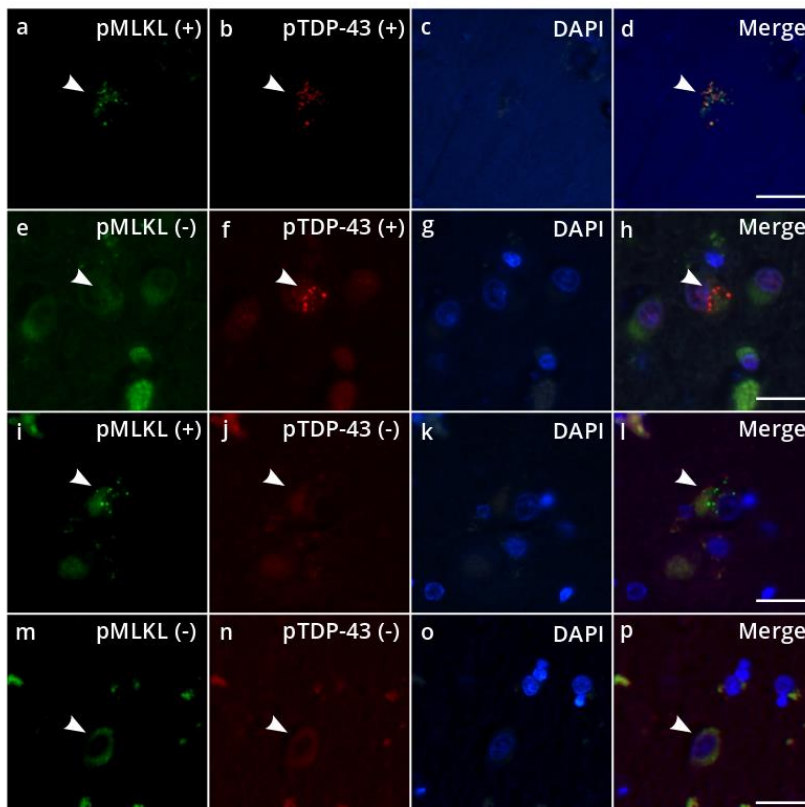
In conclusion, our findings point towards a novel role for TDP-43 as an important contributor to necrosome accumulation in GVD lesions of hippocampal neurons in ALS/FTLD patients, but not in motor neurons. This suggests that pTDP-43, similar to p-tau pathological lesions in AD, can induce or accelerate the development of GVDn+ in ALS/FTLD in specifically vulnerable neurons.

6. Supplementary information

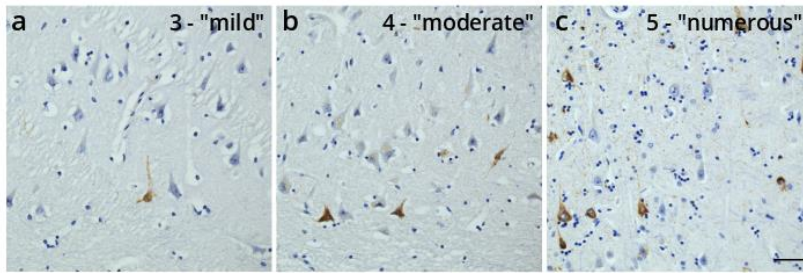


Ch. I - Suppl. Figure 1. Determination of the specificity of necroptosis antibodies in neurons with GVD. An alkaline phosphatase dephosphorylation assay was used to allow the detection of non-phosphorylated proteins after dephosphorylation. This was only done for RIPK3, as the MLKL antibody did not show proper staining in immunohistochemistry, and the RIPK1 antibody could detect GVD in normal tissue. Tissue sections of the hippocampus were incubated with a solution composed of alkaline phosphatase (Sigma-Aldrich, Saint Louis, MO, USA) diluted 1:20 in Tris-buffer with phenylmethylsulfonyl fluoride (Sigma-Aldrich), for 24 h at 30°C. Next, immunohistochemistry for pRIPK3 and RIPK3 was performed. In parallel, untreated (non-dephosphorylated) sections were processed with the same antibodies. For these experiments, the same protocol for immunohistochemistry was followed as described in Materials and Methods. **(a, b)** pRIPK3-immunoreactivity in GVD disappeared after dephosphorylation (arrowheads), confirming the removal of phosphorylated epitopes. **(c, d)** An anti-RIPK3 antibody did not detect GVD in normal tissue (arrowhead in c). However, GVD becomes detectable using this antibody after dephosphorylation (arrowhead in d). **(e)**

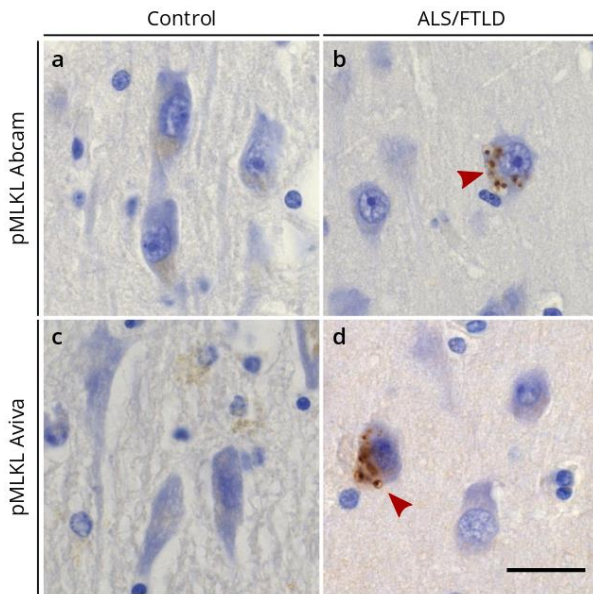
Positive immunoreactivity for RIPK1 could be detected in normal tissue, without dephosphorylation (arrowhead). Staining of representative cases (case 15, 28 and 30). Scale bar represents 25 µm.



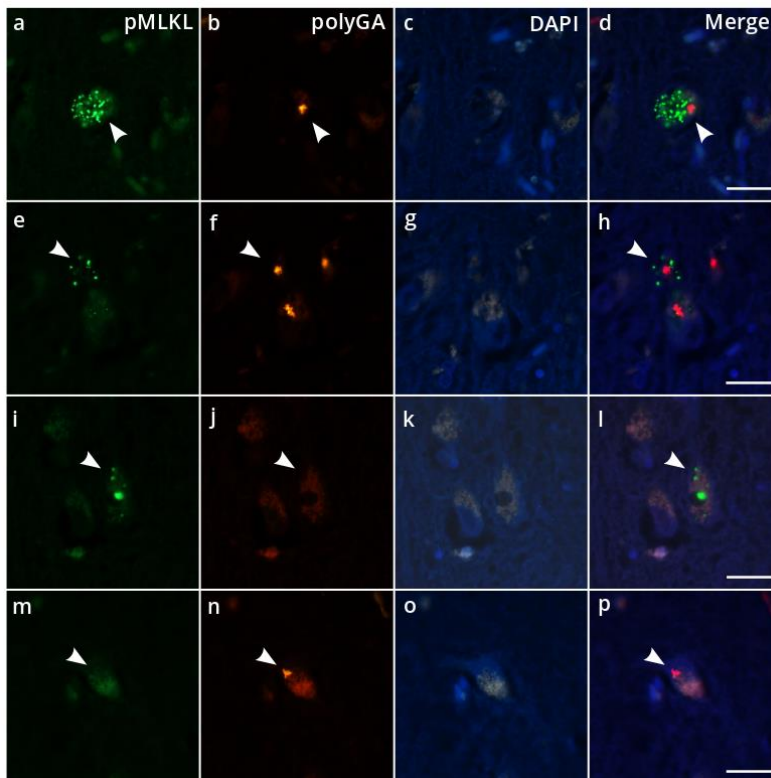
Ch. I - Suppl. Figure 2. Controls for rabbit-on-rabbit co-labelling for pMLKL and pTDP-43. **(a-d)** GVD granules in representative hippocampal CA1 pyramidal neurons in the ALS/FTLD brain positive for pMLKL **(a;** arrowhead) are immunoreactive for the established GVD marker pTDP-43 **(b;** arrowhead). **(e-h)** Leaving out the anti-pMLKL primary antibody does not result in cross-reactivity of the anti-rabbit Fab fragment with pTDP-43 (arrowhead). **(i-l)** Leaving out the anti-pTDP-43 primary antibody does not result in cross-reactivity of the anti-rabbit secondary antibody with pMLKL (arrowhead). **(m-p)** Negative control in which both primary antibodies were left out. Staining of a representative FTLD case (case 17). Scale bars represent 25 µm.



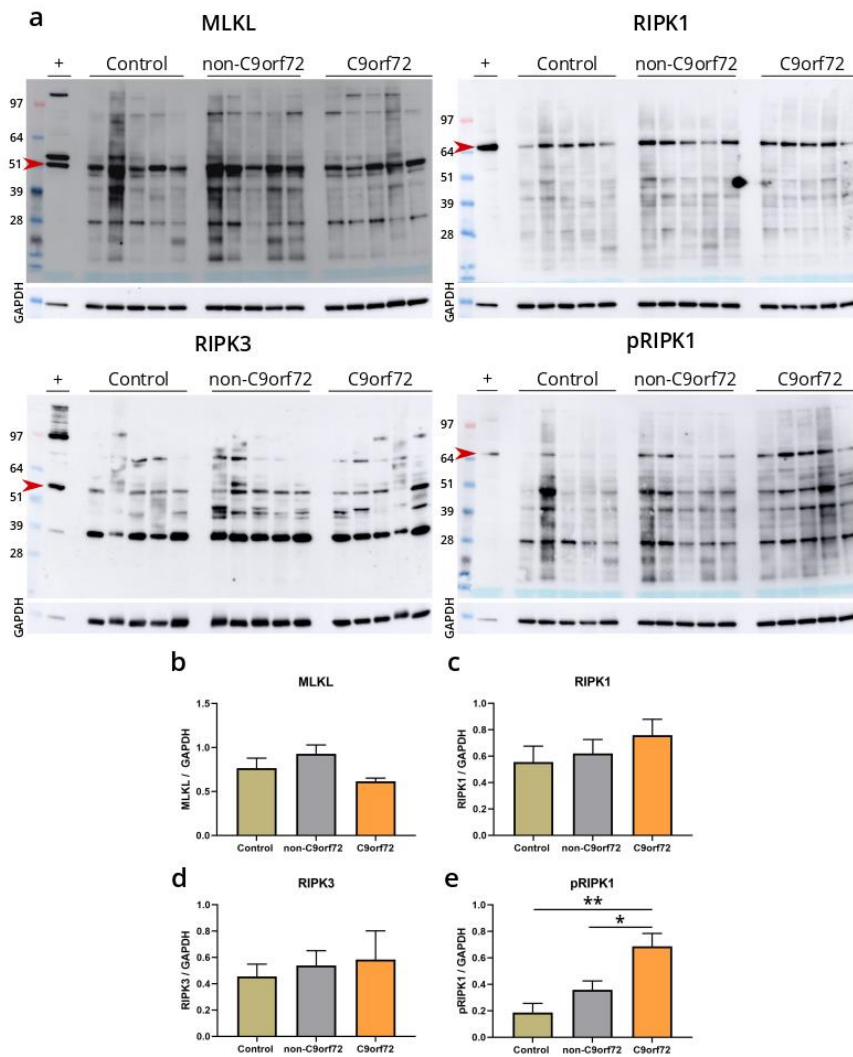
Ch. I - Suppl. Figure 3. Representative images of hippocampal pTDP-43 scoring. Representative IHC staining for pTDP-43 showing “mild” (a; case 18), “moderate” (b; case 29) and “numerous” (c; case 19) pTDP-43 inclusions in a 20x field. Scale bar 50 μm.



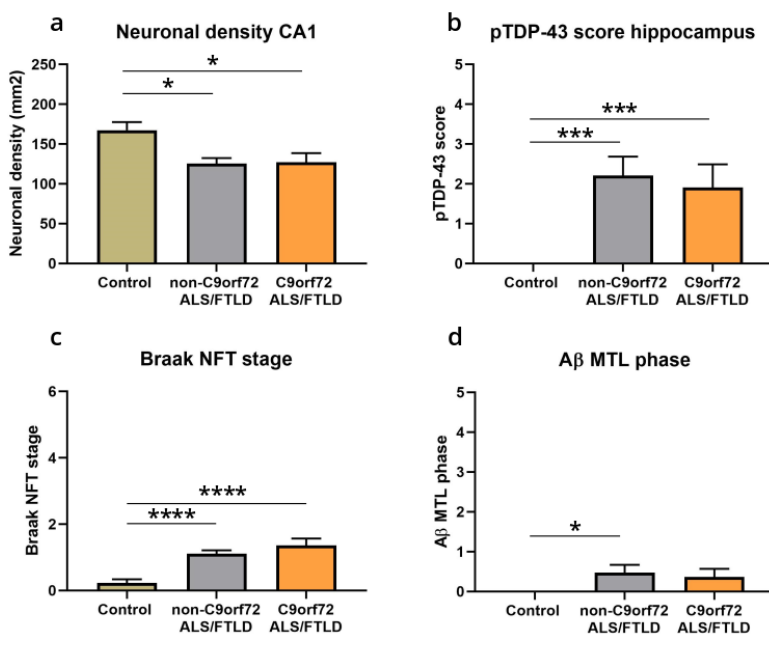
Ch. I - Suppl. Figure 4. Confirmation of pMLKL-positive GVD by a second antibody against pMLKL. (a-d) Representative immunohistochemical staining for pMLKL Abcam (a, b) and pMLKL Aviva (c, d) in the CA1 hippocampal region of a representative control (a-c; case 52) and ALS case (b-d; case 23) shows positivity for GVD granules with both antibodies in ALS (arrowheads). Scale bar represents 25 μm.



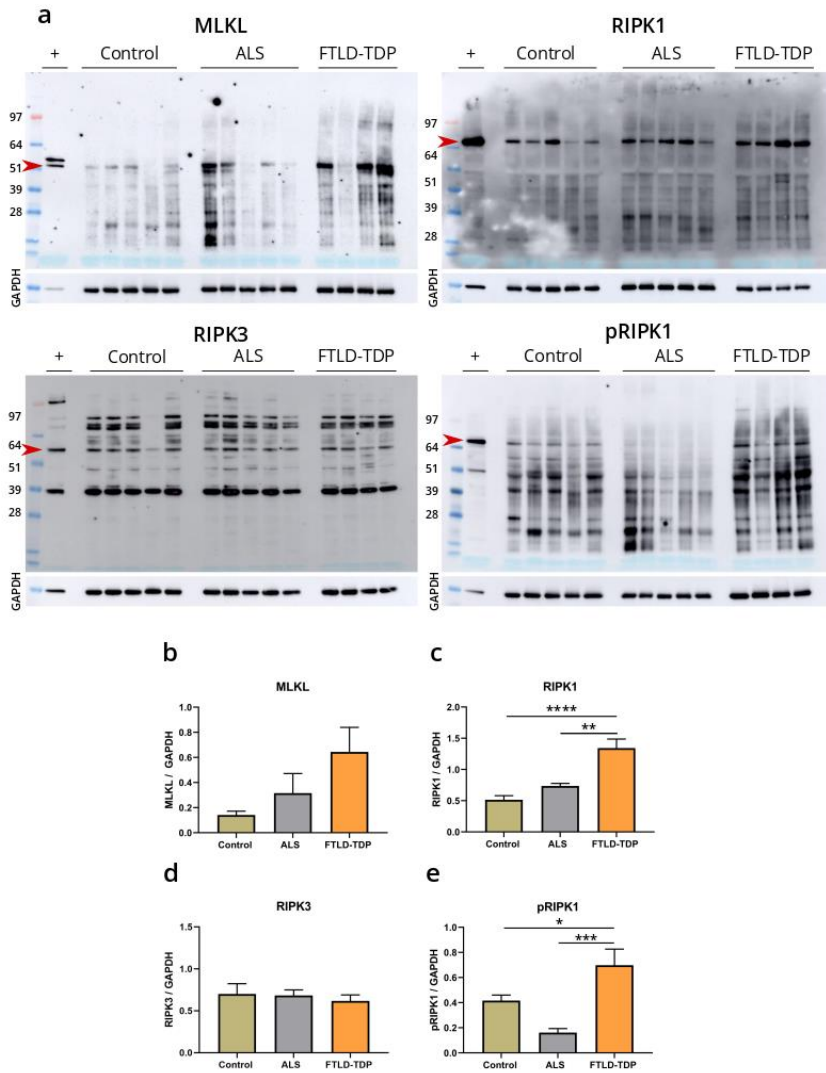
Ch. I - Suppl. Figure 5. pMLKL-positive GVD lesions and DPR pathology in the C9orf72 hippocampus. (a-p) Representative images illustrating the relation between pMLKL-positive GVD (green) and poly(GA) inclusions (red) in the hippocampal CA1 region of a representative C9orf72 FTLD-TDP case (case 30). Three different conditions could be observed: 1) pMLKL-GVD and poly(GA) inclusions in the same pyramidal neuron (a-d and e-h; arrowheads); 2) neurons positive for pMLKL-GVD without any poly(GA) inclusions (i-l; arrowhead); and 3) neurons negative for pMLKL-GVD that displayed poly(GA) inclusions (m-n; arrowhead). Scale bars represent 25 μm.



Ch. I - Suppl. Figure 6. Biochemical characterization of necroptosis-related proteins in the hippocampus. (a) Hippocampal tissue homogenates from control (n = 5), non-C9orf72 ALS/FTLD cases (n = 5) and C9orf72 ALS/FTLD cases (n = 5) on western blots probed with antibodies for MLKL, RIPK1, RIPK3 and pRIPK1. TSZ-treated SH-SY5Y cells were used as positive control (+) and GAPDH as loading control. Arrowheads indicate the predicted molecular weight of the protein. The lower MLKL band in the positive control represents the correct protein level. (b-d) Quantification of necroptosis-related proteins relative to GAPDH. Statistical analyses were performed using one-way ANOVA followed by Tukey's multiple comparisons. Data are presented as mean \pm SEM. * $p < 0.05$; ** $p < 0.01$.



Ch. I - Suppl. Figure 7. CA1 neuronal density is not different in C9orf72 compared to non-C9orf72 ALS and FTLD-TDP cases. (a) Quantitative data representing neuronal densities (neurons/mm²) in the CA1 region of the hippocampus for controls (n = 22), non-C9orf72 ALS and FTLD-TDP (n = 20) and C9orf72 ALS and FTLD-TDP (n = 10) cases. Multinomial regression corrected for age and sex was used for statistical analysis of the data. (b-d) Hippocampal pTDP-43 score (b), Braak NFT stage (c) and AβMTL phase (d) are shown for the different groups. Kruskal-Wallis test followed by Dunn's multiple comparisons was used for statistical analyses. Data are presented as mean \pm SEM. * $p < 0.05$; *** $p < 0.001$; **** $p < 0.0001$.



Ch. I - Suppl. Figure 8. Biochemical characterization of necroptosis-related proteins in ALS central cortex and FTLD-TDP frontal cortex. (a) Central cortex of ALS cases (n = 5), frontal cortex of FTLD-TDP cases (n = 4) and central/frontal cortex of control cases (n = 5) was analysed by western blots and probed with antibodies for MLKL, RIPK1, RIPK3 and pRIPK1. TSZ-treated SH-SY5Y cells were used as positive control (+) and GAPDH as loading control. Arrowheads indicate the predicted molecular weight of the protein. The lower MLKL band in the positive control represents the correct protein. **(b-d)** Quantifications of necroptosis-related proteins relative to GAPDH. Statistical analyses were performed using one-way ANOVA followed by Tukey's multiple comparisons. Data are presented as mean \pm SEM. * $p < 0.05$; ** $p < 0.01$; *** $p < 0.001$; **** $p < 0.0001$.

Ch. I - Suppl. Table 1. List of antibodies used in the study. The table summarizes information about host, clonality, supplier and catalogue number of the primary antibodies used for immunohistochemistry (IHC), immunofluorescence (IF) and western blot (WB). Dilutions for IHC, IF and WB are given.

Primary antibody	Host	Clonality	Supplier	Catalogue number	Dilution IHC	Dilution IF	Dilution WB
anti-RIPK1 (clone 38/RIP)	Mouse	Monoclonal	BD Biosciences	610458	-	-	1:1000
anti-RIPK1	Rabbit	Polyclonal	Protein Tech	17519-1-AP	1:200	-	-
anti-RIPK3	Rabbit	Polyclonal	Abcam	ab56164	1:150	-	-
anti-RIPK3	Rabbit	Polyclonal	Abcam	ab62344	-	-	1:2000
anti-MLKL (clone EPR17514)	Rabbit	Monoclonal	Abcam	ab184718	-	-	1:1000
anti-pRIPK1 (S166) (clone D8I3A)	Rabbit	Monoclonal	Cell Signaling	44590	1:400	-	1:1000
anti-pRIPK3 (S227) (clone D6W2T)	Rabbit	Monoclonal	Cell Signaling	93654	1:800	-	-
anti-pMLKL (S358) (clone EPR9514)	Rabbit	Monoclonal	Abcam	ab187091	1:100	1:50	-
anti-pMLKL (S358) (clone 6F8)	Mouse	Monoclonal	Aviva	OASG07777	1:300	-	-
anti-pTDP43 (S409/410-2)	Rabbit	Polyclonal	Cosmo Bio	TIP-PTD-P02	1:5000	-	-
anti-pTDP43 (S409)	Rabbit	Polyclonal	Cosmo Bio	TIP-PTD-P03	-	1:1000	-
anti-CK1 δ (clone AF12G4)	Mouse	Monoclonal	Abcam	ab85320	-	1:1000	-
anti- β -Amyloid (clone 4G8)	Mouse	Monoclonal	BioLegend	SIG-39220	1:5000	-	-
anti-pTau (S202/T205) (clone AT8)	Mouse	Monoclonal	ThermoFisher	MN1020	1:1000	-	-
anti-poly-GA (clone 5E9)	Mouse	Monoclonal	Merck Millipore	MABN889	1:1000	1:500	-
anti-poly-GP	Rabbit	Polyclonal	ThermoFisher	Custom-made	-	1:300	-
anti-poly-GR (clone 5A2)	Rat	Monoclonal	Merck Millipore	MABN778	-	1:50	-
anti-GAPDH (clone 6C5)	Mouse	Monoclonal	ThermoFisher	AM4300	-	-	1:10 000

Ch. I - Suppl. Table 2. Correlation matrix for pMLKL GVD stage and other parameters corrected for age and sex. Matrix showing Pearson's correlation values and p-values for the association between the pMLKL GVD stage and other variables, including A β MTL phase, Braak NFT stage, hippocampal pTDP-43 score, neuronal density in the hippocampal CA1 region and *post-mortem* interval (PMI). ** $p < 0.01$; *** $p < 0.001$.

	pMLKL-GVD stage	A β MTL phase	Braak NFT stage	pTDP-43 score	Neuron density CA1	PMI	n
pMLKL-GVD stage	-						52
A β MTL phase	r = 0.216; p = 0.159	-					52
Braak NFT stage	r = 0.491; p = 0.001**	r = 0.416; p = 0.005**	-				52
pTDP-43 score	r = 0.538; p < 0.001***	r = 0.283; p = 0.062	r = 0.465; p = 0.001**	-			52
Neuron density CA1	r = -0.193; p = 0.209	r = -0.181; p = 0.240	r = -0.397; p = 0.008**	r = -0.541; p < 0.001***	-		52
PMI	r = -0.175; p = 0.279	r = 0.070; p = 0.667	r = 0.011; p = 0.946	r = -0.246; p = 0.126	r = 0.073; p = 0.653	-	48

Ch. I - Suppl. Table 3. Linear regression analysis for neuronal density in the hippocampal CA1 region. Influence of predictor variables, i.e. the Braak NFT stage, the A β MTL phase, the hippocampal pTDP-43 score and the pMLKL GVD stage on neuronal density according to linear regression. ** $p < 0.01$; *** $p < 0.001$.

Part 1

Predictor variable	Coefficient β	p value
Braak NFT stage	-0.412	p = 0.004**

Dependent variable: hippocampal neuronal density

Predictor variable	Coefficient β	p value
A β MTL phase	-0.212	p = 0.156

Dependent variable: hippocampal neuronal density

Predictor variable	Coefficient β	p value
pTDP-43 score	-0.551	p < 0.001***

Dependent variable: hippocampal neuronal density

Predictor variable	Coefficient β	p value
pMLKL GVD stage	-0.225	p = 0.132

Dependent variable: hippocampal neuronal density

Part 2

Predictor variable	Coefficient β	p value
Braak NFT stage	-0.402	p = 0.008**
Age	-0.013	p = 0.931
Sex	0.074	p = 0.616

Dependent variable: hippocampal neuronal density

Predictor variable	Coefficient β	p value
pTDP-43 score	-0.573	p < 0.001***
Age	0.072	p = 0.610
Sex	0.005	p = 0.969

Dependent variable: hippocampal neuronal density

Part 3

Predictor variable	Coefficient β	p value
Braak NFT stage	-0.184	p = 0.208
pTDP-43 score	-0.460	p = 0.003**

Dependent variable: hippocampal neuronal density

Part 4

Predictor variable	Coefficient β	p value
Braak NFT stage	-0.188	p = 0.208
pTDP-43 score	-0.481	p = 0.003**
Age	0.081	p = 0.564
Sex	0.010	p = 0.942

Dependent variable: hippocampal neuronal density

CHAPTER II: Increased pyroptosis activation in white matter microglia is associated with neuronal loss in ALS motor cortex

This chapter is based on the following publication as first author:

Increased pyroptosis activation in white matter microglia is associated with neuronal loss in ALS motor cortex

Evelien Van Schoor (1,2,3), Simona Ospitalieri (1), Sebastiaan Moonen (1,3,4), Sandra O. Tomé (1), Alicja Ronisz (1), Orkun Ok (1), Jochen Weishaupt (5), Albert C. Ludolph (5,6), Philip Van Damme (2,3,7), Ludo Van Den Bosch (2,3), Dietmar Rudolf Thal (1,8)

1. Laboratory of Neuropathology, Department of Imaging and Pathology, KU Leuven (University of Leuven), Leuven Brain Institute (LBI), Leuven, Belgium.
2. Laboratory of Neurobiology, Department of Neurosciences, KU Leuven (University of Leuven), Leuven Brain Institute (LBI), Leuven, Belgium.
3. Center for Brain & Disease Research, VIB, Leuven, Belgium.
4. Laboratory for the Research of Neurodegenerative Diseases, Department of Neurosciences, KU Leuven (University of Leuven), Leuven Brain Institute (LBI), Leuven, Belgium.
5. Department of Neurology, Ulm University, Ulm, Germany.
6. Divisions of Neurodegeneration, Department of Neurology, Mannheim Center for Translational Neurosciences, Medical Faculty Mannheim, Heidelberg University, Mannheim, Germany.
7. Deutsches Zentrum für Neurodegenerative Erkrankungen, Ulm, Germany.
8. Department of Neurology, University Hospitals Leuven, Leuven, Belgium.
9. Department of Pathology, University Hospitals Leuven, Leuven, Belgium.

Corresponding authors: Evelien Van Schoor and Dietmar R. Thal

Acta Neuropathologica (2022) DOI: 10.1007/s00401-022-02466-9

1. Abstract

Amyotrophic lateral sclerosis (ALS) is characterized by the degeneration of motor neurons in the motor cortex, brainstem and spinal cord. Although ALS is considered a motor neuron disorder, neuroinflammation also plays an important role. Recent evidence in ALS disease models indicates activation of the inflammasome and subsequent initiation of pyroptosis, an inflammatory type of cell death. In this study, we determined the expression and distribution of the inflammasome and pyroptosis effector proteins in post-mortem brain and spinal cord from ALS patients (n = 25) and controls (n = 19), as well as in symptomatic and asymptomatic TDP-43^{A315T} transgenic and wild-type mice. Further, we evaluated its correlation with the presence of TDP-43 pathological proteins and neuronal loss. Expression of the NOD-, LRR- and pyrin domain-containing protein 3 (NLRP3) inflammasome, pyroptosis effector protein cleaved Gasdermin D (GSDMD), and IL-18 was detected in microglia in human ALS motor cortex and spinal cord, indicative of canonical inflammasome-triggered pyroptosis activation. The number of cleaved GSDMD-positive precentral white matter microglia was increased compared to controls and correlated with a decreased neuronal density in human ALS motor cortex. Neither of this was observed in the spinal cord. Similar results were obtained in TDP-43^{A315T} mice, where microglial pyroptosis activation was significantly increased in the motor cortex upon symptom onset, and correlated with neuronal loss. There was no significant correlation with the presence of TDP-43 pathological proteins both in human and mouse tissue. Our findings emphasize the importance of microglial NLRP3 inflammasome-mediated pyroptosis activation for neuronal degeneration in ALS and pave the way for new therapeutic strategies counteracting motor neuron degeneration in ALS by inhibiting microglial inflammasome/pyroptosis activation.

2. Introduction

Amyotrophic lateral sclerosis (ALS) is a neurodegenerative disorder characterized by progressive muscular paralysis resulting from degeneration of both the upper motor neurons situated in the primary motor cortex, and the lower motor neurons situated in the brainstem and spinal cord (10). This rare disease affects 1-3 individuals per 100 000 per year (3,214). ALS patients usually die due to respiratory failure within 2-5 years following disease onset (2). In approximately 10% of ALS cases there is a family history of the disease (familial ALS), whereas for most of the sporadic ALS cases the cause is unknown (18). The main pathological characteristic of 97% of ALS patients is the cytoplasmic mislocalization and aggregation of transactive response DNA-binding protein 43kD (TDP-43) in affected central nervous system (CNS) regions (25). TDP-43 inclusions are also found in about 50% of patients with frontotemporal lobar degeneration (FTLD), referred to as FTLD-TDP (216). It has become clear that ALS and FTLD belong to a disease spectrum as up to 50% of ALS patients show some features of

FTLD and hexanucleotide repeat expansions in the *C9orf72* gene are the most common genetic cause of ALS and FTLD (5). Although ALS is considered a motor neuron disorder, non-cell autonomous mechanisms, such as neuroinflammation, are believed to significantly contribute to ALS pathogenesis. This suggests that glial cells also contribute to motor neuron degeneration observed in the ALS CNS (251,252).

Inflammasomes were shown to play an important role in neuroinflammation and neurodegeneration. These are multiprotein complexes mainly located in immune cells, neurons, microglia and astrocytes in the CNS (120). They function as cytosolic scaffolds assembled by pattern recognition receptors (PRRs) and are responsible for detecting and eliminating pathogen-associated molecular patterns (PAMPs) and damage-associated molecular patterns (DAMPs). The sensors of the inflammasome can be classified into three types, including nucleotide-binding domain and leucine-rich repeat-containing receptors (NLRs), absent in melanoma-like receptors (ALRs) and pyrin. The adaptor protein apoptosis-associated speck-like protein containing a CARD (ASC) links the pyrin domain (PYD) of these sensors to the caspase recruitment domain (CARD) of pro-caspase-1. However, some inflammasomes can directly recruit pro-caspase-1, without the adaptor protein ASC (110). The assembly and activation of the inflammasome is cell-type and stimulus specific. The most investigated sensor protein is NLRP3, which is thought to be the main sensor for sterile inflammatory stimuli, while for example NLRC4 mainly acts as a sensor of bacterial infection (120,121,124).

The activation of the inflammasome through the canonical signaling pathway causes cleavage of pro-caspase-1 into active caspase-1 fragments (caspase-1 p20). Subsequently, caspase-1 cleaves biologically inactive pro-IL-1 β and pro-IL-18 into the mature inflammatory cytokines IL-1 β and IL-18. In addition, caspase-1 cleaves and activates Gasdermin D (GSDMD) leading to the release of an N-terminal region (GSDMD-NT), which oligomerizes and binds to acidic phospholipids, such as phosphoinositides on the inner part of the plasma membrane, to form death-inducing pores. This causes cell swelling, rupture of the plasma membrane and the release of IL-1 β and IL-18 to the extracellular space, inducing the pro-inflammatory type of regulated cell death known as pyroptosis. It is thought that cleaved GSDMD, which functions as the effector of pyroptosis, might target and perforate multiple organelles, in addition to the plasma membrane (120,128). Extracellular IL-18 and IL-1 β can also recruit and activate other immune cells, expanding the local inflammatory response. In the CNS, microglia, astrocytes and neurons can all undergo pyroptosis and express its related downstream molecules and receptors, taking part in the local inflammatory reaction (121).

The NLRP3 inflammasome has been implicated in several neurodegenerative disorders, as it was shown that the inflammasome could be activated by abnormal protein aggregation, including for example amyloid- β in Alzheimer's disease (133) and α -synuclein in Parkinson's disease (134). For ALS, most research related to the inflammasome and pyroptotic cell death has been conducted in mutant superoxide dismutase-1 (*SOD1*) animal models. Multiple studies showed an upregulation of the expression of several NLRP3 inflammasome components, as well as the cytokines IL-18 and IL-1 β , in the CNS of *SOD1* mice and rats compared to controls (135–138). Moreover, it was demonstrated that mutant *SOD1* could activate microglia, leading to caspase-1 activation and consequent cleavage of IL-1 β . This was not the case when microglia were deficient for NLRP3, suggesting that NLRP3 is the key inflammasome in mediating *SOD1*-induced microglial pyroptosis activation (97,139). For TDP-43, there is evidence that mutant and aggregated forms of TDP-43 can trigger NLRP3 inflammasome-dependent IL-1 β and IL-18 secretion in vitro in microglia, which was toxic to motor neurons (140,141). In the absence of microglia, TDP-43 was not toxic to motor neurons (141). Whether this NLRP3 inflammasome-related microglia activation as observed in mouse models and in vitro aggregation models plays a role in sporadic ALS patients, and whether this is related to TDP-43 pathology and neuronal degeneration, remains unclear.

3. Materials and methods

Human autopsy cases

Brain and spinal cord tissue was collected in accordance with the applicable laws in Belgium (UZ Leuven) and Germany (Ulm). The recruitment protocols for collecting the brains were approved by the ethical committees of the University of Ulm (Germany) and UZ Leuven (Belgium). This study was approved by the UZ Leuven ethical committee (Belgium). Tissues were collected with an average *post-mortem* interval of 44 h. After autopsy, the right hemisphere was dissected in coronal planes and frozen at -80°C. The left hemisphere was fixed in 4% phosphate-buffered formaldehyde. 25 ALS cases (15 sporadic and 10 *C9orf72*) and 19 non-neurodegenerative controls were included in this study (Suppl. Table 1). The diagnosis of ALS or FTD was based on clinical assessment according to the consensus criteria for ALS (7,8,229) and FTD (45,46). The *post-mortem* diagnosis of ALS and FTLD-TDP was pathologically confirmed by assessment of the pTDP-43 pathology. Braak NFT stage (230), A β MTL phase (231), and the Consortium to Establish a Registry for Alzheimer's disease (CERAD) score (232) were determined based on immunohistochemical stainings with antibodies against A β and abnormally phosphorylated tau protein (p-tau) (Suppl. Table 2).

***C9orf72* repeat expansion determination**

DNA was extracted from peripheral blood and/or cerebellum according to standard protocols. Analysis of the hexanucleotide repeat length in intron 1 of *C9orf72* was performed by fragment length analysis by PCR and repeat-primed PCR (RP-PCR) as previously described (233). In addition, the presence of poly(GA) pathology was immunohistochemically assessed in the frontal cortex. The *C9orf72* mutation status is shown in Suppl. Table 1.

Transgenic mice

Heterozygous mice overexpressing a TDP-43 construct containing the A315T mutation driven by the mouse prion protein (Prp) promoter (Prp-hTDP-43^{A315T}) were used in this study (65). Transgenic mice were bred by continuous backcrossing of heterozygous males with wild-type females on a C57BL/6 background. Due to intestinal obstruction problems in this model, the animals were given gel food from the age of two months onwards (DietGel®31M, ClearH2O, Portland, ME, US), which is known to overcome this problem (253). Five groups of mice (total n = 28) were used: (1) wild-type non-transgenic mice at six months of age (n = 3), (2) Prp-hTDP-43^{A315T} mice at six months of age (n = 4), (3) non-transgenic mice at 16 months of age (n = 4), (4) Prp-hTDP-43^{A315T} mice at 16 months of age (n = 7), and (5) symptomatic Prp-hTDP-43^{A315T} mice (n = 5; 6-14 months of age, mean age of 9 months). In group 5, mice were sacrificed 1-3 days following symptom onset, i.e., detection of impaired and reduced movement in the cage. Mouse brains and spinal cords were harvested after death and fixed in 4% paraformaldehyde for three to five days. After paraffin embedding, sections of 5 µm were cut with a microtome and used for immunohistochemistry. All animal care and experiments were approved by the KU Leuven Ethical Committee and were carried out according to the Belgian law.

Immunohistochemistry

Human samples

Five µm thick sections were cut from formalin-fixed, paraffin-embedded tissue of motor cortex and spinal cord. Sections were stained with antibodies against pTDP-43, Aβ, p-tau, cleaved GSDMD, caspase-1, IL-18, ASC and NLRP3 (Suppl. Table 2). Stainings were performed with the BOND-MAX automated IHC/ISH Stainer (Leica Biosystems, Wetzlar, Germany) using the Bond Polymer Refine Detection kit (DS9800, Leica Biosystems). Briefly, slides were deparaffinized and epitopes were retrieved with low or high pH buffer. After incubation with Envision Flex Peroxidase-Blocking Reagent (Dako, Glostrup, Denmark), slides were incubated with primary antibodies for 30 min, followed by secondary antibody incubation. DAB was used for visualization. Counterstaining with hematoxylin was carried out, followed by dehydration and mounting in an automated cover-slipper (Leica Biosystems).

Images were acquired using the Leica DM2000 LED microscope coupled to a Leica DFC 7000 T camera. Images were processed using ImageJ and combined into figures using Inkscape.

For immunofluorescence double labeling using primary antibodies from different species (Suppl. Table 2), an antibody cocktail of the respective primary antibodies was applied, followed by a cocktail of species-specific Cy2/3-conjugated secondary antibodies (Jackson ImmunoResearch, Ltd, West Grove, PA, USA). For double labeling with primary antibodies raised in the same species (Suppl. Table 2), a sequential staining was performed using a rabbit-on-rabbit staining protocol as previously described (254). Briefly, a coupling method was used to avoid cross-reactivity of secondary antibodies. The first rabbit primary antibody was used as described above, followed by a Cy2-labelled donkey anti-rabbit secondary antibody. The second rabbit primary antibody was coupled to a donkey anti-rabbit Fab fragment conjugated to a Cy3 dye for 20 min (2 µg Fab fragment per 1 µg primary antibody) prior to its incubation with the sample. Next, normal rabbit serum (Jackson ImmunoResearch) was added for another 10 min to capture the unbound Fab fragments (10 µl serum per 1 µg Fab fragment). Then, the mix was applied to the slides to visualize the second primary antibody. TrueBlack Lipofuscin Autofluorescence Quencher (Biotum, CA, USA) was applied for 30s to reduce autofluorescence. Fluorescent-labelled slides were mounted using ProLong Gold Antifade Mountant containing DAPI (Thermo Fisher Scientific, Rockford, IL, USA) for counterstaining of the nuclei. Images were acquired with a Leica SP8x confocal microscope (Leica Microsystems, Wetzlar, Germany) at a magnification of 63x using type F immersion oil (Leica Microsystems). Images were processed using ImageJ and combined into figures using Inkscape.

Mouse samples

Mouse brain sections were stained with antibodies against TDP-43, ubiquitin, GSDMD, caspase-1, p62 and Iba1 (Suppl. Table 2). Stainings were performed manually, similar to immunohistochemistry and immunofluorescence of the human slides. An extra mouse IgG blocking step was performed to prevent unspecific signal. For GSDMD, proteinase K treatment was additionally applied for 1 min.

pTDP-43 pathology and TDP-43 nuclear clearance quantification in human samples

pTDP-43 pathology was assessed in the motor cortex and the anterior horn of the lumbosacral spinal cord of human cases. The amount of pathological inclusions in a 20x microscopic field with most abundant pathology, considered as the “hotspot area”, was quantified. The abundance of pathology was expressed as a percentage of neurons affected by pTDP-43 pathology. For quantification of the percentage of neurons with TDP-43 cleared from the nucleus in layer V of the motor cortex, two images (0.632 x 0.474 mm) of anti-TDP-43 (C-terminal) stained sections were taken using a 20x objective.

Image J was used for quantifications. The percentage of neurons without TDP-43 in the nucleus was calculated in relation to all neurons present in the respective region of interest.

TDP-43 nuclear clearance quantification in mouse samples

For quantification of the percentage of neurons with TDP-43 cleared from the nucleus in the motor cortex and anterior horn of the spinal cord of all mice, two images (0.632 x 0.474 mm) of anti-TDP-43 (C-terminal) stained sections were taken with the Leica DM2000 LED microscope using a 20x objective. Image analysis was performed using ImageJ. The percentage of neurons without TDP-43 in the nucleus was calculated in relation to all neurons present in the respective region of interest.

Quantification of number of cleaved GSDMD- and caspase-1-positive glia / neurons

Human samples

For quantification of the number of cleaved GSDMD- and caspase-1-positive microglial cells and neurons in the precentral white matter and in layer V of the motor cortex, three consecutive images (0.632 x 0.474 mm) of anti-cleaved GSDMD- and anti-caspase-1-stained sections were taken with the Leica DM2000 LED microscope using a 20x objective. For the lumbar spinal cord ventral pyramidal tracts, one 20x image was acquired, while for the lateral pyramidal tracts two 20x images were used. For the lumbar spinal cord anterior horn, two 10x images (1.264 x 0.948 mm) were used. Microglial cells were identified by their shape and nuclear morphology. Image analysis was performed using ImageJ.

Mouse samples

For quantification of the number of microglial cells positive for GSDMD and caspase-1 per mm² in the motor cortex (gray and white matter) and spinal cord (anterior horn and pyramidal tracts) of all mice, four images (0.632 x 0.474 mm) of anti-GSDMD- and anti-caspase-1-stained sections were taken with the Leica DM2000 LED microscope using a 20x objective. Microglial cells were identified by their shape and nuclear morphology. Image analysis was performed using ImageJ.

Quantification of neuronal density in the motor cortex and spinal cord

Human samples

For quantification of neuronal density in layer V of the motor cortex, three consecutive images (0.632 x 0.474 mm) of a representative area of anti-cleaved GSDMD-stained sections were taken with the Leica DM2000 LED microscope using a 20x objective (221). For quantification of neuronal density in the anterior horn of the lumbosacral spinal cord, two images (1.264 x 0.948 mm) of a representative area of anti-cleaved GSDMD-stained sections were taken using a 10x objective. Criteria regarding

morphological conditions of neurons to be included were determined before quantification. Neurons were identified based on their nuclear pattern in the hematoxylin staining. Image analysis was performed using ImageJ.

Mouse samples

For quantification of neuronal density in layer V of the motor cortex and in the anterior horn of the spinal cord, two images (0.632 x 0.474 mm) of anti-TDP-43-stained sections were taken with the Leica DM2000 LED microscope using a 20x objective. Criteria regarding morphological conditions of neurons to be included were determined before quantification, similar as for the human samples. Image analysis was performed using ImageJ.

Protein extraction

For biochemistry, the spinal cord was taken and the right brain hemisphere was cut in approx. 1 cm thick slabs and frozen at -80°C. Fifty mg of brain or spinal cord tissue was weighed and mechanically homogenized in 0.5 ml 2% SDS in TBS (Tris-buffered saline) with Nuclease (Pierce™ Universal Nuclease, Thermo Fisher Scientific) and a cocktail of protease/phosphatase inhibitors (Halt, Thermo Fisher Scientific) using a micropestle. Samples were sonicated, followed by a centrifugation at 14 000 g for 30 min. The resulting supernatant was used. Protein concentrations were determined using the Pierce BCA Protein Assay Kit (Thermo Fisher Scientific).

Western blotting

For western blotting, 10 µg of protein was loaded on a Bis-Tris 4-12% gradient SDS-PAGE (Invitrogen, Thermo Fisher Scientific) in MOPS/MES-SDS running buffer (Alfa Aesar, Haverhill, MA, USA), electrophoresed at 150V for 60 min, and transferred to a nitrocellulose membrane (Semidry transfer, Biorad, Hercules, CA, USA). Membranes were blocked with 5% non-fat dried milk (AppliChem, Darmstadt, Germany) in PBS 0.1% Tween-20 (PBST). Primary antibodies and the corresponding dilutions are listed in Suppl. Table 2. Secondary antibodies were goat anti-rabbit IgG-HRP or goat anti-mouse IgG-HRP (1:10 000, polyclonal, Dako). Blots were developed with SuperSignal West Pico or Dura plus ECL reagent (Thermo Fisher Scientific). Digital images were acquired using the Amersham Imager 600 (GE Healthcare, Chicago, IL, USA). All blots were stripped (Restore Western Blot Stripping Buffer, Thermo Fisher Scientific) of bound antibodies and reprobbed with GAPDH to control for equal protein loading. Band intensities were measured using ImageJ and were normalized to GAPDH.

Statistical analysis

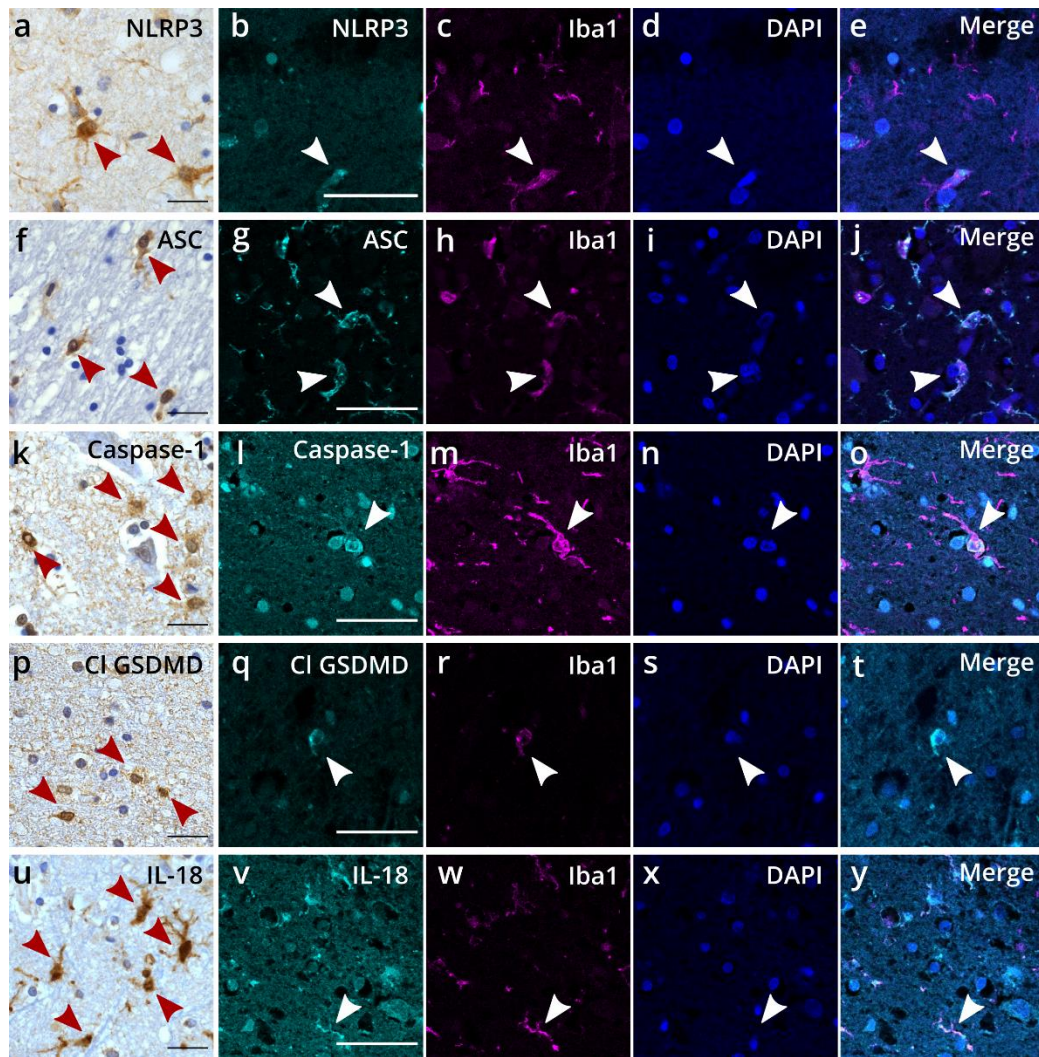
Statistical analyses were performed in IBM SPSS and Graphpad Prism software. Binary logistic regression controlled for age and sex, or a t-test or Mann-Whitney test were used to determine the difference between two groups. To examine the different mouse groups, a one-way ANOVA or Kruskal-Wallis test was used followed by a post-hoc test to correct for multiple testing. To examine correlations between motor cortex layer V or anterior horn spinal cord neuronal density and other parameters, partial Pearson's correlation (controlled for age and sex in the human cohort) was done. To estimate the effect of explanatory variables on human motor cortex layer V neuronal density, we conducted linear regression analyses. Data: mean \pm SEM. * $p < 0.05$; ** $p < 0.01$; *** $p < 0.001$; **** $p < 0.0001$.

4. Results

The canonical NLRP3 inflammasome as well as pyroptosis effector-related proteins are expressed in microglial cells in the ALS motor cortex

To investigate the expression of NLRP3 inflammasome components in the ALS brain, we performed a pathological analysis on human *post-mortem* brain tissue from ALS (n = 24) and control (n = 12) cases (Suppl. Table 1). For this, we used motor cortex, as this is the main affected brain region in ALS. Immunohistochemical staining showed positive immunoreactivity for NLRP3 (Fig. 1a), ASC (Fig. 1f) and caspase-1 (Fig. 1k) in microglial cells in the ALS motor cortex and its adjacent white matter. This was also observed in some control cases for ASC and caspase-1, and to a lesser extent for NLRP3 (Suppl. Fig. 1a-c). To further confirm that the inflammasome was expressed in microglia, we performed immunofluorescence co-staining with an antibody against Iba1 for microglia. This ensured the expression of NLRP3 (Fig. 1b-e), ASC (Fig. 1g-j) and caspase-1 (Fig. 1l-o) in microglial cells in the ALS motor cortex white and gray matter.

Next, we assessed the expression of pyroptosis effector-related proteins in the ALS motor cortex. Both cleaved GSDMD (Fig. 1p) and IL-18 (Fig. 1u) were present in ALS microglial cells, as shown by DAB immunohistochemistry. Control cases showed a few microglial cells positive for cleaved GSDMD and IL-18, but these seemed scarcer compared to ALS cases (Suppl. Fig. 1d-e). Immunofluorescence co-staining confirmed that these effector proteins were present in Iba1-positive microglial cells (Fig. 1 q-t and v-y), but not in astrocytes and oligodendrocytes, as shown by GFAP and Olig2 antibody staining respectively (Suppl. Fig. 2). Of note, antibodies against cleaved GSDMD, NLRP3 and IL-18 also faintly stained few neurons. No positive neurons were observed for ASC and caspase-1 (Table 1). Astrocytes were rarely positive for NLRP3, caspase-1 and cleaved GSDMD, and negative for ASC and IL-18. Oligodendrocytes were negative for all inflammasome and pyroptosis effector proteins (Table 1).



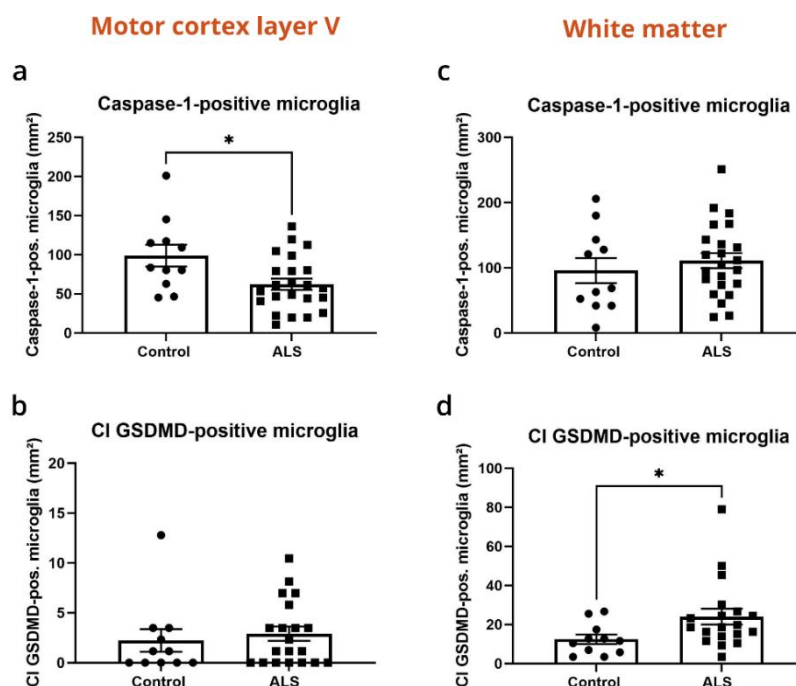
Ch. II - Figure 1. Expression of inflammasome components and pyroptosis effector-related proteins in ALS precentral white matter microglia. Immunohistochemical and immunofluorescence detection of inflammasome components NLRP3 (a-e), ASC (f-j) and caspase-1 (k-o), as well as pyroptosis effector-related proteins cleaved GSDMD (p-t) and IL-18 (u-y) in representative ALS precentral white matter. Arrowheads indicate microglial cells positive for the respective markers. Scale bars represent 50 μ m.

Ch. II - Table 1. The expression of inflammasome components and pyroptosis effector-related proteins in different cell types. +++ abundant strongly positive cells; (+++) abundant faintly positive cells; ++ some strongly positive cells; (++) some faintly positive cells; + few strongly positive cells; (+) few faintly positive cells.

	Neurons	Astrocytes	Microglia	Oligodendrocytes
NLRP3	(+)	+	+++	-
ASC	-	-	+++	-
Caspase-1	-	(+)	+++	-
Cleaved GSDMD	(++)	+	+++	-
IL-18	(+)	-	+++	-

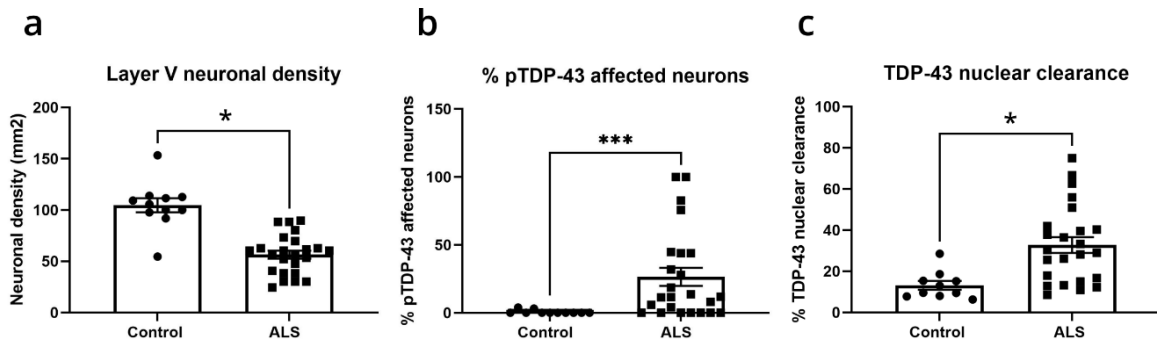
Increased presence of cleaved GSDMD-positive microglial cells in ALS precentral white matter correlates with neuronal loss

To determine whether the expression of pyroptosis-related proteins is relevant for ALS, we quantified the amount of microglia in the motor cortex positive for caspase-1 (inflammasome component) and cleaved GSDMD (pyroptosis effector). Caspase-1 was selected as inflammasome marker as this protease is responsible for the cleavage and consequent activation of downstream pyroptosis targets (i.e. GSDMD, IL-18 and IL-1 β), while cleaved GSDMD was used as a marker for pyroptosis activation, as it is considered the final executor of pyroptotic cell death. In layer V of the motor cortex, we detected a decrease in the number of caspase-1-positive microglia in ALS cases compared to controls (Fig. 2a; Suppl. Table 3; $p = 0.031$; OR = 0.975; 95% CI = 0.954-0.998; binary logistic regression corrected for age and sex). We did not observe any differences between ALS and control cases regarding cleaved GSDMD-positive microglia (Fig. 2b; Suppl. Table 3; $p = 0.345$; OR = 1.138; 95% CI = 0.870-1.488; binary logistic regression corrected for age and sex). There was also no difference between ALS and control cases in the number of neurons in layer V of the motor cortex positive for cleaved GSDMD (Suppl. Fig 3; Suppl. Table 3; $p = 0.527$; OR = 0.988; 95% CI = 0.952-1.025; binary logistic regression corrected for age and sex) and in the precentral white matter in the number of caspase-1-positive microglia (Fig. 2c; Suppl. Table 3; $p = 0.4$; OR = 1.006; 95% CI = 0.992-1.020; binary logistic regression corrected for age and sex). Interestingly, ALS cases showed a higher abundance of microglia positive for cleaved GSDMD compared to control cases in the precentral white matter (Fig. 2d; Suppl. Table 3; $p = 0.034$; OR = 1.155; 95% CI = 1.011-1.319; binary logistic regression corrected for age and sex).



Ch. II - Figure 2. Increased expression of cleaved GSDMD in ALS microglial cells in the precentral white matter. (a, b) Graphs representing the number of microglia per mm² positive for caspase-1 (a) and cleaved GSDMD (b) in layer V of the motor cortex of control and ALS cases. **(c, d)** Graphs representing the number of microglia per mm² positive for caspase-1 (c) and cleaved GSDMD (d) in the precentral white matter of control and ALS cases. Binary logistic regression corrected for age and sex was used for statistical analysis. * $p < 0.05$.

To examine whether the expression of pyroptosis-related proteins correlates with neuronal loss in ALS, we quantified neuronal densities in layer V of the motor cortex of ALS and control cases. Binary logistic regression corrected for age and sex showed a decrease in motor cortex layer V neuronal density in ALS compared to control cases (Fig. 3a; Suppl. Table 3; $p = 0.023$; OR = 0.880; 95% CI = 0.788-0.982). Additionally, we detected a significantly higher percentage of neurons affected by pTDP-43 pathology in ALS compared to control motor cortex (Fig. 3b; $p = 0.007$; Mann-Whitney test), and a significantly higher percentage of neurons with TDP-43 cleared from the nucleus in layer V of the motor cortex (Fig. 3c; Suppl. Table 3; $p = 0.022$; OR = 1.179; 95% CI = 1.023-1.358; binary logistic regression corrected for age and sex). A Pearson's partial correlation analysis corrected for age and sex revealed a significant correlation between the percentage of pTDP-43 affected neurons and a decreased motor cortex layer V neuronal density (Table 2; $r = -0.504$; $p = 0.007$). Interestingly, a decreased motor cortex layer V neuronal density correlated with a higher abundance of white matter microglia positive for cleaved GSDMD (Table 2; $r = -0.431$; $p = 0.025$). In contrast, layer V neuronal density did not significantly correlate with the number of white matter microglia positive for caspase-1 (Table 2; $r = -0.343$; $p = 0.080$). There was also no correlation between cleaved GSDMD- and caspase-1-positive white matter microglia (Table 2; $r = 0.020$; $p = 0.921$). The amount of cleaved GSDMD-positive white matter microglia did not correlate with the percentage of pTDP-43 affected neurons (Table 2; $r = -0.010$; $p = 0.960$), nor with the percentage of neurons with TDP-43 nuclear clearance (Table 2; $r = 0.116$; $p = 0.572$). In separate linear regression models with motor cortex layer V neuronal density as dependent variable, and including age and sex as additional independent variables, the percentage of neurons affected by pTDP-43 pathology ($\beta = -0.435$; $p = 0.01$) and the number of cleaved GSDMD-positive white matter microglia ($\beta = -0.455$; $p = 0.021$) were good predictors of neuronal density, whereas the number of caspase-1-positive white matter microglia was not ($\beta = -0.244$; $p = 0.179$) (Suppl. Table 4, part 1). When combining the percentage of pTDP-43 affected neurons and cleaved GSDMD-positive white matter microglia in the same model, both showed to be equally potent predictors of motor cortex layer V neuronal density (Suppl. Table 4, part 2; percentage of pTDP-43 affected neurons: $\beta = -0.486$; $p = 0.004$; cleaved GSDMD-positive white matter microglia: $\beta = -0.464$; $p = 0.007$), indicating that they independently contribute to neuronal loss.



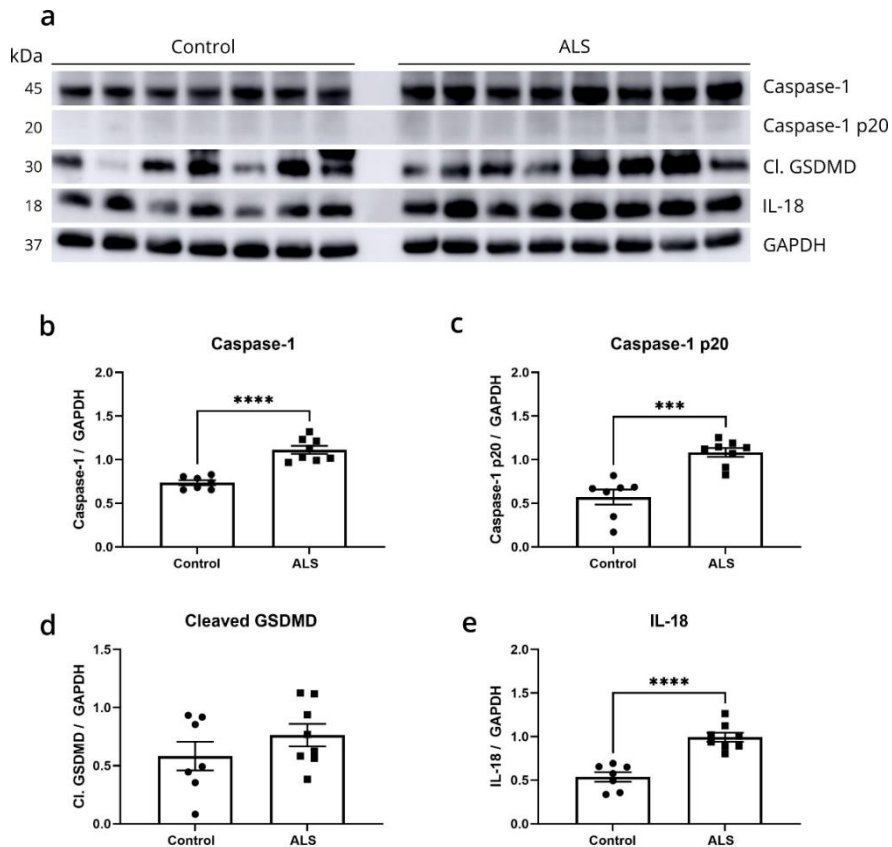
Ch. II - Figure 3. Motor cortex layer V neuronal density and pTDP-43 pathology. (a) Graph representing the neuronal density per mm² in layer V of the motor cortex of control and ALS cases. (b) Graph representing the percentage of pTDP-43 affected neurons in the motor cortex of control and ALS cases. (c) Graph representing the percentage of neurons with TDP-43 cleared from the nucleus in layer V of the motor cortex. Binary logistic regression corrected for age and sex or a Mann-Whitney test was used for statistical analysis. * $p < 0.05$; *** $p < 0.001$.

Ch. II - Table 2. Correlation matrix for motor cortex layer V neuronal density and other parameters, corrected for age and sex. Matrix showing Pearson's correlation values and p-values for the association between motor cortex layer V neuronal density and other variables, including the number of caspase-1-positive microglia in the precentral white matter, the number of cleaved GSDMD-positive microglia in the precentral white matter, the percentage of pTDP-43 affected neurons in the motor cortex, and the percentage of neurons with TDP-43 nuclear clearance in layer V of the motor cortex. * $p < 0.05$; ** $p < 0.01$.

	Caspase-1 positive microglia	Cl GSDMD-positive microglia	% pTDP-43 affected neurons	Neuronal density	% TDP-43 clearance	n
Caspase-1 positive microglia	-					25
Cl GSDMD-positive microglia	$r = 0.020$ $p = 0.921$	-				25
% pTDP-43 affected neurons	$r = 0.083$ $p = 0.682$	$r = -0.010$ $p = 0.960$	-			25
Neuronal density motor cortex layer V	$r = -0.343$ $p = 0.080$	$r = -0.431$ $p = 0.025^*$	$r = -0.504$ $p = 0.007^{**}$	-		25
% TDP-43 clearance	$r = 0.282$ $p = 0.163$	$r = 0.116$ $p = 0.572$	$r = 0.035$ $p = 0.865$	$r = -0.313$ $p = 0.119$	-	24

Elevated expression of pyroptosis-related proteins in ALS motor cortex

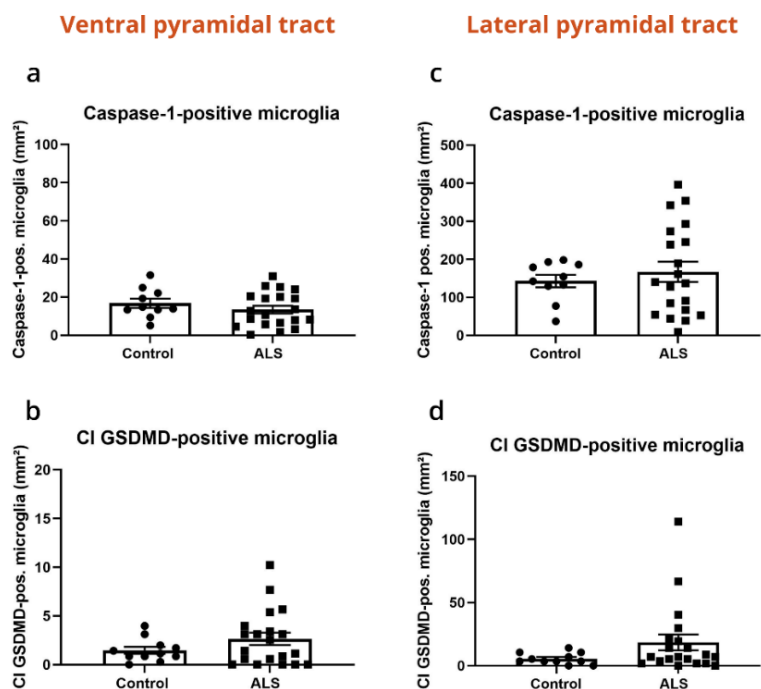
To further investigate the expression of pyroptosis-related proteins in ALS versus control motor cortex, we performed western blots on SDS-soluble motor cortex extracts. ALS cases showed an increased expression of the inflammasome component full-length caspase-1 (Fig. 4a,b; Suppl. Fig. 4a; $p < 0.0001$; unpaired t-test) as well as the active cleaved p20 fragment (Fig. 4a,c; Suppl. Fig. 4a; $p = 0.0001$; unpaired t-test). Expression of cleaved GSDMD, which represents the active cleaved fragment of GSDMD, was numerically increased in ALS cases, however not significant (Fig. 4a,d; Suppl. Fig. 4b; $p = 0.2568$; unpaired t-test). Finally, the expression of the cleaved and active form of IL-18 was significantly increased in the motor cortex of ALS compared to control cases (Fig. 4a,e; Suppl. Fig. 4c; $p < 0.0001$; unpaired t-test).



Ch. II - Figure 4. Biochemical characterization of pyroptosis proteins in the ALS motor cortex. (a) Motor cortex tissue lysates from control (n = 7) and ALS (n = 8) on western blots probed with antibodies for caspase-1, cleaved GSDMD and IL-18, with GAPDH as loading control. **(b-e)** Quantifications of pyroptosis-related proteins relative to GAPDH. Statistical analyses were performed using unpaired t-test. *** $p < 0.001$; **** $p < 0.0001$.

Presence of NLRP3 inflammasome and pyroptosis-related proteins in the ALS spinal cord does not associate with neuronal loss

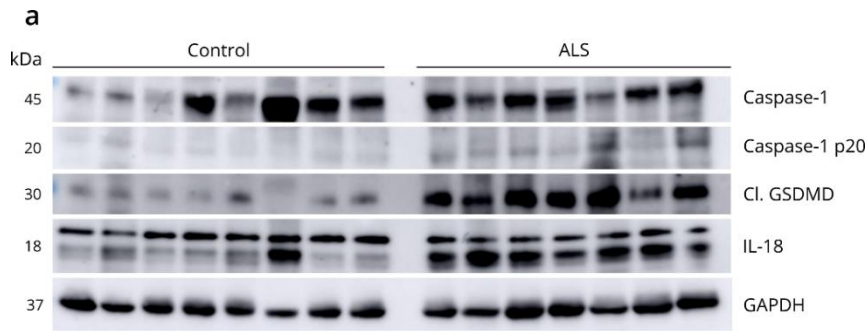
Next, we assessed the presence of the inflammasome component caspase-1 and the pyroptosis effector cleaved GSDMD in the ALS spinal cord. We analyzed the amount of microglia positive for caspase-1 and cleaved GSDMD in the ventral and lateral white matter pyramidal tracts. There was no obvious difference between ALS and control cases in the number of caspase-1-positive microglia in the ventral pyramidal tracts (Fig. 5a; Suppl. Table 3; $p = 0.270$; OR = 0.947; 95% CI = 0.860-1.043; binary logistic regression corrected for age and sex) and in the lateral pyramidal tracts (Fig. 5c; Suppl. Table 3; $p = 0.606$; OR = 1.002; 95% CI = 0.994-1.010; binary logistic regression corrected for age and sex). The number of cleaved GSDMD-positive microglia was slightly higher in ALS compared to control cases for the ventral pyramidal tracts (Fig. 5b; Suppl. Table 3; $p = 0.216$; OR = 1.285; 95% CI = 0.864-1.912; binary logistic regression corrected for age and sex), and for the lateral pyramidal tracts (Fig. 5d; Suppl. Table 3; $p = 0.172$; OR = 1.086; 95% CI = 0.965-1.224; binary logistic regression corrected for age and sex).



Ch. II - Figure 5. Expression of caspase-1 and cleaved GSDMD in ALS and control spinal cord pyramidal tract microglia. (a, b) Graphs representing the number of microglia per mm² positive for caspase-1 (a) and cleaved GSDMD (b) in the ventral pyramidal tracts of control and ALS spinal cord. **(c, d)** Graphs representing the number of microglia per mm² positive for caspase-1 (c) and cleaved GSDMD (d) in the lateral pyramidal tracts of control and ALS spinal cord. Binary logistic regression corrected for age and sex.

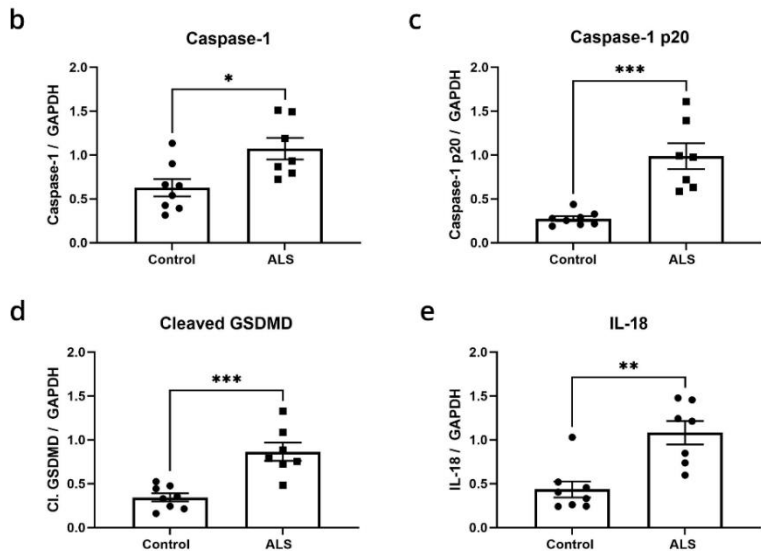
We also quantified the anterior horn neuronal density and the percentage of neurons affected by pTDP-43 pathology in the spinal cord of ALS and control cases. As expected, the anterior horn neuronal density was significantly lower in ALS compared to control cases (Suppl. Fig. 5a; Suppl. Table 3; $p = 0.017$; OR = 0.912; 95% CI = 0.846-0.984; binary logistic regression corrected for age and sex), while the percentage of pTDP-43 affected neurons was increased (Suppl. Fig. 5b; $p < 0.0001$; Mann-Whitney test). A Pearson's partial correlation corrected for age and sex did not indicate any correlation between the number of cleaved GSDMD-positive microglia in the lateral pyramidal tracts and the anterior horn neuronal density (Suppl. Table 5; $r = 0.045$; $p = 0.832$), nor with the percentage of pTDP-43 affected neurons (Suppl. Table 4; $r = 0.208$; $p = 0.318$). However, the anterior horn neuronal density correlated with the percentage of neurons affected by pTDP-43 pathology, similar to our observations in the motor cortex (Suppl. Table 5; $r = -0.544$; $p = 0.004$).

Finally, we biochemically assessed the expression of pyroptosis-related proteins in the spinal cord of ALS and control cases. ALS SDS-soluble spinal cord extracts displayed an increased expression of full-length caspase-1 (Fig. 6a,b; Suppl. Fig. 6a; $p = 0.0134$; unpaired t-test), as well as the cleaved and active p20 fragment (Fig. 6a,c; Suppl. Fig. 6a; $p = 0.0002$; unpaired t-test). Additionally, we detected an increased expression of pyroptosis effector proteins cleaved GSDMD (Fig. 6a,d; Suppl. Fig. 6b; $p = 0.0003$; unpaired t-test) and IL-18 (Fig. 6a,e; Suppl. Fig. 6c; $p = 0.0022$; Mann-Whitney test).



Ch. II - Figure 6. Biochemical characterization of pyroptosis proteins in the ALS spinal cord.

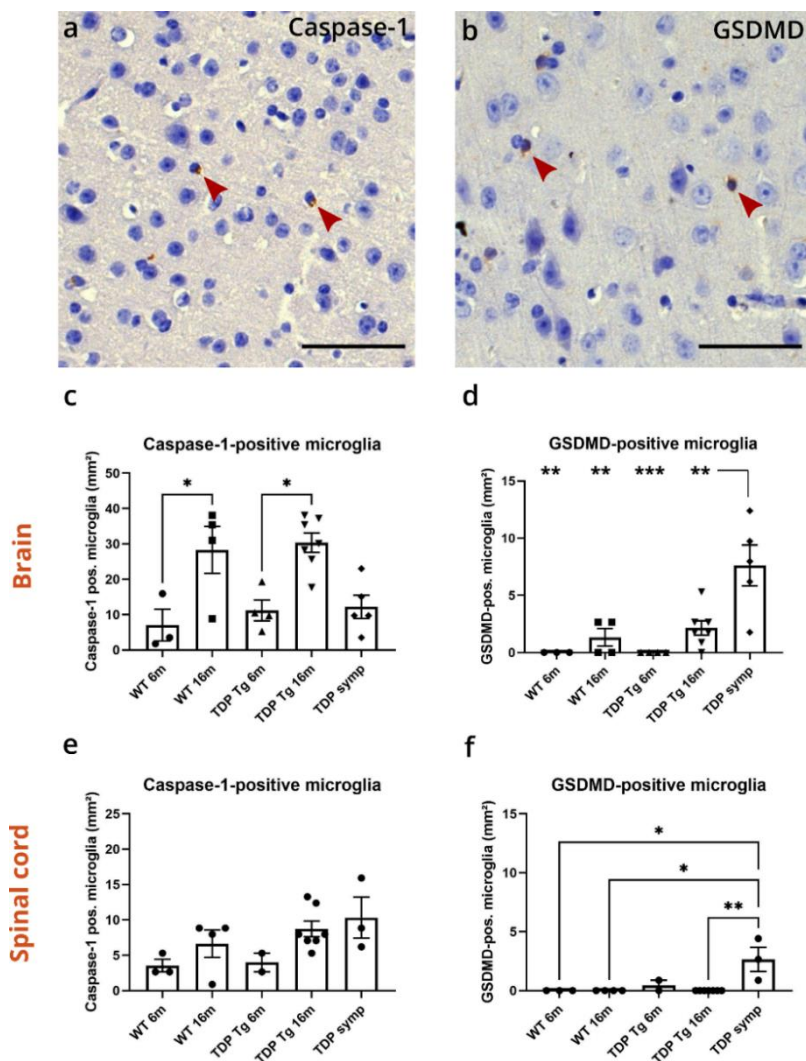
(a) Spinal cord tissue lysates from control (n = 8) and ALS (n = 7) on western blots probed with antibodies for caspase-1, cleaved GSDMD and IL-18, with GAPDH as loading control. For IL-18, the lower band is the correct molecular weight, as the upper band represents pro-IL-18. **(b-e)** Quantifications of pyroptosis-related proteins relative to GAPDH. Statistical analyses were performed using unpaired t-test or Mann-Whitney test. * $p < 0.05$; ** $p < 0.01$; *** $p < 0.001$.



Increased GSDMD reactivity in symptomatic TDP-43^{A315T} transgenic mice is associated with a decreased neuronal density in the brain

To explore whether the pyroptosis pathway was also activated in animal models of ALS, we investigated the presence of the inflammasome component caspase-1 and the pyroptosis effector protein GSDMD in the brain and spinal cord of TDP-43^{A315T} transgenic mice. We detected microglia positive for caspase-1 (Fig. 7a; Suppl. Fig. 7a-d) and GSDMD (Fig. 7b; Suppl. Fig. 7e-h) in the gray and white matter of the motor cortex and spinal cord of symptomatic TDP-43^{A315T} transgenic mice. We quantified the number of caspase-1- and GSDMD-positive microglia per mm² in the motor cortex and in the spinal cord (gray + white matter) in five different mouse groups: (1) 6 months old wild-type mice, (2) 16 months old wild-type mice, (3) 6 months old TDP-43^{A315T} transgenic mice, (4) 16 months old TDP-43^{A315T} transgenic mice, and (5) symptomatic TDP-43^{A315T} transgenic mice (6-14 months old, mean age of 9 months old). In the motor cortex, the number of caspase-1-positive microglia was significantly increased in 16 months old wild-type and 16 months old TDP-43^{A315T} transgenic mice compared to their 6 months old counterparts (Fig. 7c; wild-type: $p = 0.0289$; TDP-43^{A315T} transgenic: $p = 0.0149$; one-way ANOVA followed by Tukey's multiple comparisons). The number of caspase-1-positive microglia was

not increased in the brain of symptomatic TDP-43^{A315T} transgenic mice. In contrast, the amount of GSDMD-positive microglia was significantly increased in symptomatic TDP-43^{A315T} transgenic compared to 6 months old wild-type mice (Fig. 7d; $p = 0.0014$; one-way ANOVA followed by Tukey's multiple comparisons), 16 months old wild-type mice ($p = 0.0039$); 6 months old TDP-43^{A315T} transgenic mice ($p = 0.0006$) and 16 months old TDP-43^{A315T} transgenic mice ($p = 0.0041$). In the spinal cord, a similar increase in caspase-1-positive microglia was detected as in the brain in 16 months old wild-type and TDP-43^{A315T} transgenic mice, although not significant (Fig. 7e). Symptomatic TDP-43^{A315T} transgenic mice showed similar levels of caspase-1-positive microglia in the spinal cord compared to the 16 months old groups. Finally, we analyzed the amount of GSDMD-positive microglia in the spinal cord. Similar to as was observed in the brain, this was significantly increased in symptomatic TDP-43^{A315T} transgenic mice compared to 6 months old wild-type mice (Fig. 7f; $p = 0.0267$; Kruskal-Wallis test followed by Dunn's multiple comparisons), 16 months old wild-type mice ($p = 0.0133$), and 16 months old TDP-43^{A315T} transgenic mice ($p = 0.0038$).



Ch. II - Figure 7. Increased expression of GSDMD in motor cortex and spinal cord of symptomatic TDP-43^{A315T} transgenic mice. (a) IHC representative image of caspase-1-positive microglia (arrowheads) in the motor cortex of TDP-43^{A315T} transgenic mice. (b) IHC representative image of GSDMD-positive microglia (arrowheads) in the motor cortex of TDP-43^{A315T} transgenic mice. Scale bars represent 50 μm. (c,d) Graphs representing the number of caspase-1 (c) and GSDMD (d) positive microglia per mm² in the motor cortex of the different mouse groups. (e,f) Graphs representing the number of caspase-1 (e) and GSDMD (f) positive microglia per mm² in the spinal cord of the different mouse groups. WT 6m = 6 months old wild-type mice; WT 16m = 16 months old wild-type mice; TDP Tg 6m = 6 months old TDP-43^{A315T} transgenic mice; TDP Tg 16m = 16 months old TDP-43^{A315T} transgenic mice; TDP symp = symptomatic TDP^{A315T} transgenic mice. * $p < 0.05$; ** $p < 0.01$; *** $p < 0.001$.

Next, we focused on TDP-43, as this protein is mutated in the mouse model. No typical cytoplasmic TDP-43-positive inclusions were observed, although symptomatic TDP-43^{A315T} transgenic mice occasionally displayed dense aggregated material around the nucleus positive for TDP-43 (Suppl. Fig. 8a; arrow), while the nucleus was not stained. Nuclear clearance of physiological TDP-43 was a prominent phenotype, which we quantified for the different mouse groups. In the motor cortex, TDP-43 nuclear clearance was significantly increased in symptomatic TDP-43^{A315T} transgenic mice compared to 16 months old wild-type mice (Suppl. Fig. 8a,c; $p = 0.006$; Kruskal-Wallis test followed by Dunn's multiple comparisons). We also noticed a numerical but non-significant increase in the 16 months old TDP-43^{A315T} transgenic group. In the spinal cord anterior horn, no differences in TDP-43 nuclear clearance could be detected among the groups (Suppl. Fig. 8b,d).

We further analyzed the different mouse groups immunohistochemically using an antibody against ubiquitin, as it was previously shown that ubiquitin-positive but TDP-43-negative material could be detected in this model (65). We observed diffuse cytoplasmic ubiquitin-positive staining in neurons both in the motor cortex (Suppl. Fig. 9a) and in the spinal cord (Suppl. Fig. 9b) of the majority of symptomatic TDP-43^{A315T} transgenic mice. This ubiquitin-positive neuronal staining was also observed in one 6-months-old and two 16-months-old TDP-43^{A315T} transgenic asymptomatic mice. An antibody against SQSTM1/p62 displayed a similar neuronal staining pattern, for the first time indicating that affected neurons in symptomatic TDP-43^{A315T} transgenic mice are positive for SQSTM1/p62 (Suppl. Fig. 9c,d). Finally, we assessed the neuronal density in layer V of the motor cortex and the anterior horn of the spinal cord of the different mouse groups to evaluate whether neuronal loss was present in the model. Neuronal density was significantly decreased in the motor cortex of symptomatic TDP-43^{A315T} transgenic mice compared to 6 months old wild-type mice (Suppl. Fig. 10a; $p = 0.0307$; Kruskal-Wallis test followed by Dunn's multiple comparisons). In the spinal cord, a slight but non-significant decrease was observed in the symptomatic TDP-43^{A315T} transgenic mice (Suppl. Fig. 10b).

Using Pearson's partial correlation analysis, we found that the number of GSDMD-positive microglia in the brain significantly correlated with a decrease in motor cortex layer V neuronal density (Table 3; $r = -0.478$; $p = 0.021$). This was not the case for caspase-1-positive microglia (Table 3; $r = -0.378$; $p = 0.075$). The percentage of TDP-43 nuclear clearance correlated with layer V neuronal density (Table 3; $r = -0.414$; $p = 0.049$). There was also a trend towards a correlation between the amount of GSDMD-positive microglia and the percentage of TDP-43 nuclear clearance, although not significant (Table 3; $r = 0.408$; $p = 0.053$). A similar analysis for the spinal cord did not show any significant correlations for the abovementioned parameters (Suppl. Table 6).

Ch. II - Table 3. Correlation matrix for mouse motor cortex neuronal density and other parameters. Matrix showing Pearson's correlation values and p-values for the association between mouse motor cortex layer V neuronal density and other variables, including the number of caspase-1-positive microglia, the number of GSDMD-positive microglia, and the percentage of TDP-43 nuclear clearance. * $p < 0.05$; ** $p < 0.01$.

	Caspase-1-positive microglia	GSDMD-positive microglia	% TDP-43 clearance	Layer V neuronal density	n
Caspase-1-positive microglia	-				23
GSDMD-positive microglia	$r = -0.075$ $p = 0.733$	-			23
% TDP-43 clearance	$r = -0.168$ $p = 0.442$	$r = 0.408$ $p = 0.053$	-		23
Layer V neuronal density	$r = -0.378$ $p = 0.075$	$r = -0.478$ $p = 0.021^*$	$r = -0.414$ $p = 0.049^*$	-	23

5. Discussion

Here, we described the expression of the NLRP3 inflammasome complex comprising of NLRP3, ASC and caspase-1, as well as pyroptosis effector-related proteins cleaved GSDMD and IL-18 in microglial cells in the ALS motor cortex and spinal cord. The microglial expression of cleaved GSDMD in the precentral white matter correlated with neuronal loss in layer V of the motor cortex, but not with the amount of pTDP-43 pathology. In the spinal cord, no increase in microglial cleaved GSDMD was detected, although elevated expression of pyroptosis-related proteins was detected biochemically both in the motor cortex and in the spinal cord (Table 4). Importantly, we observed increased GSDMD expression in microglia in the brain and spinal cord of symptomatic TDP-43^{A315T} transgenic mice, which also correlated with neuronal loss in layer V of the motor cortex, similar to our observations in human tissue. To our knowledge, this is the first time that expression of the full NLRP3 inflammasome and, importantly, the pyroptosis effector-related proteins cleaved GSDMD and IL-18 was observed in ALS microglial cells and was linked to neuronal degeneration, both in human *post-mortem* tissue and TDP-43 transgenic mice.

Ch. II - Table 4. Overview for the comparison of IHC versus WB results for caspase-1 and cleaved GSDMD in the human and mouse motor cortex and spinal cord. In immunohistochemical stainings the number of cells expressing a given protein was assessed, whereas by western blot the general expression levels were determined. GM = gray matter; WM = white matter; IHC = immunohistochemistry; WB = western blot; ↑ = significant increase; ↗ = numerical trend towards increase; “=” = no noticeable difference; ↓ = significant decrease.

		CASPASE-1	
		IHC	WB
Human ALS	Motor cortex	WM = GM ↓	Pro-caspase-1 ↑ Caspase-1 p20 ↑
	Spinal cord	WM =	Pro-caspase-1 ↑ Caspase-1 p20 ↑
Mouse TDP-43 A315T	Motor cortex	=	
	Spinal cord	=	

		CLEAVED GSDMD	
		IHC	WB
Human ALS	Motor cortex	WM ↑ GM =	cl GSDMD ↗
	Spinal cord	WM ↗	cl GSDMD ↑
Mouse TDP-43 A315T	Motor cortex	↑	
	Spinal cord	↑	

In human ALS brain, we observed a correlation of the abundance of pTDP-43 pathology with neuronal loss, but not with cleaved GSDMD-positive white matter microglia although the latter lesions are also associated with motor cortex neuron loss. This suggests that the presence of pTDP-43 aggregates does not directly influence the activation of pyroptosis in white matter microglia. However, this is an end-point observation, and it is possible that during the course of the disease, pathological pTDP-43, soluble or aggregated, does serve as a trigger for inflammasome and pyroptosis activation. Evidence supports the activation of the NLRP3 inflammasome by abnormal protein aggregates in neurodegenerative diseases (133,255). This activation requires a two-step process. First, the NFκB pathway is activated through stimulation of toll-like receptors (TLRs), leading to upregulation of the expression of NLRP3, pro-caspase-1 and pro-interleukins. Secondly, the NLRP3 inflammasome can be assembled and activated by a variety of stimuli, such as reactive oxygen species (ROS), extracellular ATP, lysosomal rupture, low intracellular K⁺, and aggregated or misfolded proteins (120,123,126). Regarding ALS, *in vitro* studies showed that pathological TDP-43 could induce an NLRP3-dependent secretion of active IL-1β and IL-18 in microglia (97,140,141). This pro-inflammatory cascade was shown to be toxic to motor neurons, while in the absence of microglia, pathological TDP-43 was not detrimental to motor neurons (141). Similar results were obtained with mutant SOD1, which was shown to trigger the NLRP3-dependent cleavage of caspase-1 and IL-1β in primary mouse microglia

(97). These results support the hypothesis that pathological ALS proteins can induce pyroptosis activation in microglia. In recent years, several groups also demonstrated an upregulation of NLRP3, ASC, caspase-1, IL-1 β and IL-18 in SOD1^{G93A} mice and rats (97,135–139), which are the most commonly used animal models for ALS, although SOD1 mutations only explain 2% of ALS cases (256). Deora and colleagues also showed increased expression of the NLRP3 inflammasome in TDP^{Q331K} mutant mice (97). Furthermore, TDP-43 was shown to interact with NF κ B and to function as a suppressor of the NF κ B pathway, with a loss of TDP-43 leading to increased activation of the NF κ B pathway (257). This suggests that a loss of nuclear TDP-43, as observed in ALS, could make cells more susceptible for pyroptosis activation through a reduced inhibition of the NF κ B pathway. Although the above data indicate the importance of pathological TDP-43 and SOD1 in eliciting pyroptosis activation, it is likely that other pathological conditions often observed in ALS (e.g. ROS, extracellular ATP), which could be downstream of SOD1 and TDP-43 mutations, are responsible for NLRP3 inflammasome activation.

In human ALS cases, the abundance of cleaved GSDMD-positive microglia in the precentral white matter correlated with a decreased neuronal density in layer V of the motor cortex. Following pyroptosis activation, GSDMD-NT oligomerizes and associates with the plasma membrane to form micropores, resulting in potassium efflux, intracellular and extracellular ion imbalance, cell swelling and rupture of the plasma membrane (126). This causes massive leakage of pro-inflammatory cytokines, such as IL-1 β and IL-18, as well as other cytosolic components (120,121). In turn, IL-1 β and IL-18 bind their respective receptors on glial cells and neurons, initiating a complex spectrum of signaling pathways, further enhancing inflammatory responses and resulting in neuronal injury and death (126). Therefore, it is likely that the observed activation of the pyroptosis pathway in ALS white matter microglia contributes to neuronal degeneration in the motor cortex, possibly by affecting axonal health. However, it remains unclear whether this is the primary insult in neurodegeneration, or just one contributing factor enhancing neuronal toxicity among others. Importantly, the number of microglia in the human white matter is significantly higher compared to gray matter (258). Furthermore, a clear difference in the immune regulatory profile was identified between white and gray matter microglia, with white matter microglia displaying an increased expression of genes involved in the NF κ B pathway (259). This could make white matter microglia more susceptible for pyroptosis activation as activation of the NF κ B pathway induces elevated expression of pyroptosis-related genes, possibly explaining the increased abundance of cleaved GSDMD-positive microglia specifically in the ALS precentral white matter.

We did not observe obvious TDP-43 pathological aggregates in the brain and spinal cord of symptomatic TDP-43^{A315T} mice, although a few ubiquitin-positive neurons were detected in symptomatic TDP-43^{A315T} mice, and to a lesser extent in 6 and 16 months old TDP-43^{A315T} mice. This is in line with previous reports (65,253,260). In the motor cortex of symptomatic TDP-43^{A315T} mice, we detected an increased TDP-43 nuclear clearance. This did not significantly correlate with the amount of GSDMD-positive microglia, similar to our observations in the human brain. Importantly, a decrease in neuronal density in layer V of the motor cortex correlated with an increased presence of GSDMD-positive microglia, mirroring our human data. Others also detected a decreased number of neurons in layer V of the motor cortex (65,261). In the spinal cord, results are more contradictory with some groups reporting up to 20% loss of spinal motor neurons (65,262), while we and others could not confirm this (253). This could be due to the small number of mice from which we could obtain spinal cord tissue, which is one of the limitations of this study.

In human cases, we detected an average of 32.8% neurons cleared of nuclear TDP-43 in ALS cases using an antibody directed against the C-terminal part of TDP-43, with control cases showing an average of 13.18% neurons negative for nuclear TDP-43. Our human control cohort showed relatively high basal levels of TDP-43 nuclear depletion, especially when compared to 6 and 16 months old wild-type mice. Since previous studies (25,27) described this phenomenon but, to our knowledge, did not provide quantitative data, it is unclear whether the detection of TDP-43 nuclear clearance in control cases is a physiological finding, or whether it is due to technical reasons (antibody sensitivity in formalin-fixed tissue) or autolysis during the *post-mortem* interval. Importantly, it was shown that cellular stress can induce the depletion of TDP-43 from the nucleus (263), which also occurs in normal aging and during the agonal phase before death, possibly explaining the relatively high baseline levels of TDP-43 nuclear clearance in the human control cohort. In contrast, mice were euthanized under anesthesia and brains were immediately harvested, resulting in less cellular stress and therefore possibly lower levels of baseline TDP-43 nuclear clearance. More studies on TDP-43 nuclear clearance including other TDP-43 antibodies will be needed to clarify its biology.

Contrary to cleaved GSDMD, we did not observe an increase of caspase-1-positive microglia in ALS versus control precentral gray and white matter using immunohistochemical methods (Table 4). It is likely that mainly physiological inactive pro-caspase-1 is detected by immunohistochemistry, which might mask the detection of increased levels of the active p20 fragment as observed by western blot (Table 4). It seems that full-length pro-caspase-1 is endogenously present in microglia, as control cases also show basal caspase-1 levels. Furthermore, the abundance of caspase-1-positive microglia is five-fold higher compared to cleaved GSDMD-positive microglia in human cases, indicating a physiological expression of pro-caspase-1 in microglia. Using biochemical methods, we however observed an

increased expression of both pro-caspase-1 as well as the p20 active fragment in human ALS brain and spinal cord (Table 4), probably reflecting a higher cellular expression without an increase in the number of caspase-1 expressing microglial cells. Therefore, it is likely that in ALS microglia upscale their expression of pro-caspase-1, and that following NLRP3 inflammasome activation the p20 fragment is produced, as reflected by our western blot data (Table 4). We detected similar results in mice, as symptomatic TDP-43^{A315T} did not show an increase in caspase-1-positive microglia. However, an age-dependent effect was noted as 16 months old wild-type and TDP-43^{A315T} transgenic mice presented with a higher abundance of caspase-1-positive glia compared to their 6 months old counterparts. This age-dependent increase of caspase-1 expression was recently described in mice and humans and referred to as ‘inflammaging’, reflecting the increased expression of inflammatory proteins during the aging process (264). Additionally, the *post-mortem* interval and other comorbid neurological and agonal conditions may influence the inflammatory status in the human brain and spinal cord, likely explaining the higher baseline levels of caspase-1 and cleaved GSDMD-positive microglia in human *post-mortem* tissue compared to wild-type and TDP-43^{A315T} transgenic mice, where these parameters are better controlled. A limitation of this study is that we could not assess caspase-1 full-length and p20 fragment levels biochemically by western blot in mouse brain and spinal cord due to unavailability of frozen tissue.

Our biochemical analysis in CNS lysates showed an increased expression of active IL-18 in ALS motor cortex and spinal cord compared to control cases, indicative of an activated pyroptosis pathway. Elevated serum IL-18 levels have previously also been demonstrated in sporadic ALS patients (142). Other groups reported elevated caspase-1, NLRP3 and IL-18 levels in ALS brain tissue (137,265), which is in line with our results for caspase-1, p20 and IL-18 in the motor cortex and spinal cord. Increased NLRP3 mRNA levels were also detected in blood and in *post-mortem* tissue of ALS patients (143,144). Unfortunately, antibodies against NLRP3 and IL-1 β could not detect the respective proteins in *post-mortem* brain and spinal cord lysates by western blot in our hands, which is a limitation of this study. Regarding the active fragment of GSDMD, we showed for the first time an increased expression of cleaved GSDMD in ALS versus control cases, which was significant in the spinal cord. It is possible that in the motor cortex, baseline expression of cleaved GSDMD in neurons in both control and ALS cases, as observed by IHC, masks the increased cleaved GSDMD expression in microglial cells on western blot.

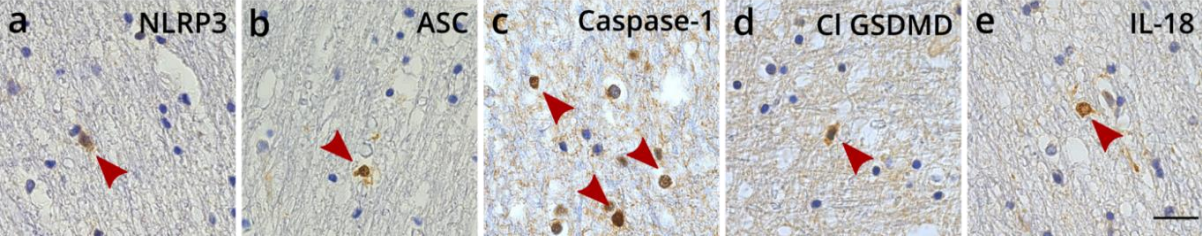
In the CNS, PRRs are thought to mainly be expressed by microglial cells and astrocytes (121). Both cell types also are assumed to be able to express NLRP3, however, for neurons this is still debated (126). In this study, we observed expression of the full NLRP3 inflammasome (i.e. NLRP3, ASC and caspase-1) as well as the pyroptosis effector-related proteins cleaved GSDMD and IL-18 in microglia. NLRP3 and cleaved GSDMD expression were additionally detected in neurons and astrocytes, although to a lesser

extent. ASC was exclusively detected in microglia, while caspase-1 was also occasionally faintly stained in astrocytes. IL-18 was absent in astrocytes, with some neurons faintly positive. Oligodendrocytes were negative for all abovementioned markers. Our results underline the importance of microglia in inflammasome-mediated pyroptosis in ALS, and are in line with several *in vitro* studies, showing that microglia express the full NLRP3 inflammasome and produce active IL-1 β and IL-18 (97,140,141). Bellezza and colleagues also demonstrated expression of the NLRP3 inflammasome in SOD1^{G93A} mouse microglial cells (135), although others found increased microglial caspase-1 and ASC expression in the same mouse model, but not NLRP3 (139). In contrast, another group postulated mainly astrocytes, but also neurons to express ASC and NLRP3, with microglia only positive for ASC in SOD1^{G93A} mice (136,137). A recent study, however, detected NLRP3 expression both in microglia and astrocytes of SOD1^{G93A} mice (97), similar to our results in the human ALS brain. Overall, evidence points towards microglia as the main cell type responsible for pyroptosis activation in ALS, although we cannot fully exclude that astrocytes and possibly neurons also contribute to NLRP3 inflammasome-mediated cytotoxicity.

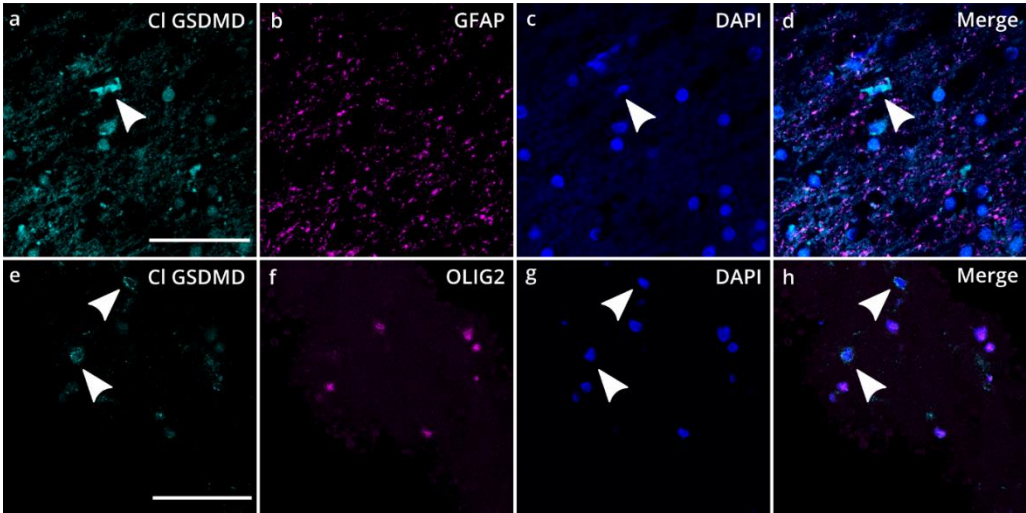
In conclusion, our findings point towards microglial NLRP3 inflammasome-mediated pyroptosis as an important player in ALS pathophysiology and neurodegeneration, with cleaved GSDMD as a useful marker for pyroptosis activation in the ALS precentral white matter. Investigation of the pathological triggers and the effects of inhibition of this pathway *in vitro* and *in vivo* will aid in the development of novel therapeutic strategies counteracting motor neuron degeneration in ALS.

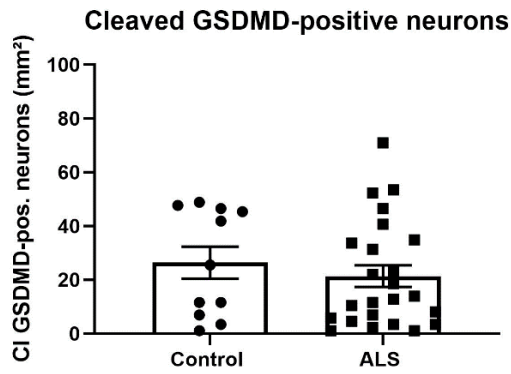
6. Supplementary information

Ch. II - Suppl. Figure 1. Expression of inflammasome components and pyroptosis effector proteins in control precentral white matter microglia. Immunohistochemical detection of inflammasome components NLRP3 (a), ASC (b) and caspase-1 (c), as well as pyroptosis effector-related proteins cleaved GSDMD (d) and IL-18 (e) in control precentral white matter. Arrowheads indicate microglial cells positive for respective markers. Control cases positive for the respective markers were selected. Scale bars represent 25 µm.

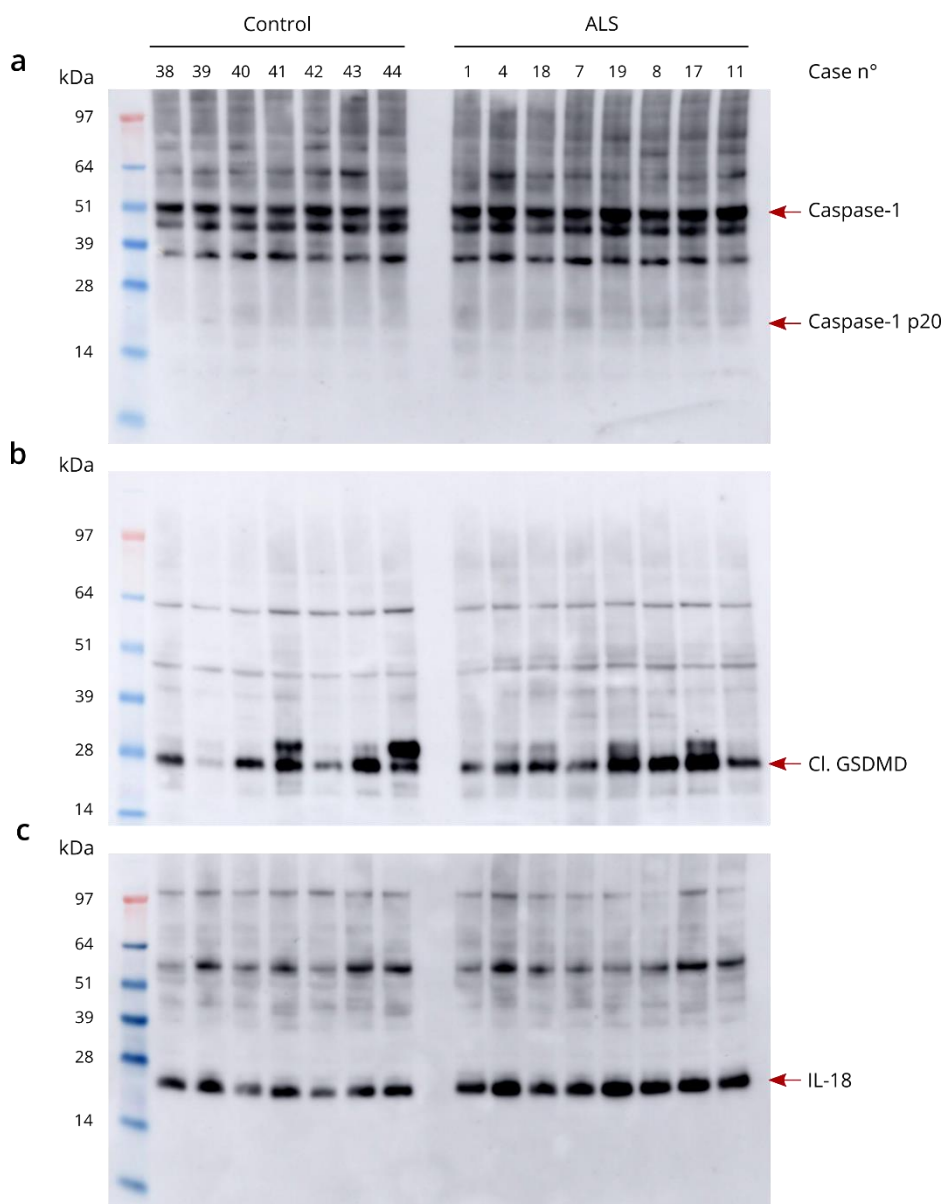


Ch. II - Suppl. Figure 2. Expression of cleaved GSDMD in ALS motor cortex in relation to astrocytes and oligodendrocytes. (a-h) Immunofluorescence detection of pyroptosis effector protein cleaved GSDMD in relation to GFAP-positive astrocytes (a-d) and Olig2-positive oligodendrocytes (e-h). Arrowheads indicate glial cells positive for cleaved GSDMD not overlapping with GFAP-positive astrocytes and Olig2-positive oligodendrocytes. Scale bars represent 50 µm.



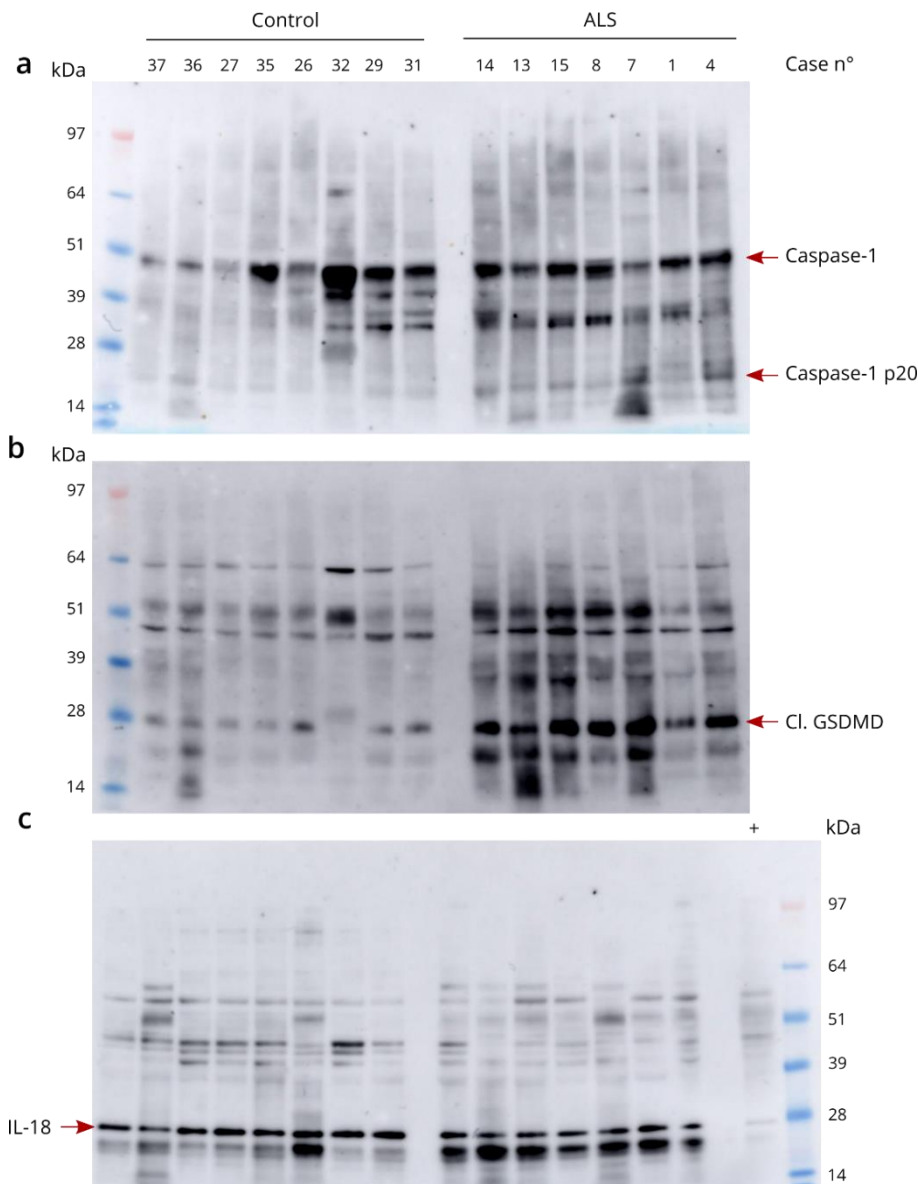
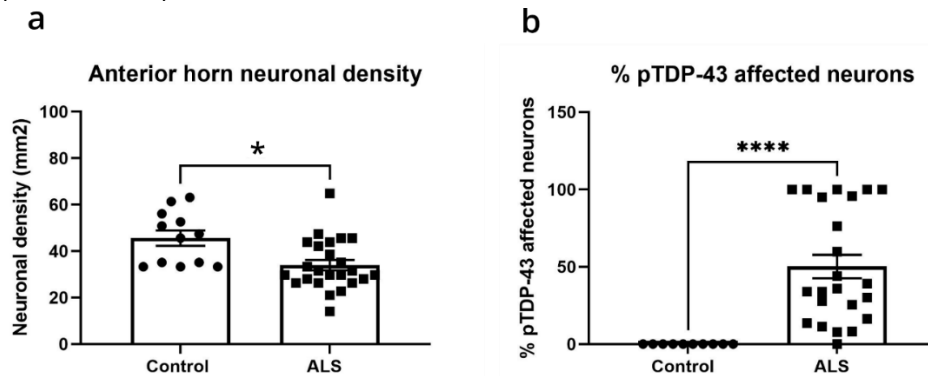


Ch. II - Suppl. Figure 3. Cleaved GSDMD expression in neurons in the ALS and control motor cortex. Graph representing the number of neurons in layer V of the motor cortex positive for cleaved GSDMD for control and ALS cases. Binary logistic regression corrected for age and sex was used for statistical analysis.



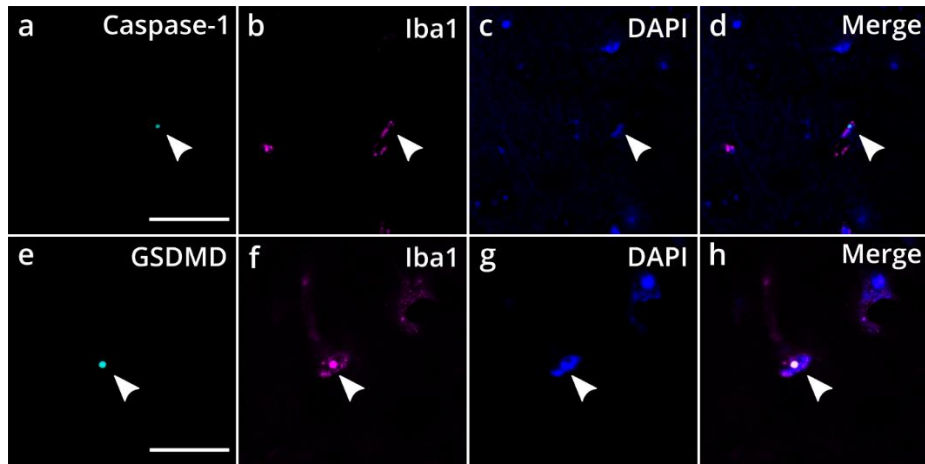
Ch. II - Suppl. Figure 4. Full western blots for the expression of pyroptosis proteins in the ALS motor cortex. (a-c) Full western blots for motor cortex tissue lysates from control (n = 7) and ALS (n = 8) probed with antibodies for caspase-1 (a), cleaved GSDMD (b) and IL-18 (c). Arrows indicate the bands at the correct molecular weight of the proteins. The case n° for each lane is indicated in a.

Ch. II - Suppl. Figure 5. Spinal cord anterior horn neuronal density and pTDP-43 pathology. (a) Graph representing the neuronal density per mm² in the anterior horn of the spinal cord of control and ALS cases. (b) Graph representing the percentage of pTDP-43 affected neurons in the spinal cord of control and ALS cases. Binary logistic regression corrected for age and sex (a) and Mann-Whitney U test (b) were used for statistical analysis. * $p < 0.05$; **** $p < 0.0001$.

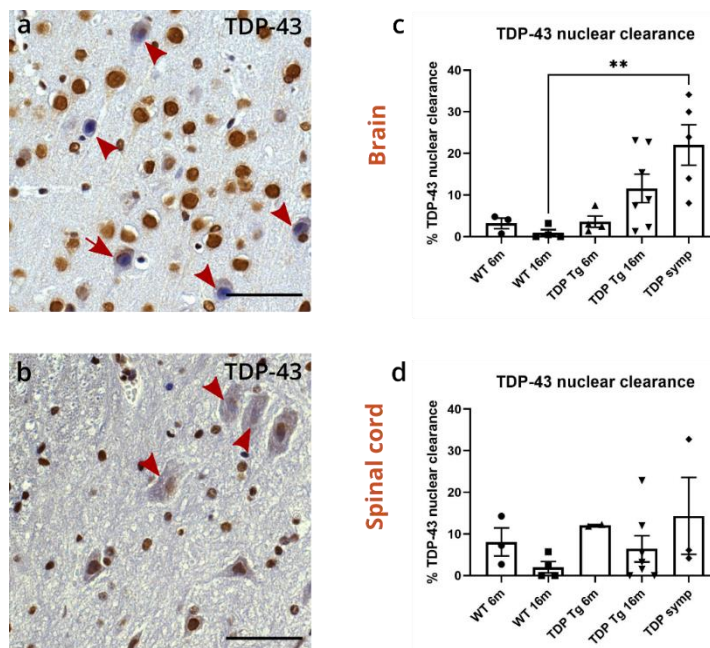


Ch. II - Suppl. Figure 6. Full western blots for the expression of pyroptosis proteins in the ALS spinal cord. (a-c) Full western blots for spinal cord tissue lysates from control (n = 8) and ALS (n = 7) probed with antibodies for caspase-1 (a), cleaved GSDMD (b) and IL-18 (c). Arrows indicate the bands at the correct molecular weight of the proteins. The extra lane for IL-18 (c) is a positive control (+). The case n° for each lane is indicated in a.

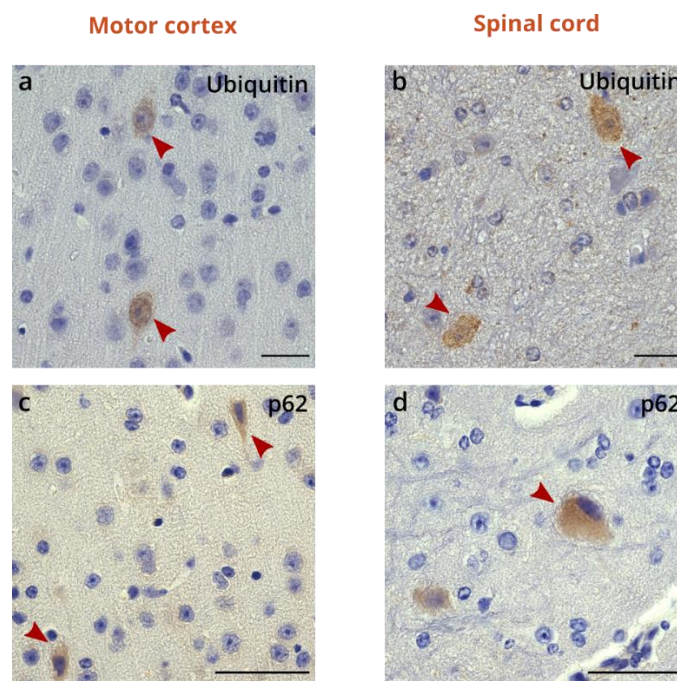
Ch. II - Suppl. Figure 7. Caspase-1 and GSDMD are expressed in microglia in TDP-43^{A315T} transgenic mice. Immunofluorescence detection of caspase-1 (a-d) and GSDMD (e-h) in Iba-1-positive microglia in the CNS of symptomatic TDP-43^{A315T} transgenic mice. Merge of all three channels is shown. Arrowheads indicate microglia positive for caspase-1 (a-d) and GSDMD (e-h). Scale bars represent 25 μ m.



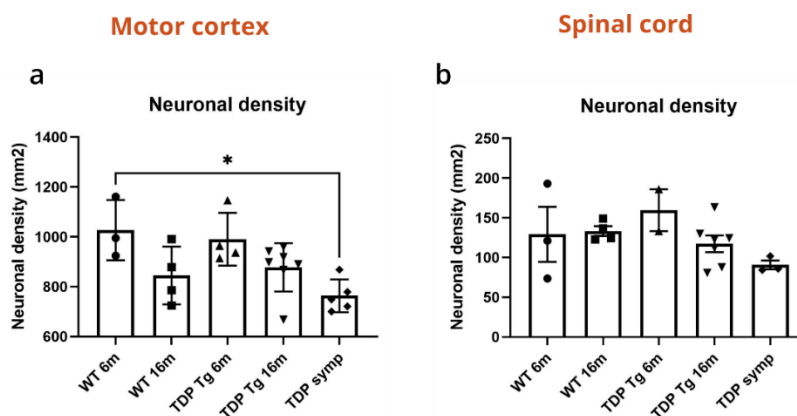
Ch. II - Suppl. Figure 8. Increased TDP-43 nuclear clearance in the motor cortex and spinal cord of symptomatic TDP-43^{A315T} transgenic mice. (a, b) Immunohistochemical representative images of an antibody staining against TDP-43 in the brain (a) and spinal cord (b) of symptomatic TDP-43^{A315T} transgenic mice. Arrowheads indicate neuronal nuclei cleared of TDP-43. Arrow indicates perinuclear dens aggregated TDP-43-positive material with the nucleus devoid of TDP-43. Scale bars represent 50 μ m. (c, d) Graphs representing the percentage of neurons cleared of nuclear TDP-43 in the brain (c) and spinal cord (d) for the different groups of mice. WT 6m = 6 months old wild-type mice; WT 16m = 16 months old wild-type mice; TDP Tg 6m = 6 months old TDP-43^{A315T} transgenic mice; TDP Tg 16m = 16 months old TDP-43^{A315T} transgenic mice; TDP symp = symptomatic TDP^{A315T} transgenic mice. ** $p < 0.01$.



Ch. II - Suppl. Figure 9. Ubiquitin and SQSTM1/p62 pathology in the motor cortex and spinal cord of TDP-43^{A315T} transgenic mice. (a, b) Immunohistochemical representative images of ubiquitin-positive cytoplasmic staining in motor neurons in the motor cortex (a) and in the anterior horn of the spinal cord (b) of symptomatic TDP-43^{A315T} transgenic mice. Arrowheads indicate neurons positive for ubiquitin. (c, d) Immunohistochemical representative images of SQSTM1/p62-positive cytoplasmic staining in motor neurons in the motor cortex (c) and in the anterior horn of the spinal cord (d) of symptomatic TDP-43^{A315T} transgenic mice. Arrowheads indicate neurons positive for SQSTM1/p62. Scale bars represent 25 μ m (a,b) and 50 μ m (c,d).



Ch. II - Suppl. Figure 10. Neuronal density in the motor cortex and spinal cord of TDP-43^{A315T} transgenic mice. Graphs representing the neuronal density per mm² for layer V of the motor cortex in the brain (a) and for the anterior horn of the spinal cord (b) for the different groups of mice. WT 6m = 6 months old wild-type mice; WT 16m = 16 months old wild-type mice; TDP Tg 6m = 6 months old TDP-43^{A315T} transgenic mice; TDP Tg 16m = 16 months old TDP-43^{A315T} transgenic mice; TDP symp = symptomatic TDP-43^{A315T} transgenic mice. * $p < 0.05$.



Ch. II - Suppl. Table 1. List of human cases. The table provides information regarding age (= age at death), sex, diagnosis, the presence of the *C9orf72* mutation, A β MTL phase, Braak NFT stage, CERAD score, disease duration (months), PMI (hours) and application (western blot / immunohistochemistry). Abbreviations: f = female; m = male; ALS = amyotrophic lateral sclerosis; FTLD = frontotemporal lobar degeneration; control = non neurodegenerative disease control; A = aneurysm; AGD = argyrophilic grain disease; ARTAG = aging-related tau astroglipathy; CM = carcinoma metastasis; GB = Guillian-Barre syndrome; I = infarction; MI = microinfarction; n.a. = not applicable; n.d. = not determined; PART = primary age-related tauopathy; p-preAD = preclinical preAD; SVD = small vessel disease; SVE = subcortical vascular encephalopathy; PMI = *post-mortem* interval; WB = western blot; IHC = immunohistochemistry.

Case n°	Age	Sex	Diagnosis	C9 mutation	A β MTL phase	Braak NFT stage	CERAD	Disease duration	PMI (hours)	Application
1	58	f	ALS, PART	0	0	2	0	18 months	24	WB, IHC
2	62	f	ALS	0	0	1	0	12 months	24	IHC
3	51	m	ALS	0	0	1	0	8 months	24	IHC
4	49	m	ALS, PART	0	0	1	0	45 months	24	WB, IHC
5	46	m	ALS	0	0	1	0	40 months	24	IHC
6	62	m	ALS, MI, I, ARTAG, PART, AGD	0	0	1	0	154 months	12	IHC
7	53	m	ALS	0	0	1	0	92 months	24	WB, IHC
8	74	m	ALS	0	1	1	0	47 months	24	WB, IHC
9	68	f	ALS	0	0	1	0	n.d.	192	IHC
10	56	f	ALS	0	1	1	0	48 months	72	IHC
11	57	f	ALS, FTLD-TDP Type B	0	1	1	0	22 months	24	WB, IHC
12	61	m	ALS, FTLD-TDP Type B	0	0	1	0	32 months	2	IHC
13	50	f	ALS	0	0	1	0	18 months	24	WB, IHC
14	54	m	ALS	0	0	1	0	88 months	6	WB, IHC
15	69	f	ALS	0	1	1	0	6 months	24	WB
16	68	m	ALS, SVD	1	2	1	0	n.d.	144	IHC
17	52	m	ALS	1	0	0	0	15 months	6	WB, IHC
18	57	m	ALS, p-preAD	1	1	1	0	17 months	n.d.	WB, IHC
19	49	m	ALS, PART	1	0	1	0	46 months	24	WB, IHC
20	48	m	ALS	1	0	1	0	18 months	24	IHC
21	57	m	ALS	1	0	1	0	19 months	20	IHC
22	75	m	ALS	1	0	2	0	n.d.	24	IHC
23	50	m	ALS, Wernicke encephalopathy	1	0	1	0	n.d.	24	IHC
24	46	f	ALS	1	0	1	0	20 months	120	IHC
25	55	m	ALS, FTLD-TDP Type B	1	0	3	0	30 months	12	IHC
26	45	m	Control, I	n.d.	0	0	0	n.a.	24	WB, IHC
27	46	m	Control	n.d.	0	1	0	n.a.	29	WB, IHC
28	74	m	Control, CM, I, MI	n.d.	0	0	0	n.a.	72	IHC
29	61	m	Control, SVD	n.d.	0	0	0	n.a.	48	WB, IHC
30	73	m	Control, SVD, CM	n.d.	0	2	0	n.a.	48	IHC
31	55	m	Control, A, I	n.d.	0	0	0	n.a.	96	WB, IHC
32	74	f	Control, AGD, SVE	n.d.	0	1	0	n.a.	24	WB, IHC
33	35	m	Control, Limbic encephalitis	n.d.	0	0	0	n.a.	72	IHC
34	54	m	Control, GB	n.d.	0	1	0	n.a.	24	IHC
35	63	f	Control, MI	n.d.	0	1	0	n.a.	96	WB, IHC
36	64	m	Control	n.d.	0	0	0	n.a.	96	WB, IHC
37	35	m	Control	n.d.	0	1	0	n.a.	48	WB, IHC
38	64	f	Control, MI	n.d.	1	1	0	n.a.	48	WB
39	66	m	Control	n.d.	2	2	0	n.a.	6	WB
40	68	f	Control, I, MI, SVD	n.d.	3	1	0	n.a.	24	WB
41	68	m	Control	n.d.	3	1	0	n.a.	48	WB
42	64	f	Control, I	n.d.	0	1	0	n.a.	n.d.	WB
43	67	f	Control, ARTAG	n.d.	3	2	0	n.a.	n.d.	WB
44	59	m	Control, I	n.d.	2	1	0	n.a.	72	WB

Ch. II - Suppl. Table 2. List of antibodies used in the study. The table summarizes information about host, clonality, supplier and catalog number of the primary antibodies used for immunohistochemistry (IHC), immunofluorescence (IF) and western blot (WB). Dilutions for IHC (human and mouse tissue), IF (human and mouse tissue) and WB (human tissue) are given.

Primary antibody	Host	Clonality	Supplier	Catalog number	Human IHC	Mouse IHC	Mouse IF	Human IF	Human WB
Cleaved GSDMD (Asp275)	Rabbit	Monoclonal	Cell Signaling	36425	1:400	-	-	1:200	-
GSDMD-NT	Rabbit	Polyclonal	Protein Tech	20770-1-AP	-	-	-	-	1:5000
Gasdermin D	Rabbit	Monoclonal	Abcam	ab219800	-	1:100	1:50	-	-
Caspase-1	Mouse	Monoclonal	Adipogen	AG-20B-0048-C100	1:100	-	-	1:50	1:1000
Caspase-1	Rabbit	Polyclonal	Abcam	ab138483	-	1:400	1:300	-	-
IL-18	Rabbit	Polyclonal	Protein Tech	10663-1-AP	1:50	-	-	1:50	1:1000
ASC	Mouse	Monoclonal	Santa Cruz	sc-514414	1:250	-	-	1:50	-
NLRP3	Rabbit	Polyclonal	ABIN	ABIN1386361	1:200	-	-	1:50	-
pTDP43 (S409/410-2)	Rabbit	Polyclonal	Cosmo Bio	TIP-PTD-P02	1:5000	-	-	-	-
pTDP43 (S409/410-1)	Mouse	Monoclonal	Cosmo Bio	TIP-PTD-M01	1:5000	-	-	-	-
TDP-43	Rabbit	Polyclonal	Protein Tech	12892-1-AP	1:1000	1:1000	-	-	-
Ubiquitin	Rabbit	Polyclonal	Protein Tech	10201-2-AP	-	1:10 000	-	-	-
Iba1	Goat	Polyclonal	Abcam	ab5076	-	-	1:200	1:200	-
GFAP	Guinea Pig	Polyclonal	Synaptic Systems	173 004	-	-	-	1:300	-
Olig2	Rabbit	Monoclonal	Abcam	ab109186	-	-	-	1:100	-
β -Amyloid (clone 4G8)	Mouse	Monoclonal	BioLegend	SIG-39220	1:5000	-	-	-	-
pTau (S202/T205) (clone AT8)	Mouse	Monoclonal	ThermoFisher	MN1020	1:1000	-	-	-	-
GAPDH (clone 6C5)	Mouse	Monoclonal	ThermoFisher	AM4300	-	-	-	-	1:10 000
SQSTM1/p62	Mouse	Monoclonal	BD Transduction	610832	-	1:250	-	-	-

Ch. II - Suppl. Table 3. Detailed information on binary logistic regression analyses.

(1) Binary logistic regression addressing the differences between control and ALS cases regarding caspase-1-positive microglia in layer V of the motor cortex, when controlled for age and sex.

	Sign.	Odds ratio	95% CI OR: lower	95% CI OR: upper
Caspase-1-pos. microglia motor cortex layer V	p = 0.031*	0.975	0.954	0.998
Age at death	p = 0.727	0.986	0.912	1.066
Sex	p = 0.504	0.511	0.072	3.656

(2) Binary logistic regression addressing the differences between control and ALS cases regarding cleaved GSDMD-positive microglia in layer V of the motor cortex, when controlled for age and sex.

	Sign.	Odds ratio	95% CI OR: lower	95% CI OR: upper
Cl. GSDMD-pos. microglia motor cortex layer V	p = 0.345	1.138	0.870	1.488
Age at death	p = 0.343	0.961	0.886	1.043
Sex	p = 0.235	0.286	0.036	2.251

(3) Binary logistic regression addressing the differences between control and ALS cases regarding cleaved GSDMD-positive neurons in layer V of the motor cortex, when controlled for age and sex.

	Sign.	Odds ratio	95% CI OR: lower	95% CI OR: upper
Cl. GSDMD-pos. neurons motor cortex layer V	p = 0.527	0.988	0.952	1.025
Age at death	p = 0.805	0.991	0.921	1.066
Sex	p = 0.491	0.533	0.089	3.193

(4) Binary logistic regression addressing the differences between control and ALS cases regarding caspase-1-positive microglia in the precentral white matter, when controlled for age and sex.

	Sign.	Odds ratio	95% CI OR: lower	95% CI OR: upper
Caspase-1-pos. microglia precentral white matter	p = 0.400	1.006	0.992	1.020
Age at death	p = 0.711	0.987	0.919	1.060
Sex	p = 0.476	0.506	0.078	3.300

(5) Binary logistic regression addressing the differences between control and ALS cases regarding cleaved GSDMD-positive microglia in the precentral white matter, when controlled for age and sex.

	Sign.	Odds ratio	95% CI OR: lower	95% CI OR: upper
Cl. GSDMD-pos. microglia precentral white matter	p = 0.034*	1.155	1.011	1.319
Age at death	p = 0.596	0.976	0.890	1.069
Sex	p = 0.089	0.143	0.015	1.349

(6) Binary logistic regression addressing the differences between control and ALS cases regarding motor cortex layer V neuronal density, when controlled for age and sex.

	Sign.	Odds ratio	95% CI OR: lower	95% CI OR: upper
Motor cortex layer V neuronal density	p = 0.023*	0.880	0.788	0.982
Age at death	p = 0.486	0.953	0.832	1.091
Sex	p = 0.710	2.002	0.052	77.547

(7) Binary logistic regression addressing the differences between control and ALS cases regarding the percentage of neurons with TDP-43 cleared from the nucleus in layer V of the motor cortex, when controlled for age and sex.

	Sign.	Odds ratio	95% CI OR: lower	95% CI OR: upper
% of neurons with TDP-43 nuclear clearance	p = 0.022*	1.179	1.023	1.358
Age at death	p = 0.587	1.027	0.932	1.133
Sex	p = 0.517	2.488	0.158	39.212

(8) Binary logistic regression addressing the differences between control and ALS cases regarding caspase-1-positive microglia in the ventral pyramidal tracts, when controlled for age and sex.

	Sign.	Odds ratio	95% CI OR: lower	95% CI OR: upper
Caspase-1-pos. microglia ventral pyr. tracts	p = 0.270	0.947	0.860	1.043
Age at death	p = 0.960	0.998	0.924	1.078
Sex	p = 0.450	0.467	0.065	3.370

(9) Binary logistic regression addressing the differences between control and ALS cases regarding caspase-1-positive microglia in the lateral pyramidal tracts, when controlled for age and sex.

	Sign.	Odds ratio	95% CI OR: lower	95% CI OR: upper
Caspase-1-pos. microglia lateral pyr. tracts	p = 0.606	1.002	0.994	1.010
Age at death	p = 0.865	1.007	0.932	1.087
Sex	p = 0.680	0.668	0.098	4.538

(10) Binary logistic regression addressing the differences between control and ALS cases regarding cleaved GSDMD-positive microglia in the ventral pyramidal tracts, when controlled for age and sex.

	Sign.	Odds ratio	95% CI OR: lower	95% CI OR: upper
Cl. GSDMD-pos. microglia ventral pyr. tracts	p = 0.216	1.285	0.864	1.912
Age at death	p = 0.875	1.006	0.934	1.084
Sex	p = 0.522	0.541	0.083	3.542

(11) Binary logistic regression addressing the differences between control and ALS cases regarding cleaved GSDMD-positive microglia in the lateral pyramidal tracts, when controlled for age and sex.

	Sign.	Odds ratio	95% CI OR: lower	95% CI OR: upper
Cl. GSDMD-pos. microglia lateral pyr. tracts	p = 0.172	1.086	0.965	1.224
Age at death	p = 0.862	1.007	0.934	1.085
Sex	p = 0.500	0.508	0.071	3.624

(12) Binary logistic regression addressing the differences between control and ALS cases regarding the anterior horn neuronal density, when controlled for age and sex.

	Sign.	Odds ratio	95% CI OR: lower	95% CI OR: upper
Anterior horn neuronal density	p = 0.017*	0.912	0.846	0.984
Age at death	p = 0.627	0.982	0.911	1.058
Sex	p = 0.725	0.703	0.099	4.991

Ch. II - Suppl. Table 4. Linear regression model for motor cortex neuronal density. Influence of predictor variables, i.e. the number of cleaved GSDMD-positive microglia in the precentral white matter, the number of caspase-1-positive microglia in the precentral white matter, and the percentage of pTDP-43 affected neurons in the motor cortex on motor cortex layer V neuronal density in different linear regression model terms as defined in parts 1 and 2. Age and sex were included in the model as potential confounders but were not statistically significant. * $p < 0.05$; ** $p < 0.01$.

Part 1

Predictor variable	Coefficient β	p value
% pTDP-43 affected neurons	-0.435	$p = 0.010^*$
Age	-0.252	$p = 0.124$
Gender	-0.003	$p = 0.983$

Dependent variable: Motor cortex layer V neuronal density

Predictor variable	Coefficient β	p value
CI GSDMD-positive microglia	-0.455	$p = 0.021^*$
Age	-0.190	$p = 0.315$
Sex	0.195	$p = 0.308$

Dependent variable: Motor cortex layer V neuronal density

Predictor variable	Coefficient β	p value
Caspase-1-positive microglia	-0.244	$p = 0.179$
Age	-0.220	$p = 0.217$
Sex	0.035	$p = 0.846$

Dependent variable: Motor cortex layer V neuronal density

Part 2

Predictor variable	Coefficient β	p value
CI GSDMD-positive microglia	-0.464	$p = 0.007^{**}$
% pTDP-43 affected neurons	-0.486	$p = 0.004^{**}$
Age	-0.248	$p = 0.134$
Sex	0.157	$p = 0.340$

Dependent variable: Motor cortex layer V neuronal density

Ch. II - Suppl. Table 5. Correlation matrix for spinal cord neuronal density and other parameters, corrected for age and sex. Matrix showing Pearson's correlation values and p-values for the association between spinal cord anterior horn neuronal density and other variables, including the number of caspase-1-positive microglia in the spinal cord lateral white matter tracts, the number of cleaved GSDMD-positive microglia in the spinal cord lateral white matter tracts, and the percentage of pTDP-43 affected neurons in the spinal cord. ** $p < 0.01$.

	Caspase-1-positive microglia	Cleaved GSDMD-positive microglia	% pTDP-43 affected neurons	Neuronal density	n
Caspase-1 positive microglia	-				23
Cleaved GSDMD-positive microglia	$r = -0.119; p = 0.571$	-			23
% pTDP-43 affected neurons	$r = -0.162; p = 0.439$	$r = 0.208; p = 0.318$	-		23
Neuronal density anterior horn	$r = -0.200; p = 0.337$	$r = 0.045; p = 0.832$	$r = -0.554; p = 0.004^{**}$	-	23

Ch. II - Suppl. Table 6. Correlation matrix for mouse spinal cord neuronal density and other parameters. Matrix showing Pearson's correlation values and p-values for the association between mouse spinal cord neuronal density and other variables, including the number of caspase-1-positive microglia, the number of GSDMD-positive microglia, and the percentage of TDP-43 nuclear clearance.

	Caspase-1-positive microglia	GSDMD-positive microglia	% TDP clearance	Neuronal density	n
Caspase-1-positive microglia	-				19
GSDMD-positive microglia	$r = 0.201; p = 0.410$	-			19
% TDP clearance	$r = -0.144; p = 0.556$	$r = 0.058; p = 0.815$	-		19
Neuronal density	$r = -0.146; p = 0.556$	$r = -0.392; p = 0.097$	$r = -0.174; p = 0.476$	-	19

CHAPTER III: Frontotemporal lobar degeneration case with an N-terminal *TUBA4A* mutation exhibits reduced TUBA4A levels in the brain and TDP-43 pathology

This chapter is based on the following publication as first author:

Frontotemporal Lobar Degeneration Case with an N-terminal *TUBA4A* mutation Exhibits Reduced TUBA4A Levels in the Brain and TDP-43 Pathology

Evelien Van Schoor (1,2,3), Mathieu Vandenbulcke (4), Valérie Bercier (2,3), Rik Vandenberghe (5,6), Julie van der Zee (7,8), Christine Van Broeckhoven (7,8), Markus Otto (9,10), Bernard Hanseeuw (11), Philip Van Damme (2,3,6), Ludo Van Den Bosch (2,3), Dietmar Rudolf Thal (1,12)

1. Laboratory of Neuropathology, Department of Imaging and Pathology, Leuven Brain Institute (LBI), KU Leuven (University of Leuven), 3000 Leuven, Belgium.
2. Laboratory of Neurobiology, Department of Neurosciences, Leuven Brain Institute (LBI), KU Leuven (University of Leuven), 3000 Leuven, Belgium.
3. Center for Brain & Disease Research, VIB, 3000 Leuven, Belgium.
4. Department of Geriatric Psychiatry, University Hospitals Leuven, 3000 Leuven, Belgium.
5. Laboratory of Cognitive Neurology, Department of Neurosciences, KU Leuven (University of Leuven), 3000 Leuven, Belgium.
6. Department of Neurology, University Hospitals Leuven, 3000 Leuven, Belgium.
7. Neurodegenerative Brain Diseases, Center for Molecular Neurology, VIB, 2610 Antwerp, Belgium.
8. Department of Biomedical Sciences, University of Antwerp, 2000 Antwerp, Belgium.
9. Department of Neurology, Ulm University, 89081 Ulm, Germany.
10. Department of Neurology, University Hospital Halle (Saale), Martin Luther University Halle-Wittenberg, 06108 Halle (Saale), Germany.
11. UC Louvain and Department of Neurology, Institute of Neurosciences, University Hospital Saint-Luc, 1200 Brussels, Belgium.
12. Department of Pathology, University Hospitals Leuven, 3000 Leuven, Belgium.

Corresponding authors: Evelien Van Schoor and Dietmar R. Thal

Biomolecules (2022) DOI: 10.3390/biom12030440

1. Abstract

Recently, disease-associated variants of the *TUBA4A* gene were identified in patients with amyotrophic lateral sclerosis (ALS) and frontotemporal dementia (FTD). Here, we present the neuropathological report of a patient with the semantic variant of primary progressive aphasia with a family history of Parkinsonism, harboring a novel frameshift mutation c.187del (p.Arg64Glyfs*90) in *TUBA4A*. Immunohistochemistry showed abundant TAR DNA-binding protein 43 kDa (TDP-43) dystrophic neurite pathology in the frontal and temporal cortex and the dentate gyrus of the hippocampus, consistent with frontotemporal lobar degeneration (FTLD). The observed pathology pattern fitted best with that of FTLD-TDP Type C. qPCR showed the presence of mutant *TUBA4A* mRNA. However, no truncated *TUBA4A* was detected at the protein level. A decrease in total *TUBA4A* mRNA and protein levels suggests loss-of-function as a potential pathogenic mechanism. This report strengthens the idea that N-terminal *TUBA4A* mutations are associated with FTLD-TDP. These N-terminal mutations possibly exert their pathogenic effects through haploinsufficiency, contrary to C-terminal *TUBA4A* mutations which are thought to disturb the microtubule network via a dominant-negative mechanism.

2. Introduction

Frontotemporal dementia (FTD) is a type of early-onset dementia characterized by atrophy of the frontal and temporal lobes. Clinical symptoms can present as behavioral changes, cognitive deficits and language dysfunction (47). Based on these clinical criteria, different phenotypes can be distinguished, including the behavioral variant (bvFTD), the nonfluent variant of primary progressive aphasia (nfPPA) and the semantic variant of primary progressive aphasia (svPPA) [2,3]. FTD can also co-exist with atypical parkinsonian disorders, such as progressive supranuclear palsy (PSP) and corticobasal syndrome (CBS), and with amyotrophic lateral sclerosis (ALS) (47). The pathology underlying FTD is referred to as frontotemporal lobar degeneration (FTLD), which can present as FTLD-TDP, FTLD-FUS or FTLD-tau, reflecting the protein that aggregates in affected brain regions (266). Up to 40% of FTD cases present with a family history of dementia or psychiatric illness, although only 10% can be explained by known gene mutations. The most frequently affected genes are *C9orf72*, *MAPT* and *GRN* (267). The *C9orf72* repeat expansion is the most common cause of FTD as well as ALS, stressing the overlap between both diseases. More recently, variants in other genes were identified in ALS/FTD patients, including variants in *TUBA4A* [6–8]. The *TUBA4A* gene encodes the alpha tubulin 4A protein, one of nine human α -tubulins, which polymerize with β -tubulin to form the structural subunits of microtubules. One of the major functions of microtubules in the central nervous system is the regulation of transport along the axon (185). *TUBA4A* is ubiquitously expressed in all cell types, but has its highest levels of expression in the brain. The expression of *TUBA4A* also increases over time,

possibly explaining why mutations in this gene cause advanced age disease phenotypes (186). Disease-associated variants of the *TUBA4A* gene were mainly identified in patients with familial ALS, some of whom had signs of cognitive impairment (183). Most of these mutations occur in the C-terminal end of the protein, which is important for its interaction with other tubulin subunits and associated proteins, such as kinesin (189). More recently, however, mutations in the N-terminal region of *TUBA4A* were observed in patients with FTD without motor neuron disease [7,12]. In this report, we present the neuropathological post-mortem analysis of an FTD patient presenting with the semantic variant (svPPA) and an R64Gfs*90 *TUBA4A* mutation, and suggest reduction of TUBA4A protein levels as a potential pathogenic mechanism.

3. Materials and methods

Human autopsy cases

Central nervous system (CNS) tissue was collected in the UZ Leuven brain biobank in accordance with the ethics review board upon written informed consent. Only autopsy of the brain with adjacent upper cervical spinal cord was granted. In addition to the FTLD-TDP case with the R64Gfs*90 *TUBA4A* mutation (case n° 1), four FTLD-TDP cases and six non-neurodegenerative controls were included in this study (Table S1, Supplementary Materials). For these four FTLD-TDP cases, genetic testing was performed for *TUBA4A*, *GRN*, *MAPT*, *VCP*, *TARDBP*, *FUS*, *SOD1*, *TBK1*, *PSEN1*, *PSEN2*, *APP*, and *C9orf72*, which was negative for cases 2, 3, and 4. One FTLD-TDP patient carried a *GRN* mutation (IVS1+5G>C; case n° 5) (Table S1, Supplementary Materials). The diagnosis of FTD was based on clinical assessment (45,46) and confirmed by ¹⁸F-FDG-PET and MRI (Figure 1). The diagnosis of FTLD-TDP was pathologically confirmed by assessment of the pTDP-43 pathology. The R64Gfs*90 *TUBA4A* mutation was identified by exonic sequencing as described in detail in Perrone et al. (194). Mutations in other ALS/FTD-related genes were excluded for this patient (case n° 1) (i.e., *C9orf72*, *MAPT*, *VCP*, *TARDBP*, *FUS*, *SOD1*, *TBK1*, *ATXN2*, *UBQLN2*, *SQSTM1*, and *TREM2*). For the control cases used in this study, genetic data were not available.

RT-qPCR

RNA was extracted from frontal cortex and temporal cortex of the R64Gfs*90 *TUBA4A* mutation case, and from frontal cortex of control cases ($n = 3$) using the RNeasy Mini Kit (Qiagen, Hilden, Germany). RNA integrity numbers (RIN) were determined using the Agilent 6000 Bioanalyzer Nano or Pico chip (Agilent Technologies, Santa Clara, CA, US). RIN values are shown in Table S1, Supplementary Materials. cDNA was generated using the GoScript™ Reverse Transcriptase kit (Promega, Madison, WI, US). cDNA was then used as template for qPCR using GoTaq Probe qPCR reagents (Promega, Madison,

WI, US). The qPCR was performed on the CFX96 RT system (Biorad, Hercules, CA, US) using a 96-well plate in technical triplicates. All signals were normalized to GAPDH (Integrated DNA Technologies, Leuven, Belgium). The $2^{-\Delta\Delta Ct}$ method was used to calculate the fold change of RNA level compared to control samples. The following primers were used for *TUBA4A*:

Forward *TUBA4A* primer: 5' GAC TCC TTC ACC ACC TTC TTC 3'

Reverse *TUBA4A* primer: 5' CGG ATC TCA TCA ATG ACC GTA G 3'

Two different locked nucleic acid (LNA) probes were used in combination and worked through competitive binding to distinguish the mutant from the wild-type *TUBA4A*:

Mutant LNA probe: 5' FAM/A+CG+T+A+C CC+G G/3IABkFQ 3'

Wild-type LNA probe: 5' HEX/CGT+A+C+C CC+G G/3IABkFQ 3'

Immunohistochemistry

Histological examination of the *TUBA4A* mutation case was performed on 5 μ m-thick sections cut from formalin-fixed, paraffin-embedded tissue of frontal cortex, cingulate gyrus, parietal cortex, temporal cortex, occipital cortex, hippocampus, entorhinal cortex, hypothalamus, basal ganglia, amygdala, thalamus, midbrain, pons, medulla oblongata, cerebellum, cervical spinal cord, and pre/postcentral cortex. Frontal and temporal cortex from sporadic FTLTDP type C cases and non-neurodegenerative controls were stained in parallel. pTDP-43 (1:5000, TIP-PTD-P02, Cosmo Bio, Tokyo, Japan) stainings were performed automatically by means of the BOND-MAX automated IHC/ISH Stainer (Leica Biosystems, Wetzlar, Germany) using the Bond Polymer Refine Detection kit (DS9800, Leica Biosystems, Wetzlar, Germany). Immunohistochemistry for C-t TDP-43 (1:1000, 12892-1-AP, Protein Tech, Manchester, UK), N-t TDP-43 (1:400, ARP38941_T100, Aviva Systems Biology, San Diego, CA, US), *TUBA4A* (1:100, AP13535b, Abgent, San Diego, CA, US) and CD68 (1:100, M0814, Dako, Agilent Technologies, Santa Clara, CA, US) was performed manually. Afterwards, hematoxylin counterstaining was performed in the Leica ST5010 Autostainer XL (Leica Biosystems, Wetzlar, Germany). To exclude Alzheimer's disease (AD), other tauopathies and Lewy Body Dementia (LBD) (230,231,268), the hippocampus, entorhinal cortex, and occipital cortex were immunostained with antibodies against A β (1:5000, 39220 clone 4G8, BioLegend, San Diego, CA, US) and phospho-tau (1:1000, clone AT8, Pierce-Endogen, Woburn, MA, US), and the medulla oblongata was immunostained using an antibody targeting α -synuclein (1:4000, clone 5G4, Millipore, Burlington, MA, US).

Immunofluorescence

Immunofluorescence double-labeling of 5 μ m sections of the frontal cortex of the R64Gfs*90 *TUBA4A* mutation case was performed for *TUBA4A* (1:100, AP13535b, Abgent, San Diego, CA, US) and TDP-43

(1:1000, 60019-2-Ig, Protein Tech, Manchester, UK), labeled with goat anti-rabbit Cy3 (1:100, 111-165-144, Jackson ImmunoResearch, West Grove, PA, US) and goat anti-mouse Cy2 (1:50, 115-225-146, Jackson ImmunoResearch, West Grove, PA, US). Slides were mounted using ProLong Gold Antifade Mountant (Thermo Fisher Scientific, Rockford, IL, US).

Protein Extraction

Human autopsy brains from the R64Gfs*90 *TUBA4A* mutation case, four FTLD-TDP cases, and five controls were used in this study. The right hemispheres were cut in approx. 1 cm slabs and frozen at -80°C . 50 mg of the brain tissue was weighed and mechanically homogenized in 0,5 mL 2% SDS in TBS (Tris-buffered saline) + Nuclease (Pierce™ Universal Nuclease, Thermo Fisher Scientific, Rockford, IL, US) + a cocktail of protease/phosphatase inhibitors (Halt, Thermo Fisher Scientific, Rockford, IL, US) using a micropestle. Samples were sonicated, followed by a centrifugation at $13,000\times g$ for 30 min. The resulting supernatant was used as the total fraction. Protein concentrations of the different fractions were determined using the Pierce BCA Protein Assay Kit (Thermo Fisher Scientific, Rockford, IL, US).

Western Blotting

Samples (10 μg) were loaded on a Bis-Tris 4–12% gradient SDS-PAGE (Invitrogen, Waltham, MA, US) and transferred to a nitrocellulose membrane (Semidry transfer, Biorad, Hercules, CA, US). Membranes were blocked with 5% milk. Primary antibodies were TUBA4A (1:10 000, ab228701, Abcam, Cambridge, UK and 1:8000, AP13535b, Abgent, San Diego, CA, US), N-t TUBA4A (1:1000, ab96743, Abcam, Cambridge, UK), and anti-HA-tag (1:1000, 3724, Cell Signaling, Danvers, MA, US). Secondary antibodies were goat anti-rabbit IgG-HRP and goat anti-mouse IgG-HRP (polyclonal, Dako, Agilent Technologies, Santa Clara, CA, US). The blots were developed with PICO plus ECL reagent (Thermo Fisher Scientific, Rockford, IL, US). Digital images were acquired using the Amersham Imager 600 (GE Healthcare, Chicago, IL, US). GAPDH (1:10,000, AM4300, Thermo Fisher Scientific, Rockford, IL, US) was used as a loading control. Band intensities were measured using ImageJ.

***TUBA4A* Constructs**

Human wild-type and W407* *TUBA4A* FLAG-tagged encoding plasmids were received from J. Landers (183). The W407* construct was used as a positive control, as this frameshift mutation is also predicted to lead to a truncated TUBA4A protein fragment. We introduced the R64Gfs*90 mutation in the wild-type *TUBA4A* plasmid by Gibson cloning using overlapping primers containing the c.187del to amplify the whole plasmid (forward primer: 5'-ACGTACCCGGGCAGTTTTTGTGGATCTGGAG-3'; reverse primer: 5'-ACTGCCCGGGTACGTGTTTTCCAGCACCAG-3'). A single clone was selected and correct insertion of the mutation (c.187del) was confirmed by sequencing. To produce mRNA, the plasmids were linearized

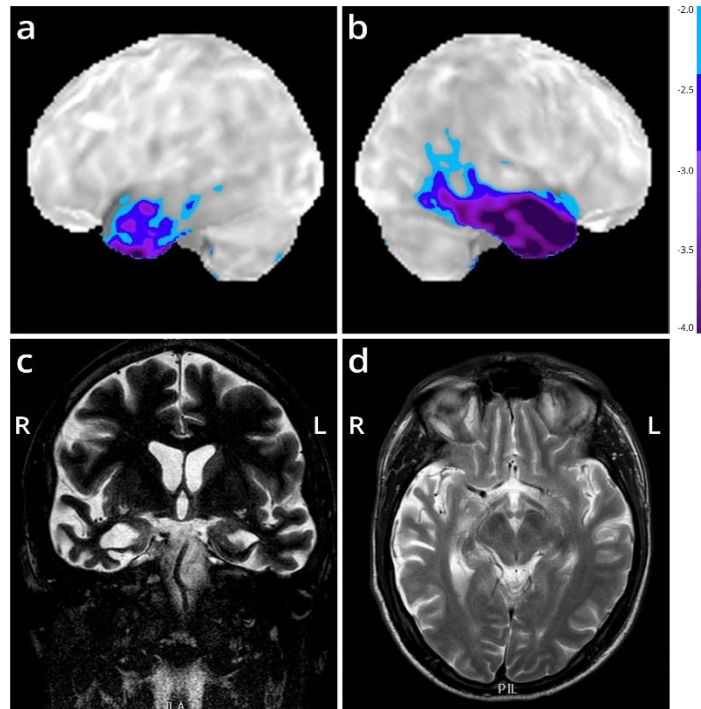
by restriction digestion, transcribed with mMESSAGE mMACHINE T7 kit (Ambion, Huntingdon, UK) and the resulting mRNA was purified with the MEGAclean Kit (Ambion, Huntingdon, UK). The mRNA concentration was measured by spectrophotometry (Nanodrop, Thermo Fisher Scientific, Rockford, IL, US). mRNA quality and length were verified by RNA gel electrophoresis.

Zebrafish Injections

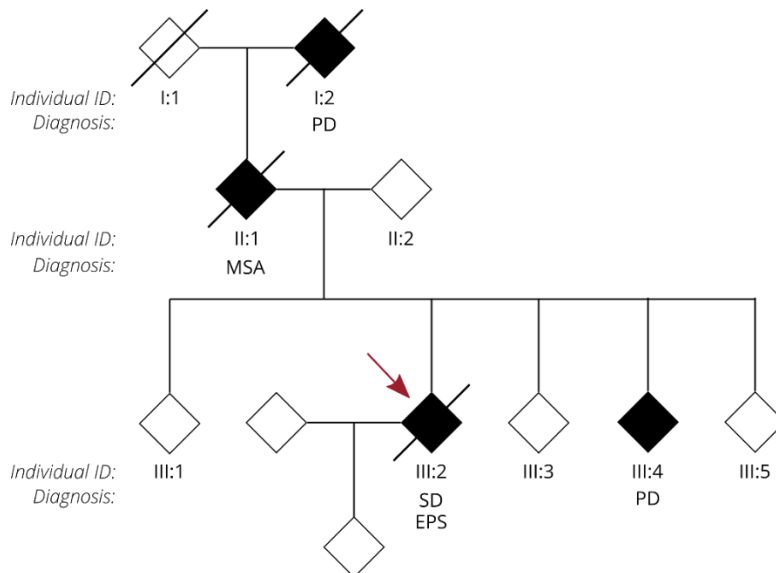
One- to two-cell-stage zebrafish embryos from the AB strain were injected in the yolk sac with 300 ng/ μ L of mRNA. Injected embryos were raised in embryo medium and kept in a 28.5 °C incubator. For western blotting, fish were manually dechorionated with forceps at 6 h post fertilization. Only morphologically normal embryos were retained and homogenized in RIPA buffer supplemented with protease and phosphatase inhibitors (Sigma-Aldrich, St. Louis, MO, US) using a micropestle on a hand-held rotor. After centrifugation (3 min, 10,000 \times *g* rpm), supernatant was collected and analyzed by western blotting.

4. Results

We present the autopsy case of a 60-year old man diagnosed at the age of 51 with the semantic variant of primary progressive aphasia. This was confirmed by MRI and 18 F-FDG-PET, showing bilateral anterior temporal atrophy, which was more right-sided, as well as hypometabolism (Figure 1). The patient showed prosopagnosia and problems with word retrieval and word comprehension. Later on, the patient also developed behavioral changes, such as obsessive-compulsive behavior, increased appetite with loss of table manners, discrete disinhibition, loss of decorum, and emotional indifference. Additionally, the patient displayed an inexhaustible glabellar reflex and extrapyramidal symptoms such as a discrete stooped posture and a decreased arm swing. The patient did not show any signs of motor neuron disease. There was a family history of Parkinsonism on the paternal side (Figure 2). The father of the patient (Figure 2, II:1) was diagnosed with multi system atrophy (Parkinsonian type). The paternal grandmother (Figure 2, I:2) suffered from Parkinson's disease since the age of 50. Additionally, a younger sibling of the patient was diagnosed with Parkinson's disease (Figure 2, III:4). Exonic sequencing of the semantic dementia patient (Figure 2, III:2, red arrow) revealed a novel frameshift mutation c.187del (p.Arg64Glyfs*90) in exon 2 of the *TUBA4A* gene, which was absent in control individuals and public databases as previously published. Mutations in other genes causative for ALS/FTD were excluded (i.e., *C9orf72*, *MAPT*, *VCP*, *TARDBP*, *FUS*, *SOD1*, *TBK1*, *ATXN2*, *UBQLN2*, *SQSTM1* and *TREM2*) (194). Genetic testing was not performed for any of the family members of the patient.



Ch. III - Figure 1. Imaging of the FTD patient with an R64Gfs*90 *TUBA4A* mutation. (a,b) Stereotactic surface projections showing lateral views of the left (a) and right (b) hemisphere of an ^{18}F -FDG-PET of the patient, with areas of significant decrease of glucose metabolism superimposed. The scan shows a regional decrease in glucose metabolism in the anterior temporal lobes, more pronounced to the right compared to the left. Color-coding refers to Z-scores with respect to a dataset of normal control subjects. (c,d) MRI (T2-weighted) at the level of the temporal lobe (coronal in (c); horizontal in (d)) shows temporal lobar degeneration typical for FTLD. L = left; R = right.

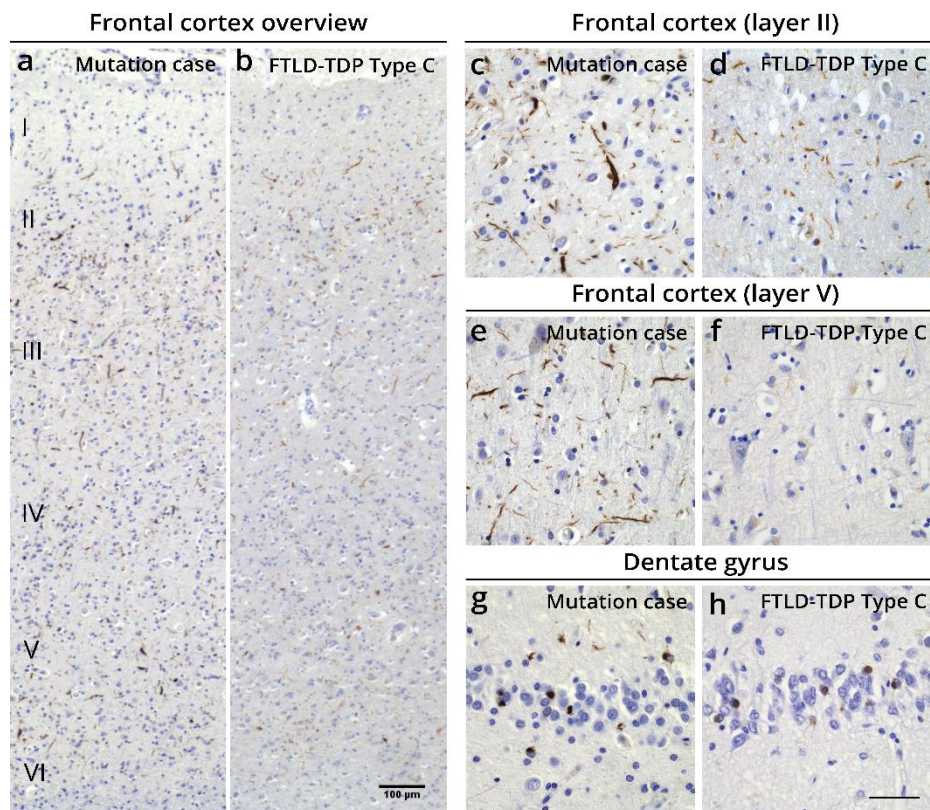


Ch. III - Figure 2. Pedigree of the family of the FTD patient with an R64Gfs*90 *TUBA4A* mutation. Diamond-shaped symbols were used for anonymity. Filled black symbols represent clinically affected patients. A diagonal line marks deceased patients. The individual ID and relevant clinical neurological diagnosis are mentioned for each patient. The FTD patient with an R64Gfs*90 *TUBA4A* mutation is indicated with a red arrow. PD = Parkinson's disease; MSA = multi system atrophy; SD = semantic dementia; EPS = extrapyramidal symptoms.

Autopsy was carried out in accordance with the UZ Leuven Ethics Committee with written informed consent. Frozen and formalin fixed tissue was stored in the UZ Leuven biobank. Macroscopically, the brain weighed 955 g and exhibited severe atrophy of the medial temporal lobe including the amygdala, enlarged ventricles and mild atherosclerosis of the circle of Willis. Microscopically, the presence of phosphorylated transactive response DNA-binding protein 43 kDa (pTDP-43)-positive dystrophic neurites and cytoplasmic inclusions in the frontal and temporal cortex confirmed the pathological diagnosis of frontotemporal lobar degeneration (FTLD), more specifically FTLD-TDP (25). Additionally, neurofibrillary tangle (NFT) pathology (Braak-NFT stage I) (269) and amyloid plaques (A β phase I) (270) were present, indicative for an early stage of preclinical Alzheimer's disease (AD) pathology. Precentral cortex pTDP-43 pathology was scarce, while the cervical spinal cord did not show any pTDP-43-positive lesions. Moderate microglia activation was present in pyramidal tracts in the medulla oblongata and precentral cortex as observed in CD68-stained sections. In the medulla oblongata, the degree of microglia activation was similar in all subregions and not accentuated in motor areas. No obvious pyramidal tract degeneration was detected in H&E stained sections. These observations suggest that the patient did not have apparent preclinical motor neuron disease. α -synuclein lesions were not detected. Extracellular melanin was observed in the substantia nigra. Mild cerebral amyloid angiopathy without capillary involvement was present, but no brain infarct or bleedings were observed.

In detail, immunohistochemistry (IHC) showed abundant pTDP-43 pathology primarily in the frontal and temporal cortex and the dentate gyrus of the hippocampus, consistent with FTLD-TDP. pTDP-43 pathology was widespread and reached the occipital cortex. The cerebellum and cervical spinal cord were devoid of pTDP-43 pathology (Table S2, Supplementary Materials). The observed pTDP-43 pathology consisted of abundant long thin, but also long and short thick dystrophic neurites and few cytoplasmic inclusions in all layers of the frontal and temporal cortex, with more prominent pathology in layers II and V (Figure 3a–h and Figure S1a, Supplementary Materials). This was also observed in the parietal and occipital cortex (Figure S1a, Supplementary Materials). The R64Gfs*90 *TUBA4A* mutation case showed more dystrophic neurites in the deeper layers of the frontal and temporal cortex and in the dentate gyrus, compared to typical FTLD-TDP Type C cases (Figure 3a–h; Figure S2, Supplementary Materials) [19,20]. No intranuclear inclusions were observed. The white matter was virtually free of pTDP-43 pathology. Antibodies against the C- and N-terminus of TDP-43 confirmed the pattern of pTDP-43 pathology, indicating that the majority of the lesions consisted of phosphorylated and non-phosphorylated full-length TDP-43 (Figure S1b, Supplementary Materials). Accordingly, this R64Gfs*90 *TUBA4A* mutation case fits best with the FTLD-TDP Type C pattern (Figure S2, Supplementary Materials) [6,7], because of the presence of abundant dystrophic neurites of various length and

thickness and few neuronal cytoplasmic inclusions both in the superficial and deep layers of the cortex, and the clinical diagnosis of semantic dementia. Of notice, the substantial layer V pathology as seen in this case is not characteristic of FTLD-TDP Type C.



Ch. III - Figure 3. Histopathological characterization of the FTLD-TDP case with an R64Gfs*90 *TUBA4A* mutation. (a–h) pTDP-43 pathology is spread over all layers of the frontal cortex in the R64Gfs*90 *TUBA4A* mutation case, whereas in a typical FTLD-TDP type C case predominantly the second layer is affected (a,b). pTDP-43 pathology in the R64Gfs*90 *TUBA4A* mutation case mainly consists of dystrophic neurites of various length and thickness, and few neuronal cytoplasmic inclusions in the frontal cortex (layers II and V depicted; (c–f)). The dentate gyrus shows typical pTDP-43-positive cytoplasmic inclusions (g,h). Scale bars represent 100 μ m (a,b) and 50 μ m (c–h).

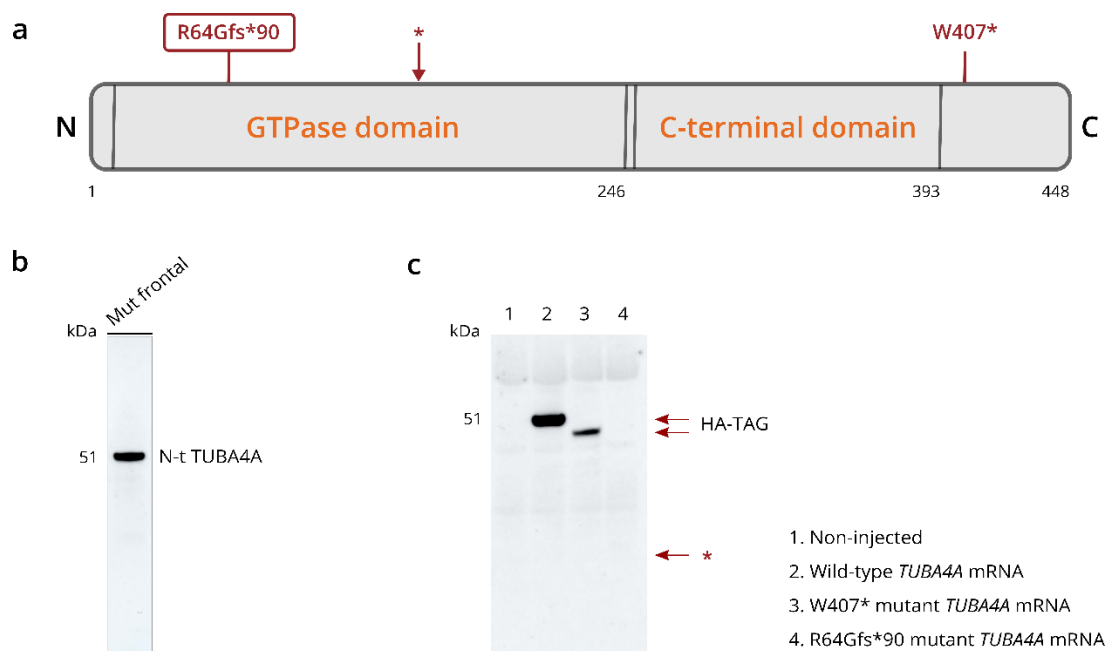
Next, we evaluated whether the R64Gfs*90 *TUBA4A* mutation was associated with changes in TUBA4A protein expression and distribution in the brain of the patient. TUBA4A IHC of the frontal and temporal cortex showed an altered neurite architecture (Figure S3a–c, Supplementary Materials). These thick neurites positive for TUBA4A did not co-localize with pTDP-43 dystrophic neurites (Figure S3d–f, Supplementary Materials). No TUBA4A aggregates were identified.

qPCR analysis using competitive probes against the WT (wild-type) and R64Gfs*90 mutant *TUBA4A* showed the presence of mutant *TUBA4A* RNA in the R64Gfs*90 *TUBA4A* mutation case (Table 1). As the R64Gfs*90 *TUBA4A* mutation leads to a premature termination codon in exon 4, 90 amino acids from the frameshift, a fragmented protein product could be expected around 17 kDa (Figure 4a; arrow). However, western blot analysis on R64Gfs*90 *TUBA4A* mutation case brain lysates using an

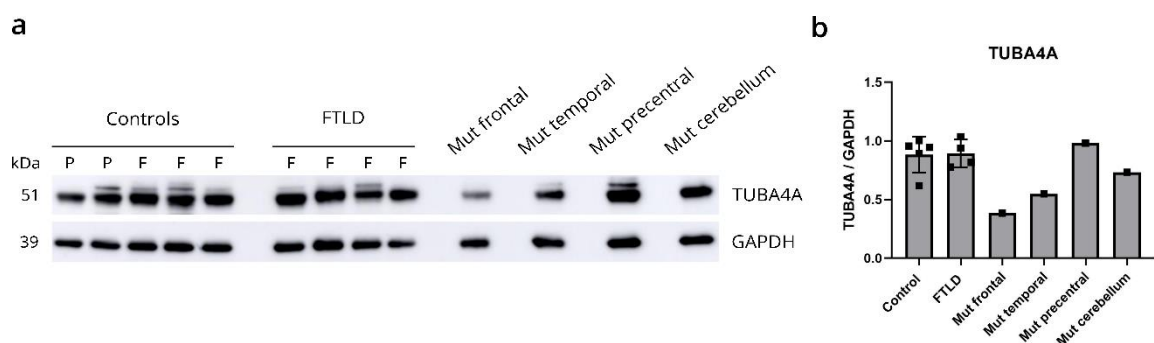
antibody directed against the N-terminal part of the TUBA4A protein did not reveal any TUBA4A fragment produced by the frameshift mutation (Figure 4b). This suggests that the mutant R64Gfs*90 *TUBA4A* is degraded at the RNA or protein level. This was confirmed by the injection of the R64Gfs*90 mutant *TUBA4A* mRNA in zebrafish embryos, showing absence of a TUBA4A fragment on western blot, in contrast to wild-type and W407* mutant TUBA4A (Figure 4c). Furthermore, qPCR analysis showed a reduction in WT *TUBA4A* mRNA compared to control cases, which can be expected from a frameshift mutation (Table 1). This was reflected at the protein level, as the total level of TUBA4A was decreased in affected brain regions of the R64Gfs*90 *TUBA4A* mutation case compared to control and other FTLD-TDP cases (Figure 5a,b).

Ch. III - Table 1. *TUBA4A* RNA levels. Fold change of R64Gfs*90 mutant *TUBA4A* and WT (wild-type) *TUBA4A* RNA levels compared to control samples ($n = 3$) and relative to GAPDH for the frontal and temporal cortex of the R64Gfs*90 *TUBA4A* mutation case. Probes were used in combination and worked through competitive inhibition. Fc = frontal cortex, Tc = temporal cortex.

	R64Gfs*90 Case Fc	R64Gfs*90 Case Tc
Mutant TUBA4A	2.29	4.78
WT TUBA4A	0.24	0.51



Ch. III - Figure 4. R64Gfs*90 *TUBA4A* mutation does not give rise to a mutant protein fragment. (a) Schematic overview of the TUBA4A protein structure indicating the location of the R64Gfs*90 and W407* mutations. The asterisk indicates the location of the early stop codon after amino acid 154 due to the R64Gfs*90 frameshift. The predicted molecular weight of the protein fragment is 16.8 kDa. (b) Western blot on the total fraction of the frontal cortex of the R64Gfs*90 *TUBA4A* mutation case using an antibody directed against the N-terminal part of TUBA4A, indicating that there was no truncated TUBA4A protein product present. (c) Western blot using an anti-HA-tag antibody on zebrafish lysates at 6 h post fertilization after the injection of wild-type, R64Gfs*90 or W407* mutant *TUBA4A* mRNA. No R64Gfs*90 TUBA4A protein fragment could be detected around 16.8 kD (asterisk), while the W407* shortened protein product was present. N = N-terminus; C = C-terminus.



Ch. III - Figure 5. R64Gfs*90 *TUBA4A* mutation causes reduction in levels of wild-type *TUBA4A* protein. (a) Biochemical analysis of the total *TUBA4A* expression levels in control cases (F = frontal, P = precentral cortex), FTLD-TDP patients (F = frontal cortex) and different brain regions of the R64Gfs*90 *TUBA4A* mutation case (frontal cortex, temporal cortex, precentral cortex and cerebellum). (b) Quantification relative to GAPDH shows decreased *TUBA4A* protein expression in affected brain regions in the R64Gfs*90 *TUBA4A* mutation case. Each data point represents a single patient.

5. Discussion

In this study, we performed a neuropathological *post-mortem* analysis on a patient with an R64Gfs*90 *TUBA4A* mutation presenting with svPPA and underlying FTLD-TDP, without a motor neuron phenotype. Histopathological and biochemical analysis of frontal and temporal cortex fitted best with FTLD-TDP Type C, with prominent pTDP-43 lesions even in the deeper cortical layers. Western blot analysis did not show a *TUBA4A* protein fragment, which was confirmed by the injection of R64Gfs*90 *TUBA4A* mRNA in zebrafish. In contrast, injection of another ALS-related frameshift *TUBA4A* mutation (W407*) led to the production of a shortened protein product. On the other hand, we observed a reduction in wild-type *TUBA4A* mRNA as well as full-length *TUBA4A* protein levels in the R64Gfs*90 *TUBA4A* patient, pointing towards haploinsufficiency as a possible underlying pathogenic mechanism. However, we cannot fully exclude the possibility that a shortened *TUBA4A* protein product was not picked up by the *TUBA4A* N-terminal antibody used in the study, although in theory it should detect the conserved epitope upstream of the mutation located at amino acid 64.

Axonal transport defects have recently been reported to be involved in several neurodegenerative disorders [21–25]. Apart from microtubules consisting of α - and β -tubulin, motor proteins such as kinesin and dynein are also important players as they move cargoes along the microtubule scaffold and contribute to cytoskeleton stability and maintenance. In addition to *TUBA4A*, genetic mutations in motor proteins (e.g., *KIF5A*, *DCTN1*) have also been associated with ALS, further strengthening the hypothesis that alterations in proteins with an important function in cytoskeleton structure and dynamics are of major importance in ALS pathobiology [21,26]. Importantly, *TUBA4A*, unlike most

other α -tubulin isoforms, does not contain a C-terminal tyrosine residue. In α -tubulin, this final tyrosine can be added or removed through the detyrosination-tyrosination cycle [27,28]. Detyrosination was shown to increase microtubule stability and is highly abundant in the axonal compartment. This suggests that sufficient expression of *TUBA4A* in the brain might be important for the formation of stable microtubules, such as in axons in neurons (185).

In 2014, several variants were identified in the C-terminal part of the *TUBA4A* gene in a cohort of ALS patients. These variants were reported to lead to classical spinal onset ALS, with, in some cases, FTD-like symptoms (183). The C-terminal region of α -tubulin is important in its interaction with β -tubulin and microtubule-associated proteins (MAPs), such as dynein and kinesin (190). Smith and colleagues showed that these ALS-related variants ineffectively formed tubulin dimers *in vitro*, and that they exhibited a decreased incorporation into protofilaments, possibly interfering with the microtubule network through a dominant-negative mechanism (183).

More recently, Mol *et al.*, described another *TUBA4A* variant (R105C) in a family with different forms of dementia, among which bvFTD with prominent disinhibited behavior and parkinsonian-like gait disturbances (195). One family member displayed unspecified dementia and comorbid Parkinsonism, and another relative was clinically diagnosed with Parkinson's disease. None of the patients displayed ALS-like symptoms. *Post-mortem* analysis of two bvFTD cases showed decreased *TUBA4A* protein levels in the brain (195), which is in line with what we observed in the R64Gfs*90 *TUBA4A* patient presented in this paper. Another group reported a nonsense R79X *TUBA4A* mutation in a patient with Parkinson syndrome and nigro-pathy. Both siblings were also affected. They did not detect any R79X *TUBA4A* protein fragment and therefore suggested haploinsufficiency as a potential mechanism, although a decrease in full-length *TUBA4A* protein levels was not investigated in this patient (196).

Of notice, both the R105C (195) and R79X (196) *TUBA4A* mutations, as well as the R64Gfs*90 *TUBA4A* frameshift mutation reported here, localize in the N-terminal part of the *TUBA4A* gene (Figure 4a). The N-terminus is mainly important in protein folding and conformation (195). However, mutations described in the N-terminal region of *TUBA4A* most likely act through a loss-of-function mechanism, as we and others showed that patients with these N-terminal *TUBA4A* mutations display a reduction in *TUBA4A* protein expression. Interestingly, the father and grandmother of the patient described here presented with multiple system atrophy (MSA) and Parkinson's disease, and the R64Gfs*90 *TUBA4A* patient exhibited an inexhaustible glabellar reflex and stooped posture with decreased arm swing. TDP-43 pathology was observed in the caudate nucleus, putamen and globus pallidus of the R64Gfs*90 *TUBA4A* patient, indicating an involvement of the nigro-striatal system without a direct impact on the substantia nigra. Given the lack of α -synuclein pathology in our patient, extrapyramidal Parkinson

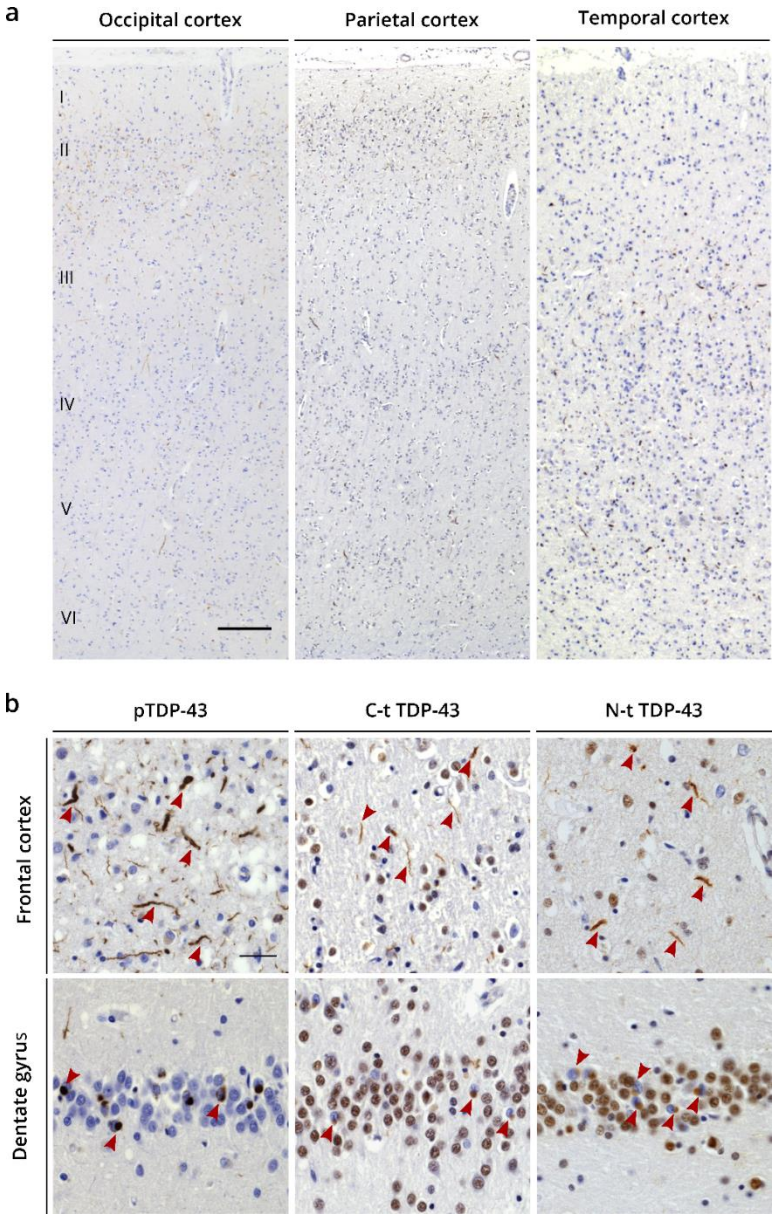
symptoms such as stooped posture and decreased arm swing may mainly be related to the affection of the nigro-striatal system by TDP-43 pathology. This further supports the notion that variants in the N-terminal region of *TUBA4A* are more likely to be associated with FTD with extrapyramidal Parkinson-like symptoms, possibly exerting its pathogenic effects through a reduction in TUBA4A, whereas variants in the C-terminal region have mainly been associated with ALS, likely disrupting the microtubule network through a dominant-negative mechanism (183). However, it remains unknown if these *TUBA4A* mutations are sufficient to develop ALS and/or FTD. Therefore, further studies assessing the impact of these mutations in different cell types *in vitro* and *in vivo* will help shed light on the pathogenicity and downstream effects, as well as on the selective vulnerability of neuronal populations.

Remarkably, some reports also showed downregulation of TUBA4A protein levels in familial as well as sporadic ALS patients in the absence of *TUBA4A* mutations, suggesting that alterations in the expression of *TUBA4A* could be of importance in sporadic ALS disease pathogenesis as well [31–33]. Helderich and colleagues described an miR-1825/*TBCB/TUBA4A* pathway, demonstrating that the reduced expression of an upstream miRNA can lead to a reduction in TUBA4A protein expression in ALS patients (197). Future models for mutant and downregulated TUBA4A are needed to better understand its mechanistic role in ALS and FTLD.

6. Conclusions

In conclusion, this report supports the importance of N-terminal *TUBA4A* mutations in FTLD-TDP without ALS-like symptoms. We and other groups observed reduced TUBA4A protein levels in affected FTLD-TDP patients, pointing towards *TUBA4A* haploinsufficiency as a potential pathogenic mechanism. Functional studies will be essential in the further elucidation of the pathogenic mechanism of both C- and N-terminal *TUBA4A* mutations. Overall, these results further emphasize the important role of cytoskeletal defects in FTLD and ALS pathobiology.

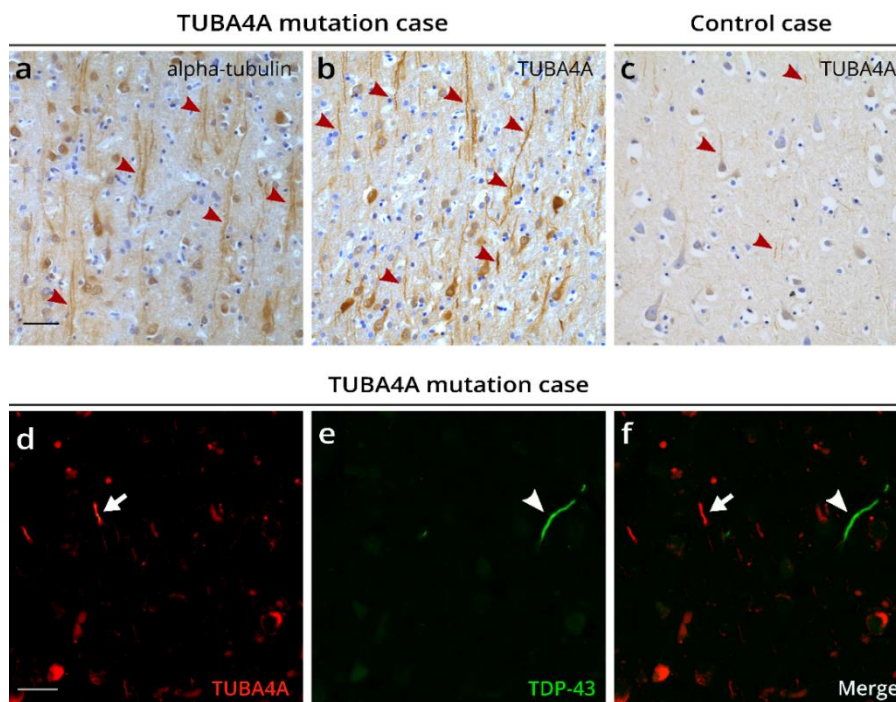
7. Supplementary information



Ch. III - Suppl. Figure 1. TDP-43 pathology in the FTLD-TDP case with an R64Gfs*90 *TUBA4A* mutation. (a) pTDP-43 pathology is spread throughout all layers of the occipital and parietal cortex and the temporal cortex of the R64Gfs*90 *TUBA4A* mutation case. **(b)** pTDP-43 lesions in the dentate gyrus and frontal cortex (layer II) of the R64Gfs*90 *TUBA4A* mutation case are immunopositive for N-t TDP-43 and C-t TDP-43 antibodies (arrowheads). Scale bars represent 200 μm (a) and 15 μm (b).

	Type A	Type B	Type C	Type D	Type E	<i>TUBA4A</i> FTLD case
I						
II						
III						
IV						
V						
VI						
WM						

Ch. III - Suppl. Figure 2. Schematic overview of the FTLD-TDP pathology pattern. This scheme provides an overview of the FTLD-TDP types that have been described previously. The pattern of the R64Gfs*90 *TUBA4A* mutation case fits best with FTLD-TDP Type C. Pathological lesions mainly consisting of dystrophic neurites were observed throughout all layers of the cortex and were absent in the white matter.



Ch. III - Suppl. Figure 3. TUBA4A immunohistochemical analysis. (a-c) Antibodies against alpha-tubulin (a) and TUBA4A (b) show a divergent staining in the R64Gfs*90 *TUBA4A* mutation case with abnormal kinking of apical dendrites (arrows in a, b) compared to control cases (arrows in c) in the frontal cortex (layer V). (d-f) TUBA4A thickened neurites (arrow) and TDP-43 dystrophic neurites (arrowhead) do not co-localize in the frontal cortex (layer V) of the R64Gfs*90 *TUBA4A* mutation case. Scale bars represent 50 μm.

Ch. III - Suppl. Table 1. Overview of the autopsy cases used for indicated experiments. The table provides information regarding age (= age at death), sex, diagnosis, the presence of a genetic mutation, Braak NFT stage, A β MTL phase, Braak LBD stage, PMI (hours) and RIN values. Case 1 is the R64Gfs*90 *TUBA4A* mutation case. Control = non-neurodegenerative control, PMI = *post-mortem* interval, RIN = RNA integrity number, IHC = immunohistochemistry, WB = western blot, n.a. = not applicable.

Case n°	Age	Sex	Diagnosis	Genetic mutation	Braak NFT stage	A β MTL phase	Braak LBD stage	PMI	RIN	IHC/WB/qPCR
1	60	m	FTLD-TDP Type C-like	<i>TUBA4A</i> <i>R64Gfs*90</i>	1	1	0	12h	4,5	IHC, WB, qPCR
2	69	f	FTLD-TDP Type C	no	1	0	0	24h	-	IHC, WB
3	62	f	FTLD-TDP Type C	no	0,5	0	0	12h	-	IHC, WB
4	79	m	FTLD-TDP Type B	no	1	0	0	24h	-	WB
5	64	f	FTLD-TDP Type A	<i>GRN</i> <i>IVS1+5G>C</i>	1	0	0	24h	-	WB
6	35	m	Control	n.a.	0	0	0	72h	-	WB
7	74	m	Control	n.a.	0	0	0	72h	-	WB
8	55	m	Control	n.a.	0	0	0	96h	-	WB
9	61	m	Control	n.a.	0	0	0	48h	6,6	WB, qPCR
10	54	m	Control	n.a.	1	0	0	24h	6,2	WB, qPCR
11	74	f	Control	n.a.	1	0	0	24h	6,5	IHC, qPCR

Ch. III - Suppl. Table 2. Overview of the central nervous system regions of the R64Gfs*90 *TUBA4A* mutation case positive (+) or negative (-) for pTDP-43 pathological lesions.

Frontal cortex	+	Thalamus	+
Precentral cortex	+	Basal nucleus of Meynert	-
Postcentral cortex	+	Amygdala	+
Parietal cortex	+	Midbrain - substantia nigra	-
Temporal cortex	+	Midbrain - red nucleus	-
Occipital cortex	+	Midbrain - formatio reticularis	+
Cingulate cortex	+	Midbrain - central gray matter	-
Entorhinal cortex	+	Midbrain - colliculi inferior	+
Hippocampus – CA region	+	Midbrain - raphe nuclei	-
Dentate gyrus	+	Pons - nuclei pontis	+
Subiculum	+	Pons - locus coeruleus	-
Insular cortex	+	Pons - parabrachial nucleus	-
Basal ganglia - caudate nucleus	+	Medulla - vagal nerve nucleus	-
Basal ganglia - claustrum	+	Medulla - inferior olivary nucleus	-
Basal ganglia - globus pallidus	+	Medulla - hypoglossal nucleus	-
Basal ganglia - putamen	+	Cerebellum	-
Hypothalamus	+	Cervical spinal cord	-

CHAPTER IV: *TUBA4A* downregulation as observed in ALS *post-mortem* motor cortex causes ALS-related abnormalities in zebrafish

This chapter is based on the following article in preparation:

***TUBA4A* downregulation as observed in ALS *post-mortem* motor cortex causes ALS-related abnormalities in zebrafish**

Evelien Van Schoor (1,2,3), Valérie Bercier (2,3), Elke Braems (2,3), Jochen Weishaupt (4), Albert C. Ludolph (4,5), Philip Van Damme (2,3,6), Dietmar Rudolf Thal* (1,7), Ludo Van Den Bosch* (2,3)

1. Laboratory of Neuropathology, Department of Imaging and Pathology, Leuven Brain Institute (LBI), KU Leuven (University of Leuven), Leuven, Belgium.
2. Laboratory of Neurobiology, Department of Neurosciences, Leuven Brain Institute (LBI), KU Leuven (University of Leuven), Leuven, Belgium.
3. Center for Brain & Disease Research, VIB, Leuven, Belgium.
4. Department of Neurology, Ulm University, Ulm, Germany.
5. Deutsches Zentrum für Neurodegenerative Erkrankungen, Ulm, Germany.
6. Department of Neurology, University Hospitals Leuven, Leuven, Belgium.
7. Department of Pathology, University Hospitals Leuven, Leuven, Belgium.

* Shared last authorship

Corresponding authors: Evelien Van Schoor and Ludo Van Den Bosch

1. Abstract

Disease-associated variants of *TUBA4A* (alpha-tubulin 4A) have recently been identified in familial ALS. Interestingly, a downregulation of TUBA4A protein expression was observed in familial as well as sporadic ALS brain tissue. To investigate whether a decreased TUBA4A expression could be a driving factor in ALS pathogenesis, we assessed whether *TUBA4A* knockdown in zebrafish could recapitulate an ALS-like phenotype. For this, we injected an antisense oligonucleotide morpholino in zebrafish embryos targeting the zebrafish *TUBA4A* orthologue. An antibody against synaptic vesicle 2 was used to visualize motor axons in the spinal cord, allowing the analysis of embryonic ventral root projections. Motor behavior was assessed using the touch-evoked escape response. In *post-mortem* ALS motor cortex, we observed reduced TUBA4A levels. The knockdown of the zebrafish *TUBA4A* orthologue induced a motor axonopathy and a significantly disturbed motor behavior. Both phenotypes were dose-dependent and could be rescued by the addition of human wild-type *TUBA4A* mRNA. Thus, *TUBA4A* downregulation as observed in ALS *post-mortem* motor cortex could be modeled in zebrafish and induced a motor axonopathy and motor behavior defects reflecting a motor neuron disease phenotype, as previously described in embryonic zebrafish models of ALS. The rescue with human wild-type *TUBA4A* mRNA suggests functional conservation and strengthens the causal relation between TUBA4A protein levels and phenotype severity. Our data unveil an important role for *TUBA4A* in ALS pathogenesis, and extend the relevance of *TUBA4A* to the majority of ALS patients, in addition to cases bearing *TUBA4A* mutations.

2. Introduction

Amyotrophic lateral sclerosis (ALS) is a fatal neurodegenerative disorder characterized by progressive paralysis resulting from the selective loss of upper and lower motor neurons. Patients usually die 2-5 years after disease onset due to respiratory failure. ALS has an incidence of 1-2 individuals per 100.000 each year. About 90% of patients display sporadic ALS, with no family history of the disease. In the remaining 10% the disease is transmitted within families, referred to as familial ALS (3). The most common disease-causing mutations are found in fused in sarcoma (*FUS*), superoxide dismutase 1 (*SOD1*), chromosome 9 open reading frame 72 (*C9orf72*) and transactive response DNA-binding protein (*TARDBP*) (3,6).

In addition, several genes with a role in cytoskeletal dynamics and axonal transport are linked to ALS, amongst which dynactin subunit 1 (*DCTN1*), kinesin family member 5A (*KIF5A*) and spastin (*SPAST*) (23). This suggests that there might be a direct causative relationship between defects in cytoskeletal integrity and neurodegeneration. More recently, Smith *et al.* found mutated variants in the alpha-tubulin 4A (*TUBA4A*) gene in ALS patients, based on exome sequencing data from a large cohort of ALS

patients and controls. These mutated variants are associated with classical spinal onset ALS, and in some cases also frontotemporal dementia (FTD)-like symptoms (183). We confirmed the importance of *TUBA4A* variants in ALS in an independent Belgian cohort (194).

TUBA4A encodes one of nine known α -tubulin isoforms, with all variants expressed from different genes. The structures of α - and β -tubulin are highly conserved throughout eukaryotes. Nevertheless, the range of human diseases associated with mutations in different tubulin isoforms indicates that specific isoforms have different functional specifications (185). In addition, the expression of different isoforms differs depending on cell type and tissue. For example, *TUBA8A* is predominantly expressed in testes and skeletal muscle, while *TUBA4A* is highly expressed in the nervous system (185,186).

Functionally, α -tubulin assembles with β -tubulin to form stable tubulin heterodimers, which dynamically polymerize into sheets of longitudinal polarized protofilaments, building the cylindrical, hollow microtubules (189,193). Stable microtubules are important for a wide range of functions in long extending axons, and serve as the tracks along which motor proteins (such as dynein and kinesin), with the help of adaptor proteins, move cargoes (186).

Motor neurons are the most asymmetric cells in nature with axons reaching a meter in length in humans. Therefore, they have a crucial requirement for proper cytoskeletal functioning. A disruption of cytoskeleton integrity could affect cell morphology, axonal branching, the establishment of neuromuscular junctions, and many other critical cell functions. In addition, it could prevent molecular motors from transporting the necessary cargoes, with a potentially deleterious effect on neuronal function (3,23,186). Interestingly, it was proposed that sporadic ALS patients display a downregulation of α -tubulin subunits in affected brain regions (197,198,271). However, whether these alterations in α -tubulin expression in the majority of ALS patients can also drive ALS disease pathogenesis is still unknown.

In this study, we confirmed a decrease in *TUBA4A* protein expression in *post-mortem* tissue from ALS patients compared to controls. Mimicking this decrease in zebrafish using antisense oligonucleotide morpholinos (AMO) directed against *tuba8l2* (ENSDARG00000031164) (272), the single zebrafish orthologue for *TUBA4A*, which is 94% conserved at the protein level. This led to abnormalities in the axons of spinal cord motor neurons, as well as motor behavior deficits. Both phenotypes were dose-dependent and could be rescued by the addition of human wild-type *TUBA4A* mRNA. Our data point towards a central role of *TUBA4A* in ALS pathogenesis, aside from cases bearing *TUBA4A* mutations.

3. Materials and methods

Human autopsy cases

Brain and spinal cord tissues were collected in accordance with the applicable laws in Belgium (UZ Leuven) and Germany (Ulm). The recruitment protocols for collecting the brains were approved by the ethical committees of the University of Ulm (Germany) and UZ Leuven (Belgium). This study was approved by the UZ Leuven ethical committee (Belgium) (S60803, S55312). Tissues were collected with an average *post-mortem* interval of 45 h. After autopsy, the right hemisphere was dissected in coronal planes and frozen at -80°C. The left hemisphere was fixed in 4% phosphate-buffered formaldehyde (PFA) (F8775, Sigma-Aldrich, St Louis, MO, US). Ten sporadic ALS cases and twelve non-neurodegenerative controls were included in this study (Suppl. Table 1). The diagnosis of ALS was based on clinical assessment according to the consensus criteria for ALS (7,8,229). Autopsy cases were not all evaluated for possible *TUBA4A* mutations due to the very low prevalence in ALS (194). The *post-mortem* diagnosis of ALS was pathologically confirmed by assessment of the pTDP-43 pathology. Braak NFT stage (230) and A β MTL phase (231) were determined based on immunohistochemical stainings with antibodies against A β and p-tau (Suppl. Table 2).

Human tissue immunohistochemistry

Histological examination was performed on 5 μ m thick sections cut from formalin-fixed, paraffin-embedded tissue of frontal, pre- and postcentral and temporal cortex, hippocampus and spinal cord. Sections were stained with antibodies against pTDP-43, TUBA4A, pTau^(S202/T205) and A β ₁₇₋₂₄ (Suppl. Table 2). Stainings were performed with the BOND-MAX automated IHC/ISH Stainer (Leica Biosystems, Wetzlar, Germany) using the Bond Polymer Refine Detection kit (DS9800, Leica Biosystems). Briefly, slides were deparaffinized and epitopes were retrieved with low or high pH buffer. After incubation with Peroxidase-Blocking Reagent (DS9800, Leica Biosystems), slides were incubated with primary antibodies for 30 min, followed by secondary antibody incubation. DAB was used for visualization, followed by counterstaining with hematoxylin. Dehydration was carried out in an autostainer, followed by mounting in an automated cover-slipper (Leica Biosystems). Images were acquired using the Leica DM2000 LED microscope coupled to a Leica DFC 7000 T camera. Images were processed using ImageJ and combined into figures using Inkscape.

Human tissue protein extraction

For biochemistry of human tissues, the right hemispheres were cut in approx. 1 cm thick slabs and frozen at -80°C. Fifty mg of motor cortex and spinal cord was weighed and mechanically homogenized in 0.5 ml 2% SDS in TBS (Tris-buffered saline) with Nuclease (88701, Pierce™ Universal Nuclease, Thermo Fisher Scientific) and a cocktail of protease/phosphatase inhibitors (78440, Halt, Thermo

Fisher Scientific) using a micropestle (CXH7.1, Carl Roth, Karlsruhe, Germany). Samples were sonicated, followed by a centrifugation at 13 000 *g* for 30 min. The resulting supernatant was used. Protein concentrations were determined using the Pierce BCA Protein Assay Kit (23225, Thermo Fisher Scientific).

Human tissue and zebrafish western blotting

For western blotting, 10 µg (human central nervous system lysates) or 20 µg (zebrafish lysates) of protein was loaded on a Bis-Tris 4-12% gradient SDS-PAGE (WG1402BOX, Invitrogen, Thermo Fisher Scientific) in MOPS-SDS running buffer (J62847.K2, Alfa Aesar, Haverhill, MA, USA), electrophoresed at 150 V for 60 min, and transferred to a nitrocellulose membrane (GE10600001, Semidry transfer, Biorad, Hercules, CA, USA). Membranes were blocked with 5% non-fat dried milk (A0830.1000, AppliChem, Darmstadt, Germany) in phosphate-buffered saline (PBS) 0.1% Tween-20 (PBST). Primary antibodies and the corresponding dilutions are listed in Suppl. Table 2. Secondary antibodies were goat anti-rabbit IgG-HRP or goat anti-mouse IgG-HRP (1:10 000, P044801-2 and P044701-2, polyclonal, Dako). Blots were developed with SuperSignal West Pico or Dura plus ECL reagent (34580 and 34075, Thermo Fisher Scientific). Digital images were acquired using the Amersham Imager 600 (GE Healthcare, Chicago, IL, USA). All blots were stripped (21063, Restore Western Blot Stripping Buffer, Thermo Fisher Scientific) of bound antibodies and reprobated with GAPDH to control for equal protein loading. Band intensities were measured using ImageJ and were normalized to GAPDH.

Antisense oligonucleotide morpholino design and *TUBA4A* mRNA transcription

An ATG blocking morpholino (AMO) against *tuba8l2*, the single human *TUBA4A* orthologue in *Danio rerio* (morpholino sequence 5'-TTGGAGTTGGATTTGTTTTTGGCCG-3') was designed and generated by Gene Tools (Philomath, USA). The standard control AMO provided by Gene Tools was used as negative control (morpholino sequence 5'- CCTCTTACCTCAGTTACAATTTATA-3'). A human wild-type *TUBA4A* HA-tagged encoding plasmid was kindly provided by Dr. J. Landers (183). To produce mRNA, plasmids were linearized by restriction digestion, transcribed with mMESSAGING mMACHINE T7 kit (AM1344, Ambion, Huntingdon, UK) and the resulting mRNA purified with the MEGAclean Kit (AM1908, Ambion). The mRNA concentration was measured by spectrophotometry (Nanodrop, Thermo Fisher Scientific). mRNA quality and length were verified by RNA gel electrophoresis.

Zebrafish injections

All zebrafish breeding was approved by the Ethical Committee for Animal Experimentation of the KU Leuven (P125/2014). All experiments were performed on embryos younger than five days post fertilization, implying these experiments are in line with the principle of 3Rs as these are not regulated as animal studies. One- to two-cell stage zebrafish embryos from the AB strain were injected in the yolk sac with the indicated amounts of morpholino and/or mRNA diluted in aqua ad iniectabilia (3521664, B. Braun, Melsungen, Germany) and supplemented with phenol red for verification of injection. Embryos were randomly assigned to different injection condition groups. Injected embryos were kept in a 28.5°C incubator. For western blotting, fish were manually dechorionated using forceps and the yolk was removed. Only morphologically normal-looking embryos, as determined by visual inspection, were collected at 48 hours post fertilization (hpf) and homogenized in RIPA buffer (R0278, Sigma-Aldrich) supplemented with protease and phosphatase inhibitors (78440, Halt, Thermo Fisher Scientific) using a micropestle on a rotor. After centrifugation (3 min, 13 000 *g*), the supernatant was collected and protein concentrations were determined using the Pierce BCA Protein Assay Kit (23225, Thermo Fisher Scientific).

Zebrafish SV2 immunohistochemistry and analysis

At 30 hpf, morphologically normal-looking zebrafish embryos, as determined by visual inspection, were manually dechorionated and deyolked, and fixed overnight at 4°C in 4% PFA in PBS. Fish were permeabilized with acetone for 1 h at -20°C, followed by blocking with 1% bovine serum albumin (BSA) (A7030, Sigma-Aldrich)/1% dimethyl sulfoxide (DMSO) (D2650, Sigma-Aldrich)/PBS for 1h at RT and immunostained with mouse anti-synaptic vesicle 2 (SV2) (1:200; Suppl. Table 2) and secondary Alexa Fluor 555 anti-mouse antibody (1:500, A-31570, Thermo Fisher Scientific) as previously described (273). For axonal length analysis, 10-15 embryos per condition per experiment were analyzed using a Leica DM 3000 LED microscope and the tracking tool in Lucia software (version 4.60, Laboratory Imaging, resolution 2448 x 2048 pixels). Five predefined and consecutive ventral root projections (i.e. the 8th up to the 12th axon) were measured by a blinded observer. Each axon was measured starting from the beginning of the ventral root projection until the end of any observable staining. The number of biological replicates equals three, which has previously been shown to be adequate to measure an effect (273). Data were normalized to the control condition.

Zebrafish touch-evoked escape response (TEER)

Morphologically normal-looking embryos, as determined by visual inspection, were manually dechorionated at 30 hpf. 10-15 embryos were used per condition per experiment with three biological replicates, which has previously been shown to be adequate to measure an effect (179). At 48 hpf,

zebrafish were individually placed in a 150 mm petri dish filled with 28.5°C embryo medium. After 30 s of habituation, an escape response was elicited by a light brush on the tail and recorded at 30 Hz with a Sony HDR-AS30V camera (resolution 1920 x 1080 pixels) until the end of the escape response (274). The videos were analyzed in ImageJ using the Manual Tracking plugin and the total distance, the maximal instant velocity and the average velocity were calculated by a blinded observer. Data were normalized to the control condition.

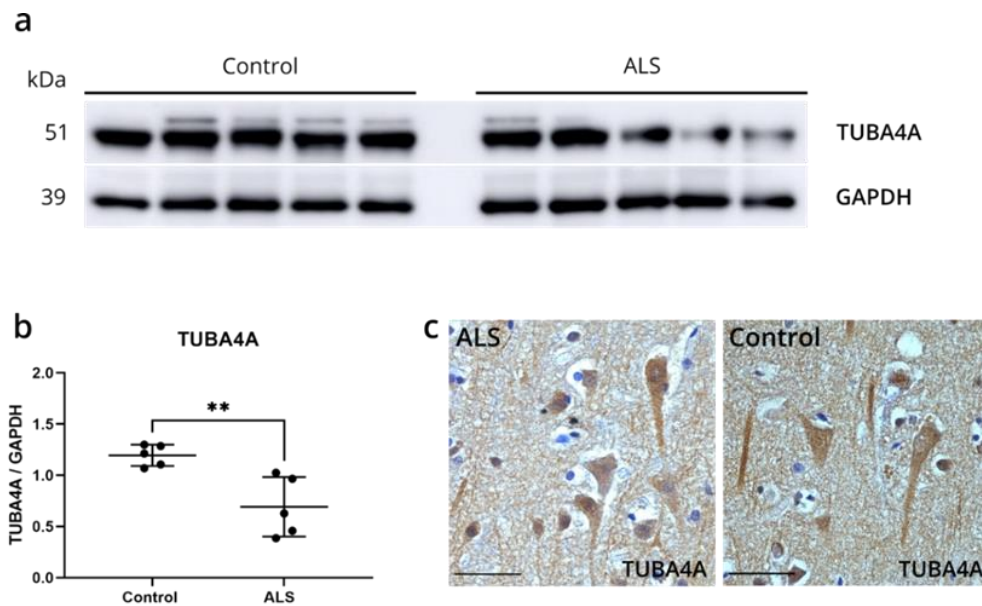
Statistical analysis

Statistical analyses were performed using Graphpad Prism 9.0 software. Normality was assessed using the Shapiro-Wilk test. Variance homogeneity was assessed using the F-test (for two groups) or the Bartlett's test (for more than two groups). A Mann-Whitney test or unpaired t-test was used to compare two groups. A one-way ANOVA or Kruskal-Wallis test followed by Dunn's or Dunnett's multiple comparisons was used to determine the significant difference between multiple groups. Data are presented as mean \pm SD or median \pm IQR. Significance levels are indicated as follows: * $p < 0.05$, ** $p < 0.01$, *** $p < 0.001$, **** $p < 0.0001$.

4. Results

ALS *post-mortem* motor cortex shows decreased TUBA4A expression

To investigate possible alterations in the expression of the TUBA4A protein in ALS, we performed western blot on SDS-soluble extracts from motor cortex from ALS and control cases using a TUBA4A-specific antibody. A significant decrease in the total protein expression of TUBA4A in ALS compared to control motor cortex was observed ($p = 0.0066$; unpaired t-test; Fig 1a,b; Suppl. Fig 1a and Suppl. Table 3). In the spinal cord, there was a trend towards decreased TUBA4A levels in ALS cases compared to controls, although significance was not reached ($p = 0.1349$; unpaired t-test; Suppl. Fig 1b,c and Suppl. Table 4). In addition, we evaluated the TUBA4A expression pattern by immunohistochemistry in ALS and control cases. This showed a dense staining of the cell body and neurites in the motor cortex (Fig 1c) and in the spinal cord (Suppl. Fig 2), both in ALS cases and controls. No TUBA4A inclusions were observed microscopically in the motor cortex or the spinal cord (Fig 1c, Suppl. Fig 2). In conclusion, these results from *post-mortem* human tissue showed that TUBA4A protein levels were reduced in sporadic ALS patient tissue.

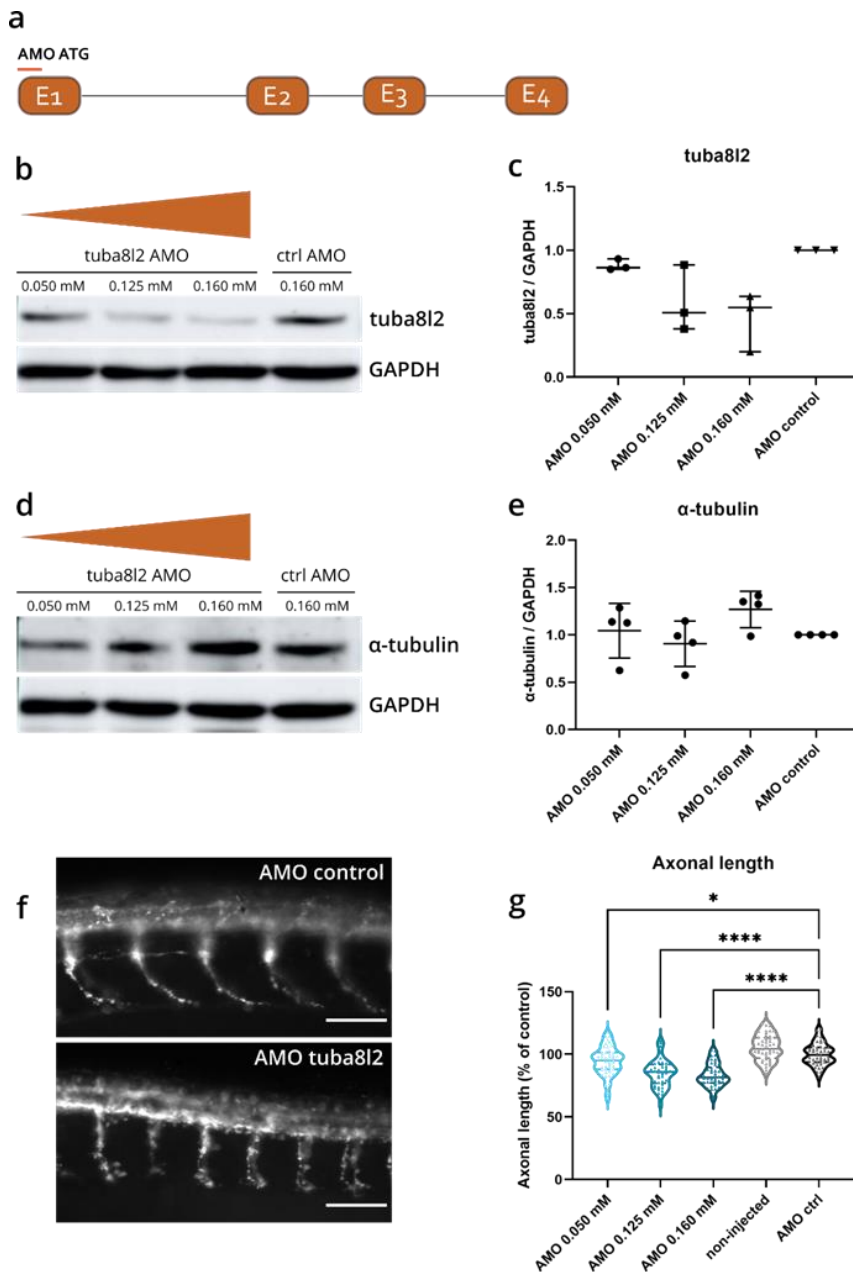


Ch. IV - Figure 1. ALS *post-mortem* motor cortex exhibits TUBA4A downregulation. (a) Western blot on SDS-soluble lysates derived from the motor cortex of control (n = 5) and ALS (n = 5) cases using an antibody against TUBA4A. GAPDH was used as a loading control. **(b)** Quantification of the expression of TUBA4A as a ratio to GAPDH in the motor cortex. $p = 0.0066$; unpaired t-test. **(c)** Immunohistochemical staining of the motor cortex of a representative ALS and control case with an antibody against TUBA4A. Scale bar represents 50 μm .

Knockdown of zebrafish *TUBA4A* orthologue induces dose-dependent axonal abnormalities and motor behavior deficits in zebrafish

To find out the potential significance of TUBA4A downregulation, we investigated whether the knockdown of *tuba8l2* is deleterious to motor axons of zebrafish embryos. This is the single zebrafish *TUBA4A* orthologue (ENSDARG00000031164), which is 94% conserved to human TUBA4A at the protein level and proven to be expressed throughout all anatomical structures in embryonic stages (at least until pec-fin stage at 72 hpf) (272). Therefore, we designed a morpholino directed against the ATG start codon of *tuba8l2* (Fig 2a). We injected different doses of the *tuba8l2* morpholino in one- to two-cell stage zebrafish oocytes and assessed *tuba8l2* protein levels by western blot at 48 hours post fertilization (hpf). The highest dose of 0.160 mM did not lead to any gross developmental phenotype (Fig. 4a). A standard morpholino was injected as control condition at a dose equaling the highest dose of the *tuba8l2* morpholino (0.160 mM). We detected a dose-dependent knockdown of *tuba8l2* levels, with the highest knockdown of 54% at 0.160 mM of morpholino (mean ratio to control: 0.46), a knockdown of 41% at a dose of 0.125 mM (mean ratio to control: 0.59) and a 12% knockdown when we injected 0.050 mM morpholino (mean ratio to control: 0.88) (Fig 2b,c; Suppl. Fig. 3). The morpholino injection did not affect the expression levels of other α -tubulin isoforms, as shown by western blot with an antibody against α -tubulin (Fig 2d,e; Suppl. Fig. 3).

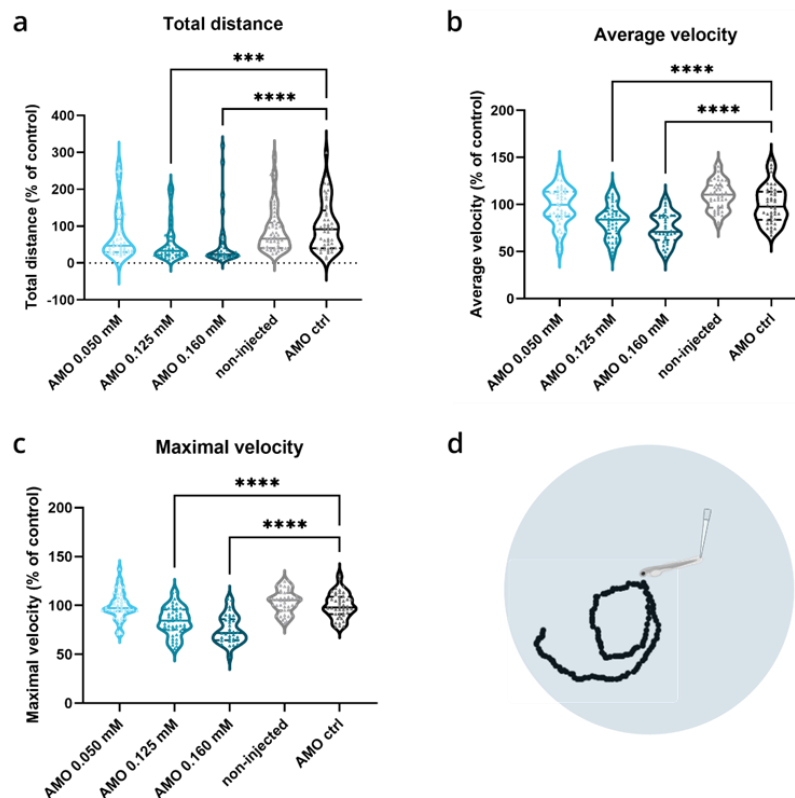
To assess the effect of the specific knockdown of *tuba8l2* on motor neuron axonal morphology, we performed SV2 immunohistochemistry to visualize the projections of the spinal cord ventral roots at 30 hpf (Fig 2f) (273). We observed a significant reduction in axonal length in the 0.160 mM *TUBA4A* morpholino condition compared to the control morpholino condition ($p < 0.0001$; one-way ANOVA with Dunnett's multiple comparisons; Fig 2g and Suppl. Table 5). This effect was dose dependent, as shown by the 0.125 mM and 0.050 mM morpholino conditions ($p < 0.0001$ and $p = 0.045$ respectively, Fig 2g and Suppl. Table 5).



Ch. IV - Figure 2. Specific tuba8l2 knockdown in zebrafish induces axonal abnormalities. (a) An ATG morpholino was designed against the *Danio rerio* *TUBA4A* orthologue *tuba8l2*. (b-e) Western blot was performed at 48 hpf after injection of different doses of ATG morpholino against *tuba8l2* (0.160 mM, 0.125 mM and 0.050 mM) as well as the injection of a control morpholino (0.160 mM). N = 3 experiments; n = 10-15 zebrafish per group per experiment. Quantification of *tuba8l2* (c) and α-tubulin (e) protein levels relative to GAPDH for the different injection conditions. (f,g) Visualization of motor axons by SV2 immunohistochemistry at 30 hpf after injection of different doses of ATG morpholino against *tuba8l2* (0.160 mM, 0.125 mM and 0.050 mM) or a control morpholino (0.160 mM). A non-injected condition was also included. $p < 0.0001$ (0.160 mM versus AMO control), $p < 0.0001$ (0.125 mM versus AMO control) and $p = 0.0450$ (0.050 mM versus AMO control); one-way ANOVA with Dunnett's multiple comparisons. Axonal length

was measured for N = 3 experiments; n = 10-15 zebrafish per group per experiment. * $p < 0.05$; **** $p < 0.0001$. AMO = morpholino; hpf = hours post fertilization.

To assess whether *tuba8l2* knockdown in zebrafish also had an effect on motor function, we performed a touch-evoked escape response (TEER) assay at 48 hpf as described before (274), with an example escape trace of the AMO control condition depicted in Fig 3d. We compared non-injected, control morpholino injected and *tuba8l2* morpholino injected conditions. This showed a significantly decreased total distance travelled (0.160 mM: $p < 0.0001$; 0.125 mM: $p = 0.0001$; Kruskal-Wallis test with Dunn's multiple comparisons; Fig 3a; Suppl. Table 6). Furthermore, we observed a significant reduction in the average (Fig 3b; Suppl. Table 7) and instant maximal (Fig 3c; Suppl. Table 8) swimming velocity in the 0.160 mM ($p < 0.0001$; one-way ANOVA with Dunnett's multiple comparisons) and 0.125 mM ($p < 0.0001$; one-way ANOVA with Dunnett's multiple comparisons) *tuba8l2* morpholino-injected compared to control morpholino injected embryos. In conclusion, we observed that the specific knockdown of the zebrafish orthologue of *TUBA4A* led to a dose-dependent axonal and motor behavior phenotype.

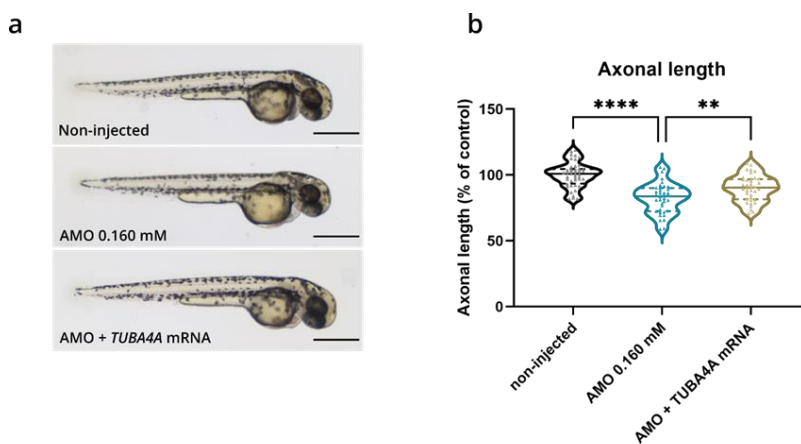


Ch. IV - Figure 3. Zebrafish motor behavior deficits are induced by *tuba8l2* knockdown. Zebrafish were subjected to a touch-evoked escape response (TEER) assay at 48 hpf after injection of different doses of ATG morpholino against *tuba8l2* (0.160 mM, 0.125 mM, 0.050 mM), or a control morpholino (0.160 mM). In addition, non-injected embryos were included in the analysis. **(a)** Total distance for 0.160 mM ($p < 0.0001$), 0.125 mM ($p = 0.0001$) and 0.050 mM ($p = 0.1936$) compared to AMO control condition. **(b)** Average velocity for 0.160 mM ($p < 0.0001$), 0.125 mM ($p < 0.0001$) and 0.050 mM ($p = 0.9814$) compared to AMO control condition. **(c)** Maximal instant velocity 0.160 mM ($p < 0.0001$), 0.125 mM ($p < 0.0001$) and 0.050 mM ($p = 0.9983$) compared to AMO control condition. Kruskal-Wallis test with Dunn's multiple comparisons (a) or one-way ANOVA with Dunnett's multiple comparisons (b,c); N = 3 experiments; $n = 10-15$ zebrafish per group per experiment, with each data point representing an individual zebrafish embryo. **(d)** Visual example of the tracking of an escape response in the AMO control condition using the TEER assay in zebrafish embryos at 48 hpf. *** $p < 0.001$; **** $p < 0.0001$. AMO = morpholino; hpf = hours post fertilization.

Axonal phenotype and motor behavior defects are rescued by human *TUBA4A* mRNA

To confirm that the observed phenotypes are indeed a direct consequence of the specific knockdown of *tuba8l2*, and to confirm functional conservation between zebrafish and human orthologues, we assessed whether we could rescue these phenotypes by the expression of human wild-type TUBA4A. In order to achieve this, we injected zebrafish eggs with human HA-tagged *TUBA4A* mRNA at the highest non-toxic dose of 300 ng/μl, and collected the fish for western blot at 48 hpf. An anti-HA antibody confirmed the expression of the HA-TUBA4A protein at 48 hpf in the *TUBA4A* mRNA-injected condition, which was absent in the control condition (Suppl. Fig 4). Next, we co-injected *TUBA4A* mRNA with the highest *tuba8l2* morpholino dose (0.160 mM), which did not lead to gross developmental defects (Fig. 4a). We analyzed the effect on spinal cord motor neurons, as previously, by measuring axonal length using SV2 immunohistochemistry at 30 hpf. This showed a rescue of the phenotype by the co-injection of human wild-type *TUBA4A* mRNA (Fig 4; $p = 0.0033$; one-way ANOVA with Dunnett's multiple comparisons; Suppl. Table 9).

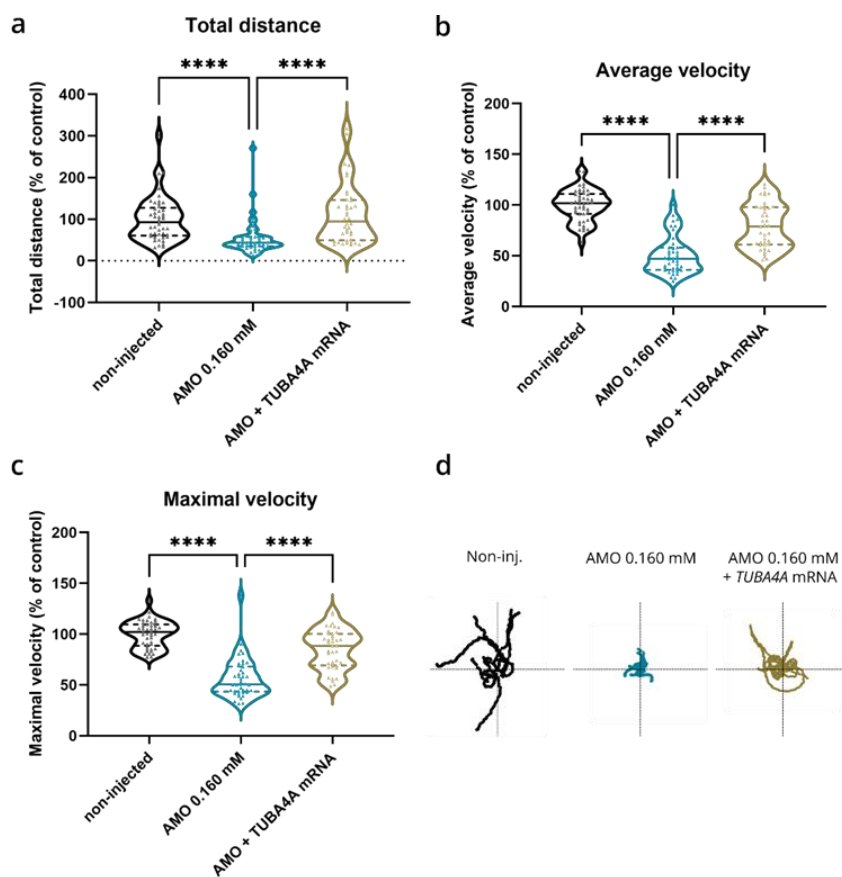
When we performed the TEER assay at 48 hpf, we also observed a complete rescue of the previously observed changes in total distance travelled (Fig 5a; $p < 0.0001$; Kruskal-Wallis test with Dunn's multiple comparisons; Suppl. Table 10), and a partial rescue of the changes in average swimming velocity (Fig 5b; $p < 0.0001$; Kruskal-Wallis test with Dunn's multiple comparisons; Suppl. Table 11) and instant maximal swimming velocity (Fig 5c; $p < 0.0001$; Kruskal-Wallis test with Dunn's multiple comparisons; Suppl. Table 12). Representative escape traces from 10 zebrafish embryos per group are depicted in Fig 5d. In conclusion, we showed that the observed axonal and motor behavior phenotype induced by the knockdown of the zebrafish orthologue for *TUBA4A* could be rescued by co-expression of human *TUBA4A* mRNA.



Ch. IV - Figure 4. Rescue of axonal length defects by the addition of human wild-type *TUBA4A* mRNA.

Zebrafish embryos were injected with an ATG morpholino against zebrafish *tuba8l2* (0.160 mM) with or without the injection of human wild-type *TUBA4A* mRNA (300 ng/μl). Non-injected embryos were also included in the analysis. (a) Representative whole body images of zebrafish embryos for the different conditions at 48 hpf (scale bars represent 500 μm). (b)

At 30 hpf, axonal length was measured for all conditions, with $p = 0.0033$ (AMO 0.160 mM versus AMO 0.160 mM + *TUBA4A* mRNA) and $p < 0.0001$ (AMO 0.160 mM versus non-injected); one-way ANOVA with Dunnett's multiple comparisons. Axonal length was measured for N = 3 experiments; $n = 10-15$ zebrafish per group per experiment; with every data point representing the average length of five measured axons for each zebrafish embryo. ** $p < 0.01$; **** $p < 0.0001$. AMO = morpholino; hpf = hours post fertilization.



Ch. IV - Figure 5. Rescue of motor behavior deficits by the addition of human wild-type *TUBA4A* mRNA. Zebrafish embryos were subjected to a touch-evoked escape response (TEER) assay at 48 hpf after injection with an ATG morpholino against zebrafish *tuba8l2* (0.160 mM) with or without the injection of wild-type human *TUBA4A* mRNA (300 ng/ μ l). Non-injected embryos were also included in the analysis. **(a)** Total distance for AMO 0.160 mM + *TUBA4A* mRNA ($p < 0.0001$) and non-injected ($p < 0.0001$) compared to AMO 0.160 mM condition. **(b)** Average velocity for AMO 0.160 mM + *TUBA4A* mRNA ($p < 0.0001$) and non-injected ($p < 0.0001$) compared to AMO 0.160 mM condition. **(c)** Maximal instant velocity for AMO 0.160 mM + *TUBA4A* mRNA ($p < 0.0001$) and non-injected ($p < 0.0001$) compared to AMO 0.160 mM condition. Kruskal-Wallis test with Dunn's multiple comparisons; $N = 3$ experiments; $n = 10-15$ zebrafish embryos per group per experiment; with each data point representing an individual zebrafish embryo. **(d)** Representative escape traces from 10 zebrafish embryos per group shown as a visual example. **** $p < 0.0001$. AMO = morpholino; hpf = hours post fertilization.

5. Discussion

In this study, we showed that a reduction of *TUBA4A* protein expression, as observed in *post-mortem* ALS tissue, leads to a decreased axonal length and a motor behavior phenotype in zebrafish upon knockdown of the zebrafish orthologue of *TUBA4A* (*tuba8l2*). Moreover, we demonstrated that these phenotypes are dose-dependent and can be rescued by the addition of wild-type human *TUBA4A* mRNA. This extends the importance of the familial ALS disease gene *TUBA4A* to sporadic ALS cases, implying that alterations in *TUBA4A* expression may be a contributing factor in ALS pathophysiology.

C-terminal mutations in *TUBA4A* were shown to be associated with classical spinal onset ALS, with in some cases FTD-like symptoms (183,194). The C-terminal part of *TUBA4A* is important for its interaction with β -tubulin and microtubule-associated proteins (MAPs) (190). Smith and colleagues demonstrated that C-terminally mutated *TUBA4A* proteins ineffectively formed tubulin dimers *in vitro*, and displayed a decreased incorporation into protofibrils, inhibiting microtubule network stability (183). On the other hand, N-terminal *TUBA4A* mutations were identified in patients presenting with FTD, possibly with extrapyramidal symptoms (194,195). We and others showed that these patients

displayed reduced TUBA4A levels in central nervous system tissues, suggesting a loss-of-function mechanism, contrary to C-terminal *TUBA4A* mutations, which could represent toxic gain-of-function (195,196,275).

Interestingly, a downregulation of TUBA4A protein expression was also suggested in the brain of sporadic ALS patients (197), which we could confirm in this study by western blotting. In addition, we detected a trend towards a decreased TUBA4A expression in the spinal cord of sporadic ALS patients. This was not significant, likely due to high variability between samples. Furthermore, IHC analysis indicated no differences in the cellular localization of TUBA4A between ALS and control cases, and no TUBA4A aggregates were detected, in line with a previous study (183). In this context, it is important to note that IHC is a qualitative rather than a quantitative method. Altogether, these data suggest that alterations in *TUBA4A* are also of importance in sporadic ALS pathogenesis.

Helferich *et al.* showed that downregulation of TUBA4A can occur through the miR-1825/*TBCB/TUBA4A* pathway, which was shown to be dysregulated in sporadic and familial ALS (197). They demonstrated miR-1825 downregulation in ALS patient tissue, which led to increased tubulin-folding cofactor B (TBCB) levels, causing a decrease in TUBA4A expression through the specific sequestration of this α -tubulin isoform by TBCB. This gives an indication of the possible upstream events leading to decreased TUBA4A levels in ALS, apart from *TUBA4A* mutations. Importantly, we demonstrated the causality of TUBA4A downregulation by showing axonal abnormalities and motor behavior deficits in zebrafish following knockdown of the *TUBA4A* orthologue *tuba8l2*. The induction of a motor axonopathy was previously also shown to be triggered by pathological protein products such as mutant SOD1 (276) and mutant TDP-43 (277), as well as by the pathological hallmarks of patients with *C9orf72* mutations, i.e. dipeptide repeat proteins (DPRs) and sense and anti-sense repeat RNA (273). Our results imply that decreased TUBA4A levels lead to an ALS-related phenotype, and therefore can be a contributing factor in ALS pathobiology.

The variety of diseases associated with mutations in various tubulin isoforms suggests functional specification of these different isoforms (185). Interestingly, expression of *TUBA4A* in the brain dramatically increases with age, which could explain why *TUBA4A* mutations or dysregulation may contribute to the development of adult-onset neurodegenerative disease, contrary to mutations in other tubulin isoforms which are involved in neurodevelopmental disorders (23,189,193). Furthermore, *TUBA4A* is the isoform with the highest expression in the human motor cortex after birth (188). Microtubule specification also occurs through tubulin post-translational modifications (PTMs), where neuronal microtubules mainly undergo dephosphorylation of the C-terminal tyrosine, acetylation at K40 and polyglutamylation (278). These PTMs accumulate as neurons differentiate and mature (188).

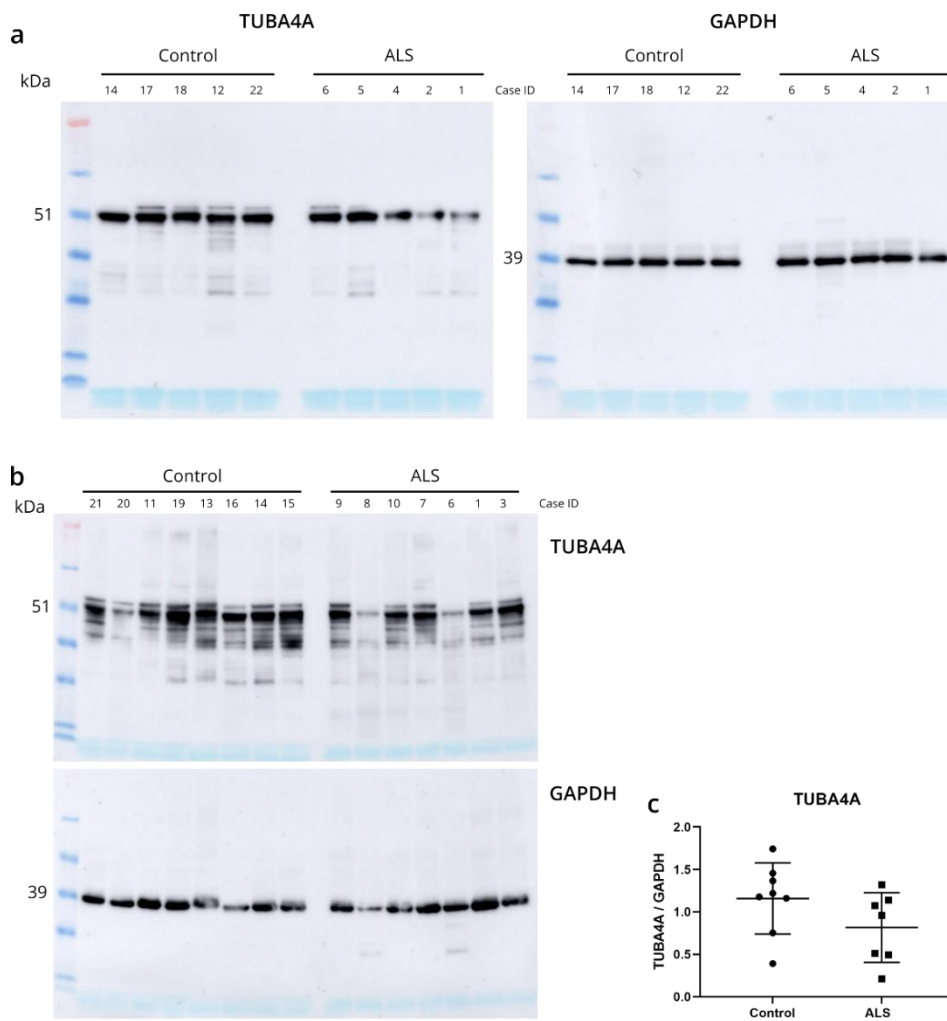
Importantly, out of nine α -tubulins, only TUBA8 and TUBA4A lack the C-terminal tyrosine residue (187,279). As detyrosinated tubulin is enriched in stable microtubules in the axon of neurons (188,191,278,279), the lack of TUBA4A might affect cytoskeletal integrity in neurons.

The dying-back hypothesis implies that abnormalities in axon connectivity and synaptic function long precede somatic cell death in ALS (162,280). Defects in cytoskeleton integrity and microtubule-dependent transport mechanisms can result in axonal trafficking disruption and dysfunctional neuromuscular junctions (23,210,279). Due to the physical length of motor neuron axons, cortical and spinal motor neurons are thought to be particularly vulnerable to this dying-back mechanism (186). Apart from *TUBA4A*, other ALS-related genes involved in cytoskeleton integrity are *DCTN1*, *KIF5A*, *PRPH*, *NF-H*, *PFN1* and *SPAST* (189,213). This stresses the causative relation between cytoskeletal defects and neurodegeneration. Therefore, it is likely that a downregulation of TUBA4A expression leads to aberrant cytoskeletal functioning, explaining the observed axonal and motor behavior phenotype in zebrafish.

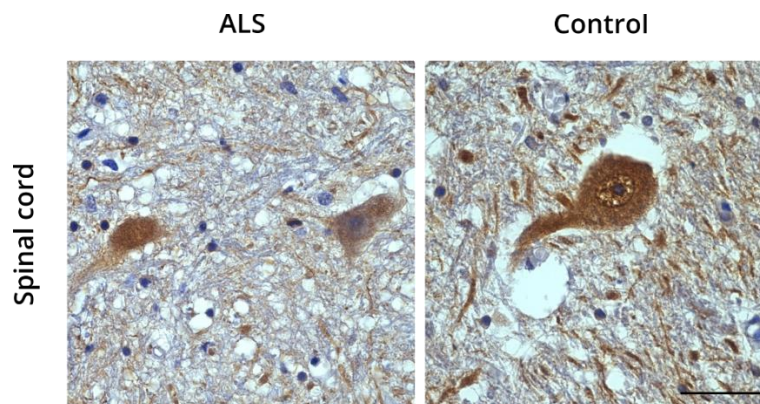
In this study, we assessed axonal and behavioral phenotypes in embryonic zebrafish stages (until 48 hpf). A limitation of the use of zebrafish to model a motor neuron disorders as ALS is the absence of corticospinal upper motor neurons projecting to the spinal cord. Additionally, the observed axonal and motor behavior phenotype could potentially be influenced by other effects induced by TUBA4A downregulation in other cell types. The use of embryonic zebrafish has its limitations to model an adult onset neurodegenerative disease. However, zebrafish experiments offer an advantage over standard cell culture models as it gives the possibility to study effects on motor behavior in addition to axonal pathology, which is not possible *in vitro*. Moreover, the zebrafish orthologue *tuba8l2* shows 94% conservation compared to human *TUBA4A* at the protein level, and we showed that TUBA4A can compensate for the loss of *tuba8l2* in our rescue experiments, suggesting functional conservation between these orthologues, with both genes able to regulate motor axon morphology and motor behavior. Although the use of morpholino-based knockdown in zebrafish can be an important avenue to explore emerging pathogenic pathways in neurodegenerative disorders, like any model, it has its limitation. Thus, research including other *in vivo* and patient-relevant *in vitro* models is needed to further unravel the downstream consequences of TUBA4A downregulation, and how this contributes to ALS-related neurodegeneration.

In conclusion, we showed an ALS-related axonal and motor behavior phenotype in zebrafish embryos following downregulation of the zebrafish orthologue for *TUBA4A*. These data support that, apart from ALS cases bearing a *TUBA4A* mutation, dysregulated TUBA4A expression plays an important role in sporadic ALS disease pathogenesis, and stresses the importance of microtubule dysfunction in ALS.

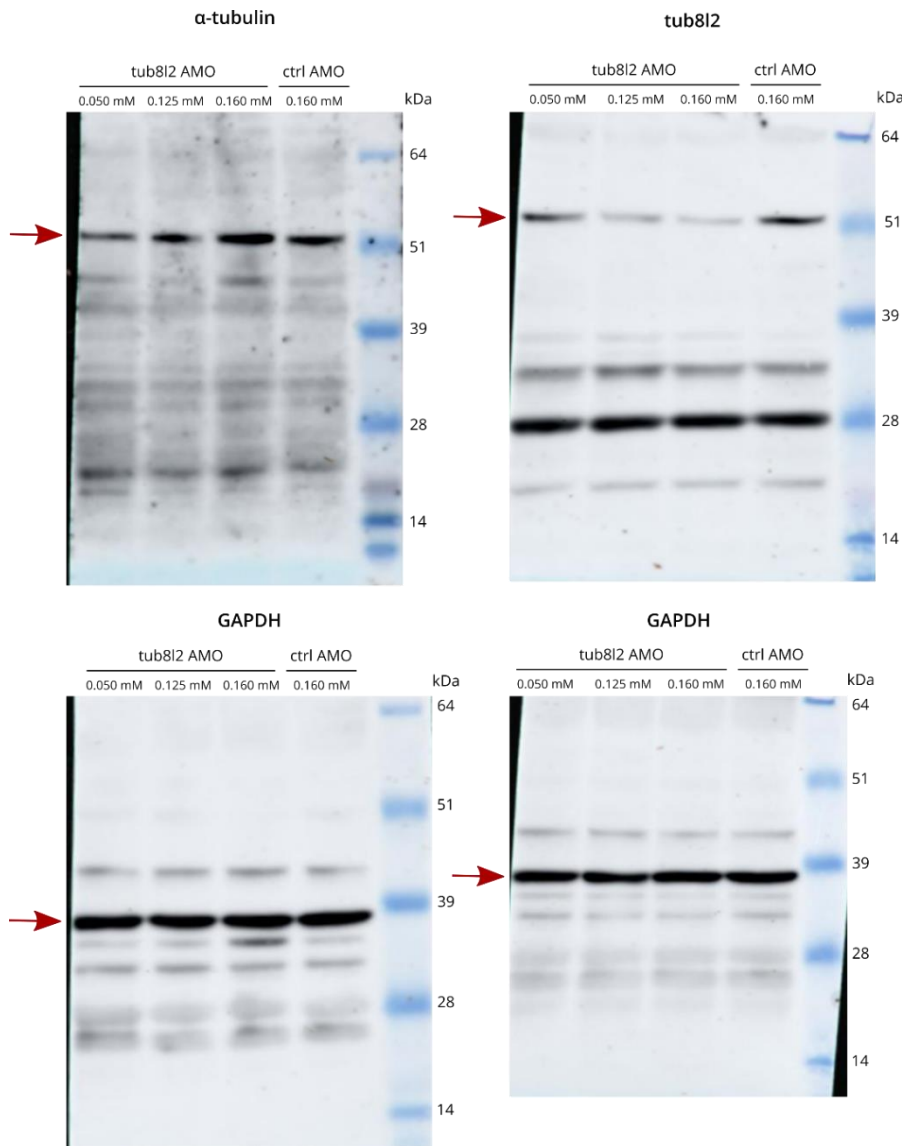
6. Supplementary information



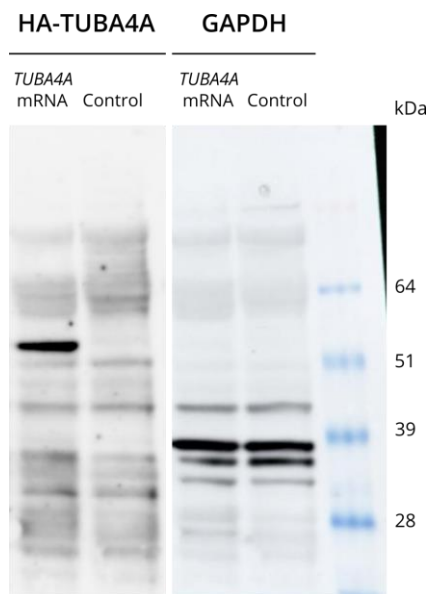
Ch. IV - Suppl. Figure 1. ALS *post-mortem* motor cortex and spinal cord full western blots for TUBA4A. (a,b) Full western blots using antibodies against TUBA4A and GAPDH on SDS-soluble lysates extracted from the motor cortex (a) and spinal cord (b) of control (n = 5 and n = 8 resp.) and ALS (n = 5 and n = 7 resp.) cases. **(c)** Quantification of the expression of TUBA4A as a ratio to GAPDH in the spinal cord. $p = 0.1349$; unpaired t-test.



Ch. IV - Suppl. Figure 2. Immunohistochemical analysis of TUBA4A in ALS and control *post-mortem* spinal cord. Immunohistochemical stainings of spinal cord of a representative ALS and control case with an antibody against TUBA4A. Scale bar represents 50 μm .



Ch. IV - Suppl. Figure 3. Full western blots showing the specific tuba8l2 knockdown in zebrafish. Western blot was performed at 48 hpf after injection of different doses of ATG morpholino against *tuba8l2* (0.160 mM, 0.125 mM and 0.050 mM) as well as the injection of a control morpholino (0.160 mM). Arrow indicates the correct band at 51 kDa for α-tubulin and tuba8l2, and at 39 kDa for the corresponding GAPDH loading control.



Ch. IV - Suppl. Figure 4. Confirmation of expression of HA-tagged wild-type TUBA4A protein after micro-injection of mRNA in zebrafish. Western blot performed at 48 hpf after injection of HA-tagged wild-type *TUBA4A* mRNA shows the expression of an HA-TUBA4A protein product using an antibody against HA. This was absent in the non-injected control condition. GAPDH was used as a loading control.

Ch. IV - Suppl. Table 1. List of human cases used in the study. The table provides information regarding age (= age at death), sex, diagnosis, A β MTL phase, Braak NFT stage, disease duration (months), PMI (hours) and application (1 = western blot motor cortex; 2 = western blot spinal cord; 3 = immunohistochemistry). Abbreviations: f = female; m = male; ALS = amyotrophic lateral sclerosis; control = non-neurodegenerative disease control; A = aneurysm; AGD = argyrophilic grain disease; ARTAG = aging-related tau astroglipathy; CM = carcinoma metastasis; GB = Guillian-Barre syndrome; I = infarction; MI = microinfarction; n.a. = not applicable; PART = primary age-related tauopathy; SVD = small vessel disease; SVE = subcortical vascular encephalopathy; PMI = *post-mortem* interval.

Case n°	Age	Sex	Diagnosis	A β MTL phase	Braak NFT stage	Disease duration	PMI (hours)	Application
1	58	f	ALS, PART	0	2	18 months	24	(1,2,3)
2	51	m	ALS	0	1	8 months	24	(1)
3	49	m	ALS, PART	0	1	45 months	24	(2)
4	46	m	ALS	0	1	40 months	24	(1)
5	62	m	ALS, MI, I, ARTAG, PART, AGD	0	1	154 months	12	(1)
6	53	m	ALS	0	1	92 months	24	(1,2,3)
7	74	m	ALS	1	1	47 months	24	(2)
8	50	f	ALS	0	1	18 months	24	(2)
9	54	m	ALS	0	1	88 months	6	(2)
10	68	m	ALS, SVD	2	2	36 months	144	(2)
11	46	m	Control	0	1	n.a.	29	(2)
12	74	m	Control, CM, I, MI	0	0	n.a.	72	(1,3)
13	45	m	Control	0	0	n.a.	24	(2)
14	61	m	Control, SVD	0	0	n.a.	48	(1,2,3)
15	55	m	Control, A, I	0	0	n.a.	96	(2)
16	74	f	Control, AGD, SVE	0	1	n.a.	24	(2)
17	35	m	Control, Limbic encefalopathy	0	0	n.a.	72	(1)
18	54	m	Control, GB	0	1	n.a.	24	(1)
19	63	f	Control, MI	0	1	n.a.	96	(2)
20	64	m	Control	0	0	n.a.	96	(2)
21	35	m	Control	0	1	n.a.	48	(2)
22	64	m	Control	0	1	n.a.	24	(1)

Ch. IV - Suppl. Table 2. List of antibodies used in the study. The table summarizes information about host, clonality, supplier and catalog number of the primary antibodies used for immunohistochemistry (IHC), immunofluorescence (IF) and western blot (WB). Dilutions are given.

Primary antibody	Host	Clonality	Supplier	Catalogue number	Dilution IHC	Dilution IF	Dilution WB
TUBA4A	Rabbit	Polyclonal	Abgent	AP13535b	1:100	-	1:8000
TUBA4A	Rabbit	Polyclonal	Abcam	ab228701	-	-	1:10 000
alpha-tubulin	Mouse	Monoclonal	Sigma	T6199	-	-	1:2000
anti-GAPDH (clone 6C5)	Mouse	Monoclonal	ThermoFisher	AM4300	-	-	1:10 000
anti- β -Amyloid (clone 4G8)	Mouse	Monoclonal	BioLegend	SIG-39220	1:5000	-	-
anti-pTDP43 (S409/410-2)	Rabbit	Polyclonal	Cosmo Bio	TIP-PTD-P02	1:5000	-	-
anti-pTau (S202/T205) (clone AT8)	Mouse	Monoclonal	ThermoFisher	MN1020	1:1000	-	-
SV2	Mouse	Monoclonal	DSHB	AB2315387	-	1:200	-

Ch. IV - Suppl. Table 3. Detailed statistical data on the comparison of control and ALS cases for TUBA4A protein expression evaluated by western blot in *post-mortem* motor cortex lysates.

	Mean (SD)	SEM	Shapiro-Wilk test	F test for equality of variances		Unpaired t-test		
			<i>p</i>	F	<i>p</i>	<i>t</i>	df	<i>p</i>
Western blot motor cortex								
Control	1.19 (0.10)	0.047	0.3683					
ALS	0.69 (0.29)	0.130	0.3308					
Within groups				7.793	0.0717	3.639	8	0.0066

Ch. IV - Suppl. Table 4. Detailed statistical data on the comparison of control and ALS cases for TUBA4A protein expression evaluated by western blot in *post-mortem* spinal cord lysates.

	Mean (SD)	SEM	Shapiro-Wilk test	F test for equality of variances		Unpaired t-test		
			<i>p</i>	F	<i>p</i>	<i>t</i>	df	<i>p</i>
Western blot spinal cord								
Control	1.16 (0.42)	0.148	0.6628					
ALS	0.82 (0.41)	0.155	0.5128					
Within groups				1.047	0.9720	1.594	13	0.1349

Ch. IV - Suppl. Table 5. Detailed statistical data on the comparison of AMO control versus different doses of AMO *tuba8l2* injection conditions for axonal length at 30 hours post fertilization.

	Mean (SD) not normalized (µm)	Mean (SD) normalized	SEM	Shapiro-Wilk test	Bartlett's test for equality of variances		One-Way ANOVA (multiple comparisons)			
				<i>p</i>	F	<i>p</i>	df1	df2	F(df1,df2)	<i>p</i>
Axonal length										
AMO control 0.160 mM	78.93 (7.251)	100 (8.82)	1.315	0.8211						
AMO <i>tuba8l2</i> 0.050 mM	74.62 (8.665)	94.61 (11.53)	1.719	0.8559						
AMO <i>tuba8l2</i> 0.125 mM	67.14 (8.189)	84.99 (10.97)	1.693	0.6616						
AMO <i>tuba8l2</i> 0.160 mM	65.77 (7.415)	83.32 (9.28)	1.432	0.3764						
Within groups					4.240	0.3745	4	214	37.4	<0.0001

Ch. IV – Suppl. Table 6. Detailed statistical data on the comparison of AMO control versus different doses of AMO *tuba8l2* injection conditions for the total distance measured by the touch-evoked escape response (TEER) at 48 hours post fertilization.

	Median (IQR) not normalized (mm)	Median (IQR) normalized	Shapiro-Wilk test	Kruskal-Wallis test (multiple comparisons)	
			<i>p</i>	F	<i>p</i>
TEER total distance					
AMO control 0.160 mM	89.38 (238.6)	91.58 (288.1)	0.0026		
AMO <i>tuba8l2</i> 0.050 mM	43.48 (254.3)	46.75 (269.0)	<0.0001		
AMO <i>tuba8l2</i> 0.125 mM	28.30 (185.6)	33.02 (196.8)	<0.0001		
AMO <i>tuba8l2</i> 0.160 mM	21.07 (257.6)	23.44 (309.3)	<0.0001		
Within groups				38.72	<0.0001

Ch. IV - Suppl. Table 7. Detailed statistical data on the comparison of AMO control versus different doses of AMO *tuba8l2* injection conditions for the average velocity measured by the touch-evoked escape response (TEER) at 48 hours post fertilization.

	Mean (SD) not normalized (mm/s)	Mean (SD) normalized	SEM	Shapiro-Wilk test	Bartlett's test for equality of variances		One-Way ANOVA (multiple comparisons)			
				<i>p</i>	F	<i>p</i>	df1	df2	F(df1,df2)	<i>p</i>
TEER average velocity										
AMO control 0.160 mM	46.42 (9.383)	100 (19.87)	2.962	0.2332						
AMO <i>tuba8l2</i> 0.050 mM	45.47 (9.578)	98.39 (20.29)	3.059	0.5979						
AMO <i>tuba8l2</i> 0.125 mM	39.14 (9.076)	82.65 (17.54)	2.615	0.6924						
AMO <i>tuba8l2</i> 0.160 mM	33.66 (6.828)	74.80 (15.96)	2.738	0.5337						
Within groups					5.202	0.2672	4	208	24.07	<0.0001

Ch. IV - Suppl. Table 8. Detailed statistical data on the comparison of AMO control versus different doses of AMO *tuba8l2* injection conditions for the instant maximal velocity measured by the touch-evoked escape response (TEER) at 48 hours post fertilization.

	Mean (SD) not normalized (mm/s)	Mean (SD) normalized	SEM	Shapiro-Wilk test	Bartlett's test for equality of variances		One-Way ANOVA (multiple comparisons)			
				<i>p</i>	F	<i>p</i>	df1	df2	F(df1,df2)	<i>p</i>
TEER maximal velocity										
AMO control 0.160 mM	84.90 (11.35)	100 (12.82)	1.911	0.6508						
AMO <i>tuba8l2</i> 0.050 mM	84.49 (12.64)	99.60 (14.19)	2.139	0.3244						
AMO <i>tuba8l2</i> 0.125 mM	71.13 (11.96)	83.90 (14.43)	2.151	0.7904						
AMO <i>tuba8l2</i> A 0.160 mM	63.66 (12.17)	75.38 (14.30)	2.452	0.1851						
Within groups					0.7548	0.8603	3	164	29.98	<0.0001

Ch. IV - Suppl. Table 9. Detailed statistical data on the comparison of AMO *tuba8l2* 0.160 mM injected versus non-injected and AMO *tuba8l2* 0.160 mM + *TUBA4A* mRNA 300 ng/ μ l conditions for axonal length at 30 hours post fertilization.

	Median (IQR) not normalized (μ m)	Mean (SD) normalized	SEM	Shapiro-Wilk test	Bartlett's test for equality of variances		One-Way ANOVA (multiple comparisons)			
				<i>p</i>	F	<i>p</i>	df1	df2	F(df1,df2)	<i>p</i>
Axonal length										
Non-injected	85.51 (30.24)	100.00 (9.44)	1.422	0.4003						
AMO <i>tuba8l2</i> 0.160 mM	68.57 (36.28)	82.27 (11.54)	1.872	0.7516						
AMO + <i>TUBA4A</i> mRNA	74.26 (23.86)	89.86 (9.89)	1.604	0.7759						
Within groups					1.755	0.4159	2	117	30.75	<0.0001

Ch. IV - Suppl. Table 10. Detailed statistical data on the comparison of AMO *tuba8l2* 0.160 mM injected versus non-injected and AMO *tuba8l2* 0.160 mM + *TUBA4A* mRNA 300 ng/ μ l conditions for the total distance measured by the touch-evoked escape response (TEER) at 48 hours post fertilization.

	Median (IQR) not normalized (mm)	Median (IQR) normalized	Shapiro-Wilk test	Kruskal-Wallis test (multiple comparisons)	
			<i>p</i>	F	<i>p</i>
TEER total distance					
Non-injected	37.42 (146.4)	92.82 (270.0)	0.0004		
AMO <i>tuba8l2</i> 0.160 mM	19.82 (90.89)	43.65 (258.5)	<0.0001		
AMO + <i>TUBA4A</i> mRNA	40.15 (164.6)	94.60 (278.9)	0.0003		
Within groups				31.18	<0.0001

Ch. IV - Suppl. Table 11. Detailed statistical data on the comparison of AMO *tuba8l2* 0.160 mM injected versus non-injected and AMO *tuba8l2* 0.160 mM + *TUBA4A* mRNA 300 ng/ μ l conditions for the average velocity measured by the touch-evoked escape response (TEER) at 48 hours post fertilization.

	Median (IQR) not normalized (mm/s)	Median (IQR) normalized	Shapiro-Wilk test	Kruskal-Wallis test (multiple comparisons)	
			<i>p</i>	F	<i>p</i>
TEER average velocity					
Non-injected	58.11 (40.15)	101.70 (70.0)	0.7264		
AMO <i>tuba8l2</i> 0.160 mM	26.38 (43.79)	47.13 (75.2)	0.0024		
AMO + <i>TUBA4A</i> mRNA	45.22 (41.00)	78.89 (74.9)	0.0528		
Within groups				68.56	<0.0001

Ch. IV - Suppl. Table 12. Detailed statistical data on the comparison of AMO *tuba8l2* 0.160 mM injected versus non-injected and AMO *tuba8l2* 0.160 mM + *TUBA4A* mRNA 300 ng/ μ l conditions for the instant maximal velocity measured by the touch-evoked escape response (TEER) at 48 hours post fertilization.

	Median (IQR) not normalized (mm/s)	Median (IQR) normalized	Shapiro-Wilk test	Kruskal-Wallis test (multiple comparisons)	
			<i>p</i>	F	<i>p</i>
TEER maximal velocity					
Non-injected	97.24 (52.72)	102.10 (55.9)	0.1656		
AMO <i>tuba8l2</i> 0.160 mM	48.35 (104.5)	50.59 (106.5)	<0.0001		
AMO + <i>TUBA4A</i> mRNA	84.74 (68.85)	88.43 (72.7)	0.2298		
Within groups				65.85	<0.0001

GENERAL DISCUSSION

In this PhD thesis, we aimed to clarify the mechanisms of neuronal and axonal degeneration in ALS. To this end, we used human *post-mortem* central nervous tissue in addition to TDP-43^{A315T} transgenic mice and zebrafish. Throughout this thesis manuscript, we addressed the three main objectives as defined at the beginning of this thesis, which led to the following findings:

- (1) The activated necrosome (i.e. pRIPK1, pRIPK3 and pMLKL) was not detected in motor neurons in the spinal cord and motor cortex of ALS patients. Nevertheless, it was present in GVD bodies in the hippocampus of ALS/FTLD-TDP patients and correlated with TDP-43 pathology in FTLD-TDP, which was associated with a decreased neuronal density in the hippocampal CA1 region. This suggests that pTDP-43, in addition to p-tau in AD, can induce or accelerate the development of necrosome-positive GVD in ALS/FTLD-TDP hippocampal regions.
- (2) The NLRP3 inflammasome, comprising of NLRP3, ASC and caspase-1, as well as pyroptosis effector proteins cleaved GSDMD and IL-18 were detected in microglia in human ALS motor cortex and spinal cord, suggestive of canonical inflammasome-triggered pyroptosis activation. In ALS, the number of cleaved GSDMD-positive microglia in the precentral white matter was increased compared to controls, and correlated with a decreased neuronal density in the motor cortex. Similar results were obtained in TDP-43^{A315T} transgenic mice, where pyroptosis was activated in microglia in the motor cortex upon symptom onset, and correlated with neuronal loss. Microglial pyroptosis activation did not correlate with pathological TDP-43 in human and mouse tissue.
- (3) An FTLD-TDP patient with an R64Gfs*90 *TUBA4A* mutation presenting with svPPA showed reduced *TUBA4A* protein levels in affected regions, suggesting haploinsufficiency as a potential underlying pathogenic mechanism. This strengthens the idea that N-terminal *TUBA4A* mutations are associated with FTLD-TDP, possibly exerting their effects through a loss-of-function mechanism, while C-terminal *TUBA4A* mutations, which are usually related to ALS, are thought to act through a dominant-negative mechanism.
- (4) Decreased *TUBA4A* protein levels were also detected in sporadic ALS patients. Mimicking this *TUBA4A* downregulation in zebrafish led to a dose-dependent motor axonopathy as well as a disturbed motor behavior phenotype, both of which could be rescued by the addition of human wild-type *TUBA4A* mRNA. These results shed light on a role for *TUBA4A* in ALS

pathogenesis, and extend the relevance of *TUBA4A* to the majority of ALS patients, in addition to *TUBA4A* mutation carriers.

1. Neuronal demise in ALS: a delicate interplay between cell death pathways?

In this thesis, we did not detect the activation of the necroptosis pathway in ALS-affected brain and spinal cord regions (**Chapter I**). On the other hand, pyroptosis was specifically activated in microglia in the precentral white matter of ALS patients, and correlated with a loss of motor neurons in the motor cortex (**Chapter II**). Although we did not investigate apoptosis activation in this thesis, previous research argues that other cell death mechanisms resembling apoptosis are involved in ALS (281). In general, it is thought that necroptosis is more of a backup cell death mechanism under the circumstances that apoptosis is hindered, while pyroptosis is believed to be a primary cellular response to potentially damaging insults, such as DAMPs (128). Importantly, necroptosis and pyroptosis signaling pathways were shown to overlap and interact. For instance, there is evidence that necroptosis activation can trigger pyroptosis through a RIPK3-MLKL-NLRP3-caspase-1 signaling axis, leading to the production of mature IL-1 β (282). Additionally, both pyroptosis and necroptosis activation lead to the release of sterile DAMPs, such as ATP, ASC specks and heat shock proteins (HSPs). These DAMPs are potent activators of the NLRP3 inflammasome, and can therefore spread the activation of cell death signaling to neighboring cells (128). An important protein that functions at the crossroads of apoptosis, necroptosis and pyroptosis is caspase-8. When caspase-8 is inhibited, activation of the necrosome is favored over apoptosis. Interestingly, when in addition MLKL is deficient, cell death can still occur, but in this instance pyroptosis is initiated through assembly of the inflammasome (112). Thus, caspase-8 seems to act as a molecular switch that modulates apoptosis, necroptosis and pyroptosis signaling pathways.

In **Chapter I**, we showed that the full necrosome, i.e. pRIPK1, pRIPK3 and pMLKL, localizes in GVD in hippocampal regions of ALS/FTLD-TDP cases, similar as previously demonstrated in patients with AD (221). Interestingly, autophagy markers such as LAMP1 were also shown to accumulate in GVD (222). Autophagy seems to be at close interplay with multiple regulated cell death pathways. It can for example drive apoptosis by degrading anti-apoptotic and cell survival factors (152), although it was also shown to be able to inhibit apoptosis through the removal of activated caspases (283). Vice versa, apoptosis signaling can inhibit autophagy, for example via cleavage of beclin-1 or ATG proteins, and can additionally convert autophagic proteins into proapoptotic stimuli, further enhancing apoptosis activation (151,152,284). Apart from influencing apoptosis through degradation, autophagy proteins can also serve as a scaffold for cell death complexes and signaling molecules (152). For instance, apoptosis complex I can connect to autophagosomal membranes, which serve as a platform for the

activation of caspase-8 (285). The same is true for the necroptosis machinery, as it can be recruited to the autophagosome through interaction with p62/SQSTM1 (156). Autophagy and necroptosis seem to oppose each other, as suppression of autophagic flux enhances RIPK1-RIPK3 interaction and consequent necroptosis (157), while the activation of necroptosis was shown to inhibit autophagic flux, and thus autophagy (150). In line with this, the activation of autophagy via inhibition of mTORC1 diminished necroptosis in cardiomyocytes, likely through suppression of RIPK1 (155). Similar to apoptosis, autophagy can also inhibit necroptosis through the degradation of necroptotic proteins, such as RIPK1 (151). Hence, the autophagy machinery seems to play an important role in regulated cell death, mainly through mutual repression of necroptosis and/or apoptosis, although autophagy proteins can serve as a scaffold for the accumulation of cell death signaling complexes, such as the necrosome.

Apart from regulating other types of cell death, the autophagy machinery can also be the direct cause of cellular demise, which is referred to as autophagy-dependent cell death (153). Prerequisites for the use of this term are that 1) the inhibition of autophagy, by genetic or chemical means, prevents the cell from dying, 2) cell death occurs without the involvement of other types of regulated cell death, and 3) the autophagic flux is increased (153,286). There are several mechanisms leading to autophagy-dependent cell death. The best known mechanism is cell death due to excessive autophagy, characterized by the excessive self-consumption of organelles and cytoplasmic content, eventually leading to cellular demise (287). A second subtype is excessive mitophagy, which leads to death due to the depletion of mitochondria and consequent energy failure (287). A final subtype is autosis, where death occurs due to the activation of the Na⁺/K⁺-ATPase pump and consequent alterations in membrane osmolarity and ion transport (287,288). It is important to distinguish autophagy-dependent and autophagy-mediated cell death, where in both cases the targeted inhibition of autophagic machinery may prevent cell death, from autophagy activation as a cellular mechanism to attenuate cell damage (i.e. autophagy-associated cell death, cf. introduction 4.1.4) (286). Altogether, apart from investigating a possible role for autophagy-dependent cell death in ALS as a stand-alone mechanism, further elucidation of the specific role of autophagy at the crossroads of regulated cell death types such as apoptosis, necroptosis and pyroptosis (i.e. autophagy-mediated cell death) will be crucial. Ultimately, this could facilitate the modulation of the autophagy system to diminish cell death without affecting other essential functions of the autophagy-lysosome machinery, such as the recycling of components and the clearance of intracellular protein aggregates and damaged organelles (284), which is pivotal, especially in the context of ALS protein pathology.

Although ALS is considered a motor neuron disorder, the role of glial cells should not be neglected. Apart from neurons, TDP-43 pathological aggregates also accumulate in glial cells, such as

oligodendrocytes and microglia, in patients with ALS and FTLTDP (33,289). We showed in **Chapter II** that pyroptosis is activated specifically in microglia, and that this correlates with motor neuron loss. It is clear that inflammation is not just a consequence of ALS, but has detrimental effects on the neuronal microenvironment (290). In the CNS, microglia are the main sensors that become activated following specific stimuli, such as pathological proteins, leading for instance to the activation of the main regulator of inflammation, i.e. NFκB (291,292). Importantly, it was shown that the specific deletion of NFκB in microglia rescued motor neurons from microglia-mediated death *in vitro*, and prolonged the survival of SOD1^{G93A} mice (293). As such, current knowledge allocates an important role to microglia in ALS neurodegeneration, although likely not as an initiator of the disease, but as an important detrimental modulator of neurodegeneration (252,292,294).

2. Cytoskeletal defects in ALS

In recent years, several ALS-related genes with a function in the cytoskeleton have been identified, among which *DCTN1*, *PFN1*, *KIF5A*, *PRPH*, *SPAST* and *TUBA4A* (23). In this thesis, we showed that *TUBA4A* alterations might have a broader relevance in ALS pathogenesis, in addition to patients with a *TUBA4A* mutation, as *TUBA4A* downregulation was observed in sporadic ALS *post-mortem* tissue and gave rise to an ALS-like phenotype in zebrafish (**Chapter IV**). In addition, we presented an FTLTDP patient with an N-terminal *TUBA4A* mutation exhibiting reduced levels of *TUBA4A* in the brain, indicative of a haploinsufficiency mechanism (**Chapter III**). These results further emphasize the importance of cytoskeletal integrity in ALS. This has also become clear in *in vitro* and *in vivo* models of ALS with mutations in genes not involved in the cytoskeleton, such as *TARDBP*, *C9orf72* and *SOD1*, where axonal transport defects are evident (168,170,172). Importantly, it was shown that the administration of a MT-modulating agent in SOD1^{G93A} mice, which reduces MT hyperdynamics, led to normalized axonal transport, as well as an amelioration of symptoms and prolonged survival (295).

Interestingly, the cytoskeleton is also interconnected with autophagy, with the autophagy machinery relying on its interaction with the cytoskeleton, and in particular MTs, for the formation and transport of autophagosomes (146,296). As such, destabilization of MTs was shown to impede autophagic flux (297). Additionally, autophagosomes formed in the axonal compartment of neurons often have to be transported over long distances to allow degradation in the neuronal cell body (298). On the other hand, autophagy activation was shown to stabilize MTs through the degradation of a MT disassembling protein (299), implying that dysregulated autophagy can have a detrimental effect on cytoskeletal integrity. Apart from autophagy, MT alterations have been related to other ALS-related pathological mechanisms, such as mitochondrial-dependent energy depletion, excitotoxicity and oxidative stress

(186,300). For example, due to their long length in motor neurons, axons require sufficient energy for axonal transport and are therefore dependent on mitochondria (301). Additionally, mitochondria are transported along the axon themselves to supply the synapse (213), illustrating the complex interplay of several ALS-related pathogenic pathways. Finally, MT dynamics can be influenced by post-translational modification of tubulin subunits, such as acetylation and detyrosination, which can affect axonal transport (213,278). For instance, it was shown that modulating tubulin acetylation ameliorated axonal transport as well as other ALS phenotypes *in vitro* and *in vivo* (169,171,210,302–304).

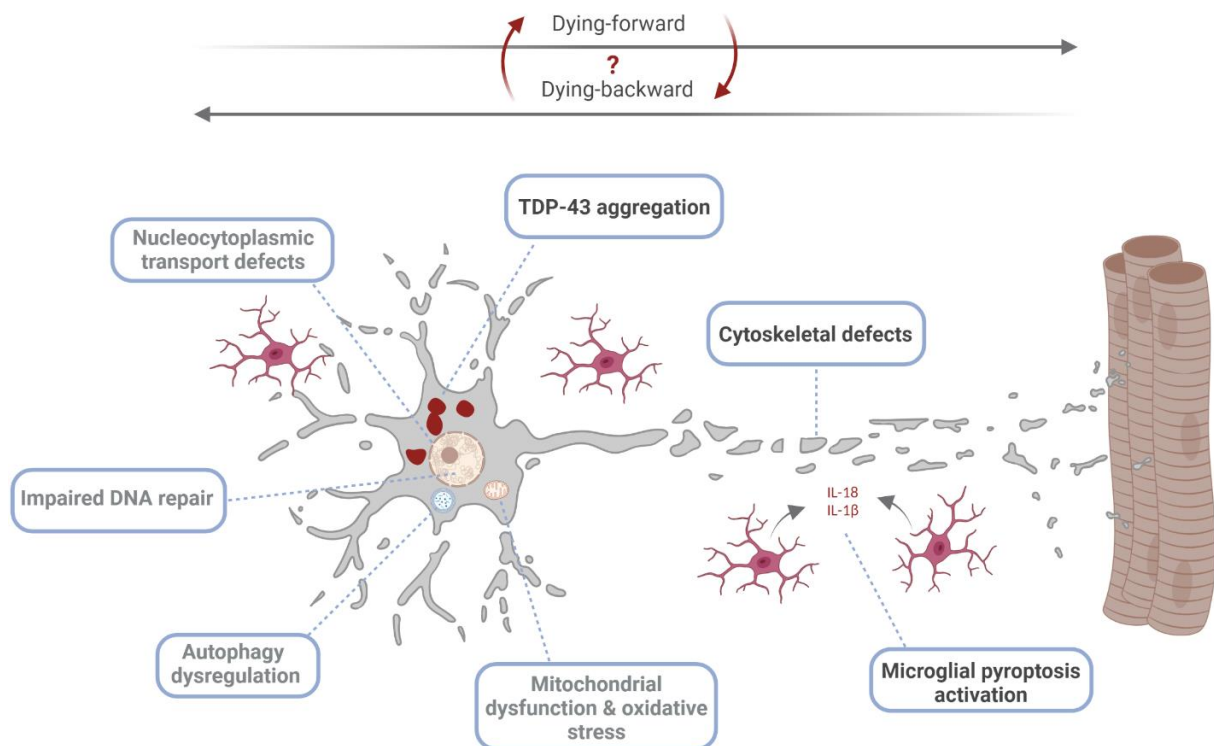
Thus, MT cytoskeletal defects can occur as a consequence of other ALS-related pathological mechanisms, such as aberrant autophagy, but also due to the physical blockage of axonal transport by protein aggregates, altered transcription or protein binding of transport proteins (213). On the other hand, we now know that alterations in cytoskeletal genes, such as *TUBA4A*, can contribute to the pathogenesis of ALS. In that case, the disruption of MT-dependent transport mechanisms could be a primary mechanism of ALS, leading to decreased protein degradation and the accumulation of damaged organelles through interference with the autophagy machinery (23,213), giving rise to protein aggregation as observed in ALS. In addition, cytoskeletal disturbances can lead to a lack of nutrients and other essential components at the synapses, resulting in the so-called 'dying-back' phenomenon, which will be discussed in the following section.

3. The dying-back versus dying-forward hypothesis

Recently, evidence points towards a 'dying-back' mechanism in ALS pathophysiology. This implies that ALS is a distal axonopathy, where molecular changes take place at the neuromuscular junction (NMJ) during the early stages of the disease, which later on progress towards the neuronal cell body (165,305). The NMJ is a specialized synapse that controls the signaling between the muscle and the axon. Disassembly of the NMJ ultimately leads to denervation of the skeletal muscle, resulting in the typical ALS clinical symptoms in the patient (306). In *SOD1^{G93A}* mice, Fischer and colleagues showed that denervation of synapses preceded the degeneration of ventral root axons, which was then followed by the loss of motor neurons in the spinal cord, suggestive of a dying-back mechanism (162). Symptom onset in these mice occurred around the same time as when approximately 60% of ventral root axons were lost (162). Most theories behind the dying-back hypothesis are based on well-known genetic causes of ALS. It is thought that for example the accumulation of pathological proteins, altered RNA processing, or mitochondrial damage could lead to insufficient maintenance of the distal axon (possibly due to axonal transport defects), resulting in denervation processes at the NMJ without initially affecting the neuronal cell body (165,307). The occurrence of mutations in ALS-related

cytoskeletal genes as well as our results on *TUBA4A* support this hypothesis, suggesting that ALS pathogenesis can start distally in the axon, leading to muscle denervation and eventually coinciding with motor neuron loss, as observed *post-mortem* in patients.

However, the inverse process, i.e. the dying-forward hypothesis, has recently regained attention. This postulates that degeneration processes start in the motor neurons in the primary motor cortex, descending downwards to ultimately reach the NMJ (308,309). This is supported by the model of corticofugal spreading of neurodegeneration, as described by Braak and colleagues (74). They suggest that pathology initiates in motor neurons in the primary motor cortex, which then, via axonal transport, propagates towards the spinal cord and other regions of the brain (74). Another finding supporting the dying-forward hypothesis, is that in ALS only the extraocular and pelvic sphincter muscles are spared. These are innervated by lower motor neurons that do not receive direct afferents from the cerebral cortex (310). In that regard, they would not be affected by dying-forward processes arising from the cerebral cortex (311). Of note, more restricted forms of ALS exist, such as PLS (only UMN involvement) and PMA (only LMN involvement), questioning the plausibility of both the dying-back and dying-forward theories. Finally, it is possible that dying-back and dying-forward mechanisms occur simultaneously, which was named the 'dying-outward' hypothesis by Baker *et al.* (312). It will be crucial to further elucidate the interplay between seemingly distinct ALS pathological mechanisms, such as protein aggregation, impaired autophagy, mitochondrial dysfunction, DNA damage, nucleocytoplasmic transport defects, the activation of cell death pathways such as pyroptosis, and cytoskeletal disturbances (Fig. 1). ALS genetics suggest a possible causative role for several of these mechanisms, suggesting that ALS pathogenesis can initiate via different pathways, eventually converging in full-blown pathology leading to neuronal and axonal degeneration.



General discussion - Figure 1. Pathological mechanisms involved in amyotrophic lateral sclerosis. Proposed disease mechanisms contributing to motor neuron degeneration in ALS include TDP-43 protein aggregation, cytoskeletal defects such as disturbed axonal transport, nucleocytoplasmic transport defects, impaired DNA repair, dysregulation of autophagy, mitochondrial dysfunction and oxidative stress, and microglial pyroptosis activation with the release of proinflammatory cytokines IL-18 and IL-1 β . Most likely, a combination of dying-forward and dying-backward mechanisms eventually leads to neurodegeneration.

4. The role of pathological TDP-43 in ALS

Regarding the aggregation of phosphorylated TDP-43, using *post-mortem* tissue, we found a correlation with necrosome-positive GVD in the hippocampus of ALS/FTLD-TDP cases (**Chapter I**), but not with microglial pyroptosis activation in ALS (**Chapter II**). The latter is in contrast with an *in vitro* study, where truncated and mutant TDP-43 significantly activated the NLRP3 inflammasome in microglia, which was toxic to motor neurons (141). Another group showed that the internalization of pathological TDP-43 by microglia led to NLRP3-dependent IL-18 cleavage (140). Upregulation of microglial NLRP3 was also detected in TDP-43^{Q331K} mice (97), which is in line with our results as we detected microglial pyroptosis activation in the motor cortex of symptomatic TDP-43^{A315T} mice (**Chapter II**). TDP-43 has also closely been linked with pyroptosis activation in the context of NF κ B signaling (313). It was shown that TDP-43 acts as a suppressor of the NF κ B transactivation pathway by inhibiting NF κ B nuclear translocation, with a loss of TDP-43 leading to increased nuclear localization of NF κ B subunits upon TNF α stimulation (257). Indeed, TDP-43 interacts with NF κ B and can function as a co-activator of the NF κ B signaling pathway (314). Conversely, a recent study demonstrated that inhibition of NF κ B could rescue TDP-43 proteinopathy and attenuate TDP-43-related

neurodegeneration in TDP-43 transgenic mouse models (315). Thus, evidence points towards an important role for TDP-43 in the activation of pyroptosis in ALS, although this is likely due to TDP-43 LOF or the presence of toxic soluble oligomers, and not attributable to aggregated forms of TDP-43.

Although we found a correlation between pTDP-43 pathology and necroptosis activation in the hippocampus of ALS/FTLD-TDP cases, a direct link is less obvious. As discussed in **Chapter I** of this thesis, GVD displays necrosome as well as autophagy components, and might thus reflect the accumulation of the necrosome on autophagy machinery, which can serve as a scaffold. Furthermore, as discussed earlier on, autophagy and necroptosis mechanisms are entangled, as suppression of autophagic flux enhances necroptosis, while activation of autophagy inhibits necroptosis (151,155,157). Autophagy has extensively been studied in the context of TDP-43 pathology. As such, stimulation of autophagy improved TDP-43 clearance and localization *in vitro* (64). Indeed, (pathological) TDP-43 is a substrate of autophagy, while in turn TDP-43 aggregation was shown to negatively influence the autophagy machinery (61,66,160). This is supportive of a toxic gain-of-function (GOF) of TDP-43, implying that the mislocalization and cytoplasmic aggregation of TDP-43 confers cellular toxicity.

In recent years, the involvement of TDP-43 in cytoskeletal disturbances in ALS has become clearer. It was shown that *TARDBP* mutations in iPSC-derived motor neurons not only lead to the cytoplasmic mislocalization and accumulation of phosphorylated TDP-43, but also to defects in mitochondrial transport along the axon. The inhibition of histone deacetylase 6 (HDAC6) could rescue this phenotype (169). HDAC6 is an enzyme that can deacetylate lysine residues from histones as well as for example α -tubulin. Thus, HDAC6 inhibition leads to higher α -tubulin acetylation levels, which is important to maintain axonal transport. Furthermore, HDAC6 plays a role in autophagy, which might explain the decreased protein aggregation following HDAC6 inhibition in the above study (302). Interestingly, TDP-43 and FUS were shown to associate with *HDAC6* mRNA, and knockdown of either of these RNA-binding proteins led to a reduced expression of *HDAC6* mRNA (316), hinting towards a possible mechanism of axonal dysregulation by pathological TDP-43. Alternatively, it was suggested that pathological protein aggregates could physically block axonal transport (213). Apart from HDAC6, TDP-43 was shown to interact with MTs, mediating the axonal transport of mRNAs from the soma to distal compartments, including the NMJ, while also being transported along axons itself. Mutations in *TARDBP* impaired axonal transport of mRNA (75,172,317). Finally, TDP-43 was shown to interact with other cytoskeletal proteins, such as PFN1 (318). Thus, an important role for TDP-43 in cytoskeletal dynamics is emerging, linking *TARDBP* mutations and protein aggregation in general to axonal transport deficits.

Overall, it is clear that TDP-43 is entangled in multiple pathological pathways and that it plays a central role in ALS. However, it is still debated whether this occurs through LOF or gain-of-function (GOF) mechanisms. Specifically, the role of TDP-43 aggregates is questioned, as numerous *in vivo* and *in vitro* studies demonstrated neurotoxicity in the absence of TDP-43 cytoplasmic aggregation, suggestive of a LOF mechanism or toxicity conferred by cytoplasmic misfolded and/or oligomeric TDP-43 (319). Thus, the balance between nuclear and cytoplasmic TDP-43, as well as the total level of TDP-43, which is controlled via autoregulatory mechanisms, deems crucial. Loss of nuclear TDP-43 is a typical hallmark of ALS, in addition to cytoplasmic aggregates. In symptomatic TDP-43^{A315T} mice, we observed clearance of TDP-43 from the nucleus in motor neurons in the motor cortex, in the absence of TDP-43 pathological aggregates (**Chapter II**). This supports a LOF hypothesis, as these mice displayed motor neurons loss and clinical symptoms of paralysis, although we cannot fully exclude the possibility that TDP-43 aggregates were not detected with the antibodies used in our study. Furthermore, given the well-known role of TDP-43 in mRNA metabolism, nuclear depletion of TDP-43 and/or dysfunctional TDP-43 can lead to mRNA splicing abnormalities and disturbed axonal trafficking of mRNA, among others (61,66,320). Finally, mislocalization of TDP-43 can alter the nuclear localization of double stranded break (DSB)-repeat proteins, resulting in the accumulation of DNA damage, which is another hallmark observed in ALS motor neurons (66) (Fig. 1).

On the other hand, there is considerable evidence pointing towards a toxic GOF of pathological TDP-43, although not necessarily through the formation of pathological aggregates. For example, Barmada and colleagues showed that the expression of mutant TDP-43 was toxic to neurons, and that this correlated with an increased cytoplasmic localization of TDP-43, but not with aggregate formation (321). Examples of toxicity mediated by TDP-43 aggregates have been mentioned earlier on, such as the inhibition of autophagy or blockage of axonal transport. Altogether, there is compelling evidence for both LOF and toxic GOF mechanisms following TDP-43 mislocalization and aggregation, indicating that both mechanisms are simultaneously at play during ALS pathogenesis. TDP-43 pathology does not only occur following mutations in *TARDBP*, but is present in 97% of ALS patients. It could be postulated that TDP-43 pathology is only a passive bystander in sporadic ALS and ALS caused by mutations in genes involved in other mechanistic pathways unrelated to protein aggregation. However, it is now evident that TDP-43 is involved in multiple pathological mechanisms in ALS, as discussed above. The question remains whether in those circumstances, the initiation of distinct pathogenic pathways, such as cytoskeletal dysfunction, converge to TDP-43 pathology, with the initiation of TDP-43 pathology as a requirement for motor neuron death, or if the induced TDP-43 pathology only enhances/accelerates the development of full-blown ALS pathology, through LOF and/or GOF mechanisms, leading to neurodegeneration.

5. Concluding remarks and future perspectives

Taken together, the findings obtained in this thesis contribute to a better understanding of the mechanisms underlying the pathogenesis of neuronal and axonal degeneration in ALS. Our results point towards a role for pyroptosis, but not necroptosis in ALS (**Chapter I & II**). Specifically, we showed microglial pyroptosis activation in the *post-mortem* ALS motor cortex as well as in TDP-43^{A315T} transgenic mice, which correlated with neuronal loss. Based on our results as well as current literature regarding cell death mechanisms in ALS, it deems important to take into account the overlap of multiple regulated types of cell death. Furthermore, elucidating the role of autophagy in cellular demise will be an interesting avenue due to its emerging role in regulated cell death, but also because mediating autophagy is of major interest in the context of alleviating protein aggregation. Importantly, the role of non-neuronal cells, such as microglia, should not be disregarded, as we detected pyroptosis activation specifically in microglia, and this might affect neuronal health and survival. Of note, astrocytes and oligodendrocytes were previously also shown to play a role in ALS disease pathogenesis (292), and should thus be taken into account as well. It is important to bear in mind that findings based on *post-mortem* brain and spinal cord tissue have limitations, as they only represent the end-stage of the disease. Therefore, further *in vivo* and *in vitro* research is needed to elucidate the exact mechanisms of pyroptosis activation during the course of the disease, as well as its contribution to the pathogenesis of ALS. In these models, the aspect of aging should be taken into account, as this remains one of the major risk factors for ALS.

Our findings on *TUBA4A* based on *post-mortem* human tissue as well as zebrafish experiments (**Chapter III & IV**) corroborate a major role for cytoskeletal disturbances in ALS. Moreover, it has become clear that cytoskeletal dysfunction can be a driver of disease onset. How this leads to the typical TDP-43 pathology observed in patients with mutations in cytoskeletal genes is still unclear, as well as to what extent TDP-43 is involved in disease pathogenesis in these cases. The same is true for patients with sporadic ALS, for whom the cause of the disease is still unclear, although it probably results from a combination of genetic and environmental factors. Also here, TDP-43 pathological aggregates are omnipresent. TDP-43 deems to play an important role in multiple ALS-related pathogenic mechanisms, likely both via LOF and GOF mechanisms.

In conclusion, the results obtained in this thesis point towards an important role for microglial pyroptosis activation in neuronal demise on the one hand, and on the other hand indicate cytoskeletal disturbances as a potential initiator of the disease. It will be crucial to find out how distinct ALS-related pathological mechanisms, such as protein aggregation, mitochondrial dysfunction, pyroptosis activation, DNA damage and cytoskeletal instability, are interconnected, as well as how ALS is initiated in different subtypes of the disease (familial versus sporadic ALS). From genetic studies, it has become

clear that ALS disease onset can initiate from different pathogenic pathways. In familial ALS, this likely only commences after a second trigger, in addition to the genetic mutation, such as cellular stress due to aging or alterations in the expression levels of certain proteins. Initiation of these distinct pathogenic pathways then eventually could lead to a similar final picture of full-blown pathology, giving rise to the typical motor neuron degeneration observed in ALS, which presumably occurs through combined dying-backward and dying-forward mechanisms. In sporadic ALS, however, it remains unclear how the pathogenic cascade is initiated, and whether this is similar in all sporadic cases. Ultimately, ALS appears to be a multifactorial disease, and it will be key to elucidate the pathogenicity of distinct affected pathways in order to achieve a multi-targeted approach that can be of benefit for the majority of ALS patients, which do not have a clear genetic cause of the disease. Herewith, the discovery of better biomarkers, as well as panels of genetic risk factors, will aid to detect the (sporadic) disease at early stages to prevent motor neuron degeneration and the consequent denervation of muscle tissue in patients that suffer from this devastating disease.

Scientific acknowledgements and personal contributions

Scientific acknowledgements

This work was performed under the supervision of Professors Dr. Dietmar R. Thal, Dr. Philip Van Damme and Dr. Ludo Van Den Bosch. Evelien Van Schoor is funded by an SB PhD Fellowship of the Research Foundation Flanders (FWO) (1S46219N). Additional financial support for this thesis was obtained from C1 internal KU Leuven funding (C14-17-107), FWO project grants G0F8516N and G065721, the ALS Liga Belgium, the KU Leuven ALS fund 'Een hart voor ALS', 'Laeversfonds voor ALS onderzoek', the E. von Behring Chair for Neuromuscular and Neurodegenerative Disorders, and 'Valéry Perrier Race against ALS fund'. We thank Alicja Ronisz and Simona Ospitalieri for technical assistance, and Dr. Valérie Bercier and Elke Braems for assistance with zebrafish experiments. We would like to acknowledge the contribution of our collaborators, Dr. Mathieu Vandenbulcke, Dr. Rik Vandenberghe, Dr. Markus Otto, Dr. Bernard Hanseeuw, Dr. Jochen Weishaupt, Dr. Albert C. Ludolph, Dr. David Brenner, Dr. Julie van der Zee and Dr. Christine Van Broeckhoven. Finally, we would like to thank the VIB Nucleomics Core for quality control of human RNA samples, Annelies Claeys for assistance with qPCR experiments, Dr. John Landers for providing *TUBA4A* plasmids, Klara Gawor for statistical support, and Dr. Lieselot Dedeene for assistance with DPR assessments. Some figures in the general introduction (Fig. 2 and 7) and Figure 1 in the general discussion were created with Biorender software.

Personal contributions

Evelien Van Schoor, Dietmar R. Thal, Ludo Van Den Bosch and Philip Van Damme were involved in project conceptualization and the experimental design. Evelien Van Schoor performed all the experiments, with the following exceptions:

- Dr. Mathieu Vandenbulcke, Dr. Rik Vandenberghe, Dr. Markus Otto, Dr. Bernard Hanseeuw, Dr. Jochen Weishaupt, Dr. Albert C. Ludolph and Dr. Philip Van Damme performed clinical neurological assessments of the patients included in the thesis manuscript.
- Dr. Dietmar R. Thal performed part of the *post-mortem* neuropathological assessments of the autopsy cases included in the thesis manuscript.
- Alicja Ronisz, Simona Ospitalieri and Sandra O. Tomé performed mouse colony breeding and biobanking, mouse euthanasia, sample collection and microtome sectioning (cf. chapter II).
- Simona Ospitalieri assisted with microtome sectioning, immunohistochemical and immunofluorescence staining of mouse and human tissue samples (cf. chapters I,II).
- Dr. Valérie Bercier and Elke Braems assisted with zebrafish experiments (cf. chapters III, IV).

Conflicts of interest statement

ACL serves on the Advisory Board of Roche Pharma (Basel, Switzerland) and Biogen (Cambridge, MA, US), and on the data and safety monitoring board of Zeneus pharma (Bray, UK). ACL received consulting fees from AB Science (Paris, France), Desitin (Buckinghamshire, UK), Novartis (Basel, Switzerland) and Teva (Jerusalem, Israel). **MV** has clinical trial research agreements on Investigator-Initiated Studies with GE Healthcare (Amersham, UK) and Cerveau Technologies, Inc. (Knoxville, TN, US). **RV**'s institution has a clinical trial agreement (RV as PI) with AbbVie (North Chicago, IL, US), Biogen (Cambridge, MA, US), Genentech (San Francisco, CA, US), Novartis (Basel, Switzerland), Roche (Basel, Switzerland), Johnson and Johnson (New Brunswick, NJ, US) and UCB (Brussels, Belgium). **MO** received honorary from Roche (Basel, Switzerland), Axon Neuroscience (Bratislava, Slovakia) and Biogen (Cambridge, MA, US) for scientific advice. **PVD** participated in advisory board meetings of Pfizer (New York City, NY, US), Biogen (Cambridge, MA, US), Cytokinetics (San Francisco, CA, US), CSL Behring (King of Prussia, PA, US), Ferrer (Barcelona, Spain), UCB (Brussels, Belgium), Argenx (Ghent, Belgium), Muna Therapeutics (Copenhagen, Denmark), Alector (San Francisco, CA, US), Augustine Therapeutics (Leuven, Belgium), Alexion Therapeutics (Boston, MA, US) and QurAlis (Cambridge, MA, US). **LVDB** received speaker honorary from UCB (Brussels, Belgium) and Grünenthal (Aachen, Germany), is head of the Scientific Advisory Board of Augustine Therapeutics (Leuven, Belgium) and is part of the Investment Advisory Board of Droia Ventures (Meise, Belgium). **DRT** received speaker honorary or travel reimbursement from Novartis Pharma AG (Basel Switzerland), UCB (Brussels, Belgium) and GE Healthcare (Amersham, UK), and collaborated with Novartis Pharma AG (Basel, Switzerland), Probiodrug (Halle (Saale), Germany), GE Healthcare (Amersham, UK) and Janssen Pharmaceutical Companies (Beerse, Belgium). The funders had no role in the design of the study; in the collection, analysis or interpretation of data; or in the writing of the thesis manuscript.

References

1. Corcia P, Meininger V. 150th anniversary of Charcot's description of amyotrophic lateral sclerosis. *Brain*. 2019;142:3306–13.
2. Wijesekera LC, Leigh PN. Amyotrophic lateral sclerosis. *Orphanet J Rare Dis*. 2009;4(3).
3. Taylor JP, Brown RH, Cleveland DW. Decoding ALS: From Genes to Mechanism. *Nature*. 2016;539(7628):197–206.
4. Hulisz D. Amyotrophic lateral sclerosis: disease state overview. *Am J Manag Care*. 2018;24:S320–6.
5. Swinnen B, Robberecht W. The phenotypic variability of amyotrophic lateral sclerosis. *Nat Rev Neurol*. 2014;10:661–70.
6. Al-Chalabi A, Hardiman O. The epidemiology of ALS: a conspiracy of genes, environment and time. *Nat Rev Neurol*. 2013;9:617–28.
7. Brooks BR, Miller RG, Swash M, Munsat TL. El Escorial revisited: Revised criteria for the diagnosis of amyotrophic lateral sclerosis. *Amyotroph Lateral Scler Other Mot Neuron Disord*. 2000;1(5):293–9.
8. De Carvalho M, Swash M. Awaji diagnostic algorithm increases sensitivity of El Escorial criteria for ALS diagnosis. *Amyotroph Lateral Scler*. 2009;10(1):53–7.
9. Ludolph A, Drory V, Hardiman O, Nakano I, Ravits J, Robberecht WIM, et al. A revision of the El Escorial criteria - 2015. *Amyotroph Lateral Scler Front Degener*. 2015;16:291–2.
10. Hardiman O, Al-Chalabi A, Chio A, Corr EM, Logroscino G, Robberecht W, et al. Amyotrophic lateral sclerosis. *Nat Rev Dis Prim*. 2017;3(17071).
11. Jaiswal MK. Riluzole and edaravone: A tale of two amyotrophic lateral sclerosis drugs. *Med Res Rev*. 2019;39:733–48.
12. Bensimon G, Lacomblez L, Meininger V. A controlled trial of riluzole in amyotrophic lateral sclerosis. *N Engl J Med*. 1994;330(9):585–91.
13. Abe K, Aoki M, Tsuji S, Itoyama Y, Sobue G, Togo M, et al. Safety and efficacy of edaravone in well defined patients with amyotrophic lateral sclerosis: a randomised, double-blind, placebo-controlled trial. *Lancet Neurol*. 2017;16(7):505–12.
14. Sawada H. Clinical efficacy of edaravone for the treatment of amyotrophic lateral sclerosis. *Expert Opin Pharmacother*. 2017;18(7):735–8.
15. Dorst J, Ludolph AC, Huebers A. Disease-modifying and symptomatic treatment of amyotrophic lateral sclerosis. *Ther Adv Neurol Disord*. 2018;11:1–16.
16. Al Sultan AA, Waller R, Heath PR, Kirby J. The genetics of amyotrophic lateral sclerosis: current insights. *Degener Neurol Neuromuscul Dis*. 2016;6:49–64.
17. Rosen DR, Siddique T, Patterson D, Figlewicz DA, Sapp P, Hentati A, et al. Mutations in Cu/Zn superoxide dismutase gene are associated with familial amyotrophic lateral sclerosis. *Nature*. 1993;362:59–62.
18. Renton AE, Chio A, Traynor BJ. State of play in amyotrophic lateral sclerosis genetics. *Nat Neurosci*. 2014;17(1):17–23.
19. Mejzini R, Flynn LL, Pitout IL, Fletcher S, Wilton SD, Akkari PA. ALS Genetics, Mechanisms, and Therapeutics: Where Are We Now? *Front Neurosci*. 2019;13(1310).
20. Kabashi E, Valdmanis PN, Dion P, Spiegelman D, McConkey BJ, Velde C Vande, et al. TARDBP mutations in individuals with sporadic and familial amyotrophic lateral sclerosis. *Nat Genet*. 2008;40(5):572–4.
21. DeJesus-Hernandez M, Mackenzie IR, Boeve BF, Boxer AL, Baker M, Rutherford NJ, et al. Expanded GGGGCC hexanucleotide repeat in non-coding region of C9ORF72 causes chromosome 9p-linked frontotemporal dementia and amyotrophic lateral sclerosis. *Neuron*. 2011;72(2):245–56.
22. Dedeene L, Van Schoor E, Race V, Moisse M, Vandenberghe R, Poesen K, et al. An ALS case with 38 (G4C2)-repeats in the C9orf72 gene shows TDP-43 and sparse dipeptide repeat protein pathology. *Acta Neuropathol*. 2019;137(5):855–8.
23. Castellanos-Montiel MJ, Chaineau M, Durcan TM. The Neglected Genes of ALS: Cytoskeletal Dynamics Impact Synaptic Degeneration in ALS. *Front Cell Neurosci*. 2020;14(594975).
24. He J, Mangelsdorf M, Fan D, Bartlett P, Brown MA. Amyotrophic Lateral Sclerosis Genetic Studies: From Genome-wide Association Mapping to Genome Sequencing. *Neurosci*. 2015;21(6):599–615.
25. Neumann M, Sampathu DM, Kwong LK, Truax AC, Micsenyi MC, Chou TT, et al. Ubiquitinated TDP-43 in frontotemporal lobar degeneration and Amyotrophic Lateral Sclerosis. *Science*. 2006;314(5796):130–3.
26. Arai T, Hasegawa M, Akiyama H, Ikeda K, Nonaka T, Mori H, et al. TDP-43 is a component of ubiquitin-positive tau-negative inclusions in frontotemporal lobar degeneration and amyotrophic lateral sclerosis. *Biochem Biophys Res Commun*. 2006;351:602–11.
27. Mackenzie IRA, Bigio EH, Ince PG, Geser F, Neumann M, Cairns NJ, et al. Pathological TDP-43 Distinguishes Sporadic Amyotrophic Lateral Sclerosis from Amyotrophic Lateral Sclerosis with SOD1 Mutations. *Ann Neurol*.

- 2007;61:427–34.
28. Vance C, Rogelj B, Hortobágyi T, Vos KJ De, Lumi A, Sreedharan J, et al. Mutations in FUS, an RNA Processing Protein, Cause Familial Amyotrophic Lateral Sclerosis Type 6. *Science*. 2009;323(5918):1208–11.
 29. Buratti E, Baralle FE. Multiple roles of TDP-43 in gene expression, splicing regulation, and human disease. *Front Biosci*. 2008;13:867–78.
 30. Hasegawa M, Arai T, Nonaka T, Kametani F, Yoshida M, Hashizume Y, et al. Phosphorylated TDP-43 in frontotemporal lobar degeneration and amyotrophic lateral sclerosis. *Ann Neurol*. 2008;64:60–70.
 31. Igaz LM, Kwong LK, Chen-Plotkin A, Winton MJ, Unger TL, Xu Y, et al. Expression of TDP-43 C-terminal fragments in vitro recapitulates pathological features of TDP-43 proteinopathies. *J Biol Chem*. 2009;284(13):8516–24.
 32. Geser F, Brandmeir NJ, Kwong LK, Martinez-Lage M, Elman L, McCluskey L, et al. Evidence of Multisystem Disorder in Whole-Brain Map of Pathological TDP-43 in Amyotrophic Lateral Sclerosis. *Arch Neurol*. 2008;65(5):636–41.
 33. Prater KE, Latimer CS, Jayadev S. Glial TDP-43 and TDP-43 induced glial pathology, focus on neurodegenerative proteinopathy syndromes. *Glia*. 2022;70:239–55.
 34. Ash PEA, Bieniek KF, Gendron TF, Caulfield T, Lin W, DeJesus-hernandez M, et al. Unconventional Translation of C9ORF72 GGGGCC Expansion Generates Insoluble Polypeptides Specific to c9FTD/ALS. *Neuron*. 2013;77:639–46.
 35. MacKenzie IR, Arzberger T, Kremmer E, Troost D, Lorenzl S, Mori K, et al. Dipeptide repeat protein pathology in C9ORF72 mutation cases: Clinico-pathological correlations. *Acta Neuropathol*. 2013;126:859–79.
 36. Dedeene L, Van Schoor E, Ospitalieri S, Ronisz A, Weishaupt JH, Otto M, et al. Dipeptide repeat protein and TDP-43 pathology along the hypothalamic–pituitary axis in C9orf72 and non-C9orf72 ALS and FTLTDP cases. *Acta Neuropathol*. 2020;140(5):777–81.
 37. Dedeene L, Van Schoor E, Vandenberghe R, Van Damme P, Poesen K, Thal DR. Circadian sleep/wake-associated cells show dipeptide repeat protein aggregates in C9orf72-related ALS and FTLTDP cases. *Acta Neuropathol Commun*. 2019;7(189).
 38. Mackenzie IRA, Frick P, Grässer FA, Gendron TF, Petrucelli L, Cashman NR, et al. Quantitative analysis and clinico-pathological correlations of different dipeptide repeat protein pathologies in C9ORF72 mutation carriers. *Acta Neuropathol*. 2015;130:845–61.
 39. Carlos AF, Josephs KA. Frontotemporal lobar degeneration with TAR DNA-binding protein 43 (TDP-43): its journey of more than 100 years. *J Neurol*. 2022;269(8):4030–54.
 40. The Lund and Manchester. Clinical and neuropathological criteria for frontotemporal dementia. *J Neurol Neurosurg Psychiatry*. 1994;57:416–8.
 41. Finger EC, Buratti E, Boeve B, Rademakers R. Frontotemporal dementias. Vol. 1281, *Advances in Experimental Medicine and Biology*. 2018.
 42. Neumann M, Lee EB, Mackenzie IR. FTLTDP pathological subtypes: clinical and mechanistic significance. *Adv Exp Med Biol*. 2021;1281:201–17.
 43. Olney NT, Spina S, Miller BL. Frontotemporal dementia. *Neurol Clin*. 2017;35(2):339–74.
 44. Coyle-Gilchrist ITS, Dick KM, Patterson K, Vázquez P, Wehmann E, Wilcox A, et al. Prevalence, characteristics, and survival of frontotemporal lobar degeneration syndromes. *Neurology*. 2016;86:1736–43.
 45. Rascovsky K, Hodges JR, Knopman D, Mendez MF, Kramer JH, Neuhaus J, et al. Sensitivity of revised diagnostic criteria for the behavioural variant of frontotemporal dementia. *Brain*. 2011;134:2456–77.
 46. Gorno-Tempini ML, Hillis AE, Weintraub S, Kertesz A, Mendez M, Cappa SF, et al. Classification of primary progressive aphasia and its variants. *Neurology*. 2011;76:1006–14.
 47. Gazzina S, Manes MA, Padovani A, Borroni B. Clinical and biological phenotypes of frontotemporal dementia: Perspectives for disease modifying therapies. *Eur J Pharmacol*. 2017;817:76–85.
 48. Greaves C V, Rohrer JD. An update on genetic frontotemporal dementia. *J Neurol*. 2019;266:2075–86.
 49. Poorkaj P, Bird TD, Wijsman E, Nemens E, Garruto RM, Anderson L, et al. Tau Is a Candidate Gene for Chromosome 17 Frontotemporal Dementia. *Ann*. 1998;43:815–25.
 50. Rademakers R, Neumann M, Mackenzie IRA. Recent advances in the molecular basis of frontotemporal dementia. *Nat Rev Neurol*. 2012;8(8):423–34.
 51. Cruts M, Gijssels I, van der Zee J, Engelborghs S, Wils H, Pirici D, et al. Null mutations in progranulin cause ubiquitin-positive frontotemporal dementia linked to chromosome 17q21. *Nature*. 2006;442:920–4.
 52. Baker M, Mackenzie IR, Pickering-Brown SM, Gass J, Rademakers R, Lindholm C, et al. Mutations in progranulin cause tau-negative frontotemporal dementia linked to chromosome 17. *Nature*. 2006;442:916–9.
 53. Wagner M, Lorenz G, Volk AE, Brunet T, Edbauer D, Berutti R, et al. Clinico-genetic findings in 509 frontotemporal dementia patients. *Mol Psychiatry*. 2021;26:5824–32.
 54. Abramzon YA, Fratta P, Traynor BJ, Chia R. The Overlapping Genetics of Amyotrophic Lateral Sclerosis and Frontotemporal Dementia. *Front Neurosci*. 2020;14(42).
 55. Panza F, Lozupone M, Seripa D, Daniele A, Watling M, Giannelli G, et al. Development of disease-modifying drugs for frontotemporal dementia spectrum disorders. *Nat Rev Neurol*. 2020;16:213–28.

56. Mackenzie IRA, Neumann M, Baborie A, Sampathu DM, Du Plessis D, Jaros E, et al. A harmonized classification system for FTLD-TDP pathology. *Acta Neuropathol.* 2011;122(1):111–3.
57. Lee EB, Porta S, Baer GM, Xu Y, Suh E, Kwong LK, et al. Expansion of the classification of FTLD-TDP: distinct pathology associated with rapidly progressive frontotemporal degeneration. *Acta Neuropathol.* 2017;134(1):65–78.
58. Tziortzouda P, Van Den Bosch L, Hirth F. Triad of TDP43 control in neurodegeneration: autoregulation, localization and aggregation. *Nat Rev Neurosci.* 2021;22:197–208.
59. Buratti E, Baralle FE. TDP-43: Gumming up neurons through protein-protein and protein-RNA interactions. *Trends Biochem Sci.* 2012;37(6):237–47.
60. Cohen TJ, Lee VMY, Trojanowski JQ. TDP-43 functions and pathogenic mechanisms implicated in TDP-43 proteinopathies. *Trends Mol Med.* 2011;17(11):659–67.
61. Prasad A, Bharathi V, Sivalingam V, Girdhar A, Patel BK. Molecular Mechanisms of TDP-43 Misfolding and Pathology in Amyotrophic Lateral Sclerosis. *Front Mol Neurosci.* 2019;12(25).
62. Baralle M, Buratti E, Baralle FE. The role of TDP-43 in the pathogenesis of ALS and FTLD. *Biochem Soc Trans.* 2013;41(6):1536–40.
63. Maniecka Z, Polyimenidou M. From nucleation to widespread propagation: A prion-like concept for ALS. *Virus Res.* 2015;207:94–105.
64. Barmada SJ, Serio A, Arjun A, Bilican B, Daub A, Ando DM, et al. Autophagy induction enhances TDP-43 turnover and survival in neuronal ALS models. *Nat Chem Biol.* 2014;10(8):677–85.
65. Wegorzewska I, Bell S, Cairns NJ, Miller TM, Baloh RH. TDP-43 mutant transgenic mice develop features of ALS and frontotemporal lobar degeneration. *PNAS.* 2009;106(44):18809–14.
66. Suk TR, Rousseaux MWC. The role of TDP-43 mislocalization in amyotrophic lateral sclerosis. *Mol Neurodegener.* 2020;15(45).
67. Fang Y-S, Tsai K-J, Chang Y-J, Kao P, Woods R, Kuo P-H, et al. Full-length TDP-43 forms toxic amyloid oligomers that are present in frontotemporal lobar dementia-TDP patients. *Nat Commun.* 2014;5(4824).
68. Valle C, Carri MT. Which TDP-43 aggregates are toxic in ALS? *Oncotarget.* 2016;7(50):81973–4.
69. Berning BA, Walker AK. The pathobiology of TDP-43 C-terminal fragments in ALS and FTLD. *Front Neurosci.* 2019;13(335).
70. Igaz LM, Kwong LK, Xu Y, Truax AC, Uryu K, Neumann M, et al. Enrichment of C-Terminal Fragments in TAR DNA-Binding Protein-43 Cytoplasmic Inclusions in Brain but not in Spinal Cord of Frontotemporal Lobar Degeneration and Amyotrophic Lateral Sclerosis. *Am J Pathol.* 2008;173(1):182–94.
71. Ravits JM, La Spada AR. ALS motor phenotype heterogeneity, focality, and spread: deconstructing motor neuron degeneration. *Neurology.* 2009;73:805–11.
72. Brettschneider J, Del Tredici K, Toledo JB, Robinson JL, Irwin DJ, Grossman M, et al. Stages of pTDP-43 pathology in amyotrophic lateral sclerosis. *Ann Neurol.* 2013;74(1):20–38.
73. Brettschneider J, Del Tredici K, Irwin DJ, Grossman M, Robinson JL, Toledo JB, et al. Sequential distribution of pTDP-43 pathology in behavioral variant frontotemporal dementia (bvFTD). *Acta Neuropathol.* 2014;127:423–39.
74. Braak H, Brettschneider J, Ludolph AC, Lee VM, Trojanowski JQ, Del Tredici K. Amyotrophic lateral sclerosis - a model of corticofugal axonal spread. *Nat Rev Dis Prim.* 2013;9(12):708–14.
75. Fallini C, Bassell GJ, Rossoll W. The ALS disease protein TDP-43 is actively transported in motor neuron axons and regulates axon outgrowth. *Hum Mol Genet.* 2012;21(16):3703–18.
76. Tomé SO, Vandenberghe R, Ospitalieri S, Van Schoor E, Tousseyn T, Otto M, et al. Distinct molecular patterns of TDP-43 pathology in Alzheimer's disease: relationship with clinical phenotypes. *Acta Neuropathol Commun.* 2020;8(61).
77. Josephs KA, Murray ME, Whitwell JL, Parisi JE, Petrucelli L, Jack CR, et al. Staging TDP-43 pathology in Alzheimer's disease. *Acta Neuropathol.* 2014;127:441–50.
78. Josephs KA, Murray ME, Whitwell JL, Tosakulwong N, Weigand SD, Petrucelli L, et al. Updated TDP-43 in Alzheimer's disease staging scheme. *Acta Neuropathol.* 2016;131:571–85.
79. Nelson PT, Dickson DW, Trojanowski JQ, Jack CR, Boyle PA, Arfanakis K, et al. Limbic-predominant age-related TDP-43 encephalopathy (LATE): consensus working group report. *Brain.* 2019;142:1503–27.
80. Smethurst P, Sidle KCL, Hardy J. Prion-like mechanisms of transactive response DNA binding protein of 43kDa (TDP-43) in amyotrophic lateral sclerosis (ALS). *Neuropathol Appl Neurobiol.* 2015;41:578–97.
81. Yang C, Tan W, Whittle C, Qiu L, Cao L, Akbarian S, et al. The C-terminal TDP-43 fragments have a high aggregation propensity and harm neurons by a dominant-negative mechanism. *PLoS One.* 2010;5(12):e15878.
82. Zhang Y-J, Xu Y-F, Cook C, Gendron TF, Roettges P, Link CD, et al. Aberrant cleavage of TDP-43 enhances aggregation and cellular toxicity. *PNAS.* 2009;106(18):7607–12.
83. Furukawa Y, Kaneko K, Watanabe S, Yamanaka K, Nukina N. A seeding reaction recapitulates intracellular formation of sarkosyl-insoluble transactivation response element (TAR) DNA-binding protein-43 inclusions. *J Biol Chem.* 2011;286(21):18664–72.

84. Nonaka T, Masuda-Suzukake M, Arai T, Hasegawa Y, Akatsu H, Obi T, et al. Prion-like Properties of Pathological TDP-43 Aggregates from Diseased Brains. *Cell Rep.* 2013;4:124–34.
85. Feiler MS, Strobel B, Freischmidt A, Helfferich AM, Kappel J, Brewer BM, et al. TDP-43 is intercellularly transmitted across axon terminals. *J Cell Biol.* 2015;211(4):897–911.
86. Smethurst P, Newcombe J, Troakes C, Simone R, Chen YR, Patani R, et al. In vitro prion-like behaviour of TDP-43 in ALS. *Neurobiol Dis.* 2016;96:236–47.
87. Ishii T, Kawakami E, Endo K, Misawa H, Watabe K. Formation and spreading of TDP-43 aggregates in cultured neuronal and glial cells demonstrated by time-lapse imaging. *PLoS One.* 2017;12(6):e0179375.
88. Ding X, Ma M, Teng J, Teng RKF, Zhou S, Yin J, et al. Exposure to ALS-FTD-CSF generates TDP-43 aggregates in glioblastoma cells through exosomes and TNTs-like structure. *Oncotarget.* 2015;6(27):24178–91.
89. Shimonaka S, Nonaka T, Suzuki G, Hisanaga SI, Hasegawa M. Templated aggregation of TAR DNA-binding protein of 43 kDa (TDP-43) by seeding with TDP-43 peptide fibrils. *J Biol Chem.* 2016;291(17):8896–907.
90. Porta S, Xu Y, Restrepo CR, Kwong LK, Zhang B, Brown HJ, et al. Patient-derived frontotemporal lobar degeneration brain extracts induce formation and spreading of TDP-43 pathology in vivo. *Nat Commun.* 2018;9(4220).
91. Laferrière F, Maniecka Z, Pérez-Berlanga M, Hruska-Plochan M, Gilhespy L, Hock EM, et al. TDP-43 extracted from frontotemporal lobar degeneration subject brains displays distinct aggregate assemblies and neurotoxic effects reflecting disease progression rates. *Nat Neurosci.* 2019;22:65–77.
92. De Rossi P, Lewis AJ, Furrer J, De Vos L, Demeter T, Zhong W, et al. FTLD-TDP assemblies seed neoaggregates with subtype-specific features via a prion-like cascade. *EMBO Rep.* 2021;22(e53877).
93. Smethurst P, Risse E, Tyzack GE, Mitchell JS, Taha DM, Chen Y, et al. Distinct responses of neurons and astrocytes to TDP-43 proteinopathy in amyotrophic lateral sclerosis. *Brain.* 2020;143:430–40.
94. Pokrishevsky E, Grad LI, Cashman NR. TDP-43 or FUS-induced misfolded human wild-type SOD1 can propagate intercellularly in a prion-like fashion. *Sci Rep.* 2016;6(22155).
95. Morrice JR, Gregory-Evans CY, Shaw CA. Necroptosis in amyotrophic lateral sclerosis and other neurological disorders. *Biochim Biophys Acta.* 2017;1863:347–53.
96. Sellier C, Campanari M, Corbier CJ, Gaucherot A, Kolb-Cheynel I, Oulad-abdelghani M, et al. Loss of C9ORF72 impairs autophagy and synergizes with polyQ Ataxin-2 to induce motor neuron dysfunction and cell death. *EMBO J.* 2016;35(12):1276–97.
97. Deora V, Lee JD, Albornoz EA, Mcalary L, Jagaraj CJ, Robertson AAB, et al. The microglial NLRP3 inflammasome is activated by amyotrophic lateral sclerosis proteins. *Glia.* 2019;68(2):407–21.
98. Re DB, Verche V Le, Yu C, Amoroso MW, Politi KA, Phani S, et al. Necroptosis drives motor neuron death in models of both sporadic and familial ALS. *Neuron.* 2014;81(5):1001–8.
99. Ito Y, Ofengeim D, Najafav A, Das S, Saberi S, Li Y, et al. RIPK1 mediates axonal degeneration by promoting inflammation and necroptosis in ALS. *Science.* 2016;353(6299):603–8.
100. Pasparakis M, Vandenabeele P. Necroptosis and its role in inflammation. *Nature.* 2015;517:311–20.
101. Grootjans S, Vanden Berghe T, Vandenabeele P. Initiation and execution mechanisms of necroptosis: an overview. *Cell Death Differ.* 2017;24:1184–95.
102. Elmore S. Apoptosis: A Review of Programmed Cell Death. *Toxicol Pathol.* 2007;35(4):495–516.
103. Yuan J, Amin P, Ofengeim D. Necroptosis and RIPK1-mediated neuroinflammation in CNS diseases. *Nat Rev Neurosci.* 2019;20:19–33.
104. Zhang S, Tang M, Luo H, Shi C, Xu Y. Necroptosis in neurodegenerative diseases: a potential therapeutic target. *Cell Death Dis.* 2017;8(e2905).
105. Wegner KW, Saleh D, Degtrev A. Complex pathologic roles of RIPK1 and RIPK3: moving beyond necroptosis. *Trends Pharmacol Sci.* 2017;38(3):202–25.
106. Wittkopf N, Günther C, Martini E, He G, Amann K, He YW, et al. Cellular FLICE-like inhibitory protein secures intestinal epithelial cell survival and immune homeostasis by regulating caspase-8. *Gastroenterology.* 2013;145(6):1369–79.
107. Moriwaki K, Chan FKM. RIP3: a molecular switch for necrosis and inflammation. *Genes Dev.* 2013;27:1640–9.
108. Xu D, Jin T, Zhu H, Chen H, Ofengeim D, Zhu C, et al. TBK1 Suppresses RIPK1-Driven Apoptosis and Inflammation during Development and in Aging. *Cell.* 2018;174:1477–1491.e19.
109. Raoul C, Estévez AG, Nishimune H, Cleveland DW, deLapeyrière O, Henderson CE, et al. Motoneuron death triggered by a specific pathway downstream of Fas: potentiation by ALS-linked SOD1 mutations. *Neuron.* 2002;35:1067–83.
110. Vande Walle L, Lamkanfi M. Pyroptosis. *Curr Biol.* 2016;26(13):R568–72.
111. Galluzzi L, Vitale I. Molecular mechanisms of cell death: recommendations of the Nomenclature Committee on Cell Death 2018. *Cell Death Differ.* 2018;25:486–541.
112. Fritsch M, Günther SD, Schwarzer R, Albert MC, Schorn F, Werthenbach JP, et al. Caspase-8 is the molecular switch for apoptosis, necroptosis and pyroptosis. *Nature.* 2019;575:683–7.
113. Zhao J, Jitkaew S, Cai Z, Choksi S, Li Q, Luo J, et al. Mixed lineage kinase domain-like is a key receptor interacting

- protein 3 downstream component of TNF-induced necrosis. *PNAS*. 2012;109(14):5322–7.
114. Zhang D-W, Shao J, Lin J, Zhang N, Lu B-J, Lin S-C, et al. RIP3, an energy metabolism regulator that switches TNF-induced cell death from apoptosis to necrosis. *Science*. 2009;325:332–6.
 115. Sun L, Wang H, Wang Z, He S, Chen S, Liao D, et al. Mixed Lineage Kinase Domain-like Protein Mediates Necrosis Signaling Downstream of RIP3 Kinase. *Cell*. 2012;148:213–27.
 116. Ros U, Peña-Blanco A, Hänggi K, Kunzendorf U, Krautwald S, Wong WWL, et al. Necroptosis Execution Is Mediated by Plasma Membrane Nanopores Independent of Calcium. *Cell Rep*. 2017;19:175–87.
 117. Chen X, Li W, Ren J, Huang D, He W, Song Y, et al. Translocation of mixed lineage kinase domain-like protein to plasma membrane leads to necrotic cell death. *Cell Res*. 2014;24:105–21.
 118. Wang T, Perera ND, Chiam MDF, Cuic B, Wanniarachchillage N, Tomas D, et al. Necroptosis is dispensable for motor neuron degeneration in a mouse model of ALS. *Cell Death Differ*. 2020;27:1728–39.
 119. Dermentzaki G, Politi KA, Lu L, Mishra V, Pérez-Torres EJ, Sosunov AA, et al. Deletion of Ripk3 prevents motor neuron death In Vitro but not In Vivo. *eNeuro*. 2019;6(1):e0308-18.
 120. Guan Y, Han F. Key Mechanisms and Potential Targets of the NLRP3 Inflammasome in Neurodegenerative Diseases. *Front Integr Neurosci*. 2020;14(37).
 121. Xie Z, Zhao G. Pyroptosis and neurological diseases. *Neuroimmunol Neuroinflammation*. 2014;1(2):60–5.
 122. Ma Y, Jiang J, Gao Y, Shi T, Zhu X, Zhang K, et al. Research progress of the relationship between pyroptosis and disease. *AM J Transl Res*. 2018;10(7):2213–9.
 123. Zhou K, Shi L, Wang Y, Chen S, Zhang J. Recent Advances of the NLRP3 Inflammasome in Central Nervous System Disorders. *J Immunol Res*. 2016;2016(9238290):9238290.
 124. Denes A, Lopez-Castejon G, Brough D. Caspase-1: is IL-1 just the tip of the ICEberg? *Cell Death Dis*. 2012;3(e338).
 125. Trageser KJ, Smith C, Herman FJ, Ono K, Pasinetti GM. Mechanisms of Immune Activation by c9orf72-Expansions in Amyotrophic Lateral Sclerosis and Frontotemporal Dementia. *Front Neurosci*. 2019;13(1298).
 126. Song L, Pei L, Yao S, Wu Y, Shang Y. NLRP3 Inflammasome in Neurological Diseases, from Functions to Therapies. *Front Cell Neurosci*. 2017;11(63).
 127. Yap JKY, Pickard BS, Chan EWL, Gan SY. The Role of Neuronal NLRP1 Inflammasome in Alzheimer’s Disease: Bringing Neurons into the Neuroinflammation Game. *Mol Neurobiol*. 2019;56:7741–53.
 128. Frank D, Vince JE. Pyroptosis versus necroptosis: similarities, differences, and crosstalk. *Cell Death Differ*. 2019;26:99–114.
 129. Zahid A, Ismail H, Jin T. Molecular and structural aspects of gasdermin family pores and insights into gasdermin-elicited programmed cell death. *Biochem Soc Trans*. 2021;49:2697–710.
 130. Sborgi L, Rühl S, Mulvihill E, Pipercevic J, Heilig R, Stahlberg H, et al. GSDMD membrane pore formation constitutes the mechanism of pyroptotic cell death. *EMBO J*. 2016;35(16):1766–78.
 131. Piancone F, La Rosa F, Marventano I, Saresella M, Clerici M. The role of the inflammasome in neurodegenerative diseases. *Molecules*. 2021;26(953).
 132. Downs KP, Nguyen H, Dorfleutner A, Stehlik C. An overview of the non-canonical inflammasome. *Mol Aspects Med*. 2020;76(100924).
 133. Heneka MT, Kummer MP, Stutz A, Delekate A, Saecker A, Griep A, et al. NLRP3 is activated in Alzheimer’s disease and contributes to pathology in APP/PS1 mice. *Nature*. 2013;493(7434):674–8.
 134. Wang X, Chi J, Huang D, Ding L, Zhao X, Jiang L, et al. α -synuclein promotes progression of Parkinson’s disease by upregulating autophagy signaling pathway to activate NLRP3 inflammasome. *Exp Ther Med*. 2020;19:931–8.
 135. Bellezza I, Grottelli S, Costanzi E, Scarpelli P, Pigna E, Morozzi G, et al. Peroxynitrite Activates the NLRP3 Inflammasome Cascade in SOD1(G93A) Mouse Model of Amyotrophic Lateral Sclerosis. *Mol Neurobiol*. 2018;55:2350–61.
 136. Debye B, Schmülling L, Zhou L, Rune G, Beyer C, Johann S. Neurodegeneration and NLRP3 inflammasome expression in the anterior thalamus of SOD1(G93A) ALS mice. *Brain Pathol*. 2018;28:14–27.
 137. Johann S, Heitzer M, Kanagaratnam M, Goswami A, Rizo T, Weis J, et al. NLRP3 inflammasome is expressed by astrocytes in the SOD1 mouse model of ALS and in human sporadic ALS patients. *Glia*. 2015;63:2260–73.
 138. Gugliandolo A, Giaccoppo S, Bramanti P, Mazzon E. NLRP3 Inflammasome Activation in a Transgenic Amyotrophic Lateral Sclerosis Model. *Inflammation*. 2018;41(1):93–103.
 139. Meissner F, Molawi K, Zychlinsky A. Mutant superoxide dismutase 1-induced IL-1 β accelerates ALS pathogenesis. *PNAS*. 2010;107(29):13046–50.
 140. Leal-Lasarte M, Franco JM, Labrador-garrido A, Pozo D, Roodveldt C. Extracellular TDP-43 aggregates target MAPK/MAK/MRK overlapping kinase (MOK) and trigger caspase-3 / IL-18 signaling in microglia. *FASEB*. 2017;7:2797–816.
 141. Zhao W, Beers DR, Bell S, Wang J, Wen S, Baloh RH, et al. TDP-43 activates microglia through NF- κ B and NLRP3 inflammasome. *Exp Neurol*. 2015;273:24–35.
 142. Italiani P, Carlesi C, Giungato P, Puxeddu I, Borroni B, Bossù P, et al. Evaluating the levels of interleukin-1 family

- cytokines in sporadic amyotrophic lateral sclerosis. *J Neuroinflammation*. 2014;11(94).
143. Moreno-García L, Miana-Mena FJ, Moreno-Martínez L, de la Torre M, Lunetta C, Tarlarini C, et al. Inflammasome in ALS Skeletal Muscle: NLRP3 as a Potential Biomarker. *Int J Mol Sci*. 2021;22(2523).
 144. Banerjee P, Elliott E, Rifai OM, O'Shaughnessy J, McDade K, Abrahams S, et al. NLRP3 inflammasome as a key molecular target underlying cognitive resilience in amyotrophic lateral sclerosis. *J Pathol*. 2022;256:262–8.
 145. Yu L, Chen Y, Tooze SA. Autophagy pathway: Cellular and molecular mechanisms. *Autophagy*. 2018;14(2):207–15.
 146. Mackeh R, Perdiz D, Lorin S, Codogno P, Poüs C. Autophagy and microtubules - new story, old players. *J Cell Sci*. 2013;126:1071–80.
 147. Geeraert C, Ratier A, Pfisterer SG, Perdiz D, Cantaloube I, Rouault A, et al. Starvation-induced hyperacetylation of tubulin is required for the stimulation of autophagy by nutrient deprivation. *J Biol Chem*. 2010;285(31):24184–94.
 148. Velazquez AFC, Jackson WT. So Many Roads : the Multifaceted Regulation of Autophagy Induction. *Mol Cell Biol*. 2018;38(21):e00303-18.
 149. Casterton RL, Hunt RJ, Fanto M. Patho-mechanism Heterogeneity in the Amyotrophic Lateral Sclerosis and Frontotemporal Dementia Disease Spectrum: Providing Focus through the Lens of Autophagy. *J Mol Biol*. 2020;432(8):2692–713.
 150. Frank D, Vaux DL, Murphy JM, Vince JE, Lindqvist LM. Activated MLKL attenuates autophagy following its translocation to intracellular membranes. *J Cell Sci*. 2019;132(5):jcs220996.
 151. Napoletano F, Baron O, Vandenabeele P, Mollereau B, Fanto M. Intersections between Regulated Cell Death and Autophagy. *Trends Cell Biol*. 2019;29(4):323–38.
 152. Doherty J, Baehrecke EH. Life, death and autophagy. *Nat Cell Biol*. 2018;20:1110–7.
 153. Denton D, Kumar S. Autophagy-dependent cell death. *Cell Death Differ*. 2019;26:605–16.
 154. Baron O, Boudi A, Dias C, Schilling M, Nölle A, Vizcay-Barrena G, et al. Karyoptosis: a novel type of cell death caused by chronic autophagy inhibition. *Curr Biol*. 2018;14(4):722–3.
 155. Abe K, Yano T, Tanno M, Miki T, Kuno A, Sato T, et al. mTORC1 inhibition attenuates necroptosis through RIP1 inhibition-mediated TFEB activation. *Biochim Biophys Acta - Mol Basis Dis*. 2019;1865(165552).
 156. Goodall ML, Fitzwalter BE, Zahedi S, Wu M, Rodriguez D, Mulcahy-Levy JM, et al. The Autophagy Machinery Controls Cell Death Switching between Apoptosis and Necroptosis. *Dev Cell*. 2016;37:337–49.
 157. Ogasawara M, Yano T, Tanno M, Abe K, Ishikawa S, Miki T, et al. Suppression of autophagic flux contributes to cardiomyocyte death by activation of necroptotic pathways. *J Mol Cell Cardiol*. 2017;108:203–13.
 158. Hiji M, Takahashi T, Fukuba H, Yamashita H, Kohriyama T. White matter lesions in the brain with frontotemporal lobar degeneration with motor neuron disease: TDP-43-immunopositive inclusions co-localize with p62, but not ubiquitin. *Acta Neuropathol*. 2008;116:183–91.
 159. Wang I, Guo B, Liu Y, Wu C, Yang C, Tsai K, et al. Autophagy activators rescue and alleviate pathogenesis of a mouse model with proteinopathies of the TAR DNA-binding protein 43. *PNA*. 2012;109(37):15024–9.
 160. Ormeño F, Hormazabal J, Moreno J, Riquelme F, Rios J, Criollo A, et al. Chaperone Mediated Autophagy Degrades TDP-43 Protein and Is Affected by TDP-43 Aggregation. *Front Mol Neurosci*. 2020;13(19).
 161. Nguyen DKH, Thombre R, Wang J. Autophagy as a common pathway in amyotrophic lateral sclerosis. *Neurosci Lett*. 2019;697:34–48.
 162. Fischer LR, Culver DG, Tennant P, Davis AA, Wang M, Castellano-sanchez A, et al. Amyotrophic lateral sclerosis is a distal axonopathy: evidence in mice and man. *Exp Neurol*. 2004;185:232–40.
 163. Dubey J, Ratnakaran N, Koushika SP. Neurodegeneration and microtubule dynamics: death by a thousand cuts. *Front Cell Neurosci*. 2015;9(343).
 164. Nagano S, Araki T. Axonal Transport and Local Translation of mRNA in Neurodegenerative Diseases. *Front Mol Neurosci*. 2021;14(697973).
 165. Moloney EB, Winter F De, Verhaagen J. ALS as a distal axonopathy: molecular mechanisms affecting neuromuscular junction stability in the presymptomatic stages of the disease. *Front Neurosci*. 2014;8(252).
 166. Rouleau GA, Clark AW, Rooke K, Pramatarova A, Krizus A, Suchowersky O, et al. SOD1 mutation is associated with accumulation of neurofilaments in amyotrophic lateral sclerosis. *Ann Neurol*. 1996;39:128–31.
 167. Xiao S, McLean J, Robertson J. Neuronal intermediate filaments and ALS: A new look at an old question. *Biochim Biophys Acta*. 2006;1762:1001–12.
 168. Bilsland LG, Sahai E, Kelly G, Golding M, Greensmith L, Schiavo G. Deficits in axonal transport precede ALS symptoms in vivo. *PNAS*. 2010;107(47):20523–8.
 169. Fazal R, Boeynaems S, Swijsen A, De Decker M, Fumagalli L, Moisse M, et al. HDAC6 inhibition restores TDP-43 pathology and axonal transport defects in human motor neurons with TARDBP mutations. *EMBO J*. 2021;40(e106177).
 170. Fumagalli L, Young FL, Boeynaems S, De Decker M, Mehta AR, Swijsen A, et al. C9orf72-derived arginine-containing dipeptide repeats associate with axonal transport machinery and impede microtubule-based motility. *Sci Adv*. 2021;7(eabg3013).

171. Guo W, Naujock M, Fumagalli L, Vandoorne T, Baatsen P, Boon R, et al. HDAC6 inhibition reverses axonal transport defects in motor neurons derived from FUS-ALS patients. *Nat Commun.* 2017;8(861).
172. Alami NH, Smith RB, Carrasco M a, Williams L a, Christina S, Han SSW, et al. Axonal transport of TDP-43 mRNA granules in neurons is impaired by ALS-causing mutations. *Neuron.* 2014;81(3):536–43.
173. Ikenaka K, Katsuno M, Kawai K, Ishigaki S, Tanaka F, Sobue G. Disruption of Axonal Transport in Motor Neuron Diseases. *Int J Mol Sci.* 2012;13:1225–38.
174. Figlewicz DA, Krizus A, Martinoli MG, Meininger V, Dib M, Rouleau GA, et al. Variants of the heavy neurofilament subunit are associated with the development of amyotrophic lateral sclerosis. *Hum Mol Genet.* 1994;3(10):1757–61.
175. Côté F, Collard J-F, Julien J-P. Progressive neuronopathy in transgenic mice expressing the human neurofilament heavy gene: A mouse model of amyotrophic lateral sclerosis. *Cell.* 1993;73(1):35–46.
176. Poesen K, Damme P Van. Diagnostic and Prognostic Performance of Neurofilaments in ALS. *Front Neurol.* 2019;9(1167).
177. Behzadi A, Calderón FP, Tjust AE, Wuolikainen A, Höglund K, Forsberg K, et al. Neurofilaments can differentiate ALS subgroups and ALS from common diagnostic mimics. *Sci Rep.* 2021;11(22128).
178. Wu C, Fallini C, Ticozzi N, Keagle PJ, Sapp PC, Piotrowska K, et al. Mutations in the Profilin 1 Gene Cause Familial Amyotrophic Lateral Sclerosis. *Nature.* 2012;488(7412):499–503.
179. Bercier V, Hubbard JM, Fidelin K, Duroure K, Auer TO, Revenu C, et al. Dynactin1 depletion leads to neuromuscular synapse instability and functional abnormalities. *Mol Neurodegener.* 2019;14(27).
180. Nicolas A, Kenna KP, Renton AE, Ticozzi N, Faghri F, Chia R, et al. Genome-wide Analyses Identify KIF5A as a Novel ALS Gene. *Neuron.* 2018;97:1268–83.
181. Münch C, Rolfs A, Meyer T. Heterozygous S44L missense change of the spastin gene in amyotrophic lateral sclerosis. *Amyotroph Lateral Scler.* 2008;9(4):251–3.
182. Meyer T, Schwan A, Dullinger JS, Brocke J, Hoffmann K-T, Nolte CH, et al. Early-onset ALS with long-term survival associated with spastin gene mutation. *Neurology.* 2005;65(1).
183. Smith BN, Ticozzi N, Fallini C, Gkazi AS, Topp SD, Kenna KP, et al. Exome-wide rare variant analysis identifies TUBA4A mutations associated with familial ALS. *Neuron.* 2014;84(2):324–31.
184. Pensato V, Tiloca C, Corrado L, Bertolin C, Sardone V, Del Bo R, et al. TUBA4A gene analysis in sporadic amyotrophic lateral sclerosis: identification of novel mutations. *J Neurol.* 2015;262(5):1376–8.
185. Breuss MW, Leca I, Gstrein T, Hansen AH, Keays DA. Tubulins and brain development – The origins of functional specification. *Mol Cell Neurosci.* 2017;84:58–67.
186. Clark JA, Yeaman EJ, Blizzard CA, Chuckowree JA, Dickson TC. A Case for Microtubule Vulnerability in Amyotrophic Lateral Sclerosis: Altered Dynamics During Disease. *Front Cell Neurosci.* 2016;10(204).
187. Janke C, Magiera MM. The tubulin code and its role in controlling microtubule properties and functions. *Nat Rev Mol Cell Biol.* 2020;21:307–26.
188. Sferra A, Nicita F, Bertini E. Microtubule dysfunction: a common feature of neurodegenerative diseases. *Int J Mol Sci.* 2020;21(7354).
189. Chakraborti S, Natarajan K, Curiel J, Janke C, Liu J. The Emerging Role of the Tubulin Code: From the Tubulin Molecule to Neuronal Function and Disease. *Cytoskeleton.* 2016;73:521–50.
190. Wall KP, Pagratis M, Armstrong G, Balsbaugh JL, Verbeke E, Pearson CG, et al. Molecular determinants of tubulin's C-terminal tail conformational ensemble. *ACS Chem Biol.* 2016;11:2981–90.
191. Boiarska Z, Passarella D. Microtubule-targeting agents and neurodegeneration. *Drug Discov Today.* 2021;26(2):604–15.
192. Brunden KR, Lee VMY, Smith AB, Trojanowski JQ, Ballatore C. Altered Microtubule Dynamics in Neurodegenerative Disease: Therapeutic Potential of Microtubule-Stabilizing Drugs. *Neurobiol Dis.* 2017;105:328–35.
193. Tischfield MA, Cederquist GY, Gupta ML, Engle EC. Phenotypic spectrum of the tubulin-related disorders and functional implications of disease-causing mutations. *Curr Opin Genet Dev.* 2011;21(3):286–94.
194. Perrone F, Nguyen HP, Van Mossevelde S, Moisse M, Sieben A, Santens P, et al. Investigating the role of ALS genes CHCHD10 and TUBA4A in Belgian FTD-ALS spectrum patients. *Neurobiol Aging.* 2017;51:177.e9-177.e16.
195. Mol MO, Wong TH, Melhem S, Basu S, Viscusi R, Galjart N, et al. Novel TUBA4A Variant Associated With Familial Frontotemporal Dementia. *Neurol Genet.* 2021;7(e596).
196. Okada K, Hata Y, Ichimata S, Yoshida K, Oku Y, Asahi T, et al. An autopsy case of pure nigropathy with TUBA4A nonsense mutation. *Neuropathol Appl Neurobiol.* 2021;47:891–3.
197. Helferich AM, Brockmann SJ, Reinders J, Deshpande D, Holzmann K, Brenner D, et al. Dysregulation of a novel miR-1825/TBCB/TUBA4A pathway in sporadic and familial ALS. *Cell Mol Life Sci.* 2018;75:4301–19.
198. Jiang YM, Yamamoto M, Kobayashi Y, Yoshihara T, Liang Y, Terao S, et al. Gene expression profile of spinal motor neurons in sporadic amyotrophic lateral sclerosis. *Ann Neurol.* 2005;57:236–51.
199. Gurney ME, Pu H, Chiu AY, Dal Canto MC, Polchow CY, Alexander DD, et al. Motor Neuron Degeneration in Mice that Express a Human Cu,Zn Superoxide Dismutase Mutation. *Science.* 1994;264(5166):1772–5.

200. Picher-Martel V, Valdmanis PN, Gould P V, Julien J, Dupré N. From animal models to human disease: a genetic approach for personalized medicine in ALS. *Acta Neuropathol Commun.* 2016;4(70).
201. Giorgio F De, Maduro C, Fisher EMC, Acevedo-Arozena A. Transgenic and physiological mouse models give insights into different aspects of amyotrophic lateral sclerosis. *Dis Model Mech.* 2019;12(dmm037424).
202. Braems E, Tziortzouda P, Van Den Bosch L. Exploring the alternative: Fish, flies and worms as preclinical models for ALS. *Neurosci Lett.* 2021;759(136041).
203. Morrice JR, Gregory-Evans CY, Shaw CA. Animal models of amyotrophic lateral sclerosis: a comparison of model validity. *Neural Regen Res.* 2018;13(12):2050–4.
204. Myszczyńska M, Ferraiuolo L. New In Vitro Models to Study Amyotrophic Lateral Sclerosis. *Brain Pathol.* 2016;26:258–65.
205. Hedges EC, Mehler VJ, Nishimura AL. The Use of Stem Cells to Model Amyotrophic Lateral Sclerosis and Frontotemporal Dementia: From Basic Research to Regenerative Medicine. *Stem Cells Int.* 2016;2016(9279516).
206. Soubannier V, Maussion G, Chaineau M, Sigutova V, Rouleau G, Durcan TM, et al. Characterization of human iPSC-derived astrocytes with potential for disease modeling and drug discovery. *Neurosci Lett.* 2020;731(135028).
207. Preman P, TCW J, Calafate S, Snellinx A, Alfonso-Triguero M, Corthout N, et al. Human iPSC-derived astrocytes transplanted into the mouse brain undergo morphological changes in response to amyloid- β plaques. *Mol Neurodegener.* 2021;16(68).
208. Xu R, Li X, Boreland AJ, Posyton A, Kwan K, Hart RP, et al. Human iPSC-derived mature microglia retain their identity and functionally integrate in the chimeric mouse brain. *Nat Commun.* 2020;11(1577).
209. Iberite F, Gruppioni E, Ricotti L. Skeletal muscle differentiation of human iPSCs meets bioengineering strategies: perspectives and challenges. *Regen Med.* 2022;7(23).
210. Stoklund Dittlau K, Krasnow EN, Fumagalli L, Vandoorne T, Baatsen P, Kerstens A, et al. Human motor units in microfluidic devices are impaired by FUS mutations and improved by HDAC6 inhibition. *Stem Cell Reports.* 2021;16:2213–27.
211. Kunze A, Lengacher S, Dirren E, Aebischer P, Magistretti PJ, Renaud P. Astrocyte–neuron co-culture on microchips based on the model of SOD mutation to mimic ALS. *Integr Biol.* 2013;5(7):964–75.
212. Alami NH, Smith RB, Carrasco MA, Williams LA, Winborn CS, Han SSW, et al. Axonal Transport of TDP-43 mRNA Granules Is Impaired by ALS-Causing Mutations. *Neuron.* 2014;81(3):536–43.
213. Guo W, Stoklund Dittlau K, Van Den Bosch L. Axonal transport defects and neurodegeneration: Molecular mechanisms and therapeutic implications. *Semin Cell Dev Biol.* 2020;99:133–50.
214. Rosenbohm A, Peter RS, Erhardt S, Lulé D, Rothenbacher D, Ludolph AC, et al. Epidemiology of amyotrophic lateral sclerosis in Southern Germany. *J Neurol.* 2017;264:749–57.
215. Müller K, Brenner D, Weydt P, Meyer T, Grehl T, Petri S, et al. Comprehensive analysis of the mutation spectrum in 301 German ALS families. *J Neurol Neurosurg Psychiatry.* 2018;89(8):817–27.
216. Gao J, Wang L, Huntley ML, Perry G, Wang X. Pathomechanisms of TDP-43 in neurodegeneration. *J Neurochem.* 2018;146:7–20.
217. McAleese KE, Walker L, Erskine D, Thomas AJ, McKeith IG, Attems J. TDP-43 pathology in Alzheimer’s disease, dementia with Lewy bodies and ageing. *Brain Pathol.* 2017;27:472–9.
218. Blokhuis AM, Groen EJM, Koppers M, Van Den Berg LH, Pasterkamp RJ. Protein aggregation in amyotrophic lateral sclerosis. *Acta Neuropathol.* 2013;125:777–94.
219. Spiers-Jones TL, Attems J, Thal DR. Interactions of pathological proteins in neurodegenerative diseases. *Acta Neuropathol.* 2017;134:187–205.
220. Cerami C, Marcone A, Galimberti D, Zamboni M, Fenoglio C, Serpente M, et al. Novel evidence of phenotypical variability in the hexanucleotide repeat expansion in chromosome 9. *J Alzheimers Dis.* 2013;35(3):455–62.
221. Koper MJ, Van Schoor E, Ospitalieri S, Vandenbergh R, Vandenbulcke M, Von Arnim CAF, et al. Necrosome complex detected in granulovacuolar degeneration is associated with neuronal loss in Alzheimer’s disease. *Acta Neuropathol.* 2019;139:463–84.
222. Funk KE, Mrak RE, Kuret J. Granulovacuolar degeneration bodies of Alzheimer’s disease resemble late-stage autophagic organelles. *Neuropathol Appl Neurobiol.* 2011;37(3):295–306.
223. Köhler C. Granulovacuolar degeneration: a neurodegenerative change that accompanies tau pathology. *Acta Neuropathol.* 2016;132:339–59.
224. Kumar S, Wirths O, Stüber K, Wunderlich P, Koch P, Theil S, et al. Phosphorylation of the amyloid β -peptide at Ser26 stabilizes oligomeric assembly and increases neurotoxicity. *Acta Neuropathol.* 2016;131:525–37.
225. Schwab C, Demaggio AJ, Ghoshal N, Binder LI, Kuret J, McGeer PL. Casein kinase 1 delta is associated with pathological accumulation of tau in several neurodegenerative diseases. *Neurobiol Aging.* 2000;21:503–10.
226. Kadokura A, Yamazaki T, Kakuda S, Makioka K, Lemere CA, Fujita Y, et al. Phosphorylation-dependent TDP-43 antibody detects intraneuronal dot-like structures showing morphological characters of granulovacuolar degeneration. *Neurosci Lett.* 2009;463:87–92.

227. Thal DR, Tredici K Del, Ludolph AC, Hoozemans JJM. Stages of granulovacuolar degeneration: their relation to Alzheimer's disease and chronic stress response. *Acta Neuropathol.* 2011;122:577–89.
228. Riku Y, Duyckaerts C, Boluda S, Plu I, Ber I Le, Millecamps S, et al. Increased prevalence of granulovacuolar degeneration in C9orf72 mutation. *Acta Neuropathol.* 2019;138(5):783–93.
229. de Carvalho M, Dengler R, Eisen A, England JD, Kaji R, Kimura J, et al. Electrodiagnostic criteria for diagnosis of ALS. *Clin Neurophysiol.* 2008;119(3):497–503.
230. Braak H, Alafuzoff I, Arzberger T, Kretzschmar H, Del Tredici K. Staging of Alzheimer disease-associated neurofibrillary pathology using paraffin sections and immunocytochemistry. *Acta Neuropathol.* 2006;112:389–404.
231. Thal DR, Rüb U, Schultz C, Sassin I, Ghebremedhin E, Del Tredici K, et al. Sequence of A β -protein deposition in the human medial temporal lobe. *J Neuropathol Exp Neurol.* 2000;59(8):733–48.
232. Mirra SS, Heyman A, McKeel DW, Sumi SM, Crain BJ, Brownlee LM, et al. The Consortium to Establish a Registry for Alzheimer's Disease (CERAD): II. Standardization of the neuropathologic assessment of Alzheimer's disease. Vol. 41, *Neurology.* 1991. p. 479–86.
233. Debray S, Race V, Crabbé V, Herdewyn S, Matthijs G, Goris A, et al. Frequency of C9orf72 repeat expansions in amyotrophic lateral sclerosis: a Belgian cohort study. *Neurobiol Aging.* 2013;34:2890.e7-2890.e12.
234. Goodpaster T, Randolph-Habecker J. A Flexible Mouse-On-Mouse Immunohistochemical Staining Technique Adaptable to Biotin-Free Reagents, Immunofluorescence, and Multiple Antibody Staining. *J Histochem Cytochem.* 2014;62(3):197–204.
235. Wiersma VI, van Ziel AM, Vazquez-Sanchez S, Nölle A, Berenjeno-Correa E, Bonaterra-Pastra A, et al. Granulovacuolar degeneration bodies are neuron-selective lysosomal structures induced by intracellular tau pathology. *Acta Neuropathol.* 2019;138:943–70.
236. Köhler C, Dinekov M, Götz J. Granulovacuolar degeneration and unfolded protein response in mouse models of tauopathy and A β amyloidosis. *Neurobiol Dis.* 2014;71:169–79.
237. King A, Sweeney F, Bodi I, Troakes C, Maekawa S, Al-Sarraj S. Abnormal TDP-43 expression is identified in the neocortex in cases of dementia pugilistica, but is mainly confined to the limbic system when identified in high and moderate stages of Alzheimer's disease. *Neuropathology.* 2010;30(4):408–19.
238. Arai T, Mackenzie IRA, Hasegawa M, Nonaka T, Niizato K, Tsuchiya K, et al. Phosphorylated TDP-43 in Alzheimer's disease and dementia with Lewy bodies. *Acta Neuropathol.* 2009;117(2):125–36.
239. Webster CP, Smith EF, Bauer CS, Moller A, Hautbergue GM, Ferraiuolo L, et al. The C9orf72 protein interacts with Rab1a and the ULK 1 complex to regulate initiation of autophagy. *EMBO J.* 2016;35(15):1656–76.
240. Wheeler JR, Matheny T, Jain S, Abrisch R, Parker R. Distinct stages in stress granule assembly and disassembly. *Elife.* 2016;5(e18413).
241. Leskela S, Huber N, Rostalski H, Natunen T, Remes AM, Takalo M, et al. C9orf72 Proteins Regulate Autophagy and Undergo Autophagosomal or Proteasomal Degradation in a Cell Type-Dependent Manner. *Cells.* 2019;8(1223).
242. Waite AJ, Bäumer D, East S, Neal J, Morris HR, Ansorge O, et al. Reduced C9orf72 protein levels in frontal cortex of amyotrophic lateral sclerosis and frontotemporal degeneration brain with the C9ORF72 hexanucleotide repeat expansion. *Neurobiol Aging.* 2014;35(7):1779.e5-1779.e13.
243. Hanna-Addams S, Liu S, Liu H, Chen S, Wang Z. CK1 α , CK1 δ and CK1 ϵ are necrosome components which phosphorylate serine 227 of human RIPK3 to activate necroptosis. *PNAS.* 2019;117(4):1962–70.
244. Bevan-Jones WR, Cope TE, Jones PS, Kaalund SS, Passamonti L, Allinson K, et al. Neuroinflammation and protein aggregation co-localize across the frontotemporal dementia spectrum. *Brain.* 2020;143:1010–26.
245. Bossù P, Salani F, Alberici A, Archetti S, Bellelli G, Galimberti D, et al. Loss of function mutations in the progranulin gene are related to pro-inflammatory cytokine dysregulation in frontotemporal lobar degeneration patients. *J Neuroinflammation.* 2011;8(65).
246. Lu C-H, Allen K, Oei F, Leoni E, Kuhle J, Tree T, et al. Systemic inflammatory response and neuromuscular involvement in amyotrophic lateral sclerosis. *Neuroimmunol Neuroinflammation.* 2016;3:e244.
247. Mccauley ME, Baloh RH. Inflammation in ALS/FTD pathogenesis. *Acta Neuropathol.* 2019;137:715–30.
248. Stadelmann C, Deckwerth TL, Srinivasan A, Bancher C, Jellinger K, Lassmann H. Activation of Caspase-3 in Single Neurons and Autophagic Granules of Granulovacuolar Degeneration in Alzheimer's Disease. *Am J Pathol.* 1999;155(5):1459–66.
249. Su JH, Kesslak JP, Head E, Cotman CW. Caspase-cleaved amyloid precursor protein and activated caspase-3 are co-localized in the granules of granulovacuolar degeneration in Alzheimer's disease and Down's syndrome brain. *Acta Neuropathol.* 2002;104:1–6.
250. Selznick LA, Holtzman DM, Han BH, Gokden M, Srinivasan AN, Johnson EM, et al. In situ immunodetectin of neuronal caspase-3 activation in Alzheimer Disease. *J Neuropathol Exp Neurol.* 1999;58(9):1020–6.
251. Philips T, Robberecht W. Neuroinflammation in amyotrophic lateral sclerosis: role of glial activation in motor neuron disease. *Lancet Neurol.* 2011;10:253–63.
252. Lee J, Hyeon SJ, Im H, Ryu H, Kim Y, Ryu H. Astrocytes and Microglia as Non-cell Autonomous Players in the

- Pathogenesis of ALS. *Exp Neurobiol.* 2016;25(5):233–40.
253. Herdewyn S, Cirillo C, Van Den Bosch L, Robberecht W, Vanden Berghe P, Van Damme P. Prevention of intestinal obstruction reveals progressive neurodegeneration in mutant TDP-43 (A315T) mice. *Mol Neurodegener.* 2014;9(24).
 254. Van Schoor E, Koper MJ, Ospitalieri S, Dedeene L, Tomé SO, Vandenberghe R, et al. Necrosome-positive granulovacuolar degeneration is associated with TDP-43 pathological lesions in the hippocampus of ALS/FTLD cases. *Neuropathol Appl Neurobiol.* 2020;47(2):328–45.
 255. Zhang X, Wang R, Hu D, Sun X, Fujioka H, Lundberg K, et al. Oligodendroglial glycolytic stress triggers inflammasome activation and neuropathology in Alzheimer's disease. *Sci Adv.* 2020;6:eabb8680.
 256. Van Damme P, Robberecht W, Van Den Bosch L. Modelling amyotrophic lateral sclerosis: progress and possibilities. *Dis Model Mech.* 2017;10(5):537–49.
 257. Zhu J, Cynader MS, Jia W. TDP-43 Inhibits NF-κB Activity by Blocking p65 Nuclear Translocation. *PLoS One.* 2015;10(11):e0142296.
 258. Lee J, Hamanaka G, Lo EH, Arai K. Heterogeneity of microglia and their differential roles in white matter pathology. *CNS Neurosci Ther.* 2019;25:1290–8.
 259. Van der Poel M, Ulas T, Mizze MR, Hsiao C, Miedema SSM, Schuurman KG, et al. Transcriptional profiling of human microglia reveals grey-white matter heterogeneity and multiple sclerosis-associated changes. *Nat Commun.* 2019;10(1139).
 260. Hatzipetros T, Bogdanik LP, Tassinari VR, Kidd JD, Moreno AJ, Davis C, et al. C57BL/6J congenic Prp-TDP43A315T mice develop progressive neurodegeneration in the myenteric plexus of the colon without exhibiting key features of ALS. *Brain Res.* 2014;1584:59–72.
 261. Zhang W, Zhang L, Liang B, Schroeder D, Zhang Z, Cox GA, et al. Hyperactive somatostatin interneurons contribute to excitotoxicity in neurodegenerative disorders. *Nat Neurosci.* 2016;19(4):557–9.
 262. Espejo-Porras F, Piscitelli F, Verde R, Ramos JA, Di Marzo V, de Lago E, et al. Changes in the endocannabinoid signaling system in CNS structures of TDP-43 transgenic mice: relevance for a neuroprotective therapy in TDP-43-related disorders. *J Neuroimmune Pharmacol.* 2015;10(2):233–44.
 263. Scotter EL, Chen HJ, Shaw CE. TDP-43 Proteinopathy and ALS: Insights into Disease Mechanisms and Therapeutic Targets. *Neurotherapeutics.* 2015;12(2):352–63.
 264. Mejias NH, Martinez CC, Stephens ME, De Rivero Vaccari JP. Contribution of the inflammasome to inflammation. *J Inflamm.* 2018;15(23).
 265. Kadhim H, Deltenre P, Martin JJ, Sébire G. In-situ expression of Interleukin-18 and associated mediators in the human brain of sALS patients: Hypothesis for a role for immune-inflammatory mechanisms. *Med Hypotheses.* 2016;86:14–7.
 266. Urwin H, Josephs KA, Rohrer JD, Mackenzie IR, Neumann M, Authier A, et al. FUS pathology defines the majority of tau-and TDP-43-negative frontotemporal lobar degeneration. *Acta Neuropathol.* 2010;120:33–41.
 267. Bang J, Spina S, Miller BL. Non-Alzheimer's dementia 1: Frontotemporal dementia. *Lancet.* 2015;386(10004):1672–82.
 268. Braak H, Del Tredici K, Rüb U, De Vos RAI, Jansen Steur ENH, Braak E. Staging of brain pathology related to sporadic Parkinson's disease. *Neurobiol Aging.* 2003;24:197–211.
 269. Braak H, Braak E. Neuropathological stageing of Alzheimer-related changes. *Acta Neuropathol.* 1991;82(4):239–59.
 270. Thal DR, Rüb U, Orantes M, Braak H. Phases of Aβ-deposition in the human brain and its relevance for the development of AD. *Neurology.* 2002;58(12):1791–800.
 271. Maraldi T, Beretti F, Anselmi L, Franchin C, Arrigoni G, Braglia L, et al. Influence of selenium on the emergence of neuro tubule defects in a neuron-like cell line and its implications for amyotrophic lateral sclerosis. *Neurotoxicology.* 2019;75:209–20.
 272. Bradford YM, Van Slyke CE, Ruzicka L, Singer A, Eagle A, Fashena D, et al. Zebrafish Information Network, the knowledgebase for Danio rerio research. *Genetics.* 2022;220(4).
 273. Swinnen B, Abreu AB, Gendron TF, Boeynaems S, Bogaert E, Nuyts R, et al. A zebrafish model for C9orf72 ALS reveals RNA toxicity as a pathogenic mechanism. *Acta Neuropathol.* 2018;135:427–43.
 274. Kabashi E, Bercier V, Lissouba A, Liao M, Brustein E, Rouleau GA, et al. FUS and TARDBP but Not SOD1 Interact in Genetic Models of Amyotrophic Lateral Sclerosis. *PLoS Genet.* 2011;7(8):e1002214.
 275. Van Schoor E, Vandenbulcke M, Vandenberghe R, van der Zee J, Van Broeckhoven C, Otto M, et al. Frontotemporal Lobar Degeneration Case with an N-Terminal TUBA4A Mutation Exhibits Reduced TUBA4A Levels in the Brain and TDP-43 Pathology. *Biomolecules.* 2022;12(440).
 276. Van Hoecke A, Schoonaert L, Lemmens R, Timmers M, Staats KA, Laird AS, et al. EPHA4 is a disease modifier of amyotrophic lateral sclerosis in animal models and in humans. *Nat Med.* 2012;18(9):1418–24.
 277. Laird AS, van Hoecke A, De Muynck L, Timmers M, van den Bosch L, Van Damme P, et al. Progranulin is neurotrophic in vivo and protects against a mutant TDP-43 induced axonopathy. *PLoS One.* 2010;5(10):e13368.
 278. Moutin MJ, Bosc C, Peris L, Andrieux A. Tubulin post-translational modifications control neuronal development

- and functions. *Dev Neurobiol.* 2021;81(3):253–72.
279. Sanyal C, Pietsch N, Ramirez Rios S, Peris L, Carrier L, Moutin M-J. The detyrosination/re-tyrosination cycle of tubulin and its role and dysfunction in neurons and cardiomyocytes. *Semin Cell Dev Biol.* 2021;
 280. Nijssen J, Comley LH, Hedlund E. Motor neuron vulnerability and resistance in amyotrophic lateral sclerosis. *Acta Neuropathol.* 2017;133(6):863–85.
 281. Sathasivam S, Shaw PJ. Apoptosis in amyotrophic lateral sclerosis: what is the evidence? *Lancet Neurol.* 2005;4:500–9.
 282. Kang T, Yang S, Toth B, Kovalenko A, Wallach D. Caspase-8 Blocks Kinase RIPK3-Mediated Activation of the NLRP3 Inflammasome. *Immunity.* 2013;38:27–40.
 283. Yang D, Kumar A, Stavrides P, Peterson J, Peterhoff CM, Pawlik M, et al. Neuronal Apoptosis and Autophagy Cross Talk in Aging PS/APP Mice, a Model of Alzheimer’s Disease. *Am J Pathol.* 2008;173(3):665–81.
 284. Yu G, Klionsky DJ. Life and Death Decisions — The Many Faces of Autophagy in Cell Survival and Cell Death. *Biomolecules.* 2022;12(866).
 285. Young MM, Takahashi Y, Khan O, Park S, Hori T, Yun J, et al. Autophagosomal Membrane Serves as Platform for Intracellular Death-inducing Signaling Complex (iDISC) -mediated Caspase-8 Activation and Apoptosis. *J Biol Chem.* 2012;287(15):12455–68.
 286. Jung S, Jeong H, Yu S. Autophagy as a decisive process for cell death. *Exp Mol Med.* 2020;52:921–30.
 287. Bialik S, Dasari SK, Kimchi A. Autophagy-dependent cell death – where, how and why a cell eats itself to death. *J Cell Sci.* 2018;131(jcs215152).
 288. Liu Y, Shoji-kawata S, Sumpter RM, Wei Y, Ginet V, Zhang L. Autosis is a Na⁺, K⁺-ATPase – regulated form of cell death triggered by autophagy-inducing peptides, starvation, and hypoxia – ischemia. *PNAS.* 2013;110(51).
 289. Neumann M. Molecular neuropathology of TDP-43 proteinopathies. *Int J Mol Sci.* 2009;10(1):232–46.
 290. Richards RI, Robertson SA, Kastner DL. Neurodegenerative diseases have genetic hallmarks of autoinflammatory disease. *Hum Mol Genet.* 2018;27:R108–18.
 291. Geloso MC, Corvino V, Marchese E, Serrano A. The Dual Role of Microglia in ALS: Mechanisms and Therapeutic Approaches. *Front Aging Neurosci.* 2017;9(242).
 292. Clarke BE, Patani R. The microglial component of amyotrophic lateral sclerosis. *Brain.* 2020;143:3526–39.
 293. Frakes AE, Ferraiuolo L, Haidet-Phillips AM, Schmelzer L, Braun L, Miranda CJ, et al. Microglia induce motor neuron death via the classical NF-κB pathway in amyotrophic lateral sclerosis. *Neuron.* 2015;81(5):1009–23.
 294. Lall D, Baloh RH. Microglia and C9orf72 in neuroinflammation and ALS and frontotemporal dementia. *J Clin Invest.* 2017;127(9):3250–8.
 295. Fanara P, Banerjee J, Hueck R V, Harper MR, Awada M, Turner H, et al. Stabilization of Hyperdynamic Microtubules Is Neuroprotective in Amyotrophic Lateral Sclerosis. *J Biol Chem.* 2007;282(32):23465–72.
 296. Kast DJ, Dominguez R. The Cytoskeleton–Autophagy Connection. *Curr Biol.* 2017;27:R318–26.
 297. Kochl R, Hu XW, Chan EYW, Tooze SA. Microtubules Facilitate Autophagosome Formation and Fusion of Autophagosomes with Endosomes. *Traffic.* 2006;7:129–45.
 298. Maday S, Holzbaur ELF. Autophagosome biogenesis in primary neurons follows an ordered and spatially regulated pathway. *Dev Cell.* 2014;30(1):71–85.
 299. He M, Ding Y, Chu C, Tang J, Xiao Q, Luo ZG. Autophagy induction stabilizes microtubules and promotes axon regeneration after spinal cord injury. *PNAS.* 2016;113(40):11324–9.
 300. Liu X, Henty-ridilla JL. Multiple roles for the cytoskeleton in ALS. *Exp Neurol.* 2022;355(114143).
 301. Theunissen F, West PK, Brennan S, Petrović B, Hooshmand K, Akkari PA, et al. New perspectives on cytoskeletal dysregulation and mitochondrial mislocalization in amyotrophic lateral sclerosis. *Transl Neurodegener.* 2021;10(46).
 302. Simões-Pires C, Zwick V, Nurisso A, Schenker E, Carrupt PA, Cuendet M. HDAC6 as a target for neurodegenerative diseases: what makes it different from the other HDACs? *Mol Neurodegener.* 2013;8(7).
 303. Govindarajan N, Rao P, Burkhardt S, Sananbenesi F, Schlüter OM, Bradke F, et al. Reducing HDAC6 ameliorates cognitive deficits in a mouse model for Alzheimer’s disease. *EMBO Mol Med.* 2013;5(1):52–63.
 304. Taes I, Timmers M, Hersmus N, Bento-Abreu A, Van Den Bosch L, Van damme P, et al. Hdac6 deletion delays disease progression in the sod1g93a mouse model of als. *Hum Mol Genet.* 2013;22(9):1783–90.
 305. Krauss R, Bosanac T, Devraj R, Engber T, Hughes RO. Axons Matter: The Promise of Treating Neurodegenerative Disorders by Targeting SARM1-Mediated Axonal Degeneration. *Trends Pharmacol Sci.* 2020;41(4):281–93.
 306. Cappello V, Francolini M. Neuromuscular Junction Dismantling in Amyotrophic Lateral Sclerosis. *Int Immunopharmacol.* 2017;18(2092).
 307. Dadon-nachum M, Melamed E, Offen D. The “Dying-Back” Phenomenon of Motor Neurons in ALS. *J Mol Biol.* 2011;43:470–7.
 308. Verma S, Khurana S, Vats A, Sahu B, Ganguly NK, Chakraborti P, et al. Neuromuscular Junction Dysfunction in Amyotrophic Lateral Sclerosis. *Mol Neurobiol.* 2022;59:1502–27.
 309. Eisen A, Braak H, Del Tredici K, Lemon R, Ludolph AC, Kiernan MC. Cortical influences drive amyotrophic lateral sclerosis. *J Neurol Neurosurg Psychiatry.* 2017;88(11):917–24.

310. Hudson AJ, Kiernan JN. Preservation of certain voluntary muscles in motoneurone disease. *Lancet*. 1988;331(8586):652–3.
311. Eisen A. The Dying Forward Hypothesis of ALS: Tracing Its History. *Brain Sci*. 2021;11(300).
312. Baker MR. ALS — dying forward, backward or outward? *Nat Rev Neurol*. 2014;11(660).
313. Bright F, Chan G, van Hummel A, Ittner LM, Ke YD. TDP-43 and Inflammation: Implications for Amyotrophic Lateral Sclerosis and Frontotemporal Dementia. *Int J Mol Sci*. 2021;22(7781).
314. Swarup V, Phaneuf D, Dupré N, Petri S, Strong M, Kriz J, et al. Deregulation of TDP-43 in amyotrophic lateral sclerosis triggers nuclear factor κ B – mediated pathogenic pathways. *J Exp Med*. 2011;208(12):2429–47.
315. Dutta K, Thammisetty SS, Boutej H, Bareil C, Julien J. Mitigation of ALS Pathology by Neuron-Specific Inhibition of Nuclear Factor Kappa B Signaling. *Neurobiol Dis*. 2020;40(26):5137–54.
316. Kim SH, Shanware NP, Bowler MJ, Tibbetts RS. Amyotrophic lateral sclerosis-associated proteins TDP-43 and FUS/TLS function in a common biochemical complex to co-regulate HDAC6 mRNA. *J Biol Chem*. 2010;285(44):34097–105.
317. Freibaum BD, Chitta R, High A a, Taylor JP. Global analysis of TDP-43 interacting proteins reveals strong association with RNA splicing and translation machinery. *J Proteome Res*. 2010;9(2):1104–20.
318. Oberstadt M, Claßen J, Arendt T, Holzer M. TDP-43 and Cytoskeletal Proteins in ALS. *Mol Neurobiol*. 2018;55(4):3143–51.
319. Hergesheimer RC, Chami AA, Assis DR De, Vourc P, Andres CR, Corcia P. The debated toxic role of aggregated TDP-43 in amyotrophic lateral sclerosis: a resolution in sight? *Brain*. 2019;142:1176–94.
320. Vanden Broeck L, Callaerts P, Dermaut B. TDP-43-mediated neurodegeneration: towards a loss-of-function hypothesis? *Trends Mol Med*. 2014;20(2):66–71.
321. Barmada SJ, Skibinski G, Korb E, Rao EJ, Wu JY. Cytoplasmic mislocalization of TDP-43 is toxic to neurons and enhanced by a mutation associated with familial ALS. *J Neurosci*. 2010;30(2).

Curriculum Vitae

Personal information

Evelien Van Schoor

Tervuursevest 15/602, 3001 Leuven, Belgium

evelien.van.schoor@gmail.com

Education

- 2017-2022 **Doctoral training in Biomedical Sciences, KU Leuven**
Thematic program: Cognitive and Molecular Neurosciences
- 2015-2017 **Master of Science, Biomedical Sciences, Ghent University - *Summa cum laude***
Specialization: Neurosciences
- 2012-2015 **Bachelor of Science, Biomedical Sciences, Ghent University - *Magna cum laude***
- 2006-2012 **Latin-Sciences, Sint-Godelieve-Instituut, Lennik**

Competences

Languages

Dutch	Native
English	Advanced
French	Basic
Spanish	B1 level

Computer skills

Microsoft Office, Graphpad Prism, SPSS, R studio (basics), Fiji, Matlab, GIMP, Inkscape

Research skills

Immunohistochemistry, immunocytochemistry, (confocal) microscopy, qPCR, cloning, biochemistry (protein extraction, SDS-PAGE, western blot), cell culture (HeLa, SH-SY5Y, iPSC, iPSC-derived motor neurons), zebrafish work (injections, immunohistochemistry, behavioral testing), rat work (stereotactic brain surgery, electroencephalography, small animal MRI)

Courses related to the PhD training

2017

Research Integrity part I (KU Leuven)

HSE in laboratories (KU Leuven)

Supervising Master's thesis (KU Leuven)

2018

Basic statistics theory (VIB)
Initiation GIMP and Inkscape (VIB)
Image ethics and poster design (VIB)
Basic statistics in R (VIB)
How to prepare for a grant interview (VIB)
Creating effective posters (VIB)

2019

Scientific writing and publishing (VIB)

2020

Research Integrity part II (KU Leuven)
Basics on Regulatory Requirements in Clinical Research (ECCRT via KU Leuven)
Scientific writing and oral presentations (VIB)

2021

Introduction to medical writing (VIB)
Regulatory Medical Writing Training Programme (VIB)
How to boost your (digital) meeting skills (VIB)
Stress and resilience for researchers (KU Leuven)
How to write a good CV & cover letter (KU Leuven)

2022

Career guidance course (VIB)
Discover your career profile (KU Leuven)

Conference attendance

ENCALS (European Network to Cure ALS) meeting, Tours, 15.05.19 – 17.05.19

Poster: An FTLD case with a *TUBA4A* mutation and TDP-43 pathology.

MNDA (Motor Neuron Disease Association) meeting, Montreal (online), 09.12.20 – 11.12.20

Poster: Necrosome-positive granulovacuolar degeneration is associated with hippocampal TDP-43 in ALS/FTLD.

SFN (Society for Neuroscience) meeting, Chicago (online), 08.11.21 – 11.11.21

Poster: *TUBA4A* knockdown in zebrafish recapitulates ALS-related abnormalities.

ENCALS (European Network to Cure ALS) meeting, Edinburgh, 01.06.22 – 03.06.22

Poster: Increased cleaved GSDMD expression in white matter microglia is associated with neuronal loss in the ALS motor cortex.

Grants

FWO-SB PhD Fellowship (2019-2022) (1S46219N)

Travel grant FWO (SFN meeting Chicago 08.11.21 – 11.11.21; online due to covid)

Supervisions

Lab rotation student Biomedical Sciences (10 days)

March 2018 – April 2018	Tessa Robberechts
November 2018 – December 2018	Eline Vonck
November 2019 – December 2019	Britt Tilkin

Summer student research (20 days)

August 2019	Dufie Strubbe
-------------	---------------

Student internship (11 months)

September 2020 – July 2021	Maria Georgopoulou
----------------------------	--------------------

Master student Biomedical Sciences (10 months)

October 2020 – June 2021	Orkun Ok
September 2021 – June 2022	Annelies Belet

Teaching / outreach activities

Day of Science

November 2018	Interactive booth
November 2021	Online lecture

Kinderuniversiteit

October 2020	Interactive lecture
September 2021	Interactive lecture + workshop

Wetenschap op Stap (Science on the go)

March 2022	Lecture + workshop in primary school
------------	--------------------------------------

Brain Awareness Week (Leuven Brain Institute)

March 2022	Lecture on brain donation
------------	---------------------------

Publications

Van Schoor, E., Ospitalieri, S., Moonen, S., Tomé, S.O., Ronisz, A., Ok, O., Weishaupt, J., Ludolph, A.C., Van Damme, P., Van Den Bosch, L., Thal, D.R. (2022) Increased pyroptosis activation in white matter microglia is associated with neuronal loss in ALS motor cortex. *ACTA NEUROPATHOLOGICA*, 144, 393-411.

Van Schoor, E., Vandenbulcke, M., Bercier, V., Vandenberghe, R., van der Zee, J., Van Broeckhoven, C., Otto, M., Hanseeuws, B., Van Damme, P., Van Den Bosch, L., Thal, D.R. (2022) Frontotemporal Lobar Degeneration Case with an N-terminal TUBA4A Mutation Exhibits Reduced TUBA4A Levels in the Brain and TDP-43 Pathology. *BIOMOLECULES*, 12 (3), Art.No. 440.

Van Schoor, E., Koper, M.J., Ospitalieri, S., Dedeene, L., Tomé, S.O., Vandenberghe, R., Brenner, D., Otto, M., Weishaupt, J., Ludolph, A.C., Van Damme, P., Van Den Bosch, L., Thal, D.R. (2020). Necrosome-positive granulovacuolar degeneration is associated with TDP-43 pathological lesions in

the hippocampus of ALS/FTLD cases. *NEUROPATHOLOGY AND APPLIED NEUROBIOLOGY*, 47 (2), 328-345.

Koper, M.J., Tomé, S.O., Gawor, K., Belet, A., **Van Schoor, E.**, Schaeverbeke, J., Vandenberghe, R., Vandembulcke, M., Ghebremedhin, E., Otto, M., von Arnim, C.A.F., Balusu, S., Blaschko, M.B., De Strooper, B., Thal, D.R. (2022). LATE-NC aggravates GVD-mediated necroptosis in Alzheimer's disease. *ACTA NEUROPATHOLOGICA COMMUNICATIONS*, 10 Art.No. 128.

Guo, W., Wang, H., Tharkeshwar, A.K., Couthouis, J., Braems, E., Masrori, P., **Van Schoor, E.**, Fan, Y., Ahuja, K., Moisse, M., Jacquemyn, M., Minner, K., Madeiro da Costa, R.F., Gajjar, M., Balusu, S., Tricot, T., Fumagalli, L., Hersmus, N., Jank, R., Impens, F., Vandenberghe, P., Ho, R., Thal, D.R., Hedge, M., Chandran, S., De Strooper, B., Daelemans, D., Van Damme, P., Van Den Bosch, L., Verfaillie, C. (2022). CRISPR/Cas9 screen in human iPSC-derived cortical neurons identifies NEK6 as a novel disease modifier of C9orf72 poly(PR) toxicity. *ALZHEIMER'S AND DEMENTIA* (published online).

Braems, E., Bercier, V., **Van Schoor, E.**, Heeren, K., Beckers, J., Fumagalli, L., Dedeene, L., Moisse, M., Geudens, I., Hersmus, N., Ho, R., Selvaraj, B., Chandran, S., Thal, D.R., Van Damme, P., Swinnen, B., Van Den Bosch, L. (2022) HNRNPK alleviates RNA toxicity by counteracting DNA damage in C9orf72 ALS. *ACTA NEUROPATHOLOGICA*, 144, 465-488.

Dedeene, L., **Van Schoor, E.**, Ospitalieri, S., Ronisz, A., Weishaupt, J.H., Otto, M., Ludolph, A.C., Scheuerle, A., Vandenberghe, R., Van Damme, P., Poesen, K., Thal, D.R. with Poesen, K. (joint last author), Van Damme, P. (joint last author), Thal, D.R. (joint last author) (2020). Dipeptide repeat protein and TDP-43 pathology along the hypothalamic-pituitary axis in C9orf72 and non-C9orf72 ALS and FTLD-TDP cases. *ACTA NEUROPATHOLOGICA*, 140 (5), 777-781.

Tome, S.O., Vandenberghe, R., Ospitalieri, S., **Van Schoor, E.**, Tousseyn, T., Otto, M., von Arnim, C.A.F., Thal, D.R. (2020). Distinct molecular patterns of TDP-43 pathology in Alzheimer's disease: relationship with clinical phenotypes. *ACTA NEUROPATHOLOGICA COMMUNICATIONS*, 8, Art.No. 61.

Van Weehaeghe, D., **Van Schoor, E.**, De Vocht, J., Koole, M., Attili, B., Celen, S., Declercq, L., Thal, D.R., Van Damme, P., Bormans, G., Van Laere, K. (2020). TSPO Versus P2X7 as a Target for Neuroinflammation: An In Vitro and In Vivo Study. *JOURNAL OF NUCLEAR MEDICINE*, 61 (4), 604-607.

Koper, M.J., **Van Schoor, E.**, Ospitalieri, S., Vandenberghe, R., Vandembulcke, M., von Arnim, C.A.F., Tousseyn, T., Balusu, S., De Strooper, B., Thal, D.R. (2019). Necrosome complex detected in granulovacuolar degeneration is associated with neuronal loss in Alzheimer's disease. *ACTA NEUROPATHOLOGICA*, 139 (3), 463-484.

Dedeene, L., **Van Schoor, E.**, Vandenberghe, R., Van Damme, P., Poesen, K., Thal, D.R. with Van Damme, P. (joint last author), Poesen, K. (joint last author) (2019). Circadian sleep/wake-associated cells show dipeptide repeat protein aggregates in C9orf72-related ALS and FTLD cases. *ACTA NEUROPATHOLOGICA COMMUNICATIONS*, 7, Art.No. 189.

Dedeene, L., **Van Schoor, E.**, Race, V., Moisse, M., Vandenberghe, R., Poesen, K., Van Damme, P., Thal, D.R. with Poesen, K. (joint last author) (2019). An ALS case with 38 (G4C2)-repeats in the C9orf72 gene shows TDP-43 and sparse dipeptide repeat protein pathology. *ACTA NEUROPATHOLOGICA*, 137 (5), 855-858.